Satellite-derived shoreline data assimilation for sandy coast evolution

Georgios Azorakos

▶ **To cite this version:**

Georgios Azorakos. Satellite-derived shoreline data assimilation for sandy coast evolution. Environmental Sciences. Université de Bordeaux, 2025. English. ⟨NNT : 2025BORD0349⟩. ⟨tel-05505134⟩

HAL Id: tel-05505134

https://theses.hal.science/tel-05505134v1

Submitted on 11 Feb 2026

HAL is a multi-disciplinary open access archive for the deposit and dissemination of scientific research documents, whether they are published or not. The documents may come from teaching and research institutions in France or abroad, or from public or private research centers.

L'archive ouverte pluridisciplinaire **HAL**, est destinée au dépôt et à la diffusion de documents scientifiques de niveau recherche, publiés ou non, émanant des établissements d'enseignement et de recherche français ou étrangers, des laboratoires publics ou privés.

HAL Authorization

université de BORDEAUX

THÈSE PRÉSENTÉE
POUR OBTENIR LE GRADE DE

DOCTEUR DE
L'UNIVERSITÉ DE BORDEAUX

ÉCOLE DOCTORALE SCIENCES ET ENVIRONNEMENTS

SPÉCIALITÉ: PHYSIQUE DE L'ENVIRONNEMENT

Par Georgios AZORAKOS

Assimilation de données satellitaires du trait de côte pour la modélisation des évolutions des littoraux sableux

Sous la direction de: **Dr. Bruno CASTELLE et Dr. Déborah IDIER**

Soutenance prévue le 8 décembre 2025

Membres du jury:

M. **Bruno CASTELLE**	Directeur de Recherche CNRS, Université de Bordeaux	Directeur de thèse
Mme **Déborah IDIER**	Directrice de Recherche, BRGM	Co-Directrice de thèse
Mme. **Marissa YATES**	Chargée de Recherche, Ecole des Ponts / Laboratoire d'Hydraulique Saint-Venant	Rapporteure
M. **Rafael ALMAR**	Directeur de Recherche, IRD	Rapporteur
Mme. **Francesca RIBAS PRATS**	Associate Professor, Universitat Politècnica de Catalunya	Examinatrice
M. **Stéphane BERTIN**	Chargé de Recherche, CNRS	Examinateur
M. **Didier SWINGEDOUW**	Directeur de Recherche CNRS, Université de Bordeaux	Examinateur

Membre invité:

M. **Vincent MARIEU**	Ingénieur de Recherche CNRS, Université de Bordeaux

- 2025 -

Résumé

Comprendre et prédire l'évolution des littoraux sableux reste un défi central de la dynamique littorale et une condition essentielle pour une gestion durable. Des prévisions fiables exigent des observations cohérentes et des modèles capables de représenter des comportements morphodynamiques complexes et non stationnaires. Cette thèse fait progresser la modélisation de l'évolution du trait de côte en intégrant des données publiques — principalement des traits de côte dérivés de satellites (SDS) — dans des cadres de calibration et d'assimilation de données, afin d'en évaluer la valeur ajoutée. En s'appuyant uniquement sur des données libres d'accès, le travail établit une base de modélisation transparente et transférable, adaptée même aux environnements littoraux disposant de données limitées.

La première partie concerne les modèles 1D d'équilibre, calibrés à partir de données SDS brutes et bruitées, sans correction de marée ni connaissance préalable du site. Grâce à un algorithme de recuit simulé, des calibrations robustes ont été obtenues au Truc Vert, site exposé et énergique du littoral atlantique. Les bons résultats obtenus dans ces conditions conservatrices démontrent que des informations pertinentes peuvent être extraites de données satellitaires de qualité modeste, soutenant ainsi leur usage pour la modélisation du trait de côte ayant un comportement d'équilibre.

L'assimilation séquentielle de données SDS s'est révélée plus complexe, le bruit des données limitant la capacité du modèle à suivre la non-stationnarité du système. Des observations in situ ont été utilisées pour explorer le rôle potentiel de paramètres ajustables variables dans le temps et leur lien avec le climat de houle. Les résultats, issus de plusieurs sites de la côte atlantique européenne, indiquent un lien faible ou absent avec le climat de vagues, suggérant que la non-stationnarité traduit avant tout des ajustements morphodynamiques locaux. Les modèles non stationnaires ont montré une amélioration modérée sur certains sites et une baisse de performance sur d'autres, influencées par la qualité des données — les sites les mieux documentés bénéficiant le plus. Ces modèles se sont toutefois distingués par une meilleure reproduction des épisodes d'érosion extrême, illustrant leur potentiel pour représenter des événements rares liés à des conditions de forçage éloignées de la moyenne. Des progrès plus marqués nécessiteraient cependant des contextes soumis à des climats de houle multimodaux.

En combinant calibration et assimilation dans une expérience internationale menée sur un site australien documenté par des images satellite et photographies aériennes anaciennes, deux modèles d'équilibre ont été couplés dans une approche hybride, montrant leur complémentarité. Cette stratégie ad hoc illustre le potentiel de modèles hybrides pour représenter la dynamique multi-échelle du trait de côte dans des cadres à complexité réduite.

Enfin, le cadre a été étendu à une configuration quasi 2D utilisant une assimilation en grille par "nudging". Appliquée à la flèche sableuse de Sacalin, dans le delta du Danube, cette approche

a permis de contraindre efficacement l'évolution spatiale du trait de côte et d'améliorer la concordance avec les observations satellitaires à long terme. Bien que les interactions entre cellules voisines ne soient pas encore prises en compte, cette avancée marque une étape importante vers une assimilation pleinement bidimensionnelle, capable de représenter les rétroactions spatiales dans l'évolution des côtes sableuses.

Dans l'ensemble, cette thèse montre que la combinaison d'observations satellitaires long terme, de modèles hybrides et d'assimilation de données constitue une voie prometteuse pour améliorer la compréhension, la prévision et, à terme, la modélisation opérationnelle de l'évolution du trait de côte dans des environnements littoraux complexes.

Abstract

Understanding and predicting the evolution of sandy shorelines remains a central challenge in coastal science and a critical requirement for sustainable management. Reliable predictions require consistent observations and models capable of representing complex, non-stationary morphodynamic behaviour. This thesis advances shoreline change modelling by integrating publicly available datasets—primarily satellite-derived shoreline (SDS) observations—within calibration and data assimilation frameworks, assessing their added value. By relying exclusively on freely accessible data, the work establishes a transparent, transferable modelling foundation applicable even in data-limited coastal environments.

The initial focus is on 1D equilibrium shoreline models, addressing calibration using uncorrected, noisy SDS data without tidal adjustments or a priori site knowledge. Using a simulated annealing algorithm, robust model calibrations were achieved at Truc Vert beach, a fully exposed, wave-dominated site with high-energy waves, large tides, complex intertidal bathymetry, and mild nearshore slopes that introduce substantial observational uncertainty. The strong model performance under these challenging and conservative conditions demonstrates that valuable information can be extracted from low-quality SDS, supporting broader applicability where simple equilibrium models are suitable.

Applying uncorrected SDS in sequential data assimilation proved more challenging due to observation noise limiting the algorithm's ability to track system non-stationarity. To explore the potential of time-varying model free parameters, in situ observations were used to assess links to wave climate and influence on predictive skill. Across multiple sites along the European Atlantic coast, the connection between parameter variability and climate was weak or absent, suggesting non-stationarity primarily reflects local morphodynamic adjustments. Non-stationary models showed slightly improved performance at some sites and reduced skill at others, with data quality influencing outcomes—sites with higher-quality observations benefited more. Notably, non-stationary models captured extremes of erosion, demonstrating their potential for representing rare but significant events, though stronger gains would require regions with multimodal wave climates.

Building on these insights, calibration and data assimilation were combined in an international benchmark experiment at a site in Australia documented with SDS data and historical aerial photographs. Two distinct equilibrium-based models were explicitly coupled within a hybrid framework, illustrating how calibration and assimilation can complement each other. This approach highlights the potential of ad hoc hybrid modelling strategies that merge separate empirical formulations to capture multi-scale shoreline dynamics within reduced-complexity frameworks.

Finally, the framework was extended to a quasi-2D configuration using grid-based data assimilation with spatial nudging. Applied to the highly dynamic Sacalin spit in the southern Danube delta, where dominant processes are not explicitly represented in the model, the approach suc-

cessfully constrained shoreline evolution across the grid and improved agreement with long-term satellite observations. Although neighbouring grid dependencies were not yet considered, this implementation represents a critical step toward fully 2D assimilation capable of resolving spatial feedbacks in shoreline evolution.

Overall, this work demonstrates that combining long-term satellite observations with hybrid modelling and data assimilation provides a powerful pathway for advancing understanding, prediction, and eventually operational forecasting of shoreline change in complex coastal systems.

Acknowledgements

I would like to thank everyone who supported me during this period and contributed to this unforgettable experience.

First and foremost, I would like to express my sincere gratitude to Bruno Castelle and Déborah Idier for their guidance, support, and patience over the past three years. It was a true pleasure to work alongside them, as they consistently challenged me academically while also supporting me as a colleague, making sure that I took the well-deserved and necessary breaks from the constant flow of events and thoughts that accompany a PhD thesis. I would also like to thank Vincent Marieu for his mental coaching, constant distractions, and occasional skepticism, all of which played an important role in shaping this work.

I am grateful to the members of my supervisory committee, Henrique Cabral, Sean Vitousek, and Mark Davidson, for ensuring both the academic quality of this work and my personal well-being throughout the PhD. I also thank the members of the jury, the two reviewers Marissa Yates and Raphaël Almar for their constructive feedback on the manuscript and for the insightful comments and stimulating discussions during and after the defence, the examiners Francesca Ribas and Stéphane Bertin, and the President of the jury Didier Swingedouw for their valuable remarks and engaging conversations during the defence.

I would also like to acknowledge the contribution of my "grand supervisor" Philippe Bonneton for making lunch an interesting and always stimulating experience, Kevin Martins for constantly raising the bar, and Maurizio D'Anna, who is always motivated to help and never short of enthusiasm when it comes to discussing shoreline modelling with me.

I would like to thank my colleagues at the METHYS lab, who had the patience to work alongside me over the past three years. Elsa, Mohammad, Betty, Marine, Carlos, Charlene, Emilie, Jacques l'océanographe, Juliette, Vania, Mila, Domi le rider, Martin, and of course my partner in crime, the other half of "Yogurt and Nirvana," Ivana Mingo, whom I can proudly call my friend.

I would also like to acknowledge my extended family of colleagues within the French academic community, in particular Salomé Frugier and Marcan Graffin, for setting high standards and for making me look forward to every opportunity to cross paths with them around the globe.

I would like to acknowledge my colleagues and friends Raimundo Ibaceta, Kilian Vos, and Kristen Splinter for supporting my academic endeavours from the moment I met them. I also extend my gratitude to my professor at the Technical University of Denmark, David Fuhrman, and to my co-supervisor during my Master's thesis, Bjarke Eltard Larsen, for helping to build the foundation that allowed me to pursue a PhD in coastal sciences. Finally, I acknowledge the influence of my professor at the Technical University of Athens, Ioannis Sympetheros, through whom I first developed an interest in coastal and marine engineering.

I also wish to thank my dear friend Clément Bouvier for always being there when I needed a

serious discussion, almost always over a beer, about life-changing decisions, and for being instrumental in my decision to apply for a PhD at the University of Bordeaux.

Finally, I would like to thank my family, my parents Sampson Azorakos and Melina Bitziou, and my two brothers Dimitris and Haris, for their constant support at every step of the way and for being the best role models one could ask for.

Last but not least, I would like to thank Marie and my extended family of friends for being there for me and helping me stay sane throughout the process. Andreea, Fabro, Emy, Pierre, Margot, Alejo, Pietro, Monsieur le Maire, Luc, Coco, Jessie, Saumon, David, Tim, Nano, Vaggelis, Pamela, Dino, Ntino, Angelica, Yuri, and so many more who could not possibly fit in a single book, but you know who you are.

Merci à toutes et tous pour la vie d'océanographe.

Contents

Résumé, Abstract . . . iv
Acknowledgement, Remerciments . . . vi
Table of figures . . . x
List of tables . . . xx

1 Introduction **1**
1.1 General context . . . 2
1.2 Thesis objective . . . 6
1.3 Organisation of the manuscript . . . 7
1.4 Acknowledgements . . . 9

2 State of the art **11**
2.1 Introduction . . . 12
2.2 Shoreline definition . . . 14
2.3 Sandy shoreline response in wave dominated environments . . . 20
2.4 Shoreline observations . . . 22
2.4.1 Nearshore remote sensing . . . 23
2.4.2 Coastal cameras . . . 24
2.4.3 In-situ surveys . . . 25
2.4.4 Airborne observations . . . 28
2.4.5 Historical shoreline observations . . . 29
2.4.6 Earth observing satellites . . . 30
2.5 Shoreline change modelling . . . 33
2.5.1 Semi empirical models . . . 35
2.5.2 Reduced complexity models . . . 38
2.5.3 Hybrid shoreline models . . . 39
2.5.4 State of the art in shoreline change modelling . . . 41
2.5.5 Model Calibration . . . 42
2.5.6 Data assimilation in shoreline change modelling . . . 43
2.6 Contribution of the present work . . . 47

3 Satellite-derived equilibrium shoreline modelling at a high-energy meso-macrotidal beach **51**
3.1 Introduction . . . 52
3.2 Field site and data . . . 54
3.2.1 Truc Vert beach . . . 54
3.2.2 Wave Data . . . 56
3.2.3 Shoreline Data . . . 56
3.3 Shoreline numerical modelling . . . 58
3.3.1 Equilibrium shoreline model . . . 58
3.3.2 Calibration . . . 59
3.3.3 Simulation setup . . . 60
3.4 Results . . . 62
3.4.1 Model calibration with different datasets . . . 62
3.4.2 How much data is enough ? . . . 64
3.5 Discussion . . . 70
3.6 Conclusion . . . 74

4 Investigating the potential of time varying free parameters in equilibrium shoreline change models through data assimilation **75**
4.1 Introduction . . . 76
4.2 Study sites, data & methodology . . . 77
4.2.1 Study sites . . . 77
4.2.2 Wave and shoreline data . . . 77
4.2.3 Equilibrium shoreline model . . . 80
4.2.4 Data assimilation . . . 81
4.3 Results . . . 82
4.4 Discussion . . . 83
4.5 Conclusions . . . 85

5 Blind testing of a hybrid equilibrium shoreline model - ShoreShop 2.0 **87**
5.1 Introduction . . . 88
5.2 Study site and data . . . 88
5.3 Shoreline Variability . . . 89
5.4 Hybrid shoreline model . . . 93
5.4.1 Equilibrium based shoreline rotation model . . . 93
5.4.2 Equilibrium based cross shore transport model . . . 94
5.4.3 Model calibration . . . 95
5.4.4 Model guidance through data assimilation . . . 95
5.5 Discussion . . . 97

6 2D Satellite-derived data assimilation in LX-Shore model. Investigation on the Sacalin spit, in The Danube Delta. 101
6.1 Introduction . . . 102
6.2 Methodology . . . 103
6.2.1 Satellite derived sediment fraction grid . . . 103
6.2.2 LX-Shore model . . . 106
6.2.3 Data assimilation method . . . 107
6.3 Study site, datasets and model setup . . . 109
6.3.1 Study site . . . 109
6.3.2 Satellite derived observations . . . 112
6.3.3 Preliminary analysis of the satellite-derived observations: evolution of the Sacalin spit . . . 113
6.3.4 LX-Shore model setup . . . 118
6.4 Results . . . 123
6.4.1 Data assimilation in LX-Shore . . . 125
6.5 Discussion . . . 129
6.6 Conclusions . . . 132

7 Conclusion and future perspectives 135
7.1 Conclusions . . . 135
7.2 Future perspectives . . . 137
Bibliographie . . . 141

Table of figures

1.1 Global distribution of sandy shorelines derived from satellite imagery; the coloured dots along the world's shoreline represent the local percentage of sandy shorelines (yellow is sand, dark brown is non-sand). The subplot to the right presents the relative occurrence of sandy shorelines per degree latitude, where the dashed line shows the latitudinal distribution of sandy shorelines reported by Hayes (1967). The lower subplot presents the relative occurrence of sandy shorelines per degree longitude. The curved, dashed grey lines in the main plot represent the boundaries of the ice-free shorelines considered in the analysis. The underlined percentages indicate the percentages of sandy shorelines averaged per continent. The figure is borrowed from Luijendijk et al. (2018). 2

1.2 Schematic example of sandy coast environments and landforms, taken from the SHORMOSAT project proposal. 3

1.3 Example of different sandy beaches. a, Bungan beach , New South Wales , Australia (August 2018). b, Truc Vert beach, Nouvelle Acquitaine, France (May 2023). c, Porsmilin beach, Brittany, France (March 2025). d, Collaroy beach, New South Wales Australia (August 2018). 3

1.4 Global coastal population distribution within 50 km from the coast in 2018. The figure is borrowed from Cosby et al. (2024). 4

1.5 Work package structure of the SHORMOSAT project, taken from the SHORMOSAT project proposal. 7

2.1 Illustration of commonly used shoreline indicators found in the literature. The figure is borrowed from Boak and Turner (2005). 15

2.2 Tentative classification of ocean waves according to wave period. The forces responsible for various portions of the spectrum are shown. The relative amplitude is indicated by the curve. The figure is modified from Holthuijsen (2007). 16

2.3 Example of visually defined shoreline proxies at Truc Vert beach, Nouvelle Aquitaine, southwest France. Picture captured by Vincent Marieu during a spring low tide in June 2014 with an Unmanned Airborne Vehicle (UAV). 17

2.4 a - d Satellite images of Truc Vert beach at different stages of the tide obtained from Sentinel 2 images between June and July 2022. e - f Beach profiles measured during spring low tide, over a 4 km window with an alongshore spacing of 20 m at Truc Vert. Surveys were performed with an RTK GNSS system mounted on an ATV. The measured profiles are indicated as grey transparent lines in panel a. . . . 18

2.5 Schematic representation of the coupled beach morphodynamic system and spatiotemporal representation of the primary modes of sandy beach variability and their drivers, modified after Castelle and Masselink (2023). 21

2.6 Sources of shoreline observations and the spatio-temporal scales they resolve. . . . 22

2.7 Setup of the field experiment of Martins et al. (2018) showing the field site and LiDAR scanner deployment. Regional map (a). (b) The LiDAR scanner deployment on the nearshore pier. (c) A schematic of the experimental setup of the Terrestrial Laser Scanners (TLS), pressure transducers (PT) and Acoustic Doppler Velocimeters (ADV), with an example of postprocessed free surface elevation (black thick line). The beach profile (thick grey line) corresponds to the surveyed profile during the previous low tide (10 April 2016). 23

2.8 Example of an ARGUS camera system (Holman and Stanley, 2007) installed to monitor the southern part of the Narrabeen-Collaroy embayment in New South Wales , Australia. Image is downmoaded from the Narrabeen data repository `http://narrabeen.wrl.unsw.edu.au/`. 24

2.9 Example of beach profile survey using the Emery (1961) method in Narrabeen beach. The image has been downloaded from the Narrabeen data repository `http://narrabeen.wrl.unsw.edu.au/`. 26

2.10 Locations of monitored sites worldwide that continue to conduct high frequency in-situ shoreline surveys spanning more than a decade with publicly available datasets. 26

2.11 Survey site. Panel a, Location map of Truc Vert beach, southwest France with location of nearby wave buoy. Panel b, GNSS-equipped ATV used to perform the monthly to bimonthly surveys since 2003. Panel c, Aerial view showing the remote Truc Vert beach with prominent rip channels. Panel d, Survey zone and reference frame used at Truc Vert beach. The figure is borrowed from Castelle et al. (2020). . 27

2.12 Timeline for the major civilian Earth observation satellites operating optical imaging sensors with global coverage. Arrows indicate the mission is ongoing and the operating entity is indicated by the fill defined in the legend of the figure. 31

2.13 Schematic representation of common waterline detection workflow algorithms. . . 32

2.14 Spatiotemporal representation of the primary modes of sandy beach variability and their drivers, including typical spatial and temporal scales resolved by the different model classes. The figure is inspired by and aspects of it have been modified from Castelle and Masselink (2023) & Hunt et al. (2023). 34

2.15 Schematic representation of the relationship between model complexity and data requirements modified after Hunt et al. (2023). 35

2.16 Schematic representation illustrating the setup and important variables of the transect based CoSMoS-COAST shoreline model. The figure is borrowed by Vitousek et al. (2023b) 40

2.17 Overview of the architecture of the LX-Shore model and main features and processes integrated. Panel a, Model architecture. Panel b, Example of a plan-view coastal area used in the model. Panel c, Example of the longshore and cross-shore sediment transports rate calculations. Figure is borrowed by Robinet et al. (2018). . 41

2.18 Example of reduced complexity/hybrid model calibration using a non-linear optimization method. 43

2.19 Conceptual illustration of including an analysis step in shoreline change simulations to assimilate data into the model and improve predictive skill. The figure was taken from the SHORMOSAT project proposal. 44

2.20 Data assimilation process following statistical and variational approaches. Please, note that the uncertainty in the state and in the observations are characterized by their covariance matrices. The figure is borrowed from Alvarez-Cuesta et al. (2024). 46

3.1 (a) Survey zone and reference frame at Truc Vert beach. (b) Location map of Truc Vert beach, southwest France indicating the position of the CANDHIS wave buoy (Cap Ferret wave buoy 03302). (c) Overview of the area. Winter (d) and summer (e) profiles measured in 2022. The thick black line indicates the alongshore average profile, while the gray lines are the individual profiles extracted every $\sim$20 m from the alongshore window considered. 55

3.2 Offshore wave conditions during the period considered in the present work extracted at the location of the buoy (see Figure 3.1). The significant wave height H_s, peak wave period T_p and mean wave direction (MWD) are depicted in the upper, middle and lower panel of the figure. The alongshore averaged surveyed shoreline positions are plotted on the right axis of the upper panel. 57

3.3 The four different satellite derived shorelines are depicted together with the in situ derived single transect (S_{IS}) and alongshore averaged ($\overline{S_{IS}}$) +1.5 m AMSL shoreline proxy. The $RMSE$, R^2 and $bias$ compared to the $\overline{S_{IS}}$ and S_{IS} as well as the total number of unique observations N for each data set are indicated in the legend. 59

3.4 Model results using the simulating annealing algorithm to calibrate the model over the entire period based on the five different datasets and comparing with the in-situ derived shoreline data $\overline{S_{IS}}$ (blue dots) and S_{IS} (blue triangles). Performance metrics and calibrated model parameters are indicated in each panel. 63

3.5 Performance indicators ($RMSE$ and R^2) of the model when calibrated using the alongshore averaged satellite derived waterline ($\overline{W_S}$) with a varying alongshore window size. The performance indicators of the model results are calculated against in-situ shoreline data with a matching window size ($\overline{S_{IS}}(y)$). Each box summarizes the results of 10 calibration runs. The horizontal red line inside the box, indicates the median value and the top and bottom edges of the blue boxes indicate the 25th and 75th percentiles respectively. Maximum whisker length extends up to 1.5 times the interquantile range and any value outside this range is considered an outlier and depicted as a red cross. 64

3.6 Model performance calibrated using synthetic shoreline with 0 % noise subsampled at dt = 7, 30, 90 and 365 days. $RMSE$ and R^2 plotted in the left and right column respectively, are calculated based on the daily subsampled synthetic shoreline considering the period following the calibration. The squares and the circles represent the mean and standard deviation of an ensemble of 10 simulations. 65

3.7 Model performance calibrated using synthetic shoreline with 200 % noise subsampled at dt = 7, 30, 90 and 365 days. $RMSE$ and R^2 plotted in the left and right column respectively, are calculated based on the daily subsampled synthetic shoreline considering the period following the calibration. The squares and the circles represent the mean and standard deviation of an ensemble of 10 simulations. 66

3.8 Model results of the investigation on the sufficient calibration window for all four alongshore averaged datasets. The considered calibration periods are indicated in the upper panel, transitioning from red to black as the calibration duration increases. The simulated shorelines are plotted in red for the model calibration finishing at 07/2009 gradually transitioning to black as the calibration window increases. Model performance was evaluated against the $\overline{S_{IS}}$ dataset considering the period following the calibration. 67

3.9 Model performance calibrated using the four alongshore averaged observed datasets, evaluated against the $\overline{S_{IS}}$ dataset considering the period following the calibration. $RMSE$ and R^2 plotted in the left and right column respectively. The squares and the circles represent the mean and standard deviation of an ensemble of 10 simulations. 68

3.10 Predicted shoreline obtained from an ensemble of 30 different model calibrations using N number of randomly selected points from the $\overline{W_S}$ data set. The ensemble mean is plotted in red while all the rest are plotted in light grey. The model's performance is evaluated against the $\overline{S_{IS}}$ (blue dots). The amount of data points N_{max} used for the calibration of the model is indicated in the legend together with the average performance indicators $\overline{RMSE}$ and $\overline{R^2}$ of the ensemble. 69

3.11 Performance indicators $RMSE$ and R^2 depicted in the lower and upper panel of the figure plotted against the number of data points used for the calibration. Each box corresponds to an ensemble of 30 simulations using N amount of data points randomly selected from the $\overline{W_S}$ dataset. The horizontal red line inside the boxes, indicates the median value and the top and bottom edges of the blue boxes indicate the 25th and 75th percentiles respectively. Maximum whisker length extends up to 1.5 times the interquantile range and any value outside this range is considered an outlier and depicted as a red cross. 70

4.1 (a - b) Location of the three study sites along the west coast of Europe. (c) Perranporth beach and the wave buoy location (red dot). (d) Overview of the monitored area of Perranporth beach. (e) Porsmilin beach and the wave extraction grid point location (red dot). (f) Close-up view of Porsmilin beach. (g) Truc Vert beach and the wave extraction grid point location (red dot). (h) close-up view of the monitored area at Truc Vert. (i - k) Available wave conditions at the three sites. Wave height (H_s) measured/extracted is indicated by the coloured dots together with the three month moving mean $\overline{H_s}$ (black solid line) and $\overline{T_p}$ (grey dashed line, plotted in the right axis). Incoming wave direction is represented by colour, with the triangle indicating the mean incoming wave direction and the blue–red shading illustrating the directional spread around this mean. 78

4.2 Normalized timeseries of shoreline fluctuation around the mean position $X/\sigma(X)$ in Perranporth (a), Porsmilin (b) and Truc Vert (c). The shoreline proxy, vertical datum used at each site, and standard deviation of shoreline position $\sigma(X)$, are indicated in the legend. The start of winter (1 December) and summer (1 April) are marked by blue circles and black squares on the nearest observations, respectively. (f) Normalized shoreline change $\Delta X/\sigma(X)$ in Perranporth versus seasonal normalized wave height fluctuations around the mean $(H_s - \overline{H_s})/H_s$ depicted in black squares and blue dots for summer and winter respectively. (e) Seasonal $\Delta X/\sigma(X)$ versus the shoreline position at the beginning of the season $X_0/\sigma(X)$ in Perranporth. (f - i) depict the same results for Porsmilin and Truc Vert. The seasonal and total coefficient of determination R^2 are indicated in each panel. . . . 79

4.3 (a - c) simulated shoreline timeseries produced by the stationary S (solid black line) and non-stationary NS model (dashed blue line) depicted together with the shoreline observations (red dots) at all three sites. Model skill (loss function) is indicated in the legend as L. (e - g) time series of non-stationary model free parameters for Perranporth (magenta solid line), Porsmilin (blue dashed line) and Truc Vert (black dashed/dotted line). Non-stationary parameters have been normalized using the value of the corresponding stationary model free parameter. (h) ERA5 timeseries of instantaneous (black dots) and monthly averaged (red line) H_s extracted offshore of Truc Vert. Winter period (December - March) is illustrated by the shaded background. 83

4.4 Changes in normalized beach memory ϕ/ϕ_{ST} between April and November plotted against winter normalized H_s. 84

5.1 Study site and input data. (a) Location of BeachX. Inset wave rose shows the location and distribution of offshore waves from ERA5. (b) Detailed map of BeachX (Curl Curl Beach, New South Wales, Australia). The color gradient at the seaside indicates bathymetry. Yellow lines represent transects. Red dots show the location of nearshore waves. (c) Nearshore (depth = 10 m) wave roses for transects 2, 5 and 8. The red solid line represents the mean beach orientation. (d) Significant wave height H_s, (e) peak wave period T_p, (f) mean wave direction Dir, (g) annual mean sea level and its trend. (h) Spatio-temporal distribution of relative (de-meaned) shoreline position (blue/negative values indicating erosion and red/positive values indicating accretion). Basemaps: CartoDB Positron (©OpenStreetMap contributors) in panel a; Esri World Imagery (© Esri — Source: Esri, i-cubed, USDA, USGS, AEX, GeoEye, Getmapping, Aerogrid, IGN, IGP, UPR-EGP and the GIS User Community) in panel b. Basemap tiles are accessed via the Contextily Python package. The figure is borrowed from Mao et al. (2025) 90

5.2 Shoreline transects T1 to T9 with the target transects plotted in blue. Shoreline observation are plotted as red points and a linear regression of the initial shoreline position at each transect is plotted as a dashed line. The red line indicates the orientation of the beach α_s relative to the north. 91

5.3 Upper panel: Beach orientation index (BOI) calculated using Equation 5.1. Lower panel: Significant wave height and direction plotted in colour of the incoming waves extracted at the offshore point of transect 2. 92

5.4 Panel a, observed and simulated beach rotation. Panel b, cross shoreline evolution of the profile due to beach rotation. Panel c, d cross shore component of shoreline evolution after modelled rotation influence has been subtracted. Panel e, observed and simulated shoreline evolution accounting for both rotation of the beach and cross shore sediment transport. 94

5.5 Observed (red dots) and simulated (black line) shoreline position timeseries during the calibration period for all three target transects. The value of the loss function for the calibrated models, is indicated in the legend. 96

5.6 Shoreline observations (red dots) and predictions for the entire period (calibration and hindcast) obtained by the calibrated (black dashed line) and guided model (blue solid line) at transect 2. Synthetic shoreline positions used to guide the model are also depicted. 97

5.7 Taylor diagram for all transects and timescales. The figure shows the normalized standard deviation (radial - x and y-axis), correlation coefficient (curved axes along the circumference of the circle), and normalized centred root mean square error (CRMSE, concentric dashed arcs). Stars, circles, squares and diamonds represent the different timescales and periods, calibration, short term, medium term post and pre 1986 respectively. The black triangle (Target) shows the observed data in a Taylor diagram with zero error. The model performance is indicated by the distance of scatter points of model predictions to the observed. The average Loss of the three transects calculated by Equation 4.2 is displayed in the legend for all timescales. 98

6.1 Panel a, Satellite image including R, G, B and SWIR bands cropped and downloaded from Google Eart Engine (Gorelick et al., 2017). Panel b, calculated MNDWI index from the multi band satellite image. Panel c, binary segmented image of land and water regions. Panel d, Grid of land and water points with a smoothed interface. The right column of the figure illustrates the workflow followed to transform the satellite images to gridded data with a smooth land-water interface. 105

6.2 Overview of the features and processes integrated in the LX-Shore model. Panel a, example of a plan-view coastal area used in the model. Panel b, example of the longshore and cross-shore sediment transports rate calculations. Figure is borrowed from Robinet et al. (2018). 107

6.3 LX-Shore model architecture for both wave options, namely computing nearshore waves using SWAN (Booij et al., 1999) or the Larson et al. (2010) formula. 108

6.4 Panel a, location of the Danube delta on the Black Sea coast. Panel b Location of the Sfantu Gheorghe lobe of the Danube delta. Panel c, the Sacalin spit, subdivided into three distinct areas based on morphological characteristics. The wave rose consists of a 40 year timeseries (1984 - 2024), extracted from the Black sea wave reanalysis dataset (Staneva et al., 2022), produced by the Copernicus Black Sea operational wave model (Ricker et al., 2024). An offshore wave point was extracted from the ERA5 reanalysis dataset (Hersbach et al., 2023b). The overlayed image is captured by Sentinel-2 satellite at 21/05/2025, and is downloaded from Google Earth Engine (Gorelick et al., 2017). 110

6.5 Panels a-f, land-water binary grid produced from the satellite images spanning the entire period of available data. Panel g, Cumulative distribution of accepted satellite observations used in the analysis. Panel h, interval between successive observations in days. The dashed vertical lines in panels g and h indicate the instance of observations depicted in panels a to f. Panel i, annual distribution of observations. 113

6.6 Upper panel: Overlayed satellite derived observations of the area covered by the Sacalin spit in May 1986 and 2025. The three distinct areas of the spit are separated by red polygons. Lower panel Observed evolution of the area covered by the Sacalin spit with reference to the initial observation Obs(0) captured in May 1984 plotted as blue squares and a seasonal (3 month backwards facing window) moving average is plotted as a red solid line. 115

6.7 Binary grid of land-water values covering the Sacalin spit produced from the Landsat satellite images, spanning the entire period of available data. The area covered by the spit at the first observation in May 1985 is depicted with red in all panels. . . 116

6.8 Observed evolution of the area covered by each distinct area of the Sacalin spit with reference to the initial observation Obs(0) captured in May 1984 plotted as blue circles (Attached barrier), black squares (Central barrier) and red diamonds (Newly formed spit). The three partitions over which area calculations have been performed are indicated in the snippet on the lower left corner of the figure. 117

6.9 Simulated evolution of the Sfântu Gheorghe river mouth and the Sacalin spit forced by the waves from the ERA 5 reanalysis dataset (Hersbach et al., 2023b) (left panels) and the Black Sea Wave reanalysis (Staneva et al., 2022) (right panels). . . 119

6.10 Simulated evolution of the Sfântu Gheorghe river mouth and the Sacalin spit for different values of the littoral drift calibration factor QF in Equation 6.3. The sediment fraction F at the initial and final timesteps of the simulation is shown in red and sand, respectively, while the satellite-derived observation corresponding to the final timestep is shown in black. 121

6.11 Temporal evolution of the absolute difference in the area covered by the Sacalin spit between simulations and observations, computed within the region shown in the inset, for all simulations presented in Figure 6.10. 122

6.12 Temporal evolution of the absolute difference between simulated and observed land area within the three defined sectors of the Sacalin spit. The areas considered in the land area analysis are outlined in the insets of each panel, while the applied littoral drift factor QF is indicated in the legend of panel (c). The error is expressed as a percentage of the total observed spit area at each comparison time and is shown for all simulations presented in Figure 6.10. 123

6.13 Percentage of timesteps each cell was found to differ from the observation for the simulation with a QF = 8 panel d in Figure 6.10. The initial and final satellite data are overlayed as grey transparent areas for reference. 124

6.14 Temporal evolution of the absolute difference in the area covered by the Sacalin spit between the simulation assimilating a satellite observation annually and the satellite derived observations. The error is computed within the region shown in the inset. The assimilation timesteps are indicated by the black diamonds along the time axis. 125

6.15 Temporal evolution of the absolute difference between simulated and observed land area within the three defined sectors of the Sacalin spit. The areas considered in the land area analysis are outlined in the insets of each panel. The error is expressed as a percentage of the total observed spit area at each comparison time, while the assimilation timesteps are indicated by the black diamonds along the time axis. 127

6.16 (Panel a, b) Absolute simulation error and wave energy flux quantiles per calendar month(10th–90th percentile shading, median line). (Panel c) Observation count per calendar month of all available images used in the present work (see Figure 6.5). The correlation and p value of the monthly statistics presented in each panel with the monthly median absolute error are indicated in the respective panel. The orange-shaded region marks the assimilation period. 128

6.17 Percentage of timesteps each cell was found to differ from the observation for the simulation assimilating observations annually. 130

7.1 A diagram illustrating the swaths of data that SWOT collects. The interferometer will produce two parallel tracks, with a Nadir track from a traditional altimeter in the gap between the swaths. The overall width of the swaths is approximately 120 km. The diagram is downloaded from `https://swot.jpl.nasa.gov/resources/104/diagram-of-swot-data-collection/` 138

List of tables

2.1 Examples of common coastal state indicators found in the literature. 19
2.2 Summary of different approaches to automatically map waterlines/shorelines on optical satellite imagery at pixel and sub-pixel resolution. The different algorithms used to map the waterline at sub-pixel resolution are indicated in the first column of the table. 33

3.1 Range of values considered in the present work. 61

Chapter 1

Introduction

Summary

1.1 General context **2**

1.2 Thesis objective **6**

1.3 Organisation of the manuscript **7**

1.4 Acknowledgements **9**

1.1 General context

The coastal zone represents a dynamic interface between oceanic and terrestrial forces. Sandy coasts, in particular, are highly dynamic systems that are continually reshaped as waves and currents transport and redistribute sediment. They account for roughly 30 % of the world's ice-free coastline (see Figure 1.1, Luijendijk et al., 2018), forming extensive environments of significant geomorphic, environmental, and socio-economic importance. Sandy coasts encompass a wide variety of settings and landforms (see Figures 1.2 and 1.3). Among the most common are large sandy barriers, which can extend for tens to hundreds of kilometres. These barriers are typically interrupted by natural features (e.g. tidal inlets, estuaries, or headlands) or anthropogenic structures (e.g. harbours, dykes, groynes), forming coastal embayments that influence sediment pathways and shoreline response. Sandy deltaic coasts also occur where, historically, river sediment supply exceeded dispersal by waves and nearshore currents.

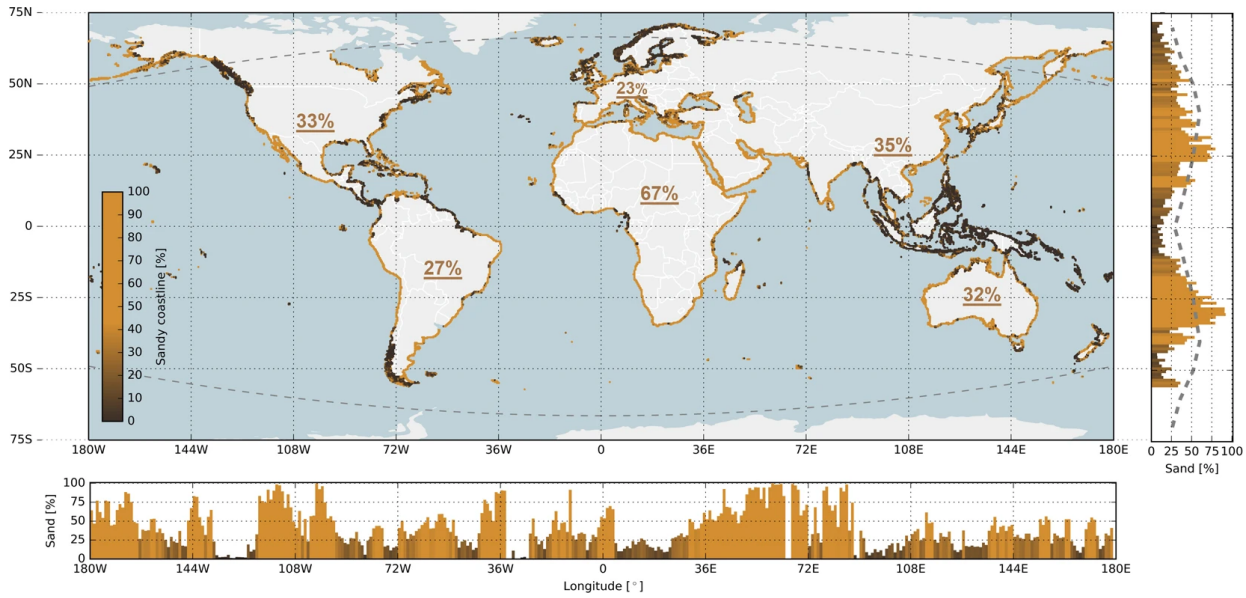

Figure 1.1: Global distribution of sandy shorelines derived from satellite imagery; the coloured dots along the world's shoreline represent the local percentage of sandy shorelines (yellow is sand, dark brown is non-sand). The subplot to the right presents the relative occurrence of sandy shorelines per degree latitude, where the dashed line shows the latitudinal distribution of sandy shorelines reported by Hayes (1967). The lower subplot presents the relative occurrence of sandy shorelines per degree longitude. The curved, dashed grey lines in the main plot represent the boundaries of the ice-free shorelines considered in the analysis. The underlined percentages indicate the percentages of sandy shorelines averaged per continent. The figure is borrowed from Luijendijk et al. (2018).

Sandy beaches evolve across a wide range of spatial and temporal scales—from local to global, and from seconds to centuries, in response to variable environmental forcing (Vitousek et al., 2017). Coastal erosion may be episodic (storm-driven), exhibit long-term variability (seasonal to decadal), or become chronic when a persistent trend is established. These changes arise from both natural factors, such as variations in water levels and wave characteristics, and anthropogenic in-

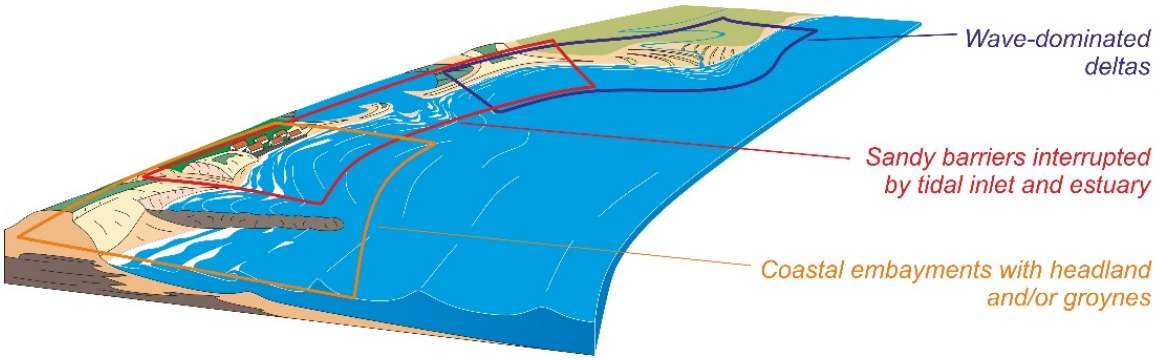

Figure 1.2: Schematic example of sandy coast environments and landforms, taken from the SHORMOSAT project proposal.

Figure 1.3: Example of different sandy beaches. a, Bungan beach , New South Wales , Australia (August 2018). b, Truc Vert beach, Nouvelle Acquitaine, France (May 2023). c, Porsmilin beach, Brittany, France (March 2025). d, Collaroy beach, New South Wales Australia (August 2018).

fluences (Splinter and Coco, 2021). Storm events can cause widespread and rapid erosion over extensive stretches of coastline within hours to days (e.g. Castelle et al., 2015; Masselink et al., 2016; Harley et al., 2017), while longer-term climate variability can drive cycles of enhanced erosion or accretion on multiannual to decadal time scales (e.g. Barnard et al., 2015; Masselink et al., 2023; Vos et al., 2023b; Graffin et al., 2023, 2025a). The impacts of sea-level rise remain the subject of active debate (Vitousek et al., 2017; Cooper et al., 2020; Vousdoukas et al., 2020; Ranasinghe, 2020), as a comprehensive understanding — and consequently a robust modelling framework — has yet to be achieved at these longer temporal scales. Finally, anthropogenic interventions, such as beach nourishment or the construction of hard structures, can exert profound and sometimes irreversible effects on shoreline variability (Aagaard et al., 2004; Ranasinghe and Turner, 2006; Ojeda et al., 2008).

Sandy shorelines provide critical recreational, ecological, economic, and flood-protection services (Barbier et al., 2011). Owing to their accessibility and favourable climate conditions, coastal areas have become some of the most densely developed and populated regions worldwide (Small and Nichols, 2003; Cosby et al., 2024). Figure 1.4 illustrates the distribution of the global population within the first 50 km from the coast, based on data from 2018 reported by Cosby et al. (2024). Currently, approximately 30 % of the world's population lives within this coastal zone, and this proportion continues to rise with ongoing urbanisation and coastal migration (Reimann et al., 2023; Cosby et al., 2024). However, infrastructure and urban development on the landward side restrict both accommodation space and sediment supply, thereby reducing the natural resilience of sandy beaches (e.g. Figure 1.3d). The combined pressures of waves, storms, rising sea levels, and confining development place growing stress on coastal systems (Barnard et al., 2021; Reimann et al., 2023), increasing the likelihood of permanent beach loss where sea-level rise accelerates and landward migration is impeded (Vitousek et al., 2017; Cooper et al., 2020).

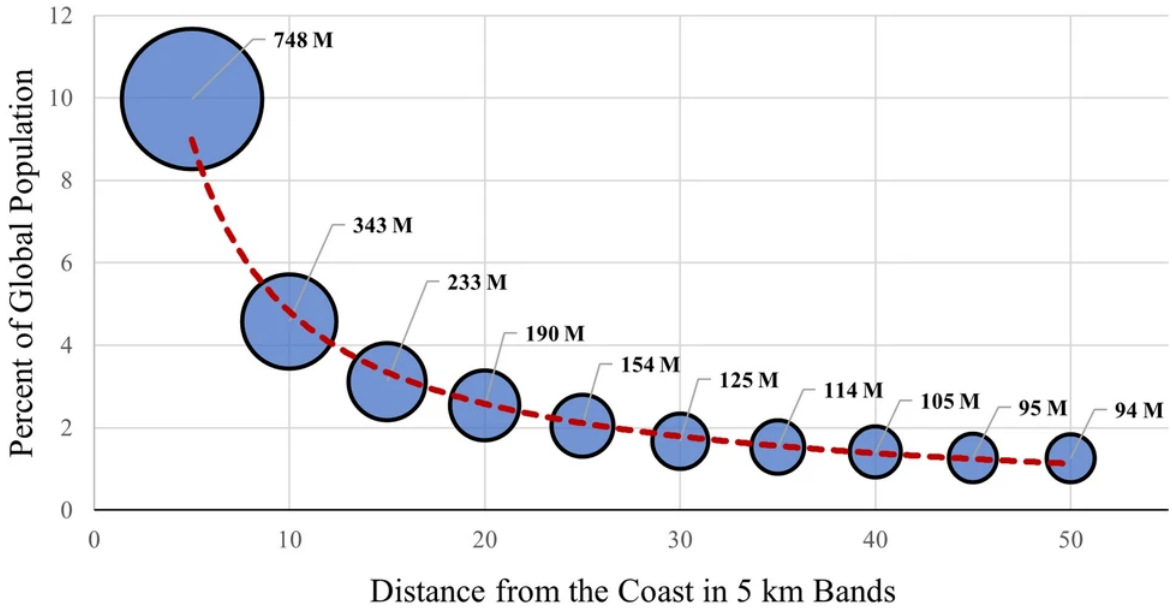

Figure 1.4: Global coastal population distribution within 50 km from the coast in 2018. The figure is borrowed from Cosby et al. (2024).

Projected changes in sea level, wave climate, storm frequency, and sediment supply vary among models and emission scenarios, resulting in wide-ranging estimates of future shoreline response (Cozannet et al., 2019; Ranasinghe, 2020). These uncertainties are further amplified by regional differences in coastal morphology, sediment budgets, and human interventions, making it difficult to generalise local-scale observations to global projections. Reducing these uncertainties requires integrating improved process understanding with consistent global datasets and robust modelling frameworks.

In the Earth sciences, models are central to advancing system understanding, supporting operational forecasting, and projecting future conditions under climate change. Within coastal science, physics-based and conceptual models have traditionally been used to represent key processes and their interactions. In some cases, sandy shoreline evolution can be hindcast with high accuracy, and recent advances in shoreline-change models — together with ensemble approaches — have demonstrated strong predictive skill in blind-testing applications (Montaño et al., 2020; Repina et al., 2025; Mao et al., 2025). However, models remain far from perfect, as they struggle to reproduce shoreline responses in complex environments or to events absent from the calibration period (Splinter et al., 2018b; Ranasinghe, 2020; Splinter and Coco, 2021; Ibaceta et al., 2022). Moreover, the predictive skill of shoreline-change models is constrained by cascading uncertainties inherited from projections of future climate conditions, including waves, hydrodynamics, and mean sea level (Cozannet et al., 2019; Toimil et al., 2020; D'Anna et al., 2021).

Managing coastal environments under a changing climate requires improved knowledge of past shoreline change and its driving processes. Yet insights into the morphodynamic behaviour of sandy shorelines - derived from both observations and modelling — remain inconsistent and fragmented (Vousdoukas et al., 2020; Cooper et al., 2020; Almar et al., 2023; Warrick et al., 2024). Shoreline dynamics vary widely depending on wave exposure, sediment characteristics and budgets, and coastal planform, while shoreline-change models are built on differing assumptions and levels of process representation. Consequently, understanding of past and future shoreline evolution is often site- or case-specific and carries substantial uncertainty.

Systematic observations of shoreline position, providing time series of sandy shoreline change, are fundamental to advancing our understanding of these dynamic environments and to supporting model development and calibration. However, high-quality shoreline records exist only at a limited number of well-monitored sites (e.g. Larson and Kraus, 1994; Turner et al., 2016b; Ludka et al., 2019; Banno et al., 2020; Castelle et al., 2020; Bertin et al., 2022; McCarroll et al., 2023; McLean et al., 2023). Airborne remote-sensing techniques, such as aerial photography and lidar scanning, have substantially increased the spatial coverage of shoreline observations, yet their temporal resolution remains limited. In contrast, space-borne remote sensing from civilian Earth-observing satellites has provided frequent, global image collections for more than five decades (Wulder et al., 2022), transforming Earth sciences—including coastal science—into data-rich disciplines. Simplified data processing in large computational clusters (Dean and Ghemawat, 2008) facilitates the

use of this extensive archive virtually anywhere on the planet (Luijendijk et al., 2018; Mentaschi et al., 2018; Almar et al., 2023; Calkoen et al., 2025).

Data assimilation serves as a bridge between models and observations, enabling improved prediction of complex dynamical systems (Fletcher, 2017). Although data-assimilation techniques are well established in atmospheric and oceanic modelling, their application in coastal sciences remains relatively recent, largely due to persistent challenges associated with data sparsity. With very few exceptions (Vitousek et al., 2023b; Alvarez-Cuesta et al., 2021a), models simulating long-term (decadal) shoreline change at regional scales have yet to fully exploit the wealth of publicly available shoreline data derived from satellite imagery. While numerous coastal morphological models have been developed (Montaño et al., 2020; Ranasinghe, 2020; Toimil et al., 2020; Splinter and Coco, 2021; Sherwood et al., 2022; Hunt et al., 2023), the most effective models are likely to be those that assimilate the highest-quality data. For perhaps 99 % of the world's coastlines, satellite observations represent the best available data—often because they are the only data, or at least the only consistent, long-term records suitable for model integration (Vitousek et al., 2023a).

1.2 Thesis objective

The present work forms part of the SHORMOSAT project (Figure 1.5) financed by Agence National de la Recherche (ANR) and focuses on improving our understanding and prediction of contemporary shoreline evolution under a changing climate. The SHORMOSAT project consortium brings together partners from the Environnements et Paléoenvironnements Océaniques et Continentaux (EPOC) laboratory at the University of Bordeaux, the French Geological Survey (BRGM), and the Centre de Recherche et d'Enseignement des Géosciences de l'Environnement (CEREGE). The project falls within work packages 2 to 6 (WP2 - WP6, see Figure 1.5) and focuses on integrating data from multiple publicly available sources within hybrid shoreline modelling frameworks. A key component involves generating long-term, satellite-derived datasets of waterlines and shoreline positions, as well as relevant products that support coastal morphodynamic analysis and modelling over periods exceeding four decades (1984 - present). This effort further aims to develop robust and systematic satellite-to-model workflows that emphasise a clear and objective definition of the shoreline, the selection of relevant proxies, and methodological repeatability, enabling consistent application across diverse coastal settings and advancing progress toward a universal approach.

Data from multiple sources have been integrated into hybrid modelling frameworks to calibrate model parameters and assess model performance. In parallel, data-assimilation workflows and algorithms will be developed and implemented to incorporate observations into these frameworks, with the aim of creating a new data-assimilation module within the established LX-Shore hybrid shoreline change model. Data assimilation will implicitly account for processes not represented in the model structure, thereby extending the range of model applicability. Moreover, through data-

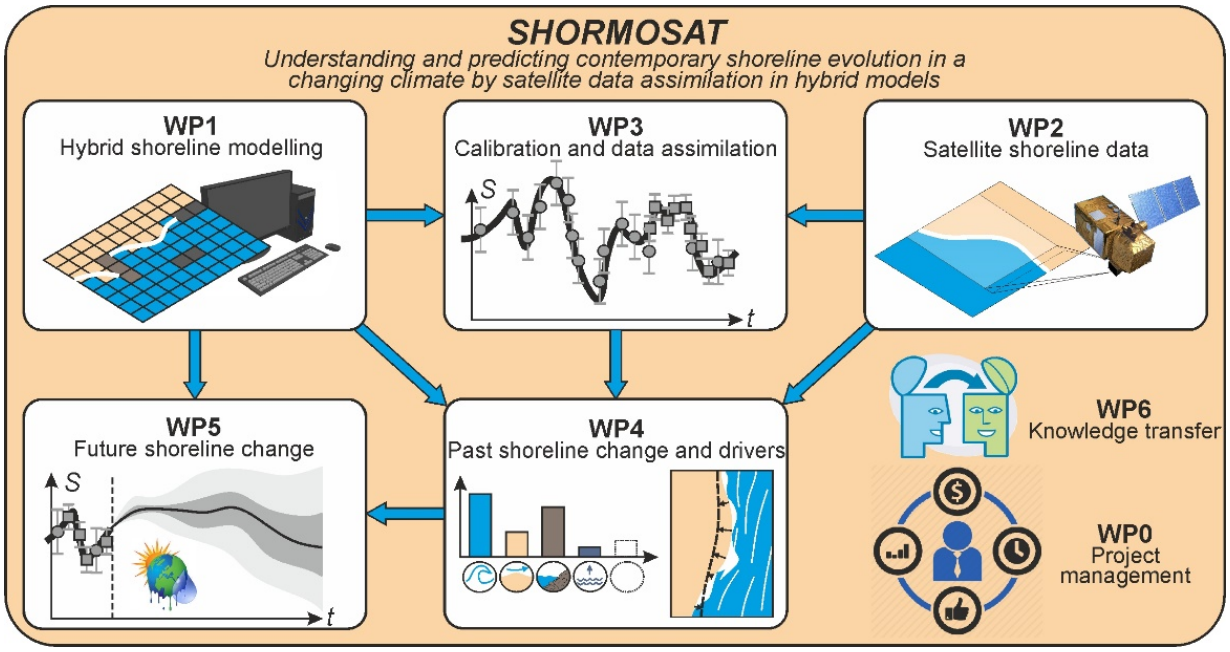

Figure 1.5: Work package structure of the SHORMOSAT project, taken from the SHORMOSAT project proposal.

assimilation workflows, sources of error within the hybrid modelling frameworks will be identified, and links between parameter variability and environmental forcing will be systematically explored.

The integration of long-term datasets from multiple publicly available sources into hybrid modelling frameworks, across diverse coastal environments, aims to investigate the dominant spatial and temporal modes of shoreline variability and to quantify the respective contributions of different forcing mechanisms within each environment. Ultimately, the insights gained will inform future research exploring shoreline evolution up to 2100, building on IPCC projections and addressing key uncertainties associated with sea-level rise, model parameters, and the potential timing and locations of critical coastal changes—such as the possible demise of sandy beaches.

1.3 Organisation of the manuscript

The manuscript is structured to progressively develop and test a series of modelling frameworks designed to improve the understanding and prediction of shoreline evolution using publicly available datasets. The overall logic follows a transition from theoretical background and data foundations, through progressively more complex modelling and data assimilation approaches, culminating in a quasi-two-dimensional application and the identification of future research perspectives.

Chapter 2 presents the state of the art, establishing the conceptual and methodological context of the study. It begins with a general introduction to the key processes governing shoreline evolution and the importance of defining the shoreline consistently across scales and data types.

Section 2.2 discusses the challenges and conventions surrounding shoreline definition, emphasising the implications of proxy choice for model calibration and validation. Section 2.3 reviews the morphodynamic response of sandy shorelines in wave-dominated environments, identifying the physical controls and feedbacks that underpin the models later applied.

Sections 2.4 and its subsections provide an overview of shoreline observation techniques, from in-situ surveys and coastal cameras to airborne and satellite-based methods. Particular attention is given to the advantages and limitations of Earth observation satellites (Section 2.4.6) and their growing role in producing long-term, spatially consistent shoreline datasets. Section 2.5 introduces the main families of shoreline change models, including semi-empirical and reduced-complexity approaches, before focusing on hybrid models that combine different empirical formulations. The following subsections review the current state of shoreline modelling, emphasizing model calibration and the growing integration of data assimilation techniques. Finally, Section 2.6 outlines the specific contributions of the present work, setting the stage for the following application-based chapters.

Chapter 3 presents the first application of these concepts by calibrating a one-dimensional equilibrium shoreline model using satellite-derived waterlines that have not been corrected for the horizontal displacement of the shoreline caused by the instantaneous water level at the time of satellite overpass. Focusing on Truc Vert beach, a high-energy, meso-macrotidal environment on the Atlantic coast of France, the chapter investigates the extent to which reliable model calibration can be achieved using raw, noisy satellite data. The methods presented in Sections 3.3 and 3.4 evaluate model skill under varying data quality and quantity, while Section 3.5 discusses the broader implications for automated, large-scale shoreline modelling.

Chapter 4 extends the analysis to the temporal variability of model parameters through sequential data assimilation. Using in-situ shoreline data from multiple sites along the European Atlantic coast, it explores the hypothesis that free-parameter variability reflects changes in wave climate. The results and discussion assess both the potential and the limitations of time-varying (non-stationary) models, showing modest performance improvements in some cases, particularly where data quality is high. These findings inform the subsequent development of hybrid frameworks capable of combining calibration and assimilation.

Chapter 5 introduces such a hybrid equilibrium shoreline model, developed and blind-tested within the ShoreShop 2.0 international benchmark workshop Mao et al. (2025). The chapter details how two equilibrium-based models—one representing shoreline rotation and another describing cross-shore sediment transport—were explicitly coupled and guided through data assimilation. The combined framework demonstrated strong performance across timescales from years to decades, successfully reproducing observed shoreline variability and ranking among the top-performing submissions.

Building on these one-dimensional developments, Chapter 6 extends the modelling framework

into a quasi-two-dimensional (2D) configuration within the LX-Shore model Robinet et al. (2018), applying it to the Sacalin Spit in the Danube Delta. This chapter presents a grid-based data assimilation approach based on spatial nudging, allowing colour-derived land–water transitions to constrain model evolution across a 2D grid. The results demonstrate the capacity of the assimilation scheme to compensate for unrepresented processes such as overwash, barrier breaching, and fluvial sediment supply, while revealing distinct morphodynamic phases and spatial patterns of erosion and accretion.

Finally, Chapter 7 synthesises the main conclusions and future perspectives. It summarises the methodological advances and key findings from the calibration, data assimilation, and hybrid modelling experiments, highlighting the importance of observation frequency, data quality, and model structure. The chapter concludes by outlining directions for future work, including the integration of multimodal wave climate representations, the development of fully coupled 2D assimilation frameworks, and the operational use of global satellite datasets for predictive coastal morphodynamics.

1.4 Acknowledgements

This work was done in the framework of the SHORMOSAT project and funded by Agence Nationale de la Recherche (ANR) grant number ANR-21-CE01-0015. This study includes the monitoring site of Truc Vert labelled by the Service National d'Observation (SNO) Dynalit (https://www.dynalit.fr). The Observatoire de la Côte de Nouvelle-Aquitaine (OCNA) and Observatoire Aquitain des Sciences de l'Univers (OASU) provide additional financial support for the surveys. We thank Stéphane Bujan for performing the Truc Vert beach field surveys. NORGAS-UG wave hindcast data was provided by LOPS-Ifremer.

Chapter 2

State of the art

Summary

2.1 Introduction 12

2.2 Shoreline definition 14

2.3 Sandy shoreline response in wave dominated environments 20

2.4 Shoreline observations 22

2.4.1 Nearshore remote sensing 23

2.4.2 Coastal cameras 24

2.4.3 In-situ surveys 25

2.4.4 Airborne observations 28

2.4.5 Historical shoreline observations 29

2.4.6 Earth observing satellites 30

2.5 Shoreline change modelling 33

2.5.1 Semi empirical models 35

2.5.2 Reduced complexity models 38

2.5.3 Hybrid shoreline models 39

2.5.4 State of the art in shoreline change modelling 41

2.5.5 Model Calibration 42

2.5.6 Data assimilation in shoreline change modelling 43

2.6 Contribution of the present work 47

2.1 Introduction

Evidence of human coastal settlements extend back to the Palaeolithic era and the emergence of anatomically modern Homo sapiens, underscoring the longstanding significance of observing and understanding shoreline dynamics as a foundational element of human civilization (Marean, 2010, 2014; Dillehay et al., 2012; Clarkson et al., 2017). It is not until late prehistoric times when humans adopted sedentary lifestyles that we observe the first examples of coastal infrastructure (Marriner et al., 2017; Gupta et al., 2024). The port of Byblos (present day Lebanon) built by the Phoenician civilization around 3000 BC is often credited as the earliest known coastal infrastructure, followed by harbour works, navigation aids (e.g. lighthouses) and seawall fortification in ancient Egypt and Greece (Marriner et al., 2017). Tidal-dockyards from approximately the same period are found in the ancient city of Lothal (present-day Gujarat, India) (Gupta et al., 2024) and evidence of ancient coastal infrastructure in the Americas (fish weirs, clam gardens, and Maya harbours) (Cobos, 2008) show independent and very early developments of coastal engineering.

Until the first half of the 20th century coastal science and engineering was mainly concerned with large issues of national defence, transportation and flooding. Pioneering work in wave and shoreline forecasting in support of the war effort in 1930s and 1940s, was followed by large expansion in funding and facilities (Kamphuis, 2006). Post war optimism combined with significant advances in science and technology facilitated the rise of the modern consumer society. The growing demands for transportation (shipping and ports), protection against flooding and erosion, and tourism created the need for modern coastal engineering (Kraus, 2018). This development was formalized with the organization of the first International Conference on Coastal Engineering (ICCE) in 1950 (Johnson, 1950).

In the 1970s following societal changes, coastal science and engineering arrived at the era of coastal management (Kamphuis, 2006). Coastal engineering and management focus shifted from simply maximizing economic value towards quality of life. Sustainable development and environmental concerns became a big part of design strategies. Climate change and global warming appeared as terms (Broecker, 1975) in scientific publications, increasing uncertainties and concerns of future coastal hazards. Stakeholders, property owners, environmental groups, industry, coastal communities and government bodies participated in discussions regarding coastal management (Kamphuis, 2006). As public debate grew, the need to study coastline morphodynamic behaviour was more pressing than ever, prompting significant advances in observation, modelling, understanding and predicting shoreline behaviour.

Over past decades, most geoscience disciplines, including coastal science and engineering, have entered the era of big data (Gorelick et al., 2017; Calkoen et al., 2025). Advances in Earth-observing satellite programs, together with increased computational capacity, have transformed these fields into data-rich domains of study. To fully exploit the potential of global datasets, further progress is required in both the automation of monitoring and the assimilation of observations

into predictive models (Vitousek et al., 2023a). In particular, the monitoring and analysis of sandy coastal change at appropriate spatiotemporal scales will be essential for advancing our understanding of the morphodynamic behaviour of these environments.

The following chapter establishes the conceptual, observational, and modelling foundations necessary to understand and predict shoreline change. It begins by defining the shoreline within the context of coastal science and engineering (Section 2.2), addressing both its physical interpretation and the variety of operational definitions used across disciplines and datasets. Clarifying this concept is essential, as the shoreline acts simultaneously as a geomorphic indicator, a dynamic interface, and a key modelling boundary condition. Section 2.3 then examines sandy shoreline response in wave-dominated environments, summarizing the dominant processes—such as cross-shore and longshore sediment transport—and their influence on shoreline variability across temporal scales from individual storm events to multi-decadal evolution. Together, these sections establish the theoretical foundation for interpreting the observational and modelling approaches discussed thereafter.

Section 2.4 reviews the state of the art in shoreline observation, highlighting the diverse methods available for monitoring coastal change. The section progresses from ground-based to spaceborne perspectives, reflecting the evolution of observational capacity. Nearshore remote sensing and coastal camera systems (Sections 2.4.1–2.4.2) provide continuous, high-frequency measurements of beach and shoreline dynamics at local scales, while in-situ surveys (Section 2.4.3) remain the benchmark for high-accuracy datasets used in validation and process studies. Airborne techniques (Section 2.4.4), including LiDAR and photogrammetry, have extended both spatial coverage and vertical resolution, enabling the generation of detailed digital elevation models of the coastal zone. Historical observations (Section 2.4.5) provide long-term context for shoreline evolution, and Earth-observing satellites (Section 2.4.6) now deliver globally consistent, repeatable, and long-duration records. The emergence of automated satellite-derived shoreline (SDS) extraction techniques allows quantification of shoreline variability at unprecedented spatial and temporal scales, establishing satellite data as a cornerstone of contemporary coastal monitoring.

Section 2.5 transitions from observation to modelling, reviewing the principal approaches used to simulate and predict shoreline change. Semi-empirical models (Section 2.5.1) establish simplified yet physically meaningful relationships between wave forcing and shoreline response. Reduced-complexity models (Section 2.5.2) represent key morphodynamic processes through parameterized formulations, enabling computationally efficient simulations on large spatiotemporal scales while retaining essential dynamics. Hybrid models (Section 2.5.3) combine complementary modelling philosophies or data sources—such as coupling cross-shore and longshore processes or integrating empirical and process-based components—to capture a broader range of coastal behaviours. Section 2.5.4 synthesizes the current state of the art in shoreline change modelling, identifying persistent challenges related to model transferability, representation of multi-scale processes, and quantification of uncertainty. Model calibration (Section 2.5.5) is then discussed, with

emphasis on optimization strategies and the growing role of satellite-derived datasets in objectively constraining model parameters. Section 2.5.6 introduces recent advances in data assimilation techniques—sequential, variational, and ensemble-based approaches—that dynamically integrate observations into model simulations, improving predictive capability and enabling exploration of non-stationary behaviour under evolving environmental forcing.

Finally, Section 2.6 situates the contribution of the present work within this broader context.

2.2 Shoreline definition

Defined as the intersection between water and land surfaces, the shoreline position—and its temporal evolution—is of fundamental significance to coastal scientists. While this definition of shoreline appears conceptually straightforward, its practical application is far more complex. Instantaneous waterline position is subject to significant variability influenced by wave motion, tidal variation, storm surge, wave setup, wave run-up, and the stochastic nature of the sea surface. On sandy coasts, nearshore hydrodynamic processes result in cross shore and alongshore sediment transport within the littoral zone further modulating waterline position across a wide range of spatial and temporal scales. Given the inherently dynamic nature of sandy coastlines, any adopted definition must incorporate a spatio-temporal framework that reflects the variability relevant to the context of investigation (Boak and Turner, 2005). In practice however, data availability and source often dictate the choice of the adopted definition. The most commonly used shoreline proxies found in the literature are illustrated in figure 2.1.

The instantaneous waterline position does not necessarily reflect average or equilibrium conditions (Smith and Zarillo, 1990). Horizontal location of the waterline can vary substantially—ranging from a few centimetres to several hundred meters, depending on factors such as beach slope, tidal range, and prevailing wave conditions (Castelle et al., 2021; Konstantinou et al., 2023). Following the definition of Munk (1950) and Holthuijsen (2007) (see figure 2.2), within short timescales the equilibrium state of the ocean's surface and therefore the waterline position is disturbed by the propagation of waves. The shortest observed surface waves have a period less than $1/4$ s, are affected by tension in the interface of water and air and are called capillary or surface tension waves. Gravity-driven waves with periods shorter than 30 s are generated by wind. They are referred to as wind sea when produced by local winds at the observation point, and as swell when they have propagated away from their generation area. Wind generated waves propagating away from the generation area travel in groups distinguished by their period and wave height forming infra-gravity waves. These waves can be observed in the coastal zone, commonly referred to as surf beat and their period is typically a few minutes long. Landslides and earthquakes release a large amount of energy on the ocean surface almost instantaneously that can generate long waves with periods ranging from a few minutes to several hours, commonly referred to as tsunamis. Low atmospheric pressure and high winds during a severe storm can cause large scale elevation of the

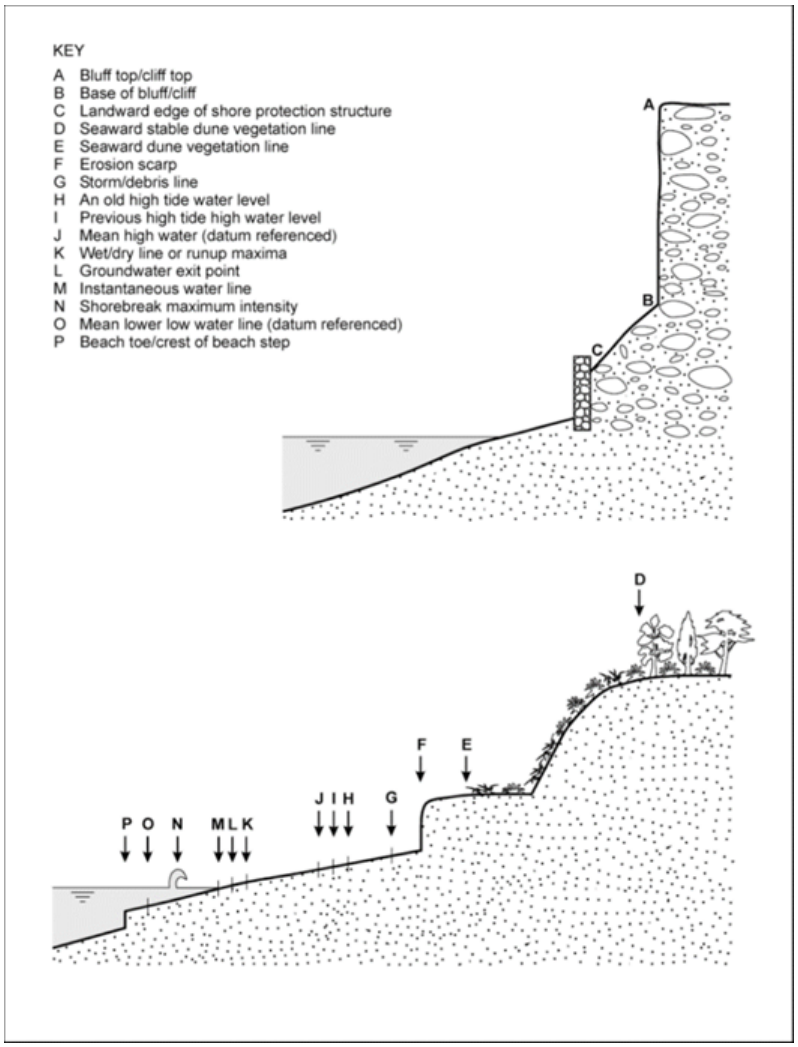

Figure 2.1: Illustration of commonly used shoreline indicators found in the literature. The figure is borrowed from Boak and Turner (2005).

ocean surface. This disturbance is called a storm surge and can last anywhere between a few hours to several days. The gravitational pull of planetary bodies in close proximity to Earth, like the Moon and the Sun, acts upon the ocean surface generating astronomical tides, whose periods roughly follow the orbital cycle of these bodies, with the most dominant components being diurnal and semi-diurnal. Trans-tidal waves, which are the longest of the short term wave category can be caused by storms (storm surge) and low frequency fluctuations of the earth's crust. Finally closed basins such as the Adriatic sea experience standing waves called seiches, with frequencies equal to the resonance frequency of the basin in which they occur. Each disturbance of the ocean surface contributes to fluctuations in the position of the waterline, which must therefore be interpreted as a time dependent variable within an appropriate temporal framework.

Because the waterline boundary is highly dynamic and can exhibit large variations between different environments, coastal scientists have adopted the use of coastal state indicators (CSIs) to quantitatively describe the state of the coast and its evolutionary trends (Boak and Turner, 2005; Davidson et al., 2007). While shoreline proxies are maybe the most commonly used CSIs, the choice of the relevant indicator depends on the observation method and the context of the inves-

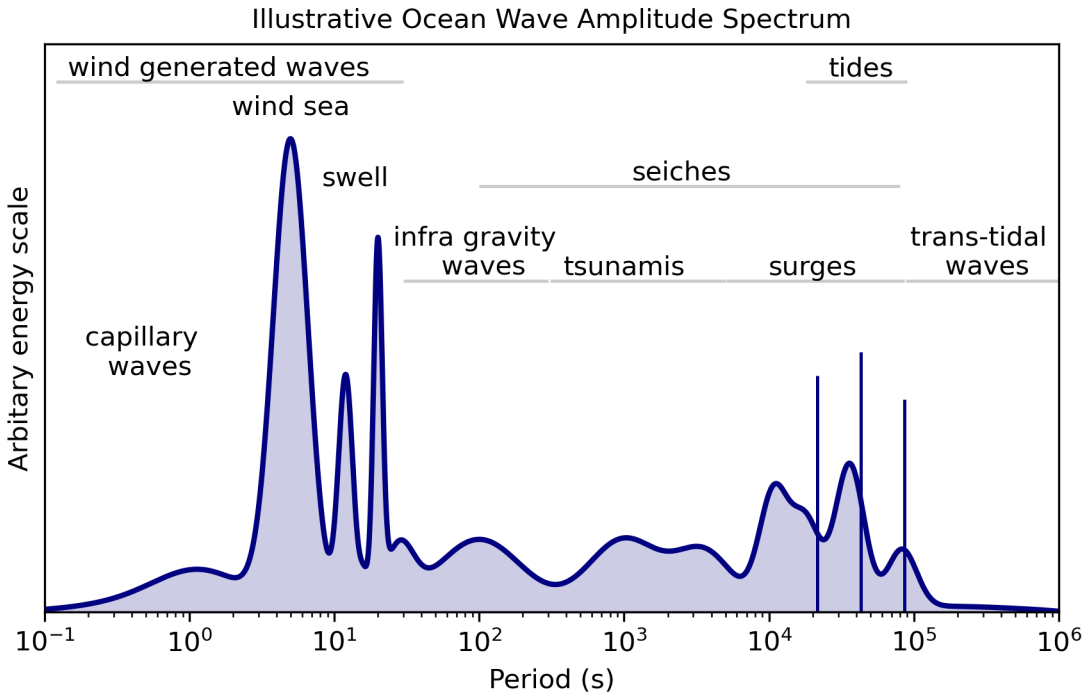

Figure 2.2: Tentative classification of ocean waves according to wave period. The forces responsible for various portions of the spectrum are shown. The relative amplitude is indicated by the curve. The figure is modified from Holthuijsen (2007).

tigation (Van Koningsveld et al., 2005; Boak and Turner, 2005). CSIs can be grouped into three categories based on their definition, detection approach, and method of derivation.

The first group consists of features that can be visually identified on a beach like the instantaneous water line or a high water mark (HWM) (Leatherman and Pajak, 2002; Masselink and Puleo, 2006). In figure 2.3 a few examples of visually defined shoreline proxies common in beach/dune systems are illustrated in the high energetic, meso-macrotidal Truc Vert beach, located on the coast of Nouvelle Aquitaine, in southwest France. Indicators classified in the second group are defined by the horizontal position of a predefined elevation based on a tidal datum like the horizontal position of the mean sea level (MSL) or the lowest astronomical tide (LAT) contours. Figure 2.4 (a–d) shows Sentinel-2 images of Truc Vert captured at different stages of the tidal cycle, while panels (e–f) depict measured beach profiles at two distinct times, indicating the mean and extreme tidal elevations.

The third group of coastal indicators are the ones that cannot be directly observed and need to be derived from observation such as the volume of sand above a certain elevation, the orientation and curvature of a stretch of coastline. These indicators cannot be directly observed but can be calculated from digital elevation models (DEM) of the nearshore zone and combination of multiple profiles (Burvingt et al., 2018; Bertin et al., 2022; Abdulsalam et al., 2025). Volume of sand is often seen as a beach state indicator rather than a coastal one as changes in volume might not necessarily reflect changes in the horizontal position of the coastline, although they often do and have been

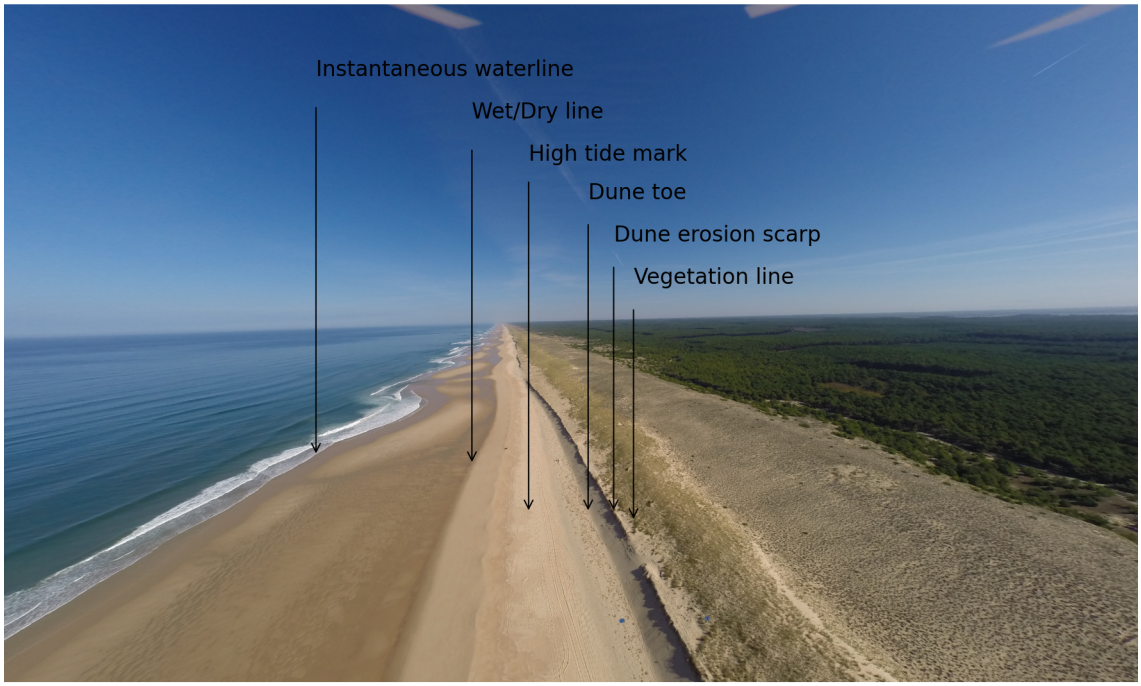

Figure 2.3: Example of visually defined shoreline proxies at Truc Vert beach, Nouvelle Aquitaine, southwest France. Picture captured by Vincent Marieu during a spring low tide in June 2014 with an Unmanned Airborne Vehicle (UAV).

consistently used by coastal scientists (Turner et al., 2016b; McCarroll et al., 2023).

In Table 2.1, several of the most common CSIs found in the literature are summarized. The High Water Line (HWL), corresponding to the highest visible run-up mark on the beach, is the most widely used CSI. However, as it is a visually detected indicator, its definition—when explicitly stated—varies considerably between studies, encompassing interpretations such as the wet/dry boundary, the line of storm debris, or the highest visible erosion or accretion mark, among others (Boak and Turner, 2005). A substantial body of research has demonstrated that the visual identification and subsequent interpretation of the waterline can represent a major source of uncertainty in shoreline mapping (Moore, 2000; Stockdon et al., 2002; Vos et al., 2019a; Castelle et al., 2021; Konstantinou et al., 2023).

With the emergence of camera-based beach monitoring systems (Aarninkhof and Holman, 1999) and the increasing potential of remotely sensed, visually identified CSIs, a coordinated effort was undertaken to develop consistent and practical indicators to support coastal zone management (Van Koningsveld et al., 2005; Davidson et al., 2007). Nevertheless, whenever possible, the coastal science community has often preferred elevation-based CSIs (Shepard, 1950; Shepard and Inman, 1951; Zeigler and Tuttle, 1961; Morton, 1991; Turner et al., 2016b; Castelle et al., 2020; Bertin et al., 2022; McCarroll et al., 2023; McLean et al., 2023), as these can be objectively defined, leave minimal room for interpretation, and allow uncertainties to be quantified and reported.

Besides the temporal fluctuations of the waterline, alongshore variability in shoreline position must also be considered when defining a CSI. As with temporal scales, the alongshore extent

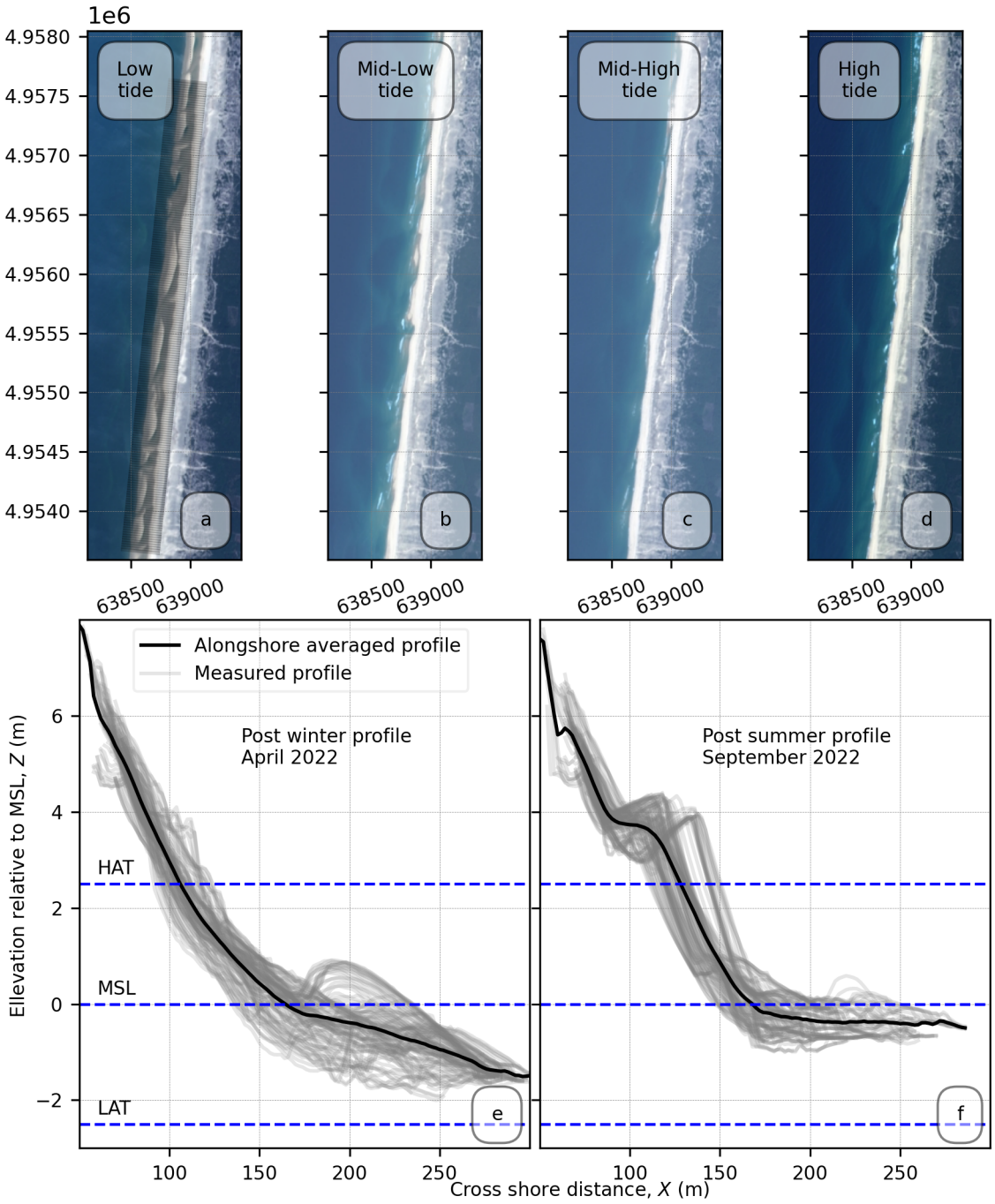

Figure 2.4: a - d Satellite images of Truc Vert beach at different stages of the tide obtained from Sentinel 2 images between June and July 2022. e - f Beach profiles measured during spring low tide, over a 4 km window with an alongshore spacing of 20 m at Truc Vert. Surveys were performed with an RTK GNSS system mounted on an ATV. The measured profiles are indicated as grey transparent lines in panel a.

should reflect the objectives and context of the investigation. Single transects or point measurements often fail to capture the full configuration and variability of the beach. Periodic morphological features such as beach cusps and megacusps can locally distort the shoreline contour, introducing noise and uncertainty (Castelle et al., 2019a). These perturbations, together with gradients in longshore and cross-shore sediment transport (Harley et al., 2015), complicate the extraction of a representative shoreline and emphasize the need for a carefully defined spatial extent and

resolution. Ultimately, the coastal setting, dominant morphodynamic behaviour, and geomorphological processes under study (Burvingt et al., 2017; Splinter et al., 2018b; Castelle et al., 2019b; Masselink et al., 2023) should guide the choice of alongshore resolution.

Coastal state indicator	Definition	Source	Reference
Vegetation line	Seaward/landward vegetation edge of the dune	Optical	Muir et al. (2024)
Dune crest	Top of the dune backing the beach	Optical & elevation based	Río and Gracia (2013)
Dune toe	Seaward base of the dune backing the beach	Optical & elevation based	Mauff et al. (2018)
Dune erosion scarp	Erosion scarp on dune backing the beach	Optical & elevation based	Lerma et al. (2019)
High water line (HWL)	Highest observed water mark on the beach face	Optical	Moore et al. (2006)
Berm	Accretionary morphologic feature on the backshore	Elevation based	Banno et al. (2020)
Highest/lowest astronomical tide line (HAT, LAT)	Highest/lowest elevation of the astronomical tide	Elevation based	Castelle et al. (2014)
Mean sea level (MSL)	Mean tidal elevation	Elevation based	Castelle et al. (2014)
Wet/Dry line	Border between wet and dry part of the beach, between LAT and HWL	Optical	Crowell et al. (1997)
Instaneous waterline	Position of the waterline at the instance of observation	Optical	Harley et al. (2019)
Beach orientation	Orientation of the Shoreline	Optical & elevation based	Short and Trembanis (2004)
Beach width	Distance between a fixed landward point and the waterline/shoreline	Optical & elevation based	Cabezas-Rabadán et al. (2019)
Beach/Dune volume	Volume of the beach/dune above a specific elevation contour e.g. LAT or dune toe over a defined area	Elevation based DEM	Burvingt et al. (2018) Bertin et al. (2022)

Table 2.1: Examples of common coastal state indicators found in the literature.

The appropriate CSI should therefore be regarded as case-specific, determined by the context of the investigation and the dominant morphodynamic processes of the site. In practice, however, data availability and observation methods have often dictated the choice of indicator. Advances in remote sensing have expanded the use of space-borne observations in coastal science (Kuleli

et al., 2011; Pardo-Pascual et al., 2012; García-Rubio et al., 2015; Vos et al., 2019a), providing high-frequency and near-global coverage. This accessibility has, to some extent, rendered the data availability argument obsolete, while making the need for consistent definitions of visually derived shoreline indicators more pressing than ever. There is no "one-size-fits-all" solution, and the study of coastal dynamics requires selecting one or more CSIs appropriate to the study's objectives and setting. In the modern era of abundant multi-source data, CSIs should be clearly defined, reproducible, and, as far as possible, free from interpretation and operator bias.

2.3 Sandy shoreline response in wave dominated environments

Individual wave components shown in Figure 2.2, interact with one another and the solid boundaries they encounter, generating complex hydrodynamic conditions that can drive sediment transport and continuously shape beach morphology on sandy coasts (Fredsøe and Deigaard, 1992). The mutual interactions between sandy beach morphology and hydrodynamic processes including wave, tide and wave driven currents result in a morphodynamic loop, illustrated in the upper panel of Figure 2.5. On any given sandy shoreline, morphological changes can be forced by changes in the hydrodynamic conditions occurring over a range of spatial and temporal scales as illustrated in the lower panel of Figure 2.5. The shaded areas distinguish the different temporal scales of morphodynamic response that can be roughly defined as instantaneous, individual events, engineering and geological.

While individual waves act as episodic events primarily influencing the instantaneous waterline and shoreline position over their respective cycles (Elfrink and Baldock, 2002), their cumulative effect over a tidal cycle (Masselink et al., 2009) and beyond reveals cyclical and seasonal patterns that ultimately govern shoreline change (Castelle et al., 2019b). Seasonal variations in incoming wave energy, storm intensity and frequency are usually reflected by seasonal variations in beach morphology (Yates et al., 2011). Similarly, interannual changes in environmental conditions with mild and energetic winters interchanging are further affecting the position of the shoreline (Masselink et al., 2023). On longer timescales usually on the order of decades and beyond the wave conditions can be characterized by long term statistics and are referred to as wave climate. Variations in wave climate usually reflect changes in shoreline position in the form of long term trends and long period cyclical patterns (Vos et al., 2023a; Graffin et al., 2025a).

Spatial variability in beach morphology, much like its temporal evolution, is primarily controlled by variability in the hydrodynamic forcing along the coast (Castelle et al., 2022). Swash dynamics, rip-current formation and alongshore gradients in incoming wave energy, govern the distribution and evolution of coastal forms such as cusps and mega cusps (Harley et al., 2015). These are also self-organization processes (Coco and Murray, 2007) that introduce additional noise into shoreline time series if not accounted for. Variations in shoreline orientation and wave exposure influence alongshore variable morphodynamic response especially in embayed environments

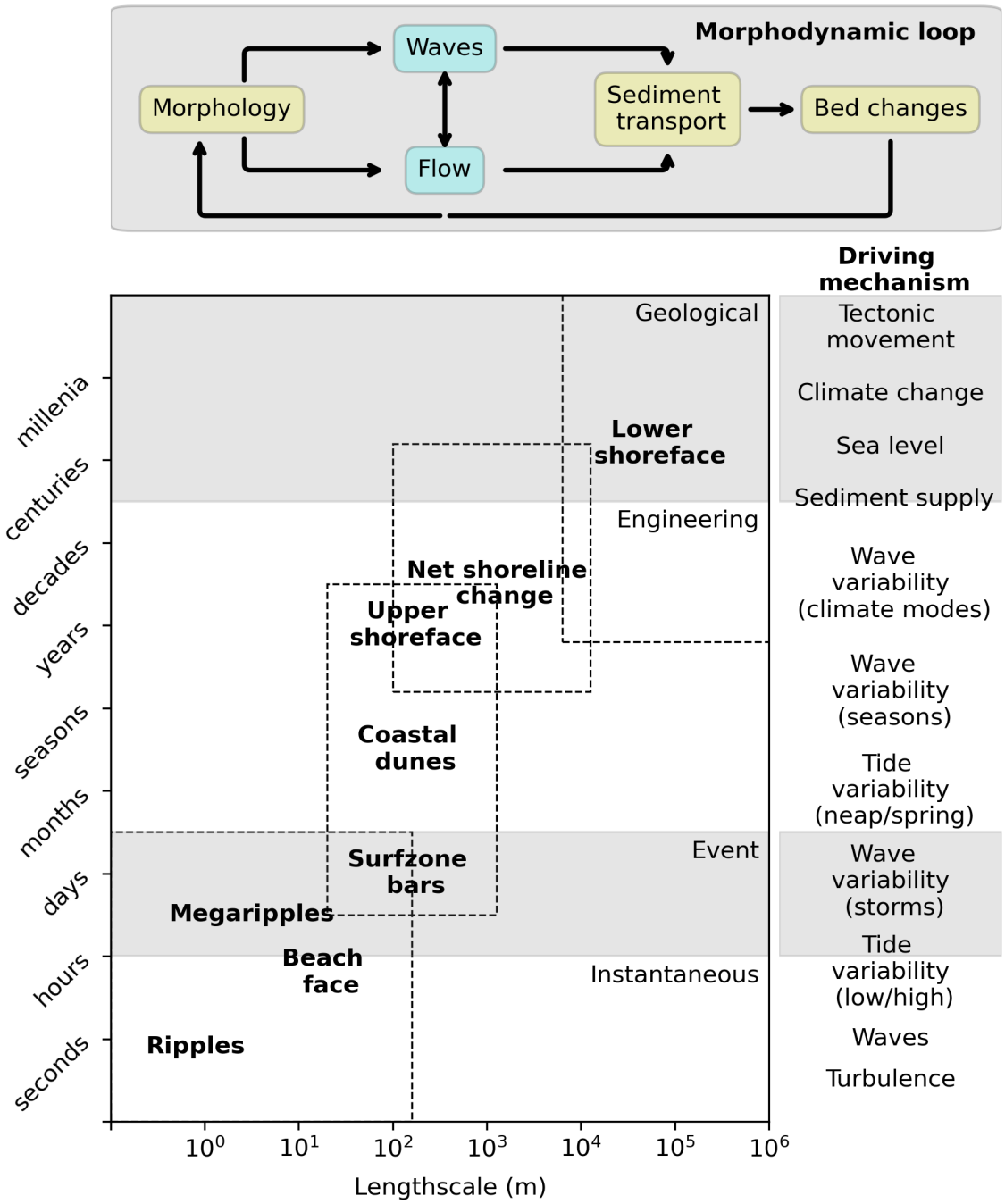

Figure 2.5: Schematic representation of the coupled beach morphodynamic system and spatiotemporal representation of the primary modes of sandy beach variability and their drivers, modified after Castelle and Masselink (2023).

(Splinter et al., 2018b). Sediment characteristics, the presence of morphological discontinuities such as tidal inlets, estuaries, headlands and tidal regime, further contribute to the alongshore variability of coastal morphological responses (Scott et al., 2011).

Human interventions can exert significant and often irreversible impacts on shoreline morphology (Aagaard et al., 2004; Ranasinghe and Turner, 2006; Ojeda et al., 2008). Coastal structures and beach nourishment can locally modify the morphodynamic response of the beach, while nearshore infrastructure reduces accommodation space and restricts the natural landward migration of the

coastline (Vitousek et al., 2023a), thereby contributing to coastal squeeze (Pontee, 2013). In addition, fluvial infrastructure such as dams and irrigation systems limit the sediment supply delivered to the nearshore zone (Zăinescu et al., 2019), further influencing sediment budgets and coastal dynamics. The morphology of sandy shorelines is also influenced by longer-term processes such as sea-level change, tectonic movements, and variations in sediment supply (Larson and Kraus, 1995; Murray, 2007). However important, these processes occur over longer timescales falling within the geological regime and are therefore beyond the scope of the present work.

2.4 Shoreline observations

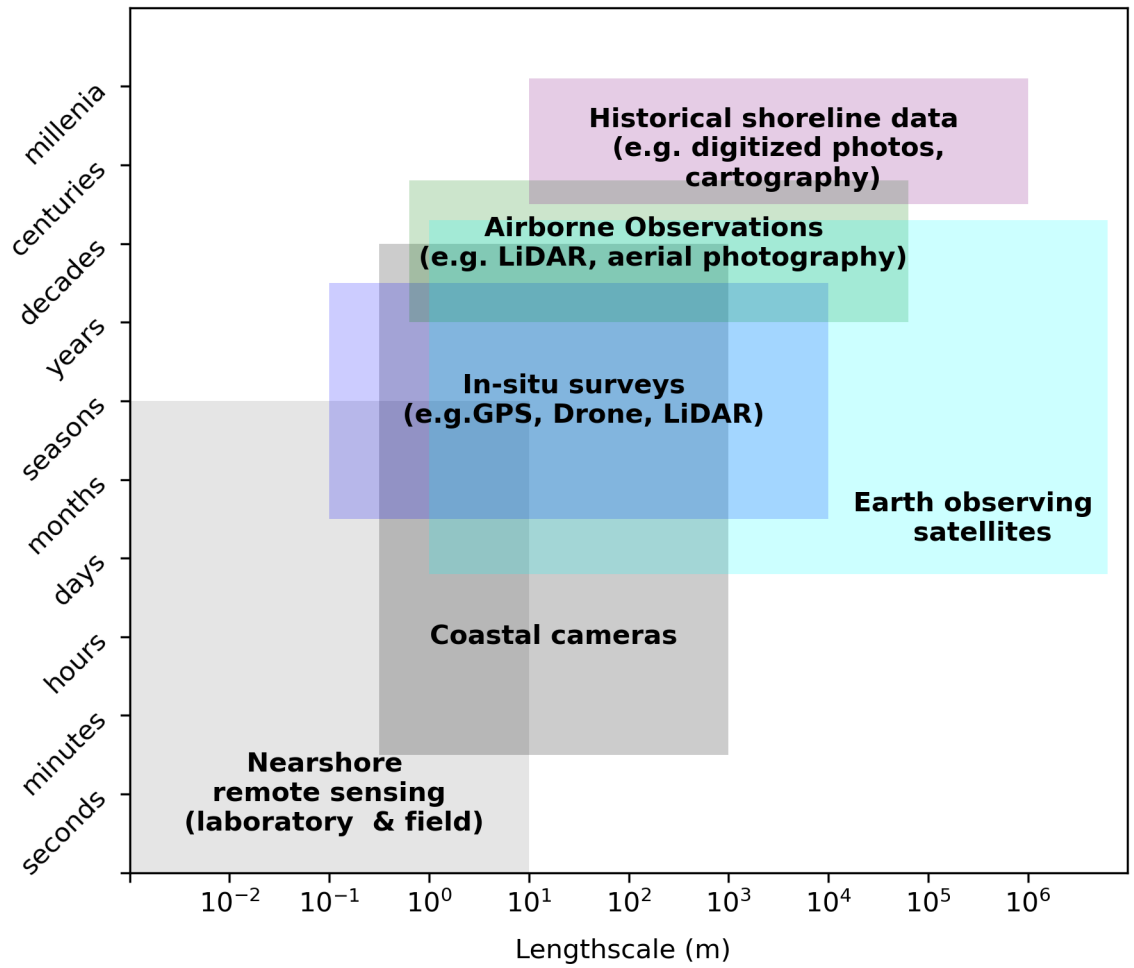

Figure 2.6: Sources of shoreline observations and the spatio-temporal scales they resolve.

The multi-scale nature of waterline fluctuations (Figure 2.2) and morphodynamic processes on sandy beaches (Figure 2.5) is directly reflected in shoreline monitoring approaches. The choice of technique must be consistent with the CSI of interest and the spatio-temporal scales under investigation, spanning from flow dynamics at the smallest scales to global variations over geological timescales. Figure 2.6 illustrates the most commonly used observational sources as a function of the scales they resolve. The scope of the present work is confined to the local-to-regional morphodynamic behaviour of wave dominated sandy shorelines, covering timescales from a few days to

several decades. The following section provides a concise overview of the available observation sources documented in the literature that are commonly employed in the study of coastal dynamics, with emphasis on techniques capable of resolving the scales of interest addressed in this work.

2.4.1 Nearshore remote sensing

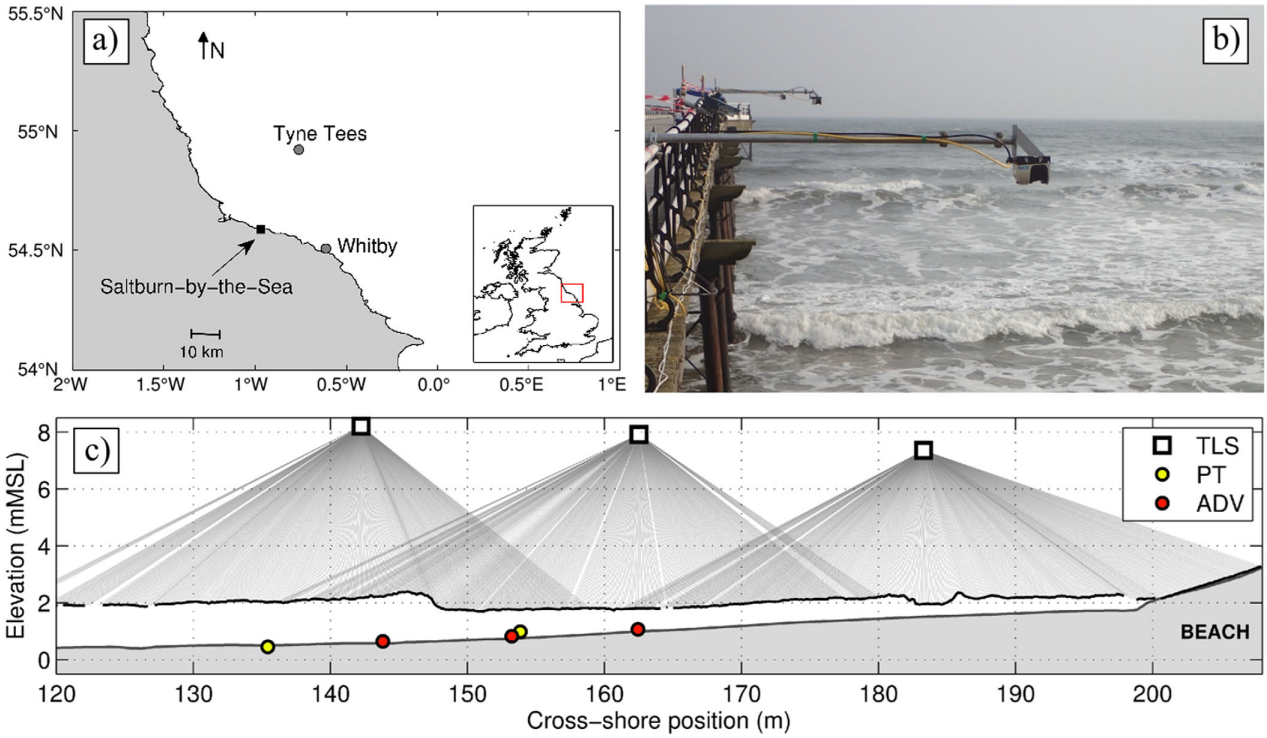

Figure 2.7: Setup of the field experiment of Martins et al. (2018) showing the field site and LiDAR scanner deployment. Regional map (a). (b) The LiDAR scanner deployment on the nearshore pier. (c) A schematic of the experimental setup of the Terrestrial Laser Scanners (TLS), pressure transducers (PT) and Acoustic Doppler Velocimeters (ADV), with an example of postprocessed free surface elevation (black thick line). The beach profile (thick grey line) corresponds to the surveyed profile during the previous low tide (10 April 2016).

Nearshore remote sensing has evolved significantly over the past decades. Early video-based applications were pioneered by Hotta et al. (1981), who recorded swash oscillations in a wave flume, followed by Holman and Guza (1984), who used time-lapse photography to quantify wave run-up on a natural beach. These studies demonstrated the potential of optical techniques to capture hydrodynamic processes non-intrusively and at high temporal resolution. Building on this foundation, the advent of high-frequency laser scanning introduced a new level of detail, enabling near-synchronous, high-resolution measurements of both morphological and hydrodynamic features in coastal environments. With accuracy often comparable to or exceeding traditional remote sensing and intrusive methods (Blenkinsopp et al., 2010; Brodie et al., 2015), laser scanning has become a preferred tool for investigating intra-wave hydro- and morphodynamic processes. Fixed LiDAR systems, in particular, have delivered detailed, high-frequency observations of beach profiles extending from dune crest to nearshore breaking waves in both laboratory and field settings

(Blenkinsopp et al., 2010, 2012; Vousdoukas et al., 2014; Almeida et al., 2015; Hofland et al., 2015; Martins et al., 2016, 2017, 2018; Phillips et al., 2019; Conti et al., 2024, 2025). Figure 2.7 illustrates the experimental setup of Martins et al. (2018), where LiDAR scanners and cameras were deployed in combination to monitor the hydro- and morphodynamic processes.

2.4.2 Coastal cameras

Visual observation of the shoreline from elevated vantage points has long provided crucial insights into nearshore hydrodynamics for lifeguards, scientists, and engineers (Shepard, 1936; Shepard et al., 1941). The introduction of video-based techniques offered a step change, delivering low-cost, high-frequency, and spatially dense measurements of coastal processes (Aagaard and Holm, 1989; Lippmann and Holman, 1989). These methods quickly proved transformative, supporting a wide range of applications and major contributions to the field (Lippmann and Holman, 1990; Holman and Stanley, 2007; Holman and Haller, 2013; Splinter et al., 2018b). An example of an ARGUS video monitoring station (Holman and Stanley, 2007) at the Narrabeen-Collaroy embayment in New South Wales in Australia is illustrated in Figure 2.8.

Figure 2.8: Example of an ARGUS camera system (Holman and Stanley, 2007) installed to monitor the southern part of the Narrabeen-Collaroy embayment in New South Wales , Australia. Image is downmoaded from the Narrabeen data repository `http://narrabeen.wrl.unsw.edu.au/`.

Over the following decades, sustained technological progress and international collaboration culminated in the establishment of the Coastal Imaging Research Network (CIRN) in 2016 (Palmsten and Brodie, 2022). CIRN's mission is to use imagery to advance understanding of processes

shaping coastal, estuarine, and riverine environments, with data and knowledge sharing forming a cornerstone of its approach (Palmsten and Brodie, 2022; McCann et al., 2022). Since the 1980s, video monitoring systems have been deployed in both laboratory and field settings to investigate a broad range of processes, including dune, shoreline, and swash dynamics (Almar et al., 2008; Palmsten and Holman, 2012; Pianca et al., 2015; Ribas et al., 2020; Jaud et al., 2025), sandbar evolution, nearshore bathymetry and intertidal morphology (Jiménez et al., 1997; Plant and Holman, 1997; Uunk et al., 2010; Holman et al., 2013; Bergsma et al., 2016; Bergsma and Almar, 2018; Soloy et al., 2021), as well as longshore currents, rip currents, and wave dynamics (Holland and Holman, 1999; Stockdon and Holman, 2000; Turner et al., 2007; Plant et al., 2008; de Vries et al., 2011; Almar et al., 2012; Vieira et al., 2025).

Recreational beach cameras are now widespread across popular coastal destinations, typically providing low-elevation images or videos that surfers and beachgoers use to qualitatively assess wave conditions. Bracs et al. (2015) demonstrated that, with appropriate rectification and site-specific calibration, such imagery can achieve reasonable accuracy in shoreline detection. Building on this potential, Sánchez-García et al. (2017) proposed a method for projecting camera images onto georeferenced planes using only the horizon as a geometric constraint, thereby extending the scientific utility of these networks. More recently, consumer-grade cameras have been incorporated into formal coastal monitoring applications (Pikelj et al., 2018). A key example is the CoastSnap initiative developed by Harley et al. (2019), which harnesses crowd-sourced smartphone images taken from fixed vantage points of known location and orientation to monitor shoreline change.

2.4.3 In-situ surveys

Topographic coastal surveys are among the most accurate sources of shoreline position data and are commonly treated as ground truth for validating remote sensing techniques (Aarninkhof et al., 2003; Harley et al., 2011; Vos et al., 2019a). The earliest documented morphodynamic ground surveys were conducted in the mid-1930s at La Jolla, California, by the Scripps Institution of Oceanography (Shepard, 1950; Shepard and Inman, 1951). Since then, repeated topographic measurements along fixed beach profiles have become a standard method for quantifying shoreline change (Moore, 2000). Common approaches include the use of traditional surveying instruments such as theodolites and levels, as well as simplified techniques designed for efficiency, such as the widely adopted Emery method (Emery, 1961, see Figure 2.9). An example of a beach profile being surveyed using the Emery (1961) method is illustrated in Figure 2.9, highlighting the labour-intensive nature of these surveys that has historically limited their spatial and temporal coverage (Boak and Turner, 2005). Early field campaigns, including those by Shepard (1950) and Zeigler and Tuttle (1961), laid the groundwork for modern beach morphodynamic research and long-term coastal monitoring. Figure 2.10 highlights several of the most frequently cited monitored sites worldwide that continue to conduct in-situ shoreline surveys spanning more than a decade. The information presented in Figure 2.10 is not exhaustive, as many more monitoring programmes exist

globally, it illustrates the scarcity of high-quality, in-situ derived, and publicly available shoreline datasets.

Figure 2.9: Example of beach profile survey using the Emery (1961) method in Narrabeen beach. The image has been downloaded from the Narrabeen data repository `http://narrabeen.wrl.unsw.edu.au/`.

Figure 2.10: Locations of monitored sites worldwide that continue to conduct high frequency in-situ shoreline surveys spanning more than a decade with publicly available datasets.

Driven by the need to better understand medium- to long-term shoreline morphodynamics, dedicated coastal monitoring programs have been established worldwide. Notable examples include the national coastal monitoring program in the Netherlands, ongoing since 1964 (Ruessink

and Kroon, 1994; Wijnberg and Terwindt, 1995); the Narrabeen–Collaroy program in New South Wales, Australia, initiated in 1976 (Harley et al., 2011; Turner et al., 2016b); the Field Research Facility (FRF) in Duck, North Carolina, U.S.A., established in 1972 (Larson and Kraus, 1994; Zhang and Larson, 2021); the Hazaki Oceanographical Research Station (HORS) in Japan, operating since 1986 with (Banno et al., 2020); and the Bengello (Moruya) Beach program in New South Wales, Australia, monitored since 1972 (Thom and Hall, 1991; McLean and Shen, 2006; McLean et al., 2023). Maintaining these long-term monitoring programs at weekly or biweekly frequency is highly labour intensive, both in data acquisition and post-processing. Nevertheless, the resulting datasets have underpinned numerous studies advancing the understanding of fundamental coastal processes, including beach state evolution and the interaction between cross-shore and longshore sediment transport in driving morphodynamic variability (Splinter et al., 2018b). Among the most influential outcomes of these efforts is the internationally recognized Morphodynamic Beach State Model proposed by Wright et al. (1985).

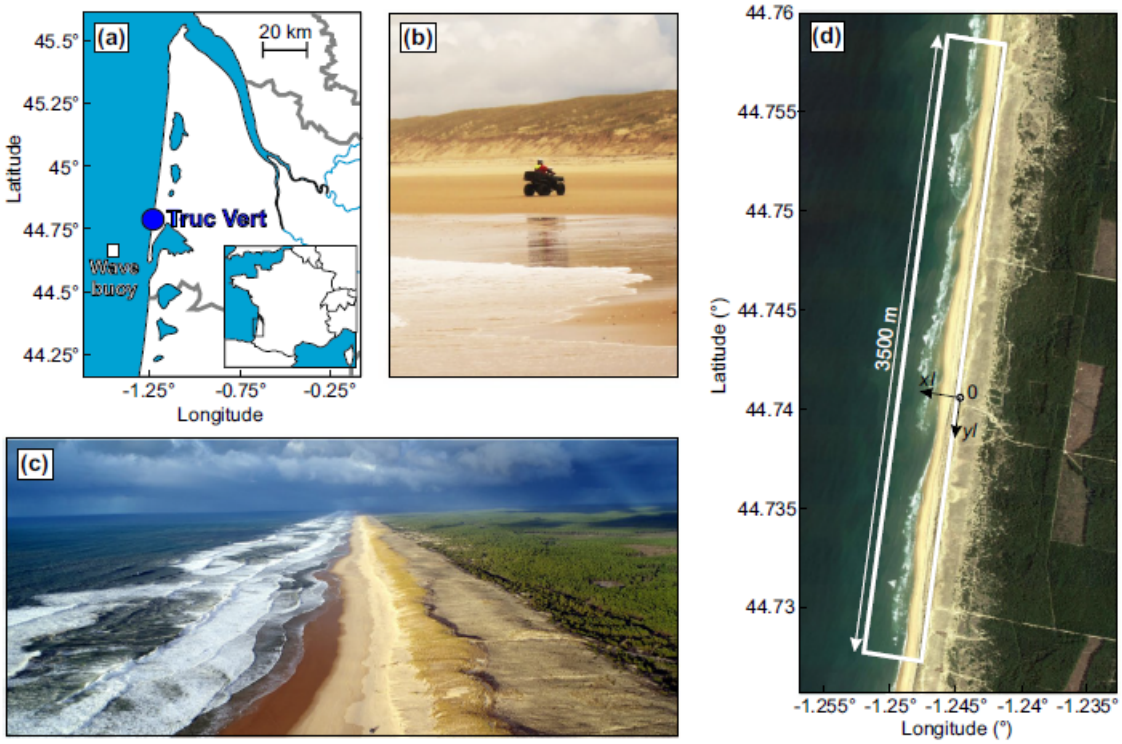

Figure 2.11: Survey site. Panel a, Location map of Truc Vert beach, southwest France with location of nearby wave buoy. Panel b, GNSS-equipped ATV used to perform the monthly to bimonthly surveys since 2003. Panel c, Aerial view showing the remote Truc Vert beach with prominent rip channels. Panel d, Survey zone and reference frame used at Truc Vert beach. The figure is borrowed from Castelle et al. (2020).

Rapid advancements in the availability of precision GPS and the affordability of RTK-GNSS equipment in the early 2000s greatly improved shoreline monitoring by enhancing accuracy, efficiency, and data density. These developments not only strengthened existing programs (Harley et al., 2011; Turner et al., 2016b; McLean et al., 2023) but also enabled the establishment of new ones (Bertin et al., 2022; Fernández-Mora et al., 2023). Mounting RTK-GPS receivers on all-terrain vehicles (ATVs) allowed for high-frequency, three-dimensional surveys of extensive sub-

aerial beach areas (Yates et al., 2011; Harley et al., 2011; Turner et al., 2016b; Ludka et al., 2019; Castelle et al., 2020; McCarroll et al., 2023). Such datasets have deepened understanding of coastal processes, including beach rotation (Harley et al., 2011, 2015) and storm-sequence response (Coco et al., 2014), while the integration of long-term records has supported regional-scale analyses of beach response to extreme events and wave climate variability (Masselink et al., 2016, 2023).

Figure 2.11 presents the example of the well-monitored, remote site of Truc Vert, located on the coast of Nouvelle Aquitaine in southwest France and exposed to the Atlantic Ocean. Bimonthly topographic surveys are conducted at Truc Vert using an ATV (panel b in Figure 2.11) equipped with an RTK-GNSS receiver. The alongshore coverage of these surveys extends approximately 2.5 km around the point of origin, as shown in panel d of Figure 2.11. Panel c provides an aerial view of the site, highlighting the characteristic rip channels and megacusp formations. Truc Vert serves as an example of the labour-intensive nature of in situ coastal monitoring and remains one of the few sites worldwide providing publicly available, high-frequency, in situ–derived shoreline datasets. The Truc Vert dataset is thoroughly described in Castelle et al. (2020).

2.4.4 Airborne observations

Airborne LiDAR surveys have been routinely employed since the late 1990s to observe beach/ dune topography (Andrews et al., 2002; Sallenger. et al., 2003) and nearshore bathymetry in shallow coastal areas with clear waters (Irish and White, 1998; Aleman et al., 2015). LiDAR derived DEMs enabled the detection of coastal morphological features and facilitated site specific modelling applications at regional scales ($O \sim 100$ km) (Stockdon et al., 2002). The high cost of data collection and post processing requirements however, have limited the temporal resolution of airborne LiDAR surveys to annual or multiannual in most cases (Saye et al., 2005; Yates et al., 2009a; Mauff et al., 2018; Lerma et al., 2019; Laporte-Fauret et al., 2022; Vandenhove et al., 2025). The large spatial coverage of airborne LiDAR surveys with a vertical accuracy of 15 cm (Sallenger. et al., 2003) offers great potential for regional studies of seasonal to interannual morphodynamic nearshore processes. Unmanned aerial vehicles (UAV) provide an efficient and cost-effective survey tool for topographic mapping and measurement in the coastal zone (Turner et al., 2016a,b). LiDAR or camera equipped UAV survey equipment and data processing methods are readily available off the shelf tools suitable for use by coastal scientists (L'udovít Kovanič et al., 2023). Although UAVs can overcome the temporal sparsity of aerial LiDAR surveys and photography, this comes at the expense of spatial coverage (Sestras et al., 2025).

Aerial photographs remain one of the most widely used sources for shoreline mapping (Crowell et al., 1991; Moore, 2000). Black-and-white vertical imagery began in the 1920s, with stereo photographs available by the late 1930s (Anders and Byrnes, 1991). These archives provide the only long-term ($O \sim$100 years) global record of high-resolution shoreline observations, though temporal resolution varies between sites. Aerial photography also represents the first historical

source enabling extraction of multiple CSIs.

To derive topographic features, aerial photographs must be corrected for distortions from aircraft tilt, altitude variation, and topographic relief (Crowell et al., 1991; Moore, 2000), which are generally less pronounced in post-1950 imagery (Anders and Byrnes, 1991). Advances in softcopy photogrammetry now allow for DEM and orthophoto generation from scanned stereo pairs (Moore, 2000; Boak and Turner, 2005). Incorporating datum-referenced elevation information further enhances their value, making aerial photography one of the most important data sources for historical CSI determination. The first documented coastal use of aerial photography was by Williams (1947), who extracted nearshore bathymetry during World War II. Since then, aerial imagery has been extensively used to study shoreline evolution, dune and bar dynamics, and volumetric beach changes across diverse coastal environments (Short, 1975; Frihy, 1988; Jiménez et al., 1997; Chaaban et al., 2012; Montreuil and Bullard, 2012; Ford, 2013; Castelle et al., 2018b; Carvalho et al., 2020).

2.4.5 Historical shoreline observations

Historical ground-based photographs can provide valuable information for periods when other datasets are scarce or absent. Coastal scientists have long used them as contextual evidence, for instance to identify morphological features such as sand spits or tidal channels. Despite being among the earliest shoreline data sources, they have rarely supported quantitative analyses of coastal evolution (Boak and Turner, 2005), due to uncertainties from high oblique angles, unknown vantage points, limited scale and control information, and the lack of records on wave or tidal conditions at the time of capture. Nevertheless, Valverde et al. (2025) demonstrated that ground-oblique images can support quantitative shoreline assessment with uncertainties below 10 m. Given the generally poor quality of historical photographs and compounding interpretive uncertainties, their value for large-scale quantitative shoreline mapping remains limited.

Maps and charts constitute the earliest systematically produced spatial data and can be viewed as direct precursors to modern cartography. From a European perspective, the history of cartography spans more than seven centuries, beginning in the late 13th century (Ritchie, 1991). Early maps, however, often lack documentation on survey techniques, shoreline definitions, or positional accuracy (Carr, 1962). A surge in scientific progress in the late 17th century stimulated more rigorous mapping of land and sea (Ritchie, 1991), while Franco–British collaborations established geodetic principles as the foundation for standardized surveying. Following the determination of the Earth's shape in 1736 (Levallois, 1988) and the founding of the Ordnance Survey in 1791 (Baily and Nowell, 1996), cartography advanced rapidly toward reliable, standardized map production. Subsequent improvements in instrumentation and methodology have continually enhanced map accuracy.

Ordnance Survey maps, which extend landward from the high-water mark, represent some of

the oldest reliable shoreline datasets in the United Kingdom and Ireland (Baily and Nowell, 1996). Similarly, the U.S. Coast Survey's "T-sheets," first produced in the 1830s, provide early systematic documentation of the High Water Line, typically inferred from visible indicators such as vegetation limits, driftwood deposits, or rock discolouration (Boak and Turner, 2005). Historical maps nevertheless contain numerous potential errors, including scale inconsistencies, datum shifts, projection distortions, and material degradation (e.g., shrinkage, folds, or tears) (Anders and Byrnes, 1991; Crowell et al., 1991). Additional uncertainty arises from the surveyor's interpretation of the shoreline itself. Despite these limitations, historical maps and charts remain indispensable when no alternative data exist.

2.4.6 Earth observing satellites

Civilian Earth observation satellites have been providing publicly available, global imagery since the launch of Landsat 1 in 1972 (Wulder et al., 2022). Over time, both spatial resolution and revisit frequency have improved, producing an ever-expanding archive of satellite data (Belward and Skøien, 2015). In parallel, high resolution commercial products have become increasingly accessible through subscription-based services (e.g. Planet, 2023). Figure 2.12, illustrates the timeline of all major civilian earth observing satellite missions, operating optical imaging sensors producing publicly available and commercial image collections. These space-borne observations transformed coastal science into a data rich discipline, enabling coastal change studies at virtually any location worldwide (Vos et al., 2019a). Early local applications exploiting this abundant source of data to study shoreline evolution began appearing in the early 1990s (Blodget et al., 1991). However, it was only with advances in high-performance computing and the emergence of large-scale, cloud-based platforms as a universal resource (Gorelick et al., 2017) that automation became feasible, enabling regional and planetary scale applications (Donchyts et al., 2016; Luijendijk et al., 2018; Mentaschi et al., 2018; Bishop-Taylor et al., 2021; Castelle et al., 2022, 2024; Vos et al., 2023a; Graffin et al., 2025a; Calkoen et al., 2025).

The coastal science community quickly capitalized on the opportunity of multispectral satellite imagery with global coverage, developing more than 40 different algorithms to automatically or semi-automatically map shorelines on multispectral satellite imagery (Toure et al., 2019; McAllister et al., 2022). Within five years satellite derived shoreline (SDS) data have become an established monitoring technique (Vitousek et al., 2023a). Figure 2.13 presents a typical waterline detection workflow using satellite imagery, based loosely on the CoastSat algorithm (Vos et al., 2019b) but representative of a generic shoreline detection approach. The acquired image is quality controlled and preprocessed on a large cloud computer (e.g. Gorelick et al., 2017), allowing the user to download scenes cropped at a specific region of interest (ROI) including only the relevant, user defined spectral bands. This process reduces the size of the data from several giga-bytes to less than 1 mega byte per 5 km^2 (e.g. image of Truc Vert in Figure 2.13). Shoreline detection algorithms make use of the visible bands (red, blue and green), the near-infrared (NIR) and the

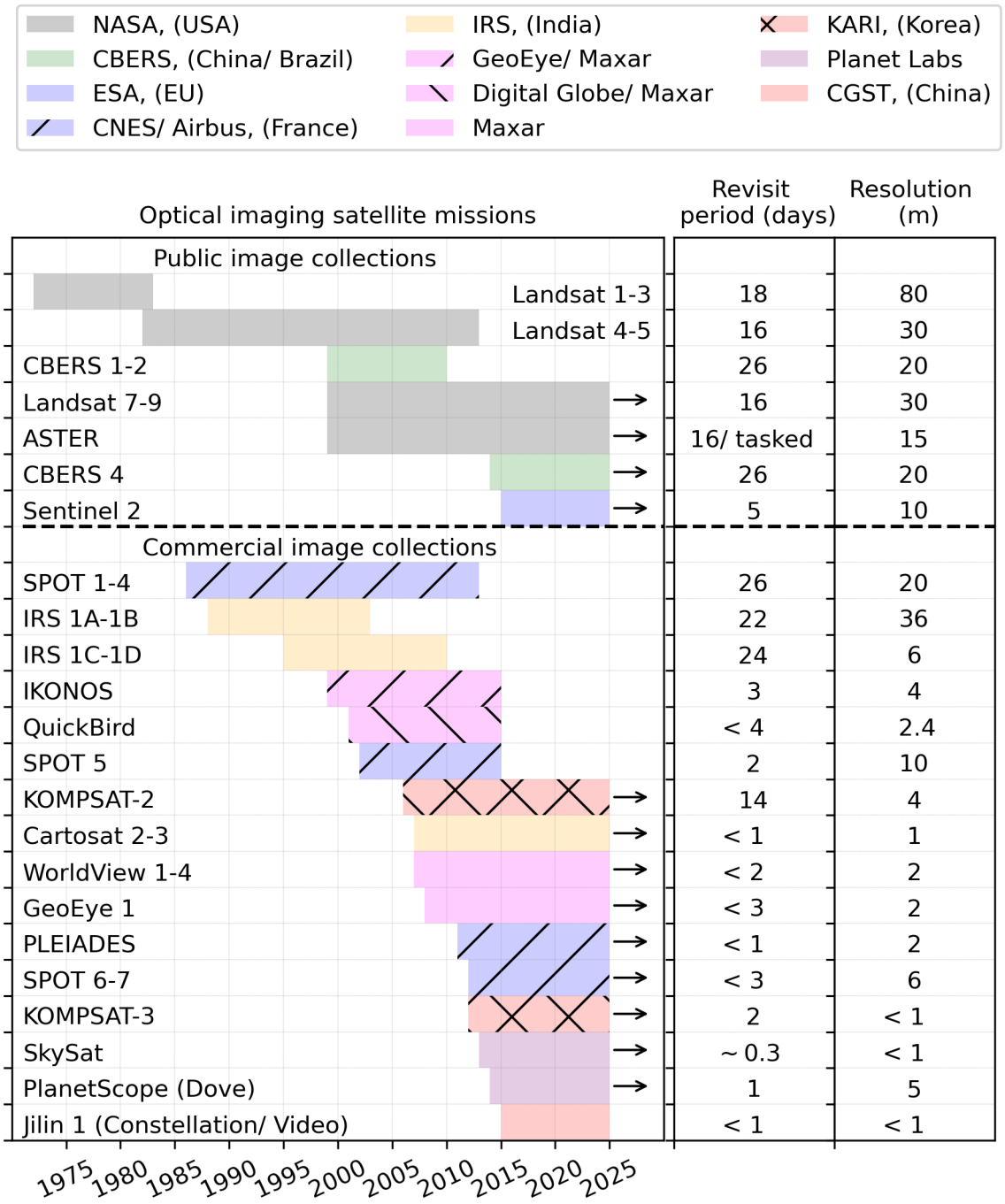

Figure 2.12: Timeline for the major civilian Earth observation satellites operating optical imaging sensors with global coverage. Arrows indicate the mission is ongoing and the operating entity is indicated by the fill defined in the legend of the figure.

short-wave infrared (SWIR1). Common approaches make use of indices to distinguish between water and land pixels such as the normalized difference water index (NDWI) or the modified version (MNDWI) (Xu, 2006). Successively the image is segmented, whereby pixels are classified into predetermined classes (e.g. "sand", "water", "whitewater", "vegetation", see Figure 2.13), facilitating spatially mapping of coastal environments. To achieve sub-pixel resolution, usually a thresholding algorithm is deployed to maximize inter class variance (e.g. Otsu, 1979). The final step is computing the iso-valued contour based on the optimal threshold by deploying a contouring algorithm to obtain the waterline position at sub-pixel resolution. In table 2.2 the most common

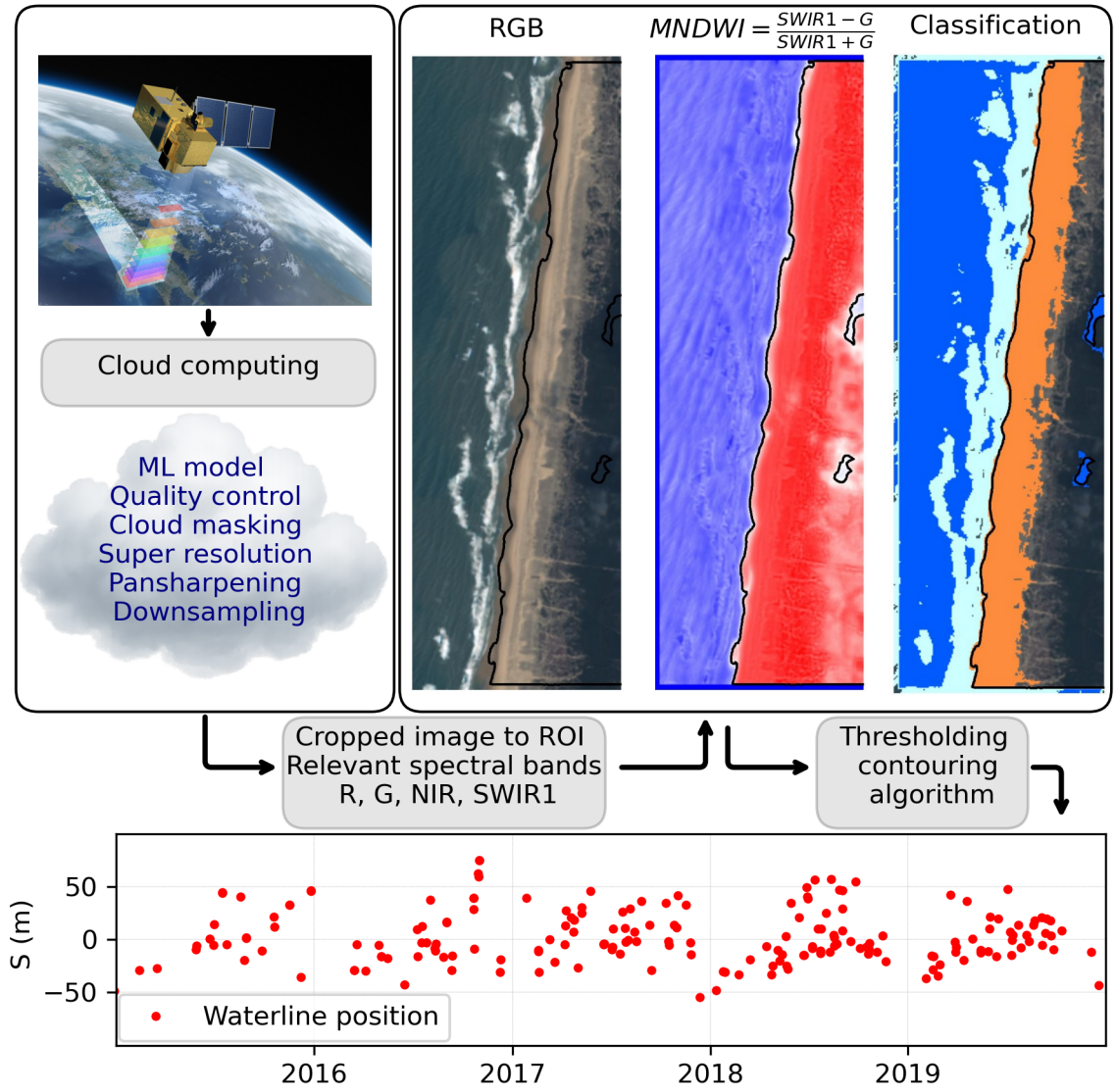

Figure 2.13: Schematic representation of common waterline detection workflow algorithms.

methods found in the literature, to automatically map the position of the waterline/shoreline at pixel and sub-pixel resolution from satellite imagery are summarized.

As discussed in Section 2.2, the horizontal position of the observed waterline is not always representative of the true shoreline and is highly dependent on hydrodynamic and morphodynamic conditions at the time of image acquisition, with reported deviations of up to ~ 50 m (Castelle et al., 2021; Konstantinou et al., 2023; Graffin et al., 2023; Vos et al., 2023b). Post-processing of satellite derived waterlines using tide and hydrodynamic models to account for tidal elevation, surges and wave run-up can reduce these errors, though information about the beach slope is required which may not be available at all sites. Alongshore averaging can further minimize the effect of localized water level fluctuations (e.g. swash), the appropriate extent however is site specific (e.g. Vos et al., 2019b; Castelle et al., 2020). Vos et al. (2023b) performed a benchmarking study to quantify the performance of five of the most commonly used SDS algorithms (Luijendijk et al., 2018; Vos et al., 2019b; Sánchez-García et al., 2020; Almeida et al., 2021; Mao et al., 2021) against in-situ observations. All methods were found to perform well in microtidal sites with an average root

Automated shoreline extraction algorithms from optical satellite imagery	
Pixel resolution	Yamano et al. (2006); Bayram et al. (2008); Maiti and Bhattacharya (2009) Kuleli et al. (2011); García-Rubio et al. (2015); Hagenaars et al. (2018) Xu (2018) Luijendijk et al. (2018); Almeida et al. (2021); Mao et al. (2021)
Sub-pixel resolution Marching squares	Cipolletti et al. (2012); Liu et al. (2017); Vos et al. (2019a,b) Bishop-Taylor et al. (2021); Doherty et al. (2022)
Sub-pixel resolution Max gradient	Pardo-Pascual et al. (2012); Almonacid-Caballer et al. (2017) Sánchez-García et al. (2017, 2020)
Sub-pixel resolution Soft classification	Foody et al. (2005); Muslim et al. (2006); Dewi et al. (2018)

Table 2.2: Summary of different approaches to automatically map waterlines/shorelines on optical satellite imagery at pixel and sub-pixel resolution. The different algorithms used to map the waterline at sub-pixel resolution are indicated in the first column of the table.

mean square error of $\sim$10 m, while in high energy, gently sloping, meso-macrotidal environments, errors surged to $\sim$30-40 m. While global, dense SDS datasets hold considerable promise, their application in detailed analyses still demands substantial effort, particularly in the quality control of mapped shorelines.

However, optical imagery has inherent limitations as it cannot penetrate dense cloud cover, limiting observation frequency in high latitudes and during winter periods, and can only provide a two-dimensional representation. To overcome these constraints, new approaches are increasingly drawing on alternative satellite sensors such as Synthetic Aperture Radars (SAR) and LiDAR equipped satellites. SAR offers the advantage of cloud penetration and may provide a reliable means of monitoring coastal change in persistently cloud-contaminated regions. LiDAR missions such as ICESat-2 deliver high-resolution coastal topography, while satellite altimetry has long been employed to estimate sea surface dynamics. Most recently, the launch of SWOT (Surface Water Ocean Topography) has enabled sea surface elevation measurements at unprecedented spatial resolutions. With these continual developments, coastal scientists are approaching the capability to resolve the full spectrum of coastal physical drivers and their responses at a global scale.

2.5 Shoreline change modelling

Shoreline-evolution models span a wide spectrum of complexity and computational demand, from fully process-based to purely data-driven approaches (Sherwood et al., 2022; Hunt et al., 2023). Figure 2.14 illustrates the approximate spatiotemporal scales of these modelling frameworks relative to sandy beach morphodynamic response. Process-based models explicitly couple hydrodynamics, waves, sediment transport, and morphology through the conservation of mass and momentum (e.g. Roelvink et al., 2009). While skillful at simulating storm-scale impacts (O days) locally (O 100 m), their substantial data requirements (e.g. detailed bathymetry and topography)

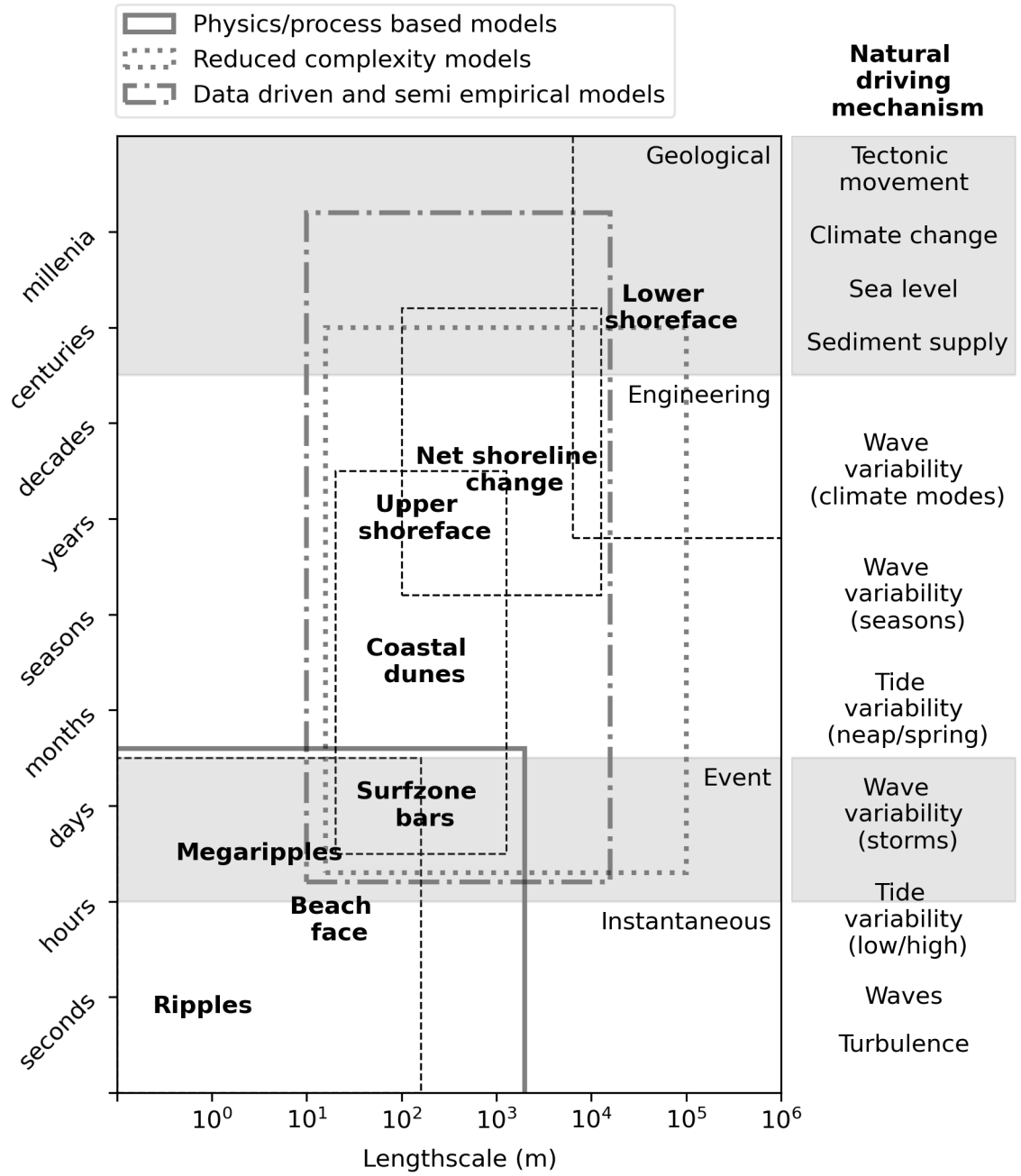

Figure 2.14: Spatiotemporal representation of the primary modes of sandy beach variability and their drivers, including typical spatial and temporal scales resolved by the different model classes. The figure is inspired by and aspects of it have been modified from Castelle and Masselink (2023) & Hunt et al. (2023).

and computational costs render regional or long-term applications impractical. Moreover, predictions over extended timescales often degrade due to cascading uncertainties arising from initial and boundary condition dependencies, omitted physical processes, and system nonlinearities.

Reducing model complexity has proven effective in improving the robustness of long-term shoreline predictions (Murray, 2007; Kaergaard and Fredsoe, 2013), while also drastically lowering computational demands. This approach gave rise to the family of reduced-complexity models,

which focus on representing only the dominant processes driving change, offering an efficient and reliable alternative to more physics-heavy models (e.g. Davidson et al., 2013; Robinet et al., 2018). At the far end of the spectrum, purely data-driven models map shoreline response directly to environmental forcing without explicitly embedding physical process knowledge (e.g. Simmons and Splinter, 2025; Calcraft et al., 2025b,a). Although such models can be powerful, their limited interpretability and lack of physical transparency constrain their broader use in operational and policy-relevant applications.

As highlighted by Hunt et al. (2023), model complexity is closely linked to data requirements (Figure 2.15). The increasing availability of high-quality observational datasets now provides new opportunities to develop hybrid frameworks that blend reduced-complexity modelling with data-driven techniques, paving the way for more accurate, scalable, and computationally efficient predictions of shoreline evolution.

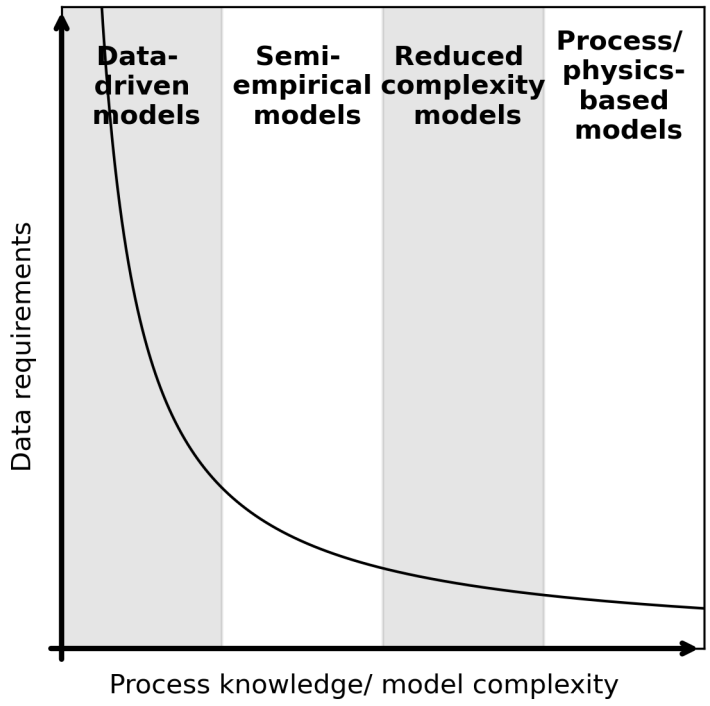

Figure 2.15: Schematic representation of the relationship between model complexity and data requirements modified after Hunt et al. (2023).

In what follows, we will focus first on semi-empirical, reduced complexity and hybrid shoreline change models, as these are the types of models to be used on this thesis work), and then on existing calibration and data assimilation methods designed for improving shoreline modelling skills.

2.5.1 Semi empirical models

Semi-empirical models establish a direct relationship between wave forcing and coastal response through simplified formulations that embed basic system knowledge. These models do not

explicitly resolve nearshore processes such as wave shoaling, dissipation, hydrodynamics, or sediment transport. Their simplicity makes them computationally efficient but also highly dependent on relatively long observational datasets for calibration of free parameters (Splinter et al., 2018b) and can often constrain their general applicability (Hunt et al., 2023). Frequently, the simplicity of these models restricts their widespread application, with some prominent models only being applicable to coastlines dominated by either longshore and/or cross-shore transport processes (Hunt et al., 2023).

Equilibrium shoreline change models belong to the family of semi-empirical models and are based on the assumption that coastal systems fluctuate around a static or dynamic equilibrium state, the latter typically represented by a weighted moving average of antecedent wave conditions (Vitousek et al., 2025). The concept was first introduced by Wright et al. (1985) to predict beach state transitions, and since then numerous variations have been developed to model shoreline evolution in the cross-shore direction (e.g. Miller and Dean, 2004; Yates et al., 2009b; Davidson and Turner, 2009; Davidson et al., 2013; Splinter et al., 2014), beach rotation (e.g. Turki et al., 2013; Jaramillo et al., 2021a), and sandbar evolution (e.g. Plant et al., 1999).

In the following subsections, two widely used equilibrium shoreline change models are presented, namely the ShoreFor model developed by Davidson et al. (2013) to simulate shoreline evolution in the cross-shore direction, and the equilibrium-based beach rotation model developed by Jaramillo et al. (2021a). Both models illustrate the structure and principles of the equilibrium concept and have been used in the present study to simulate shoreline evolution on several sites.

ShoreFor model

The ShoreFor model simulates the displacement of the shoreline as a function of the nearshore wave power and a disequilibrium state of the beach. In the approach of Davidson et al. (2013) the rate of shoreline change dx/dt (m/s) is defined as:

$$\frac{dx}{dt} = c^{\pm} P^{0.5} (\Omega_{eq} - \Omega) \tag{2.1}$$

where the model's forcing term is the product of the incident wave power P (W) computed using linear wave theory, and the model free parameter $c^{\pm}$ representing the response rate of the shoreline with units of velocity per measure incident wave power. The parameter $c^{\pm}$ is separated into accretion c^{+} when $\Omega_{eq} > \Omega$ and erosion c^{-} when $\Omega_{eq} < \Omega$ components, accounting for the fact that accretion and erosion are observed to evolve at different rates. Davidson et al. (2013) included a term b in their formulation accounting for linear trends stemming from longer term processes that are not explicitly addressed in the model. The term inside the parenthesis in equation 2.1 is a disequilibrium term which is based on the premise that shoreline state and morphological change

are inter-related. Ω is the so called dimensionless fall velocity defined as:

$$\Omega = \frac{H_s}{T_p w_s} \tag{2.2}$$

where H_s and T_p are the instantaneous significant wave height and peak wave period respectively and w_s is the terminal fall velocity of the beach's median grain diameter d_{50} calculated using Stoke's law. The time varying equilibrium condition Ω_{eq} is a weighted average of the antecedent dimensionless fall velocity Ω defined as:

$$\Omega_{eq} = \sum_{j=0}^{2\phi} \Omega_j 10^{-j/\phi} \left[\sum_{j=0}^{2\phi} 10^{-j/\phi} \right]^{-1} \tag{2.3}$$

where j is the number of days prior to the present time and the memory decay ϕ is a model free parameter indicating the number of days it takes for the weighting to reach 10%, 1% and 0.1% of the instantaneous value at ϕ, 2ϕ and 3ϕ days prior to the present. The formulation used in the present work and shown in Equation 2.3 incorporates all past beach state information for the past 2ϕ days, yielding a minimum weighting factor of 1%.

The ShoreFor model has been applied across a wide range of sites worldwide, demonstrating strong and consistent performance in shoreline change modelling, often ranking above average in benchmarking studies (Splinter et al., 2014; Montaño et al., 2020; Mao et al., 2025). Beyond shoreline evolution, variations of the model have been successfully employed to simulate sandbar rhythmicity (Stokes et al., 2015), beach volume variability (Burvingt et al., 2018), and temporal changes in beach slope (Labarthe et al., 2023), highlighting the flexibility of its robust equilibrium framework. Moreover, its successful integration into hybrid modelling frameworks to represent the cross-shore component of shoreline evolution further illustrates its compatibility and versatility (Robinet et al., 2018).

Equilibrium based shoreline rotation model

The rate of beach rotation change $d\alpha_s/dt$ ($^\circ$/s) in the model of Jaramillo et al. (2021a) is calculated as:

$$\frac{d\alpha_s(t)}{dt} = L^{\pm} P(\Delta\alpha_s(\theta)) \tag{2.4}$$

where the model's forcing term is the product of the incident wave power P (W) computed using linear wave theory, and the model free parameter $L^{\pm}$ representing the response rate of the shoreline with units of degrees per incident wave power. The response rate is separated into clockwise L^{+} when $\Delta\alpha_s(\theta) > 0$ and counter clockwise L^{-} when $\Delta\alpha_s(\theta) < 0$ components, accounting for the fact that clockwise and counter-clockwise rotation can evolve at different rates. The orientation disequilibrium term $\Delta\alpha_s(\theta)$ is defined as:

$$\Delta\alpha_s(\theta) = \alpha_s - \frac{\theta - b}{\alpha\prime} \tag{2.5}$$

where α_s is the orientation of the beach, θ (°) is the incoming wave direction and b (°) and $\alpha\prime$ (-) are model free parameters. In total, the model free parameters that need to be calibrated are b, $\alpha\prime$ and the rotation rate $L^{\pm}$.

The beach rotation model developed by Jaramillo et al. (2021a) was applied to two well-monitored South Pacific sites, Tairua Beach in New Zealand and Narrabeen Beach in Australia, demonstrating strong predictive skill. These benchmark sites are frequently used for model comparison and validation (Montaño et al., 2020; Repina et al., 2025), and the model's predictions ranked within the top 30% in the benchmarking study by Mao et al. (2025). The model has also been successfully integrated into hybrid modelling frameworks to represent the rotational component of shoreline evolution over time, further underscoring its compatibility and adaptability (Jaramillo et al., 2021b).

2.5.2 Reduced complexity models

Reduced-complexity models often focus on simulating specific processes that are critical to the morphodynamic response under investigation (see Figure 2.14). This modelling class spans a wide spectrum, ranging from relatively simple formulations to more advanced frameworks incorporating increased dimensionality, detailed treatments of wave shoaling and dissipation, explicit sediment transport calculations, and mass/volume conservation principles (Hunt et al., 2023). Many reduced-complexity models are designed to represent both longshore and cross-shore sediment transport components, as well as the influence of natural headlands or coastal structures.

Beach profile models extend cross-shore predictions by explicitly simulating wave shoaling, dissipation of incident wave energy, sea-level variability, and sediment transport along the beach profile (e.g. Larson, 1989; Davidson, 2021). Longshore sediment transport models describe how sediment stirred up by waves is redistributed by alongshore currents generated by wave energy dissipation under oblique wave incidence (e.g. Bijker, 1971; USACE, 1984; Deigaard et al., 1986; Kamphuis et al., 1986). Building on this principle, the one-line model first introduced by Pelnard-Considére (1957) assumes that gradients in alongshore sediment transport drive a cross-shore translation of a coastal profile with constant shape. Since its inception, numerous variants of the one-line model have been developed to predict shoreline evolution along longshore sediment transport dominated coasts (e.g. Hanson, 1989; Ashton and Murray, 2006; Kristensen et al., 2016; Roelvink et al., 2020; van Rijn and Huisman, 2025).

2.5.3 Hybrid shoreline models

In recent years, hybrid modelling frameworks have emerged that couple different reduced-complexity approaches, or integrate reduced-complexity and semi-empirical models, to capture interactions among multiple drivers of shoreline change while maintaining computational efficiency. Most of these frameworks couple cross and longshore sediment transport processes through equilibrium and pseudo one-line models (Vitousek et al., 2017; Robinet et al., 2018; Antolínez et al., 2019; Alvarez-Cuesta et al., 2021a; de Santiago et al., 2021; Jaramillo et al., 2021b). These efforts mark an important step toward bridging the gap between process and the scale representation needed for long-term or large-scale shoreline prediction.

Two characteristic examples of reduced complexity hybrid models are presented in the following subsections. Namely the transect based CoSMoS-COAST model developed by Vitousek et al. (2017, 2021, 2023b) and the grid based LX-Shore model developed by Robinet et al. (2018), both of which have been showcasing great skill in recent benchmarking studies (Montaño et al., 2020; Mao et al., 2025; Repina et al., 2025).

CoSMoS-Coast

The CoSMoS-COAST model developed by Vitousek et al. (2017, 2021, 2023b) is a transect based hybrid shoreline model. The model integrates a modified version of the cross-shore model developed by Yates et al. (2009b) with an one-line model and a formulation to account for a geometrical retreat of the shoreline due to sea level rise based on Bruun (1962). A schematic representation of the model structure and main variables of the CoSMoS-COAST model is illustrated in Figure 2.16.

The model discretization is based on transects perpendicular to the coastline so that the shoreline position moves landward/seaward, like on a rail (Vitousek et al., 2017). This framework does not account for high-angle wave instability or the associated growth of large-scale shoreline features such as spits, sand waves, and capes (e.g. Ashton and Murray, 2006; Kaergaard and Fredsoe, 2013; Robinet et al., 2018; Roelvink et al., 2020).

The most recent development by Vitousek et al. (2023b) introduced a littoral cell-based data assimilation module using an ensemble Kalman filter. The model was applied to simulate the entire California coastline (approximately 1,760 km) and achieved a root-mean-square error (RMSE) below 10 m for nearly half the region during the validation period. CoSMoS-COAST has consistently ranked among the top-performing models in multiple benchmarking studies (Montaño et al., 2020; Mao et al., 2025; Repina et al., 2025). A notable strength of this implementation is the integration of an extended Kalman filter, which enables efficient calibration with limited observations, assimilation of near-real-time data, and quantification of uncertainty through confidence intervals for both model parameters and predictions.

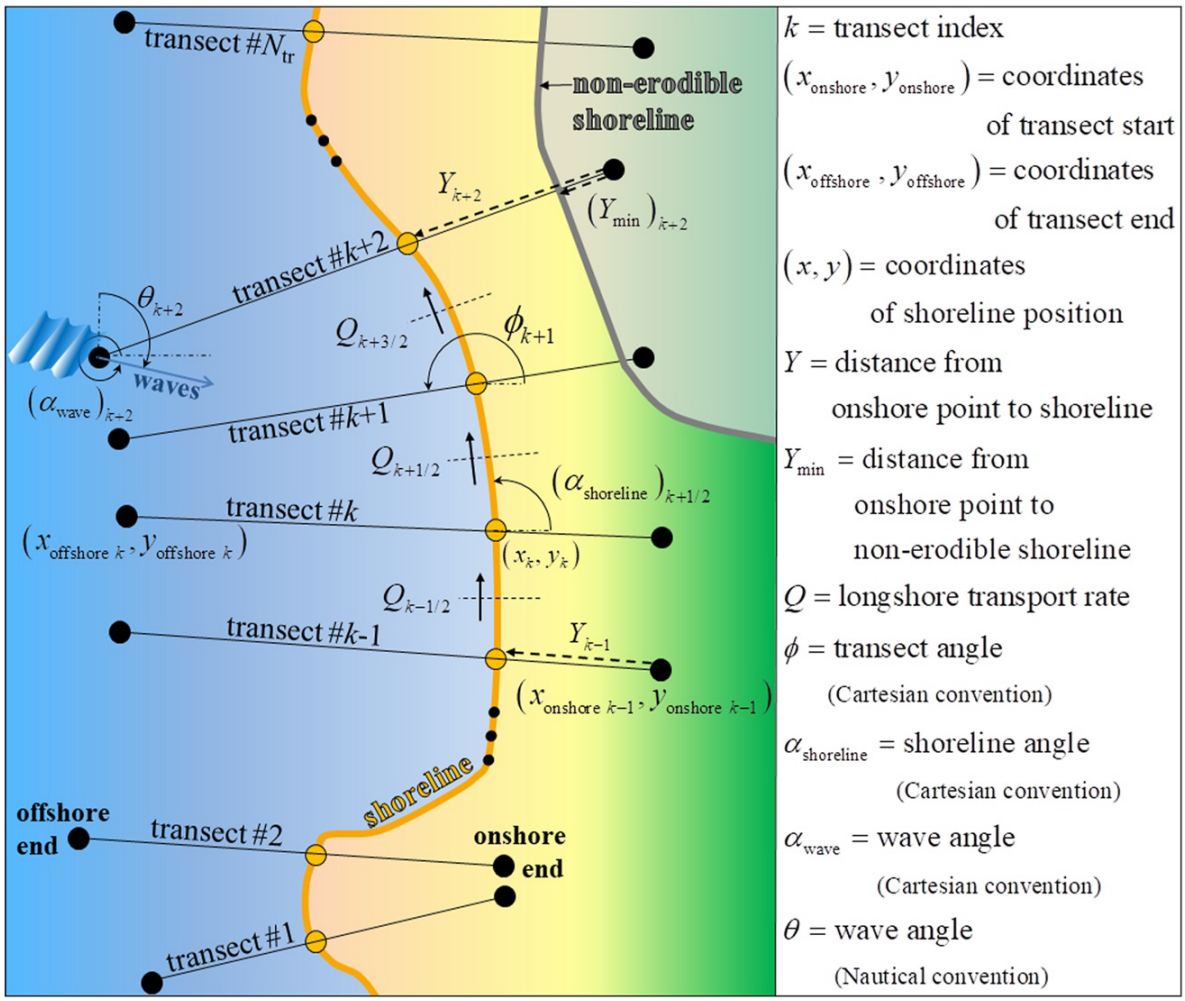

Figure 2.16: Schematic representation illustrating the setup and important variables of the transect based CoSMoS-COAST shoreline model. The figure is borrowed by Vitousek et al. (2023b)

LX-Shore model

The reduced-complexity LX-Shore model developed by Robinet et al. (2018) is a cellular-based one-line model that represents the coastline on a 2D plan-view grid, where each cell contains a fractional sediment value (F). This cellular representation facilitates the simulation of longshore-transport–driven shoreline dynamics in complex morphologies, such as spits, barrier islands, and enclosed lagoons. A schematic overview of the LX-Shore model and the integrated processes is presented in Figure 2.17. For sediment flux calculations, LX-Shore integrates longshore sediment transport formulations (e.g. Kamphuis, 1991) with the cross-shore model of Davidson et al. (2013). The resulting framework dynamically couples shoreline change with the nearshore wave field, which can be provided either by coupling with a spectral wave model (Booij et al., 1999) or estimated using the formulation of Larson et al. (2010). The Larson et al. (2010) formula, provides a simplified solution to the wave energy flux conservation equation combined with Snell's law. To avoid sediment transport and wave propagation in areas shielded from incoming wave energy (shadow zones), the solution developed by Ashton and Murray (2006) is implemented when using the Larson et al. (2010) formula.

Compared to most of the other reduced complexity models (e.g. Vitousek et al., 2017; Antolínez et al., 2019), the main specificity of LX-Shore model is its grid-based architecture, enabling the simulation of complex coastal geometries and shoreline instabilities. This structure also makes it highly compatible with satellite-derived data, presenting an opportunity for model–data integration. Recent developments include the incorporation of sediment bypass around headlands and breakwaters (Durand et al., 2024), as well as shoreline translation driven by sea-level rise (Traboulsi et al., 2025). The model has been applied across diverse environments and has consistently performed above average in benchmarking studies (Montaño et al., 2020; Mao et al., 2025).

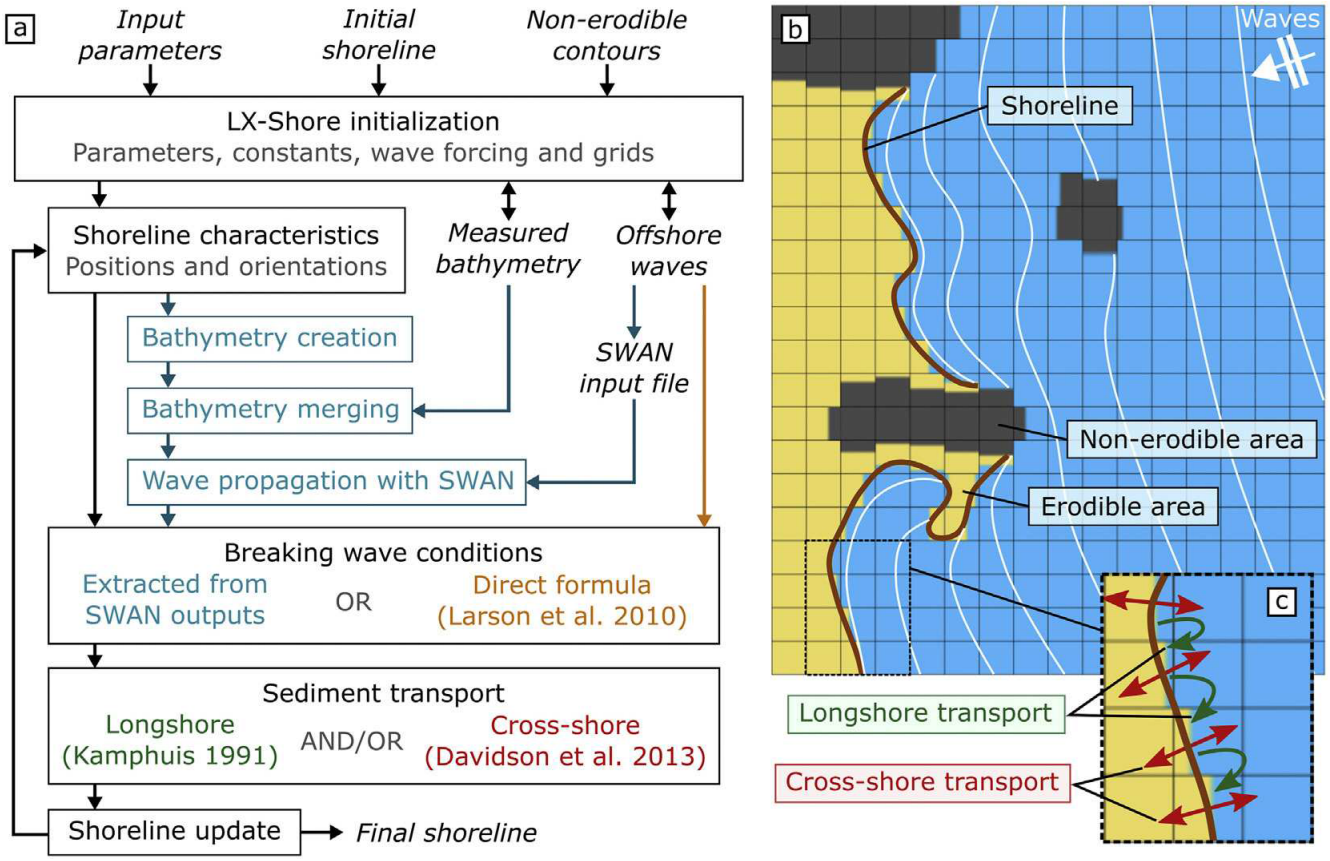

Figure 2.17: Overview of the architecture of the LX-Shore model and main features and processes integrated. Panel a, Model architecture. Panel b, Example of a plan-view coastal area used in the model. Panel c, Example of the longshore and cross-shore sediment transports rate calculations. Figure is borrowed by Robinet et al. (2018).

2.5.4 State of the art in shoreline change modelling

Collaborative benchmarking studies are central to advancing shoreline change prediction, as they critically assess current capabilities, expose limitations, and highlight pathways for improvement (Montaño et al., 2020; Repina et al., 2025; Mao et al., 2025). Results from the blind test competition reported by Mao et al. (2025) demonstrated that most models can now reproduce 5 and even 50 years of shoreline evolution, within the intrinsic accuracy of the available calibration and validation data (RMSE $\leq$ 10 m), an achievement that underscores the significant progress of

the past decades.

Yet, important challenges remain. Models struggle to represent coastlines with strong inherited geology (e.g. headlands, rocky outcrops), complex planforms, and headland bypassing as these challenge numerical implementation. Mixed sediment environments, tidal inlets, river deltas, and other zones with multiple sediment sources and sinks present additional obstacles. Most reduced-complexity and hybrid models continue to rely on the simplified Bruun (1962) approach for simulating sea-level rise impacts—an assumption now recognized as flawed in most real-world settings (Cooper et al., 2020). Addressing these challenges will require the development of new modelling frameworks that better capture the interactions between physical processes, sediment pathways, and sea-level rise, ensuring that predictions remain robust.

2.5.5 Model Calibration

Model calibration is a fundamental step in shoreline modelling, involving the systematic adjustment of model parameters to minimize discrepancies between simulated and observed shoreline positions. It is essentially an optimization problem where the choice of calibration metric, or loss function, strongly influences which aspects of the system are prioritized (Montaño et al., 2020; Mao et al., 2025). Calibrating over a specific period can introduce biases if that window is dominated by particular phenomena, such as storms or seasonal trends, while overfitting can reduce predictive skill under new conditions (Splinter et al., 2017; Simmons and Splinter, 2025; Calcraft et al., 2025b). Careful selection of both the calibration metric and the temporal of the calibration dataset (Splinter et al., 2018a) data essential to ensure reliable and robust model performance.

While the broader literature on optimization problems offers a vast array of methods, from classical linear techniques to sophisticated non-linear and global optimization algorithms, their application within the shoreline modelling domain remains limited. In practice, calibration is often performed manually through trial-and-error. This approach however is both labour intensive and does not yield optimal model performance, especially for non-linear models such as reduced complexity shoreline change models. Applying relatively simple linear approaches such as multi-linear regression (e.g. Schepper et al., 2021) can significantly improve efficiency of the calibration process and model skill. More advanced non-linear optimization techniques (e.g. Bertsimas and Tsitsiklis, 1993) have been applied in some cases to calibrate model free parameters (e.g. D'Anna et al., 2020; Labarthe et al., 2023; Chen et al., 2025). These however, remain the exception rather than the norm, highlighting a significant gap between available optimization methodologies and their adoption in coastal model calibration. When employed to maximize model skill expressed through a quantifiable metric (e.g., correlation, Brier skill, root mean square error, loss), non-linear optimization algorithms add substantial value as they can efficiently handle multiple free parameters, improve convergence, and avoid local minima in the chosen metric.

An example of a non-linear optimization algorithm, the simulated annealing method developed

by Bertsimas and Tsitsiklis (1993), was deployed to calibrate the ShoreFor equilibrium shoreline model described in Section 2.5.2. A large number of iterations ($O \sim 10^6$) were performed to explore the model's free-parameter space and identify the optimal combination by minimizing the selected loss function (see upper panel Figure 2.18). The algorithm successfully avoided local minima and identified the optimal model parameters for the calibration period.

Building on advances in data science, shoreline modelling studies have recently begun exploring non-linear optimization algorithms similar to those used in pattern recognition (e.g., LSTM Simmons and Splinter, 2025; Calcraft et al., 2025b,a). Owing to their stochastic nature, these algorithms show strong potential for identifying shoreline trends and seasonal behaviour from satellite-derived waterline data collected in high-energy, macrotidal environments, which are often characterized by noisy and low-frequency observations (Graffin et al., 2025b). The careful selection and application of suitable non-linear optimization algorithms could greatly enhance the use of satellite-derived shoreline datasets for model calibration and improve the predictive skill of shoreline change models.

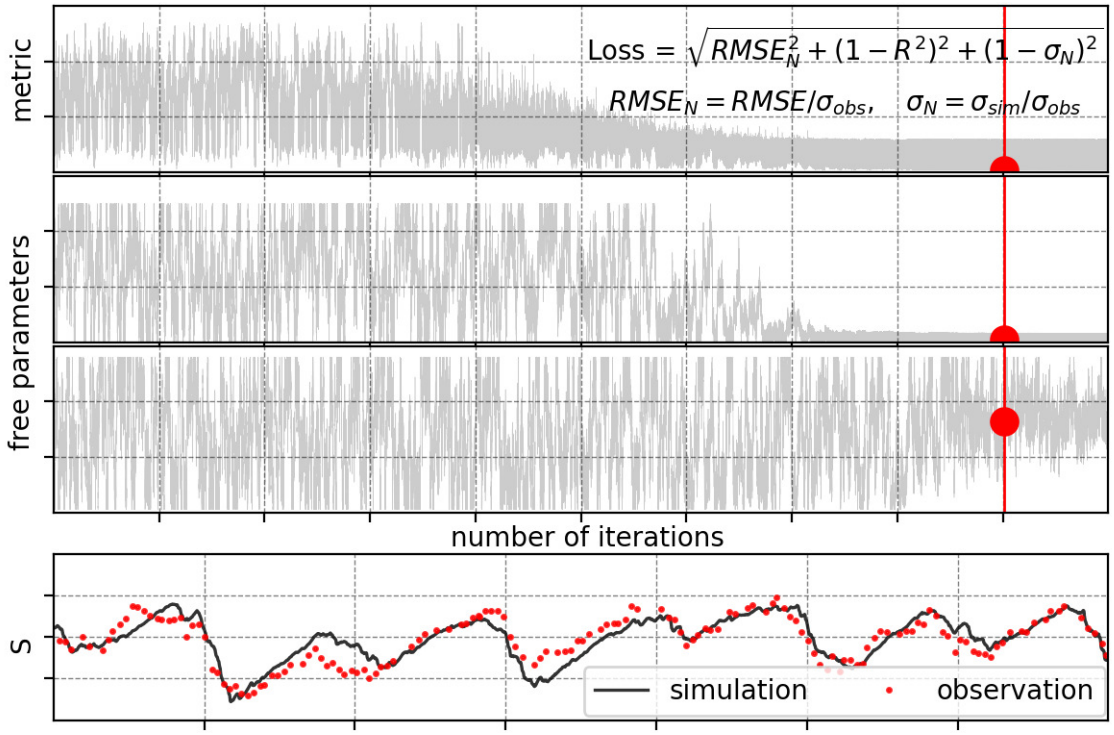

Figure 2.18: Example of reduced complexity/hybrid model calibration using a non-linear optimization method.

2.5.6 Data assimilation in shoreline change modelling

Data assimilation techniques are particularly well suited for morphological simulations, where numerous tunable parameters and empirical coefficients require calibration. Since all existing models inevitably neglect certain physical processes—either by design in reduced-complexity and

data-driven approaches, or due to incomplete initial and boundary conditions in physics-based models—they often struggle to reproduce shoreline dynamics with the fidelity of direct observations. Data assimilation offers a pathway to close this gap, by systematically integrating observations into model simulations and thereby enhancing their predictive skill.

These methods automatically adjust the model state (i.e., the model solution and/or its parameters) during a simulation to best fit available observations (e.g., shoreline position), using optimal interpolation that accounts for uncertainties in both model predictions and observations (Vitousek et al., 2023a). A conceptual example of this process is shown in Figure 2.19, illustrating how a data assimilation step can improve model predictions by implicitly accounting for processes not explicitly represented in the model. It should be noted that the data assimilation approach depicted in Figure 2.19 represents the initial concept proposed within the SHORMOSAT project, rather than the specific implementation developed in the present work (Chapter 6).

Given the abundance of freely available satellite imagery, data assimilation represents a natural next step in advancing shoreline prediction modelling. These techniques have long been credited with enabling reliable weather forecasting (Mclaughlin et al., 2006) and are now standard practice across many geophysical disciplines (Lahoz and Schneider, 2014). However, their application in coastal science remains limited. To the authors' knowledge, existing coastal data assimilation studies are confined to depth inversion problems (e.g., Birrien et al., 2013; Wilson et al., 2014) and shoreline prediction modelling (Long and Plant, 2012; Vitousek et al., 2017, 2023b; Ibaceta et al., 2020; Alvarez-Cuesta et al., 2021a, 2024).

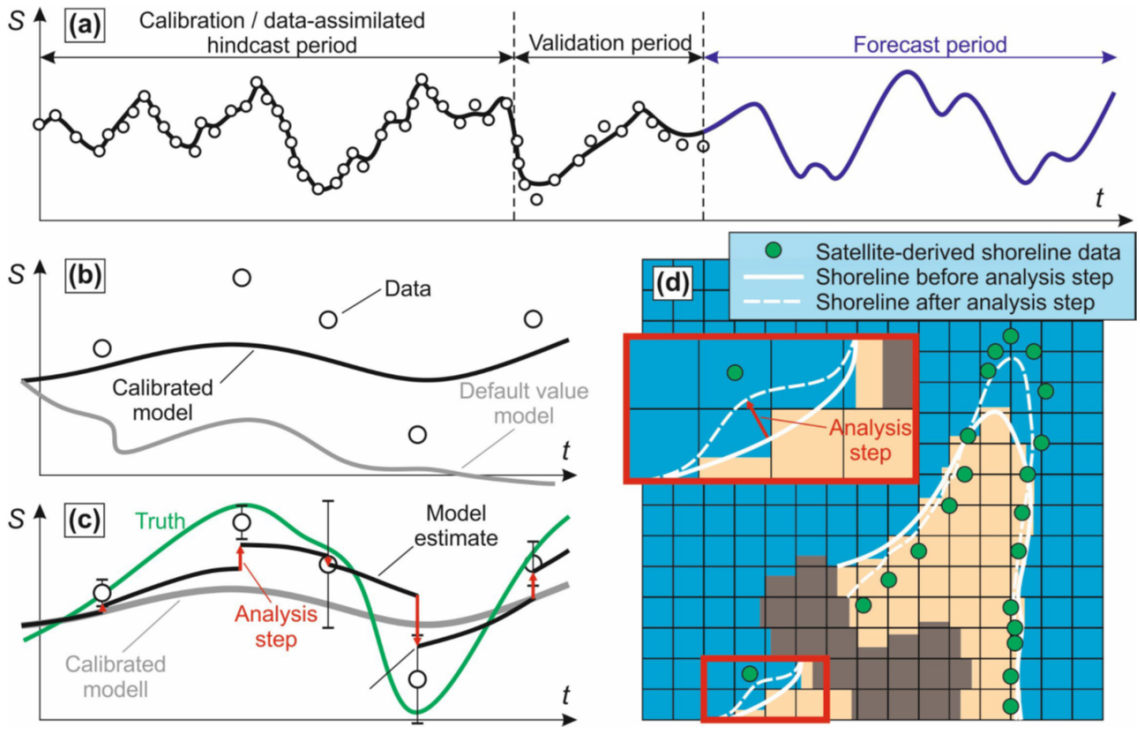

Figure 2.19: Conceptual illustration of including an analysis step in shoreline change simulations to assimilate data into the model and improve predictive skill. The figure was taken from the SHORMOSAT project proposal.

To date, most data assimilation applications implemented in shoreline modelling have largely relied on sequential approaches such as Kalman filters (e.g., Kalman, 1960; Evensen, 2009). The first documented application of data assimilation in shoreline modelling was by Long and Plant (2012), who coupled an extended Kalman filter (eKF) with a cross-shore model including a linear longshore transport term, using synthetic observations. Vitousek et al. (2017) advanced this concept with the CoSMoS-COAST model (briefly discussed in Section 2.5.2), assimilating high-quality, low-frequency LiDAR observations along the California coast through an ensemble Kalman filter (EnKF). Similarly, Alvarez-Cuesta et al. (2021a) applied an EnKF to assimilate satellite-derived shorelines into a multiprocess model of an urbanized section of the Spanish Mediterranean coast.

Ibaceta et al. (2020, 2022) combined an EnKF with the Splinter et al. (2014) version of the ShoreFor model (see Section 2.5.2) to assimilate video-derived shoreline observations from the west coast of Australia and investigate the temporal variability of model free parameters, which they linked to changing wave conditions. Vitousek et al. (2021) used a similar EnKF approach to assimilate camera-based shoreline observations, quantifying uncertainty in shoreline predictions arising from wave forcing. Most recently, Vitousek et al. (2023b) introduced a littoral-cell-based EnKF module into the CoSMoS-COAST model, incorporating spatial dependencies along the entire California coastline and assimilating tide-corrected, satellite-derived shoreline observations.

Figure 2.20 presents the two main approaches currently used—and, to date, the only ones applied—in shoreline change modelling studies to assimilate observations. In sequential approaches (also referred to as statistical methods by Alvarez-Cuesta et al., 2024), such as Kalman filter based algorithms (e.g., Kalman, 1960; Evensen, 2009) (panels a and b in Figure 2.20), model states or parameters are updated whenever new observations become available. In contrast, variational methods (e.g., 4D-Var; panel c in Figure 2.20) adjust model states and parameters simultaneously across an entire time window of observations, potentially yielding more consistent corrections. Alvarez-Cuesta et al. (2024) directly compared these two approaches in the context of shoreline modelling, highlighting the respective trade-offs between sequential and variational assimilation.

Sequential and variational data assimilation approaches offer complementary advantages in coastal shoreline modelling. The stochastic Ensemble Kalman Filter (SEnKf) propagates an ensemble of system states to update the model with new observations, making it easy to implement and suitable for high-dimensional or moderately nonlinear systems, though it may underrepresent system covariance and risk filter divergence (Alvarez-Cuesta et al., 2024). The extended Kalman Filter (eKf) linearizes model equations around the current state using tangent linear and adjoint operators, providing accurate updates for moderately nonlinear systems with small state vectors (Evensen, 2009). Variational methods like 4D-Var adjust model states over an entire assimilation window by minimizing a cost function, offering robust corrections but requiring strong constraint assumptions that can reduce performance with noisy data (Kalnay et al., 2007). Kalman filter approaches generally outperform 4D-Var for low-quality observations, while eKf and 4D-Var excel

when the system is far from the reference state or moderately nonlinear (Kalnay et al., 2007). For large state vectors, SEnKf offers a more computationally efficient solution than eKf, highlighting trade-offs between accuracy, complexity, and cost (Alvarez-Cuesta et al., 2024).

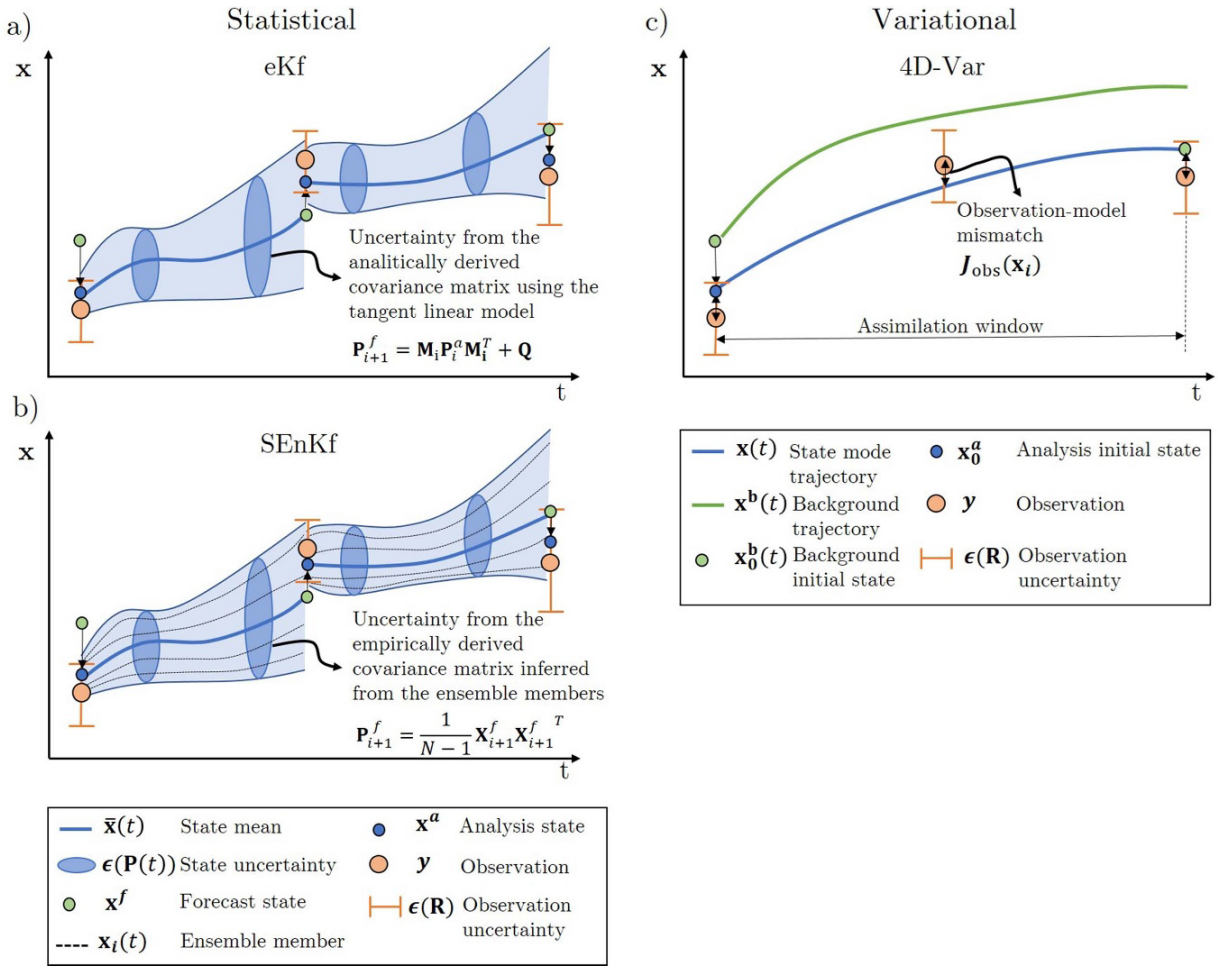

Figure 2.20: Data assimilation process following statistical and variational approaches. Please, note that the uncertainty in the state and in the observations are characterized by their covariance matrices. The figure is borrowed from Alvarez-Cuesta et al. (2024).

Data assimilation has emerged as a powerful tool in shoreline change modelling, enabling dynamic calibration by incorporating observations as they become available and adjusting model parameters in real time (Vitousek et al., 2017, 2023b; Alvarez-Cuesta et al., 2021a). This capability paves the way for operational shoreline forecasting, analogous to weather prediction systems. By continuously integrating new data, these approaches can detect and accommodate gradual or abrupt shifts in system dynamics, such as changes in storminess, wave directionality, or sediment supply, thereby tracking system non-stationarity and capturing temporal variability in model behaviour. Beyond enhancing short-term predictive skill, data assimilation provides a means to quantify how model parameters and equilibrium states evolve under varying environmental forcing, offering new insight into the links between climate variability and shoreline response. However, their performance often still depends on local system knowledge and careful parameter derivation (e.g., Ibaceta et al., 2020; Alvarez-Cuesta et al., 2024), which constrains universal applicability.

The question of how model free parameters evolve or adapt under changing climate has re-

cently gained attention, with several studies exploring time-varying calibration schemes and non-stationary model formulations to explicitly account for climate-driven variability (e.g., Splinter et al., 2017; Ibaceta et al., 2022; Alvarez-Cuesta et al., 2024; Chen et al., 2025). These works demonstrate that parameters traditionally treated as constant may vary through time in response to shifts in dominant wave regimes, emphasizing the need for adaptive frameworks that reflect evolving system behaviour (Ranasinghe, 2020; Splinter and Coco, 2021). In this context, data assimilation not only strengthens predictive capability but also serves as a diagnostic tool for understanding the drivers of long-term coastal change, providing a pathway toward dynamically adaptive shoreline models capable of responding to future, non-stationary conditions.

The simplicity of semi-empirical models and the flexible structure of reduced-complexity frameworks make them well suited for the integration of data assimilation algorithms. To date, such methods have been successfully implemented in semi-empirical (e.g., Yates et al., 2009b; Davidson et al., 2013; Splinter et al., 2014; Jaramillo et al., 2021a) and transect-based hybrid models (e.g., Vitousek et al., 2017, 2021, 2023b; Alvarez-Cuesta et al., 2021a). Conceptually, the LX-Shore model (Robinet et al., 2018) offers a distinct advantage through its grid-based architecture, which aligns naturally with satellite-derived observations and presents an exciting opportunity for satellite-derived data integration.

The wide range of existing shoreline change models (Toimil et al., 2020; Ranasinghe, 2020; Splinter and Coco, 2021; Sherwood et al., 2022; Hunt et al., 2023), as well as model ensembles, have already demonstrated skill in reproducing shoreline evolution over short to medium timescales (Montaño et al., 2020; Repina et al., 2025; Mao et al., 2025). However, the most powerful and broadly applicable framework is likely to be the one that effectively assimilates satellite-derived observations. By constraining models with these global, high-frequency datasets, data assimilation can keep simulations on track, impose realistic boundary conditions, and implicitly account for unresolved processes (e.g. tidal inlets, estuary mouths, headlands, coastal structures, sediment sources and sinks, anthropogenic influences). Beyond improving model performance, assimilation also helps identify the primary sources of error and clarify links between time-varying free parameters and environmental conditions. This dual role both increases the accuracy of shoreline predictions and paves the way for operational coastal forecasting systems, similar to modern weather forecasts.

2.6 Contribution of the present work

Modelling and predicting the future of sandy shorelines is a central challenge in coastal research and critical for sustainable management. The present work builds upon the state of the art in shoreline change modelling by advancing the use of publicly available datasets, particularly satellite-derived shoreline observations, using a range of calibration and data assimilation approaches.

In Chapter 3, the study explores the direct integration of uncorrected satellite-derived waterlines and shorelines (i.e., without tidal or water-level adjustments) into modelling frameworks using non-linear optimization algorithms for model calibration, and explicitly examines the data requirements, such as observation density and record length, needed to reliably constrain a reduced-complexity equilibrium shoreline change model. Chapter 4 extends this approach by investigating the temporal non-stationarity of model parameters at a regional scale using in-situ observations, providing complementary insight into how shoreline systems respond to changing environmental forcing. This represents a step toward addressing the limitations associated with local calibration and the dependence on site-specific knowledge that often constrains data assimilation algorithms (Ibaceta et al., 2020; Alvarez-Cuesta et al., 2024).

Chapter 5 introduces and evaluates a hybrid shoreline modelling framework that couples complementary equilibrium-based processes with calibration and data assimilation, demonstrating both stability and predictive skill within the international benchmarking experiment of Mao et al. (2025). In the chapter it is further shown how data assimilation can be used to maintain model stability under limited data availability by constraining the model with observed or inferred shoreline trends.

Expanding upon the hybrid and assimilation frameworks, Chapter 6 introduces a quasi-two-dimensional (2D) implementation of data assimilation, moving beyond alongshore-averaged representations toward a grid-based formulation that integrates spatially distributed satellite observations. The method applies a spatial nudging scheme to assimilate land–water classifications directly derived from optical satellite imagery, enabling the model to reproduce observed shoreline dynamics across a 2D grid. The implementation of two-dimensional, grid-based data assimilation provides the basis for resolving spatial dependencies and feedbacks that are often neglected in one-dimensional approaches (e.g., transect-based models Vitousek et al., 2017; Alvarez-Cuesta et al., 2021a).

Overall, the thesis advances the field of coastal morphodynamic modelling along three interconnected fronts. First, Chapter 3 establishes a framework for calibrating equilibrium-based shoreline models using uncorrected and noisy satellite-derived shoreline (SDS) data, demonstrating that valuable information can be extracted even in the absence of data correction or site-specific tuning. Building on this foundation, Chapter 4 explores the temporal variability of model free parameters and their links to wave forcing through data assimilation, providing new perspectives on how shoreline systems adjust to changing environmental conditions. Furthermore, Chapter 5 demonstrates how data assimilation can be implemented to maintain model stability by imposing observed or inferred shoreline trends. Finally, Chapter 6 introduces a proof of concept for quasi-two-dimensional assimilation of satellite-derived shoreline observations within a grid-based modelling framework. Although neighbouring grid dependencies were not explicitly considered, this implementation represents a critical step toward fully two-dimensional data assimilation in coastal morphodynamic models.

Collectively, the contributions of this thesis establish a flexible and transferable modelling framework that supports continuous observation integration, accounts for non-stationarity in model parameters, quantifies uncertainty in space and time, and addresses key structural limitations of existing shoreline change models. By relying exclusively on open access data and satellite-based observations, the proposed workflows are broadly applicable across diverse coastal settings and offer a scalable pathway toward improved shoreline prediction under changing environmental conditions.

Chapter 3

Satellite-derived equilibrium shoreline modelling at a high-energy meso-macrotidal beach

Building directly on the framework introduced in Chapter 2, this chapter presents the first practical application of satellite-derived datasets to the calibration of a one-dimensional equilibrium shoreline model. The objective is to test whether reliable model calibration can be achieved using freely available, uncorrected satellite-derived shorelines (SDS), without the need for in-situ data or site-specific corrections. The analysis focuses on Truc Vert beach, a high-energy meso-macrotidal environment on the French Atlantic coast, selected as an ideal benchmark for assessing model robustness under challenging observational conditions.

By systematically comparing model performance across datasets of varying quality and temporal resolution, the chapter evaluates the trade-off between data availability and predictive accuracy. Results demonstrate that meaningful calibration can be obtained even from noisy SDS, provided that appropriate temporal and spatial aggregation is applied. These findings confirm the potential of satellite observations to extend the applicability of equilibrium shoreline models to data-scarce regions. The insights gained here form the methodological and conceptual basis for the data assimilation experiments developed in Chapter 5, where temporal non-stationarity in model parameters is explicitly addressed.

The present chapter has been published in the peer review journal *Coastal Engineering* (Azorakos et al., 2024).

Azorakos, G., Castelle, B., Marieu, V., & Idier, D. (2024). Satellite-derived equilibrium shoreline modelling at a high-energy meso-macrotidal beach. *Coastal Engineering, 191*, 104536. https://doi.org/10.1016/j.coastaleng.2024.104536

3.1 Introduction

Coastal areas constitute some of the most populated and developed land zones in the world (Small and Nichols, 2003) with high natural and socio-economical significance (Ghermandi and Nunes, 2013). Luijendijk et al. (2018) found that $\sim$ 24% of the global ice free sandy shorelines are eroding at rates exceeding 0.5 m/year, while Vousdoukas et al. (2020) suggested that these numbers are projected to increase under the influence of climate change. Although more in depth analysis is needed (Cooper et al., 2020), these findings highlight the importance of monitoring, understanding and predicting sandy shoreline evolution.

Sandy coasts can be highly dynamic environments constantly adjusting their position in response to a variety of processes spread over a wide spatio-temporal range. Changes in sediment availability and mean sea level influence shoreline response on the timescales ranging from decades to millenia (Larson and Kraus, 1995; Murray, 2007). On shorter timescales and on cross-shore transport dominated sites, shoreline response is often dictated by variations in incident wave conditions from the time scale of single storms to seasonal and interannual variability in the incident wave climate (Castelle and Masselink, 2023). Anthropogenic factors can also have a significant and potentially irreversible impact on the shoreline position (Aagaard et al., 2004; Ranasinghe and Turner, 2006; Ojeda et al., 2008).

Reduced complexity shoreline models, such as Yates et al. (2009b); Davidson et al. (2013); Splinter et al. (2014); Vitousek et al. (2017); Robinet et al. (2018); Antolínez et al. (2019); Tran and Barthélemy (2020) to name a few, have enabled the scientific coastal community to successfully simulate sandy shoreline evolution from timescales of days (single storms) to years (seasonal and interannual variability) and even to decades (long term shoreline trends) (Splinter et al., 2013; Castelle et al., 2014; Robinet et al., 2020). Not resolving all the complex processes explicitly reduces the computational cost of these models. While process based models need more data like complete topography and bathymetry of an area, reduced complexity models require mainly shoreline position datasets spanning over several years for their calibration (Montaño et al., 2020). Of particular relevance are equilibrium shoreline models that show very good skill on cross-shore transport dominated sites (Splinter et al., 2014). Splinter et al. (2013) showed that due to the empirical and data driven nature of these equilibrium models, high-quality observational datasets spanning more than 5 years are needed for the calibration of the free parameters. High-quality observational datasets however are limited to a few surveyed sites (Turner et al., 2016b; Ludka et al., 2019; Castelle et al., 2020; Bertin et al., 2022; McCarroll et al., 2023), or video-monitored beaches (Splinter et al., 2014; Pianca et al., 2015; Ibaceta et al., 2020) in the world, thus limiting the application of equilibrium data driven models.

Publicly available satellite imagery, cradled a new approach in remote sensing and provided long term (more than 30 years) high temporal resolution (approximately bi-weekly) shoreline data covering the entire planet (Vos et al., 2019a). However, Vos et al. (2019a, 2023b) recognized

issues with shoreline detection on satellite images at gently sloping and meso-macrotidal environments, where low tide images must also be discarded due to the presence of complex bar/rip systems. Castelle et al. (2021) showed that satellite derived shorelines (SDS) at a high energy meso-macrotidal coast can deviate by more than 30 m from the surveyed shoreline position and proposed ways to address the issue. While astronomical tide and runup adjustment provides the best correction at Truc Vert in southwest France (Castelle et al., 2021), Konstantinou et al. (2023) showed that optimal water level correction (astronomical tide and/or set-up and/or runup) strongly depends on beach state. Konstantinou et al. (2023) also showed that low image availability due to e.g. areas with high cloud cover can dramatically restrict temporally the type of phenomenon that can be detected (e.g., seasonal/interannual variability). Finally, open SDS datasets are often extracted along single transects, which are spaced by hundreds of metres, and may not be representative of the true shoreline variability on intermediate beaches due to the presence of alongshore variable features like migrating megacusp embayments. Transect spacing and alongshore averaging are therefore important processing parameters affecting SDS accuracy. These observations question the reliability of uncorrected SDS data in gently sloping, high-energy and meso-macrotidal environments, especially when lacking in-situ derived shoreline data to compare with. To which extent such SDS data can be used to calibrate data driven equilibrium shoreline models is virtually unknown.

Most studies using SDS observations to date, focused on interannual shoreline variability (e.g. Castelle et al., 2022) or long term trends (e.g. Luijendijk et al., 2018), rather than their potential for modelling applications. A handful of studies integrating SDS observations in dynamic shoreline models have emerged recently. Alvarez-Cuesta et al. (2021a,b, 2024) incorporated 30 years of SDS data into a dynamic shoreline modelling system to simulate 40 km of the Mediterranean Spanish coast. Ibaceta et al. (2022) assimilated SDS data into their model in order to track variability in model free parameters while simulating 14 years of shoreline evolution at a microtidal beach on the east coast of Australia. Vitousek et al. (2023a) integrated SDS observations into their shoreline model to hindcast 20 years of coastal change over the entire coast of California. Vitousek et al. (2023a) demonstrated that model calibration with water level corrected SDS yielded similar skill to model calibration with in- situ observations at a meso tidal beach. However, the influence of the type of water level correction was not addressed, and the uncorrected SDS were not tested in model calibration. Crucially, uncorrected SDS datasets do not require local beach slope, astronomical tide data and breaking wave parameters for further correction, and can be thus generated at any site globally.

In the present work we investigate the possibility of using SDS datasets to calibrate the state-of-the-art equilibrium shoreline model proposed in Davidson et al. (2013), by testing different water level corrections at the high energy meso-macrotidal beach of Truc Vert, southwest France. Eleven years of SDS data were used and a simulated annealing non-linear optimization algorithm (Bertsimas and Tsitsiklis, 1993) was systematically applied to various SDS datasets (different water level corrections, alongshore averaging lengths, duration and sampling frequency) in order to find the best fit model parameters and further address model skill by comparing with field data. The study

site, data used and methodology adopted in the present work are detailed in sections 3.2 and 3.3. The results are presented and briefly discussed in section 3.4 while a detailed discussion and the conclusions follow in sections 3.5 and 3.6. Pending further validation, the findings of the present study suggest that uncorrected SDS data can potentially be used to calibrate data driven equilibrium shoreline models in high energy meso-macrotidal environments without a priori knowledge of the site.

3.2 Field site and data

3.2.1 Truc Vert beach

The coast of Nouvelle Aquitaine in southwest France (Figure 3.1b) stretches approximately 250 km along a straight, low-lying shoreline backed by high vegetated coastal dunes (Laporte-Fauret et al., 2020) excluding a few small stretches interrupted by coastal resorts (Castelle et al., 2018c). The offshore wave climate is generated in the north Atlantic ocean predominantly by eastward tracking extra tropical cyclones (Castelle et al., 2020). In the present work the remote beach of Truc Vert (panel a in Figure 3.1), located approximately 2 km away from the nearest inland car park beach entry, is chosen as a case study. Besides a mechanical profiling of the coastal dune backing the beach that took place in the early 1980s (Robin et al., 2021), the beach has never been nourished, affected by hard structures or by any direct anthropogenic activity.

Truc Vert is a high energy meso-macrotidal double barred open beach backed by tall ($\sim$ 20-25 m above Mean Sea Level) and wide ($\sim$ 250 m) coastal dunes (see Figure 3.1). The tide is semi-diurnal with an annual mean spring tidal range of $\sim$ 3.7 m and largest tidal range of $\sim$ 5 m. The wave climate is seasonally modulated with monthly average significant wave height $\overline{H_s}$ and peak wave period $\overline{T_p}$ ranging from 1.11 m and 9 s in July, with a dominant west-northwest direction, to 2.4 m and 12.8 s in January with a dominant west direction (Castelle et al., 2017a).

The sediment composition primarily consists of medium quartz sand, with a median diameter of $d_{50} \approx 350\ \mu m$. The beach sediment displays substantial variability ranging from 200 μm to 700 μm, associated with a wide range of bedforms such as bar/rip channels, megacusps, cusps, and megaripples (Gallagher et al., 2011). The outer bar is subtidal and modally crescentic, while the inner bar, situated in the intertidal zone, is mostly classified as a transverse bar and rip and during the summer months tends to transition into a low tide terrace (see Figure 3.1). The average spacing between rips is approximately 400 m for the inner bar and 700 m for the outer bar, although these values can vary considerably over space and time. The presence of rip channels incising the inner bar leads to significant alongshore variations in beach morphology, with pronounced megacusp embayments (Figure 3.1 a) in the alignment of the rip channels typically evolving on seasonal timescales. The outer bar on the other hand, can drive larger scale beach variability during severe

storms which can persist for several years (Castelle et al., 2020).

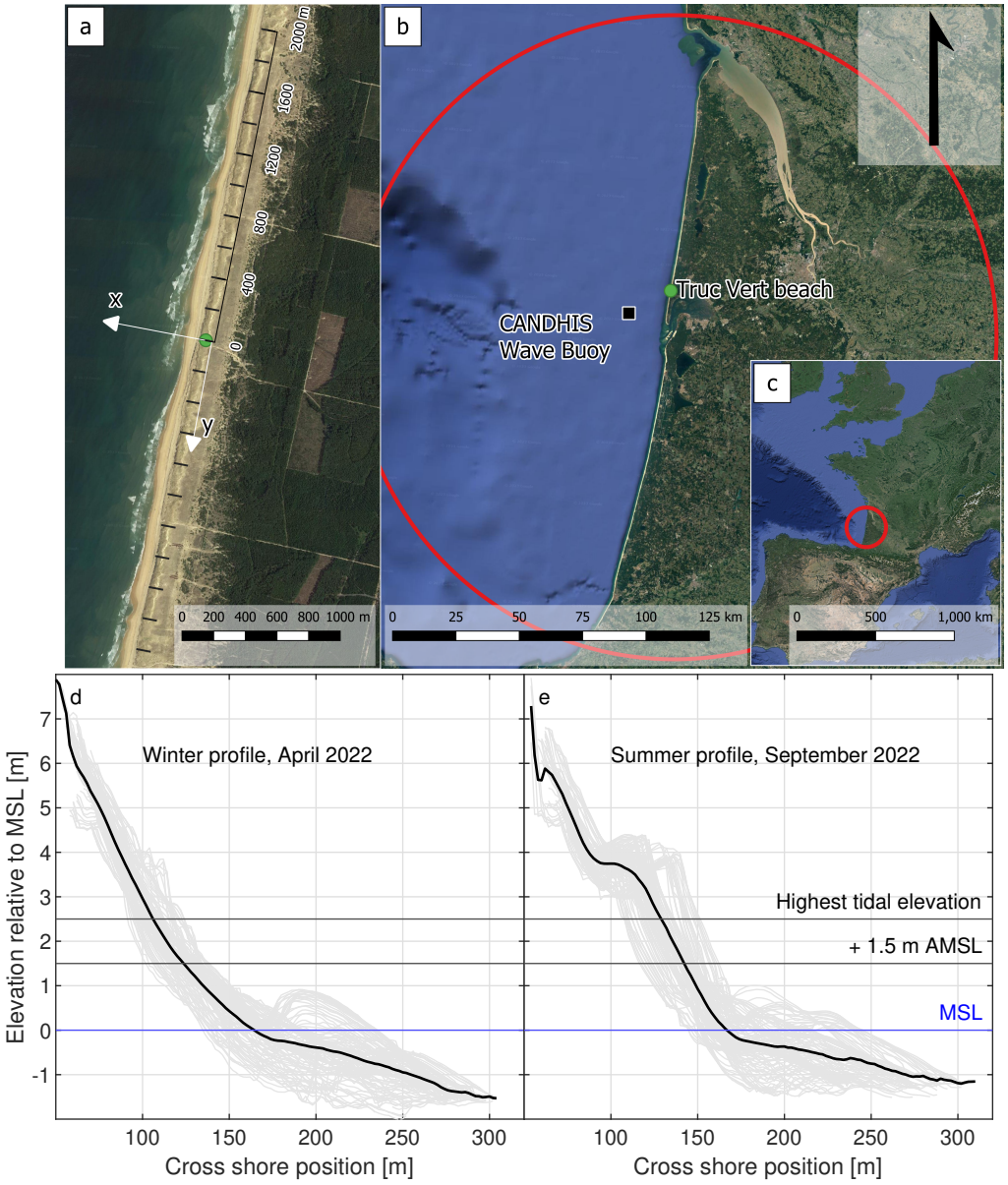

Figure 3.1: (a) Survey zone and reference frame at Truc Vert beach. (b) Location map of Truc Vert beach, southwest France indicating the position of the CANDHIS wave buoy (Cap Ferret wave buoy 03302). (c) Overview of the area. Winter (d) and summer (e) profiles measured in 2022. The thick black line indicates the alongshore average profile, while the gray lines are the individual profiles extracted every ∼20 m from the alongshore window considered.

In the long term Truc Vert beach can be considered stable (Castelle et al., 2018a), despite the fact that the highly interannually variable winter wave energy can result in severe beach and dune erosion (Castelle et al., 2015; Masselink et al., 2016). The shoreline evolution is mainly dominated by cross shore processes showing strong seasonal and interannual variability, with moderate and extreme winters alternating (Robinet et al., 2016; Masselink et al., 2016).

3.2.2 Wave Data

Due to the lack of continuous wave measurements from the CANDHIS directionnal wave buoy, which is moored in ∼50 m depth offshore of Truc Vert beach (see Figure 3.1), hourly wave time-series were extracted from the NORGAS-UG regional wave hindcast (Boudière et al., 2013), at the grid point coinciding with the location of the buoy. The NORGAS-UG regional model covers the Atlantic coast of France on an unstructured mesh. The nearshore is resolved with mesh elements of ∼200 m while the model resolution becomes coarser further offshore with mesh elements of ∼10 km in the deepest parts of the domain.

The wave model results have been validated against several measured data and yielded correlation coefficients of 0.96-0.99, RMSE of 0.15-0.21 m and a bias of -0.02-0.04 m (Michaud et al., 2016). The significant wave height H_s, peak wave period T_p and mean wave direction (MWD) extracted from the aforementioned wave hindcast are depicted in Figure 3.2. The timeseries shows the typical seasonal and interannual variability of the incident wave climate at Truc Vert beach with a prevailing W-NW wave incidence. The surveyed shoreline is depicted in panel a of Figure 3.2 together with H_s.

3.2.3 Shoreline Data

Five different shoreline / waterline datasets extending from January 2009 to December 2019 have been considered in the present work, summarized and depicted in Figure 3.3. The single transect (S_{IS}) extracted at $y = 0$ (see Figure 3.1, a) as well as the alongshore averaged in-situ shoreline timeseries ($\overline{S_{IS}}$), have been derived from monthly to bimonthly sampled topographic GNSS surveys, performed during spring low tide at Truc Vert beach (see Figure 3.1) in the frame of a long-term monitoring program established in 2003 (Castelle et al., 2020). S_{IS} and $\overline{S_{IS}}$ correspond to the 1.5 m elevation Above Mean Sea Level (AMSL) shoreline proxy (see Figure 3.1), as this has been found to best correlate with the beach-dune volume (Robinet et al., 2016). The overbar denotes alongshore averaging over the survey domain, which increased from approximately 600 m in 2009 to slightly over 2300 m in 2016. In the present work, the alongshore-averaged in situ shoreline $\overline{S_{IS}}$ is considered as the true shoreline to which both satellite-derived and simulated shoreline data will be further compared. Unless stated otherwise the alongshore domain considered in the present work is the largest available at each point in time which after 2016 is stabilized to ∼ 2.4 km.

The satellite-derived, alongshore-averaged, uncorrected waterline $\overline{W_S}$, tide-corrected shoreline $\overline{S_{ST}}$ and tide and runup corrected shoreline $\overline{S_{STR}}$ depicted in Figure 3.3 were generated by Castelle et al. (2021). These datasets were computed from the waterlines W derived from optical satellite imagery along 4 km of coastline at Truc Vert (see panel a in Figure 3.1). The extraction of the instantaneous waterline position W, was performed using the python toolkit Coast-

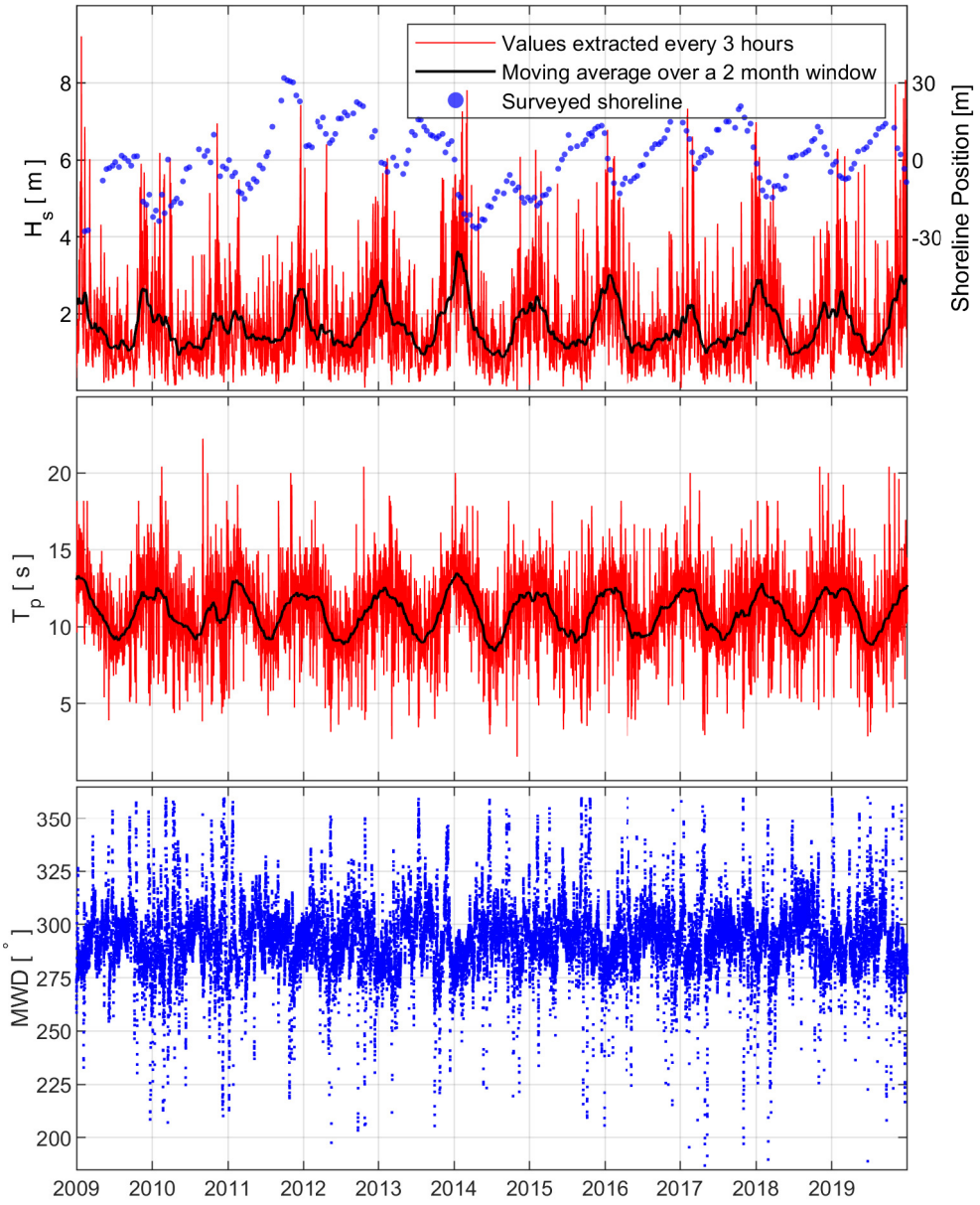

Figure 3.2: Offshore wave conditions during the period considered in the present work extracted at the location of the buoy (see Figure 3.1). The significant wave height H_s, peak wave period T_p and mean wave direction (MWD) are depicted in the upper, middle and lower panel of the figure. The alongshore averaged surveyed shoreline positions are plotted on the right axis of the upper panel.

Sat (Vos et al., 2019b) which is freely available on GitHub (`https://github.com/kvos/CoastSat`). CoastSat is a Google Earth Engine enabled open-source Python toolkit that allows the user to obtain waterline position time-series at any sandy coastline worldwide from publicly available satellite imagery. Landsat 5, 7 & 8 (L5, L7 & L8) images with a spatial resolution of 30 m and Sentinel-2 (S2) images with a spatial resolution of 10 m can be retrieved to a user defined window. In succession the images are being processed to remove cloudy pixels and enhance spatial resolution. The methodology for the extraction of the instantaneous waterline position is described in detail in Vos et al. (2019a).

Castelle et al. (2021) applied water level corrections by translating horizontally the waterline W using a constant beach slope of 0.05 and the water level at the coast at the satellite flyover time. The water level at the coast was estimated using a coastal model hindcast of water level (Pineau-Guillou, 2013) validated at Truc Vert by Castelle et al. (2020). To estimate the wave run up component of the instantaneous water level at the satellite flyover time Castelle et al. (2021) used the run up formulations proposed by Senechal et al. (2011) that has been calibrated at Truc Vert and can be scaled using offshore wave height alone at Truc Vert. The two waterline datasets, namely W_S and $\overline{W_S}$ include all usable satellite images since 2009. The two water level corrected datasets $\overline{S_{ST}}$ and $\overline{S_{STR}}$, include all images extracted when total water level η_t exceeds 0.5 & 0.2 m respectively. Although disregarding low tide images improved the quality of the timeseries, it significantly reduces the amount of observations. For a detailed and in depth description of the methodology and analysis resulting to the three satellite derived datasets, the reader is refereed to Castelle et al. (2021).

The raw waterline data extracted from the satellite images W_S as well as its 4-km alongshore averaged dataset $\overline{W_S}$ can deviate from the shoreline position significantly, especially in a high energy meso-macrotidal environment like Truc Vert. The computed root mean square error for the $\overline{W_S}$ dataset reported in Castelle et al. (2021) is in the order of 30 m and the correlation is poor with $R^2 < 0.5$ (see panel c in Figure 3.3). The single transect satellite derived waterline W_S shows similar agreement when compared against the in situ derived shoreline position S_{IS} considering the same transect (see panel d in Figure 3.3) with a slightly smaller error. Alongshore averaging and applying tide and/or wave runup correction on the satellite derived waterline positions can largely improve the agreement with in situ shoreline $\overline{S_{IS}}$ (Castelle et al., 2021; Konstantinou et al., 2023). It is important to note that the comparison ($RMSE$, R^2 & $bias$) consider satellite images and beach surveys separated by up to 10 days.

3.3 Shoreline numerical modelling

3.3.1 Equilibrium shoreline model

In the present work the empirical equilibrium shoreline model ShoreFor developed by Davidson et al. (2013), presented in Section 2.5.1, was used to simulate shoreline evolution. Following the work of D'Anna et al. (2022) a constant SLR_{rate} of 3.31 mm/year is applied, the contribution of which to shoreline retreat is calculated using the Bruun rule (Bruun, 1962). The SLR driven shoreline retreat is negligible in the time scales addressed in the present work.

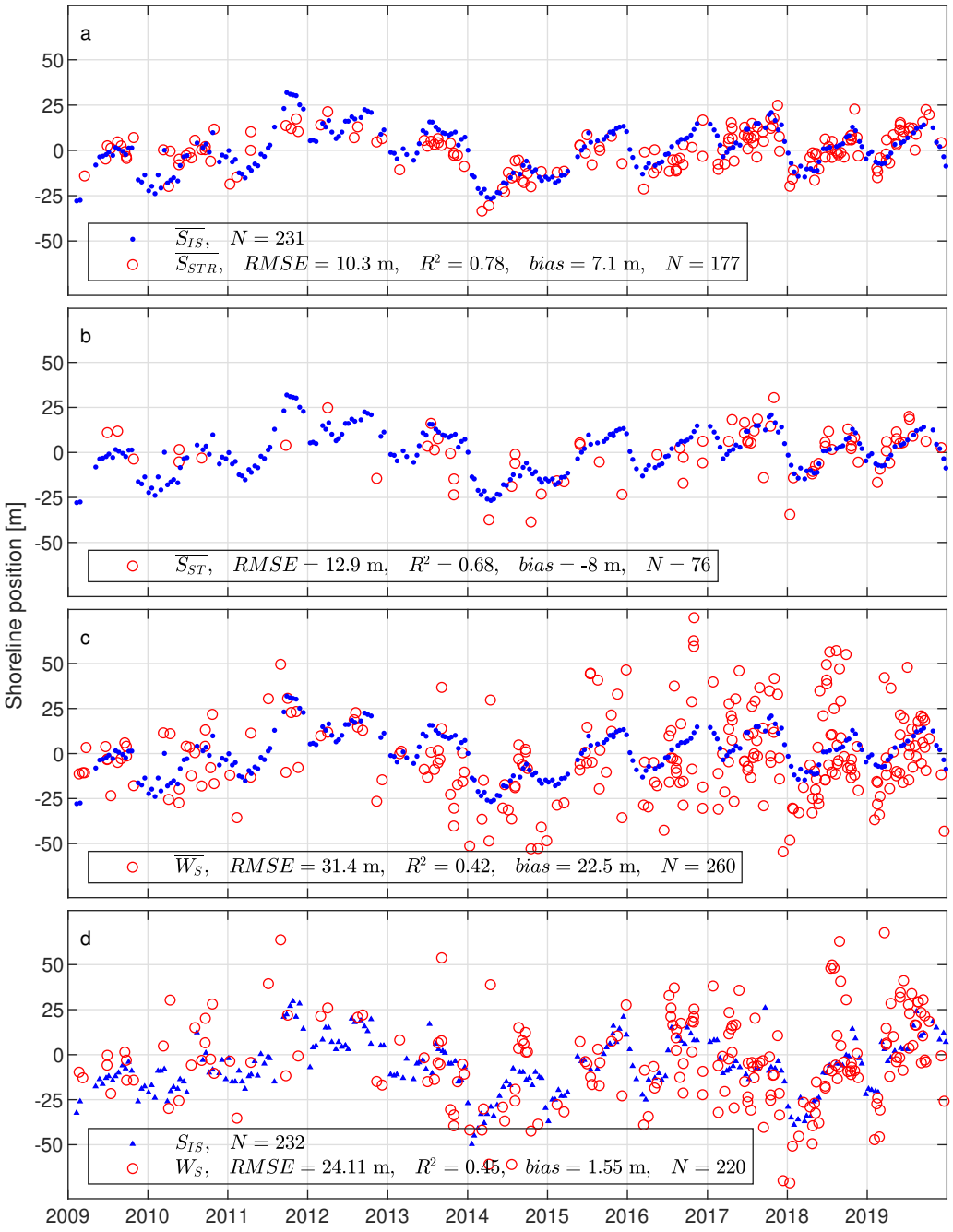

Figure 3.3: The four different satellite derived shorelines are depicted together with the in situ derived single transect (S_{IS}) and alongshore averaged ($\overline{S_{IS}}$) +1.5 m AMSL shoreline proxy. The $RMSE$, R^2 and $bias$ compared to the $\overline{S_{IS}}$ and S_{IS} as well as the total number of unique observations N for each data set are indicated in the legend.

3.3.2 Calibration

The model requires the calibration of two model free parameters, namely the accretion/erosion rate $c^{\pm}$ and the memory decay ϕ. An extra term is added allowing the model to adjust its initial position by dx_0. This term is introduced to account for uncertainties in the first shoreline data point. To calibrate the model free parameters the simulated annealing algorithm proposed by Bertsimas and Tsitsiklis (1993) was implemented. Simulated annealing is a non-linear probabilistic method, that can be used to find the global minimum of a cost function without getting stuck in local

minima. The implementation of the simulated annealing algorithm was already successful in the calibration of equilibrium models in Castelle et al. (2014), D'Anna et al. (2020), Labarthe et al. (2023) and more. In this contribution, the mean squared error (MSE) between the observed and simulated shoreline was used as a cost function in the optimization without accounting for any sources of uncertainty.

A timeseries of simulated shoreline evolution and the corresponding cost function C, are calculated based on a set of initial model parameters $\mathbf{P_0}$. Successively, one of the model parameters is randomly selected and modified within the defined range, based on a defined noise. The cost function is calculated for the new set of model parameters $\mathbf{P(i)}$ and compared to the initial value. As long as the new solution is an improvement $C(i) < C$, the same step is repeated with the new solution as initial value $\mathbf{P_0} = \mathbf{P(i)}$ & $C = C(i)$ until the number of iterations defined by the user is reached. In case the new solution is not an improvement $C(i) \geq C$ then the next step is defined based on the following probability:

$$\mathbb{P}(\mathbf{P_0}, \mathbf{P(i)}, T(i)) = \exp[-(C(i) - C)/T(i)]$$

where $T(i)$ is a positive integer called the temperature parameter. The temperature controls the probability of accepting worse solutions. Initially, the temperature is high, allowing the algorithm to accept worse solutions with relatively high probability. The algorithm uses a cooling schedule to gradually decrease the temperature parameter with every iteration based on a defined cooling coefficient. As the temperature decreases, the algorithm becomes more selective, preferring only better solutions. The temperature parameter plays a crucial role in Simulated Annealing. A high temperature allows the algorithm to explore a wide range of solutions, including worse ones, helping to escape local minima.

The initial model parameters $\mathbf{P_0}$ are defined as the average value of the considered range. The noise amplitude used to inflate each parameter, corresponds to 5% of the bounds' difference. Our preliminary analysis showed that in order to achieve an acceptable solution, the algorithm needed to be initialized with a large temperature T_0, slowly decreasing and allow for a large number of iterations ($O \geq 10^5$).

3.3.3 Simulation setup

The present work aims to evaluate the performance of the state of the art equilibrium shoreline evolution model proposed by Davidson et al. (2013), when calibrated against satellite-derived waterline and shoreline datasets with different water level corrections and sampling frequencies, and thus varying uncertainties (see Figure 3.3). To assess the performance of the model and further explore the requirements in SDS quality and quantity to robustly calibrate an equilibrium shoreline model, three different numerical experiments have been designed. All the experiments were

Model parameter	Simulated annealing range	Units
c^+ / c^-	$[0; 2.5] \times 10^{-6}$ / $[0; 1.0] \times 10^{-6}$	$\mathrm{m}^{1.5}\ \mathrm{s}^{-1}\ \mathrm{W}^{0.5}$
ϕ	$[25; 1400]$	days
dx_0	$[-10; 10]$	m

Table 3.1: Range of values considered in the present work.

conducted under the assumption that there is no a priori knowledge of the simulated coastal environment. This was implemented by investigating a range of calibration parameters (Table 3.1) beyond the limits found in the literature (e.g. Davidson et al., 2013; Splinter et al., 2014; D'Anna et al., 2020, 2022).

As an initial test the model has been calibrated against all five datasets depicted in Figure 3.3, using the entire period (January 2009 - December 2019) and comparing the model results with the in situ derived shoreline data $\overline{S_{IS}}$ and S_{IS}. This experiment was designed to asses whether the information of the shoreline position can be extracted from the different datasets and to which extent each of the five datasets can be used to calibrate the empirical equilibrium shoreline model and provide accurate hindcast.

Given the alongshore variability in shoreline position due to prominent megacusp embayments, the next experiment was designed to investigate a minimum threshold in the alongshore averaging window necessary to obtain satisfactory model results. To do so, 40 different shoreline datasets were generated from the satellite-derived waterlines W using alongshore averaging windows extending from 100 m to 4000 m around the origo point (see Figure 3.1), in increments of 100 m. All of these alongshore averaged datasets were used to calibrate the model against the entire period (January 2009 - December 2019). Model performance was systematically assessed against in situ derived shoreline data $\overline{S_{IS}}(y)$ after 2016, using the same window as the calibration dataset. The variable y represents the alongshore distance considered for each window (see Figure 3.1). Importantly, in order to avoid erroneous interpretations of the results, account for the stochastic nature of the simulated annealing algorithm and ensure repeatability, the calibration was run 20 times for every dataset.

The final numerical experiments were designed to explore the amount and quality of data required to obtain fair model skill. These experiments were inspired by the work of Splinter et al. (2013), where they investigated the influence of noise, morphological sampling interval and calibration duration in empirical equilibrium shoreline models including Davidson et al. (2013). Similar to the work of Splinter et al. (2013) and more recently Alvarez-Cuesta et al. (2024), in order to properly investigate the influence of sampling frequency as well as noise in the dataset, a synthetic shoreline was generated S_{SYN} using Eq. 2.1 and the wave timeseries depicted in Figure 3.2. Subsequently the synthetic shoreline was inflated by normally distributed noise with a magnitude, equal to 100% and 200% of the standard deviation of the synthetic shoreline timeseries to account for measurement errors and other unresolved processes. Finally the synthetic shoreline timeseries were subsamled in intervals of $dt = 1, 7, 14, 30, 60, 90, 182$ & 365 days. The resulting 24 synthetic

shoreline timeseries were used to calibrate the model, which performance was evaluated against the daily subsampled synthetic shoreline with 0% noise. The duration of an adequate calibration period was investigated in increments of 6 months for all aforementioned synthetic shorelines as well as the four observed alongshore averaged shoreline timeseries depicted in Figure 3.3. The performance of the models calibrated using the alongshore averaged shoreline and waterline data was evaluated against the true shoreline ($\overline{S_{IS}}$) timeseries of the subsequent period. All simulations for both the synthetic and observed datasets, were repeated 10 times to account for the stochastic nature of the simulated annealing algorithm.

Lastly the importance of sampling frequency was further investigated using the alongshore averaged uncorrected waterline data $\overline{W_S}$ over the entire period from January 2009 to December 2019. In this experiment, N amount of data points were randomly sampled from the entire dataset which were then used to calibrate the model over the entire period. Successively the model's performance was evaluated against the true shoreline ($\overline{S_{IS}}$). Eleven datasets were investigated in total with the most scarce one being populated by $N = 25$ points randomly distributed over the entire period and increasing the amount of points in increments of 25 arriving at the complete dataset. The experiment was repeated 30 times for each dataset.

3.4 Results

3.4.1 Model calibration with different datasets

Figure 3.4 shows model results when calibrated with each of the five datasets (namely $\overline{S_{IS}}$, $\overline{S_{STR}}$, $\overline{S_{ST}}$, $\overline{W_S}$ and W_S), which are compared against the in-situ shoreline proxies $\overline{S_{IS}}$ and S_{IS}. For all five datasets, the model was calibrated using the entire period depicted in Figure 3.4. All the alongshore averaged datasets, both in-situ and satellite derived, produce an acceptable model with RMSE $<$ 10 m and $R^2 \approx 0.6$ (Figure 3.4). This is not surprising for in-situ shoreline proxy $\overline{S_{IS}}$, with model skill similar to previous equilibrium model applications at Truc Vert (Castelle et al., 2014; Splinter et al., 2014; D'Anna et al., 2020). More unexpected is that similar model skill is obtained with all the alongshore-averaged SDS despite the error and noise in the dataset (see Figure 3.3). This is particularly true for the uncorrected waterline $\overline{W_S}$, with RMSE of approximately 30 m and seasonal and interannual patterns barely depictable (Figure 3.3). Results improve as uncertainties are reduced with each applied correction (tide and/or runup correction), despite the fact that both these datasets contain less data points (Figure 3.3). In contrast, the model calibrated with the single transect waterline dataset W_S (Figure 3.4e) shows very poor performance with a coefficient of determination of $R^2 \approx 0.2$ and a RMSE $>$ 10 m, which will be discussed later in the paper.

Given that only the single transect dataset yielded poor results, the influence of alongshore

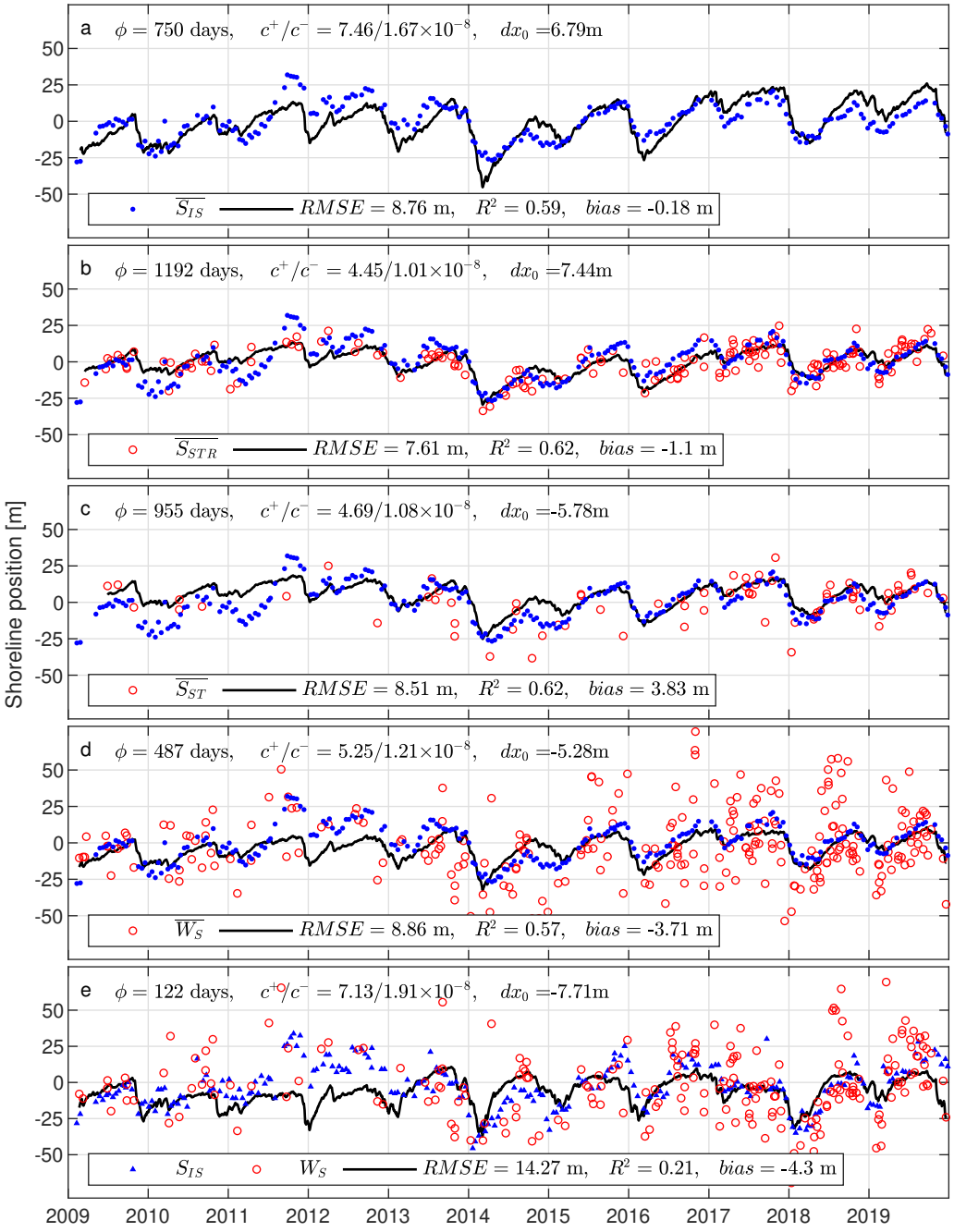

Figure 3.4: Model results using the simulating annealing algorithm to calibrate the model over the entire period based on the five different datasets and comparing with the in-situ derived shoreline data $\overline{S_{IS}}$ (blue dots) and S_{IS} (blue triangles). Performance metrics and calibrated model parameters are indicated in each panel.

averaging window on model skill was investigated (Figure 3.5). Results show that the minimum window width to obtain good model skill is $L \geq 1.2$ km. Both the RMSE of the model and the correlation coefficient improve significantly with $L \geq 1.2$ km, while a slight further improvement is observed when $L \geq 2.2$ km. These values coincide with approximately 1.5 and 3 times the wavelength of the megacusp embayments ($\sim$ 700 m) observed in Truc Vert beach. It should be noted that the in situ data are limited to a window of $\sim$ 2.4 km. Thus, beyond this point the calibration results have been compared against alongshore averaged shoreline positions using the largest available window ($\sim$ 2.4 km). The findings of this experiment are discussed in detail in

Section 3.5.

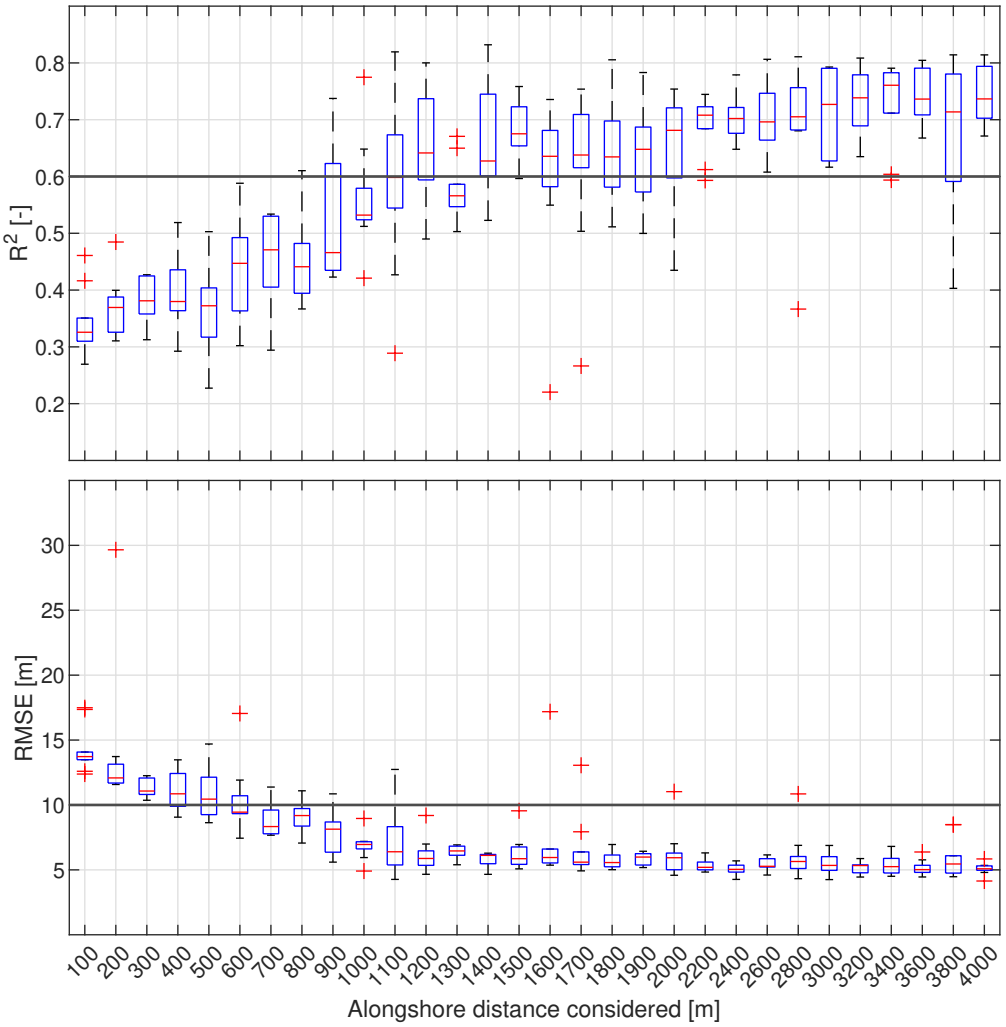

Figure 3.5: Performance indicators ($RMSE$ and R^2) of the model when calibrated using the alongshore averaged satellite derived waterline ($\overline{W_S}$) with a varying alongshore window size. The performance indicators of the model results are calculated against in-situ shoreline data with a matching window size ($\overline{S_{IS}}(y)$). Each box summarizes the results of 10 calibration runs. The horizontal red line inside the box, indicates the median value and the top and bottom edges of the blue boxes indicate the 25th and 75th percentiles respectively. Maximum whisker length extends up to 1.5 times the interquantile range and any value outside this range is considered an outlier and depicted as a red cross.

3.4.2 How much data is enough ?

In Figures 3.6 and 3.7 the results of the investigation on the adequate calibration period, influence of noise and sampling frequency on model performance using a synthetic shoreline are summarized for the case of 0 % and 200 % noise respectively. The sampling frequency of the shoreline used for calibration is indicated in the upper right corner of each panel. The mean (squares) and standard deviation (circles) R^2 and $RMSE$ of the 10 simulation ensemble are plotted in the left and right hand column respectively.

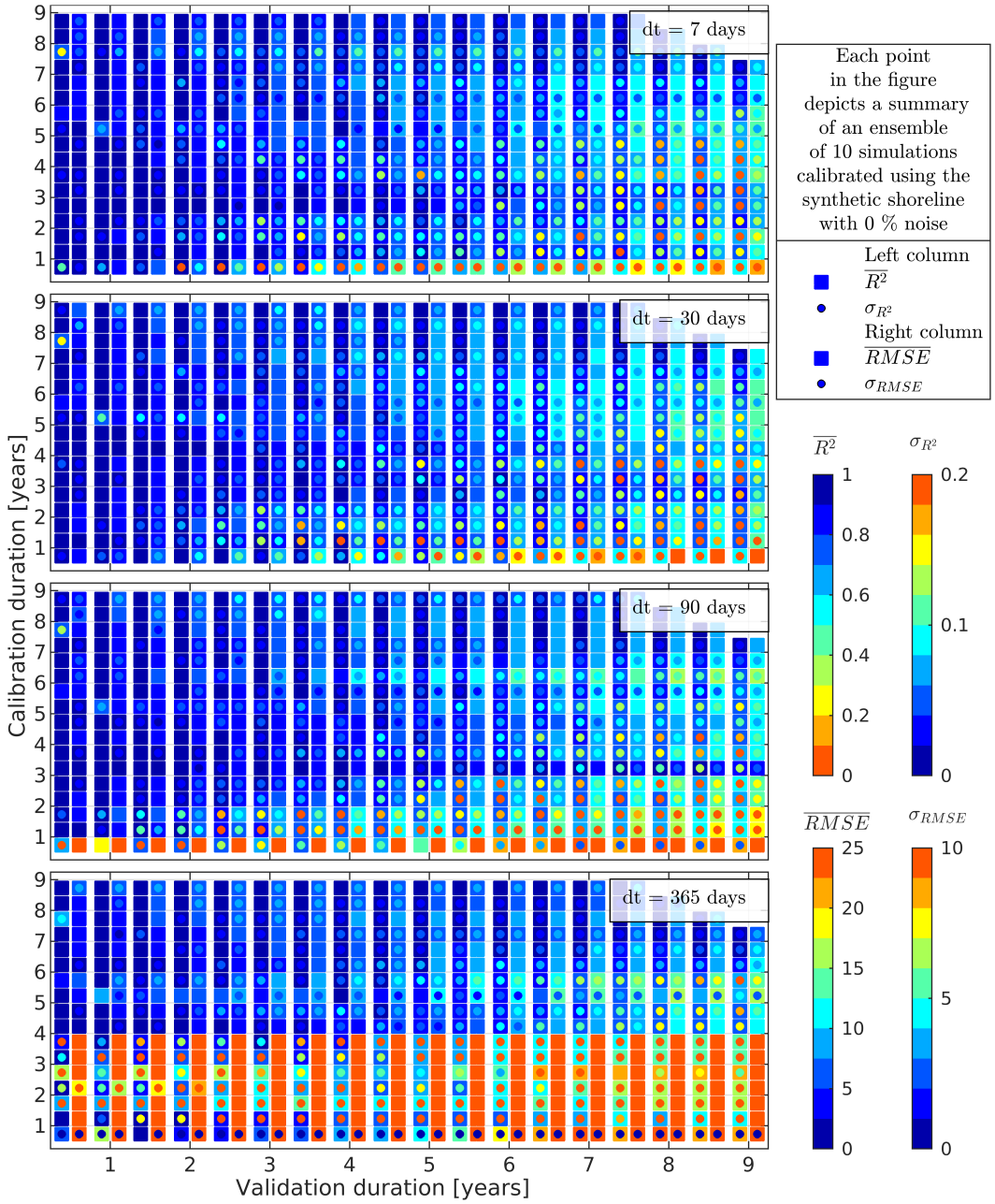

Figure 3.6: Model performance calibrated using synthetic shoreline with 0 % noise subsampled at $dt = 7$, 30, 90 and 365 days. $RMSE$ and R^2 plotted in the left and right column respectively, are calculated based on the daily subsampled synthetic shoreline considering the period following the calibration. The squares and the circles represent the mean and standard deviation of an ensemble of 10 simulations.

The influence of sampling frequency is weak in the 0 % noise case for dt $\leq$ 90 days (see Figure 3.6). Further reducing sampling frequency significantly reduces model skill, especially when less than 4 years of data are used for calibration. Considering a calibration period of 4 years or more, all four datasets enable the generation of models with very similar skill. The larger $RMSE$ around the 5 year calibration duration is due to the model producing an erroneous trend.

The effect of noise in the dataset on model skill is almost negligible as long as the sampling frequency is kept within dt $\leq$ 30 days (see Figures 3.6 and 3.7). Reducing sampling frequency to

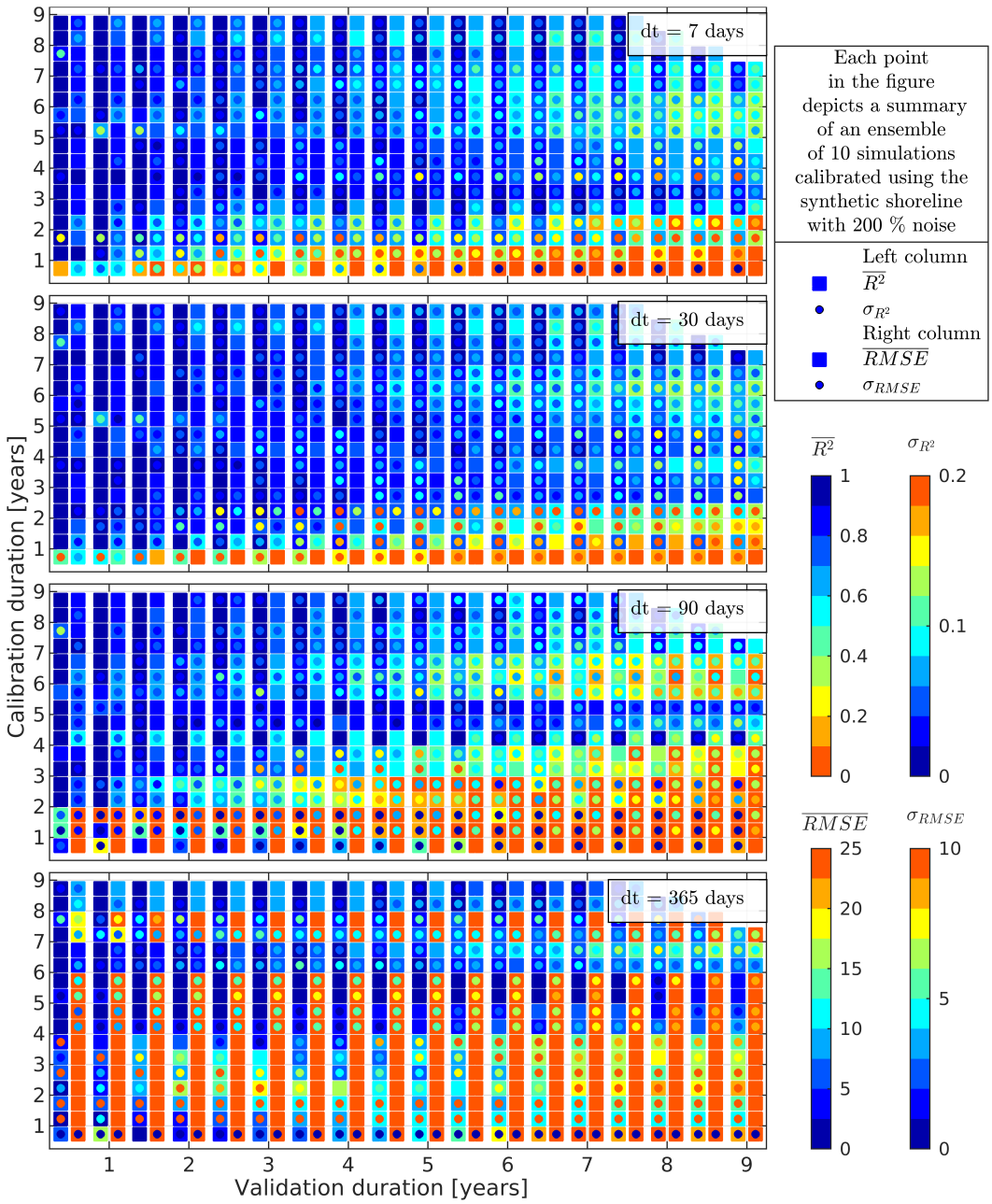

Figure 3.7: Model performance calibrated using synthetic shoreline with 200 % noise subsampled at $dt = 7, 30, 90$ and 365 days. $RMSE$ and R^2 plotted in the left and right column respectively, are calculated based on the daily subsampled synthetic shoreline considering the period following the calibration. The squares and the circles represent the mean and standard deviation of an ensemble of 10 simulations.

dt $\geq$ 90 days in the dataset with 200 % noise significantly reduces model skill, however when a calibration period larger than 3 years is considered results improve. Further reducing the sampling frequency to dt = 365 days, yields a model that fails to reproduce the shoreline evolution. When calibrating over 4 years or more, the model manages to capture the shoreline variability while still fails to reproduce the shoreline trend. These findings are very promising and are discussed in detail in Section 3.5.

In Figure 3.8 the predicted shorelines from the investigation on the adequate calibration period

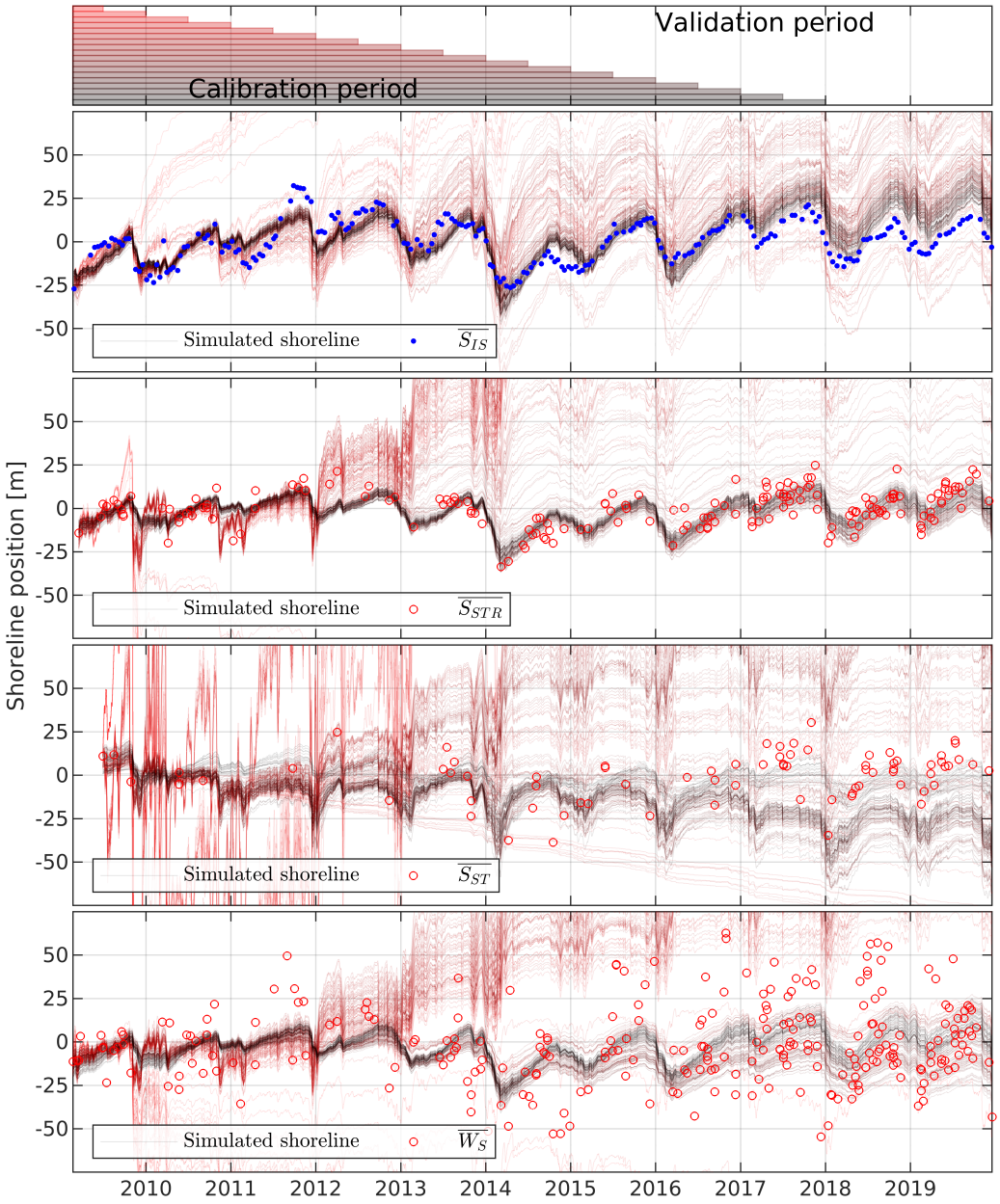

Figure 3.8: Model results of the investigation on the sufficient calibration window for all four alongshore averaged datasets. The considered calibration periods are indicated in the upper panel, transitioning from red to black as the calibration duration increases. The simulated shorelines are plotted in red for the model calibration finishing at 07/2009 gradually transitioning to black as the calibration window increases. Model performance was evaluated against the $\overline{S_{IS}}$ dataset considering the period following the calibration.

using the four alongshore averaged datasets are depicted together with the dataset used for the calibration. In Figure 3.9 the results of the analysis are depicted in the same format as for the synthetic cases. Results for all datasets, indicate a pivot point in model skill when calibration duration exceeds 4 years. This finding agrees with the work of Splinter et al. (2014) and our tests on the synthetic shoreline dataset. Excluding the $\overline{S_{ST}}$ dataset the models produced considering a calibration period of 4 years or more, show very good model skill. The increase in $RMSE$ in the model calibrated with the $\overline{W_s}$ considering a 6 year period is attributed to an erroneous trend generated by the model. This trend is present in the $\overline{W_s}$ dataset between 2009 and 2015,

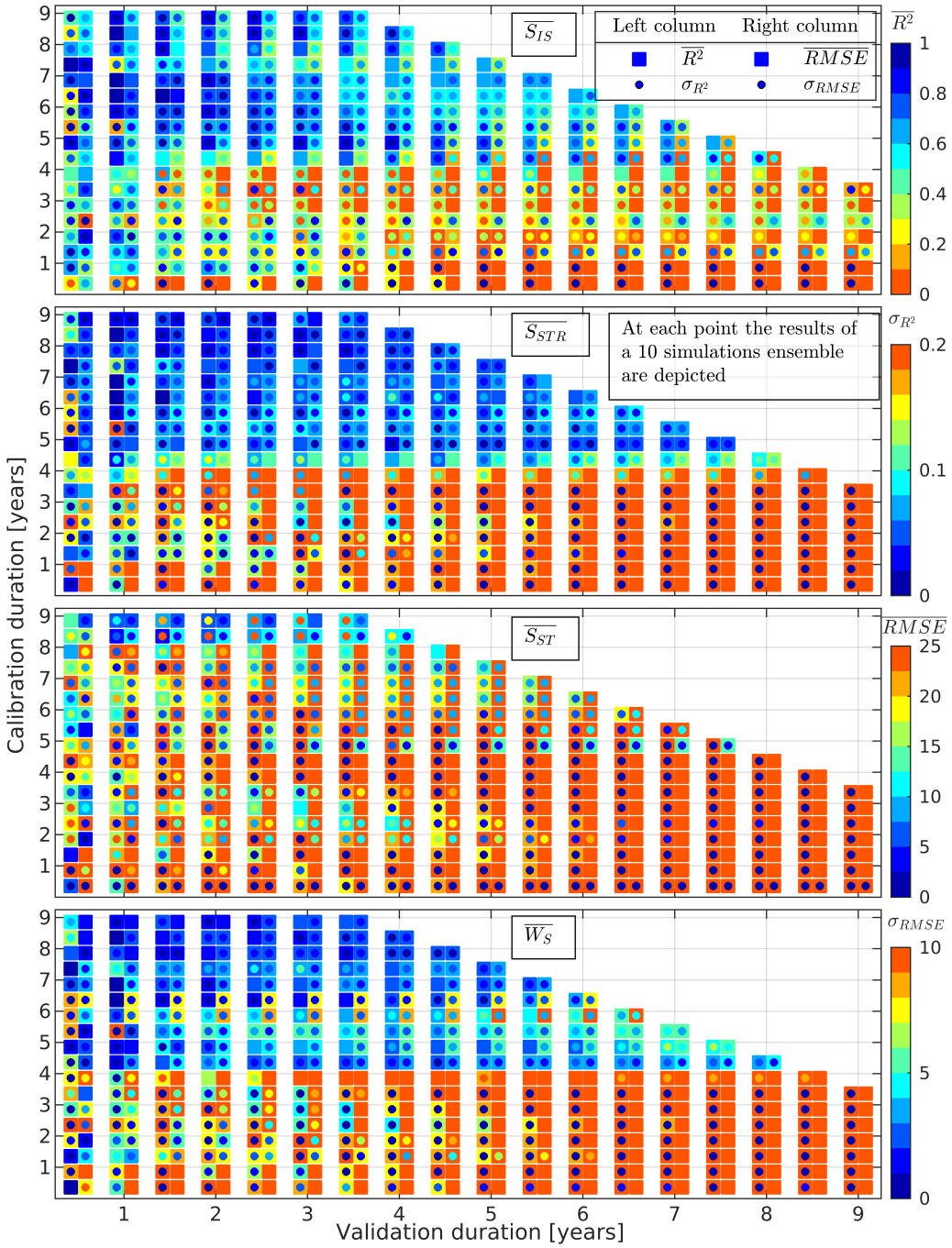

Figure 3.9: Model performance calibrated using the four alongshore averaged observed datasets, evaluated against the $\overline{S_{IS}}$ dataset considering the period following the calibration. $RMSE$ and R^2 plotted in the left and right column respectively. The squares and the circles represent the mean and standard deviation of an ensemble of 10 simulations.

leading to model parameters that would reproduce it. These findings open new perspectives for SDS applications which are discussed in more detail in Section 3.5.

Finally the results on the influence of sampling frequency in the alongshore averaged uncorrected SD waterline $\overline{W_S}$ on model skill are depicted in Figures 3.10 and 3.11. In Figure 3.10 four examples are shown having a total number of observations over the entire 11 year period of N = 25, 100, 175 and 275 plotted from the upper to the lower panel, respectively. The results are summarised in Figure 3.11 in terms of performance metrics ($RMSE$ and R^2). These findings indicate

that even with a dataset of 25 points distributed randomly over the 11 year period the simulated annealing algorithm manages to find an acceptable solution. However, the majority of the runs based on calibration with only 25 points yield very poor results. Increasing the number of points shows a significant improvement in the repeatability of the solution. When using the complete dataset (N_{max} = 275 points), the algorithm never fails to find an acceptable solution. These results are discussed in detail in section 3.5.

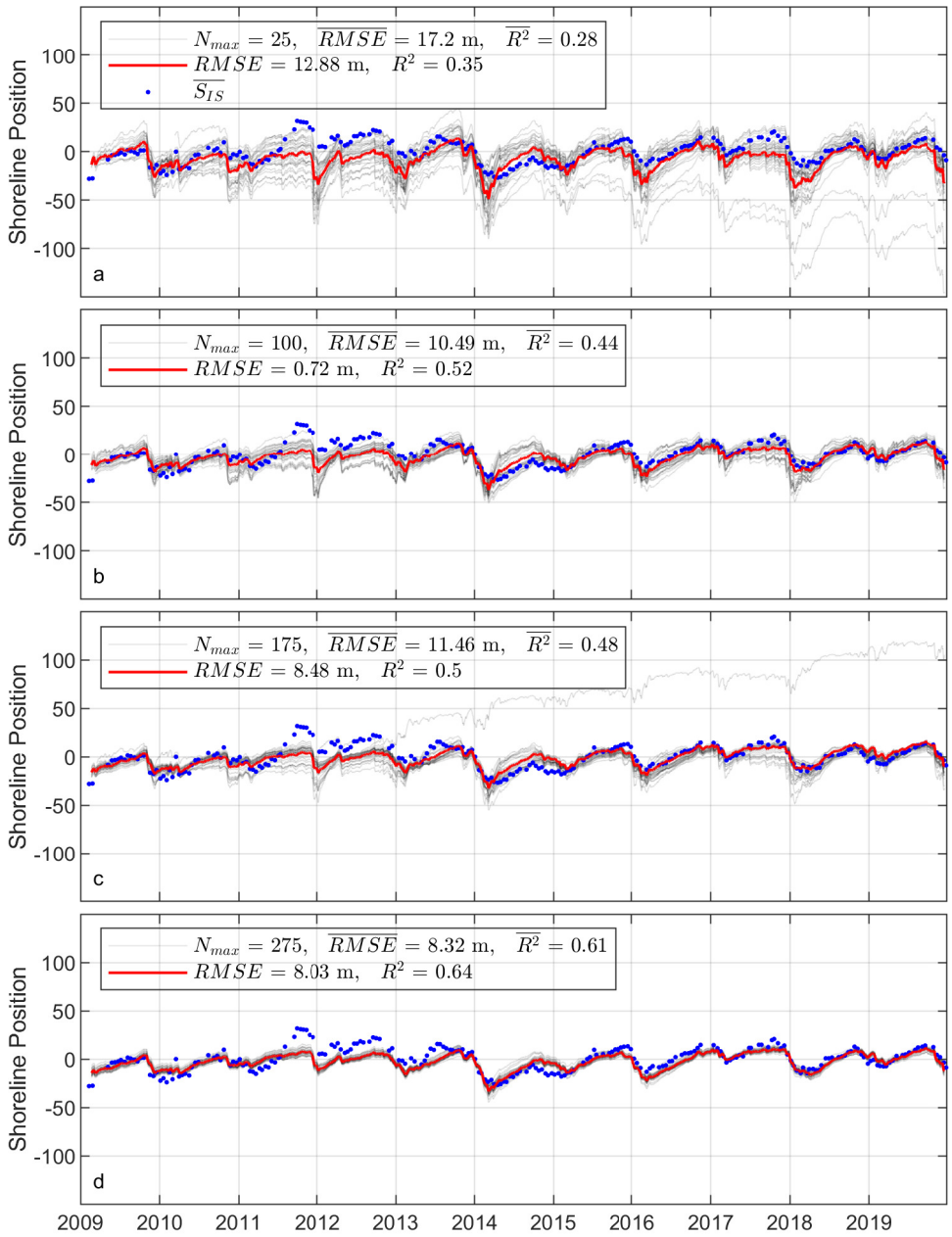

Figure 3.10: Predicted shoreline obtained from an ensemble of 30 different model calibrations using N number of randomly selected points from the $\overline{W_S}$ data set. The ensemble mean is plotted in red while all the rest are plotted in light grey. The model's performance is evaluated against the $\overline{S_{IS}}$ (blue dots). The amount of data points N_{max} used for the calibration of the model is indicated in the legend together with the average performance indicators $\overline{RMSE}$ and $\overline{R^2}$ of the ensemble.

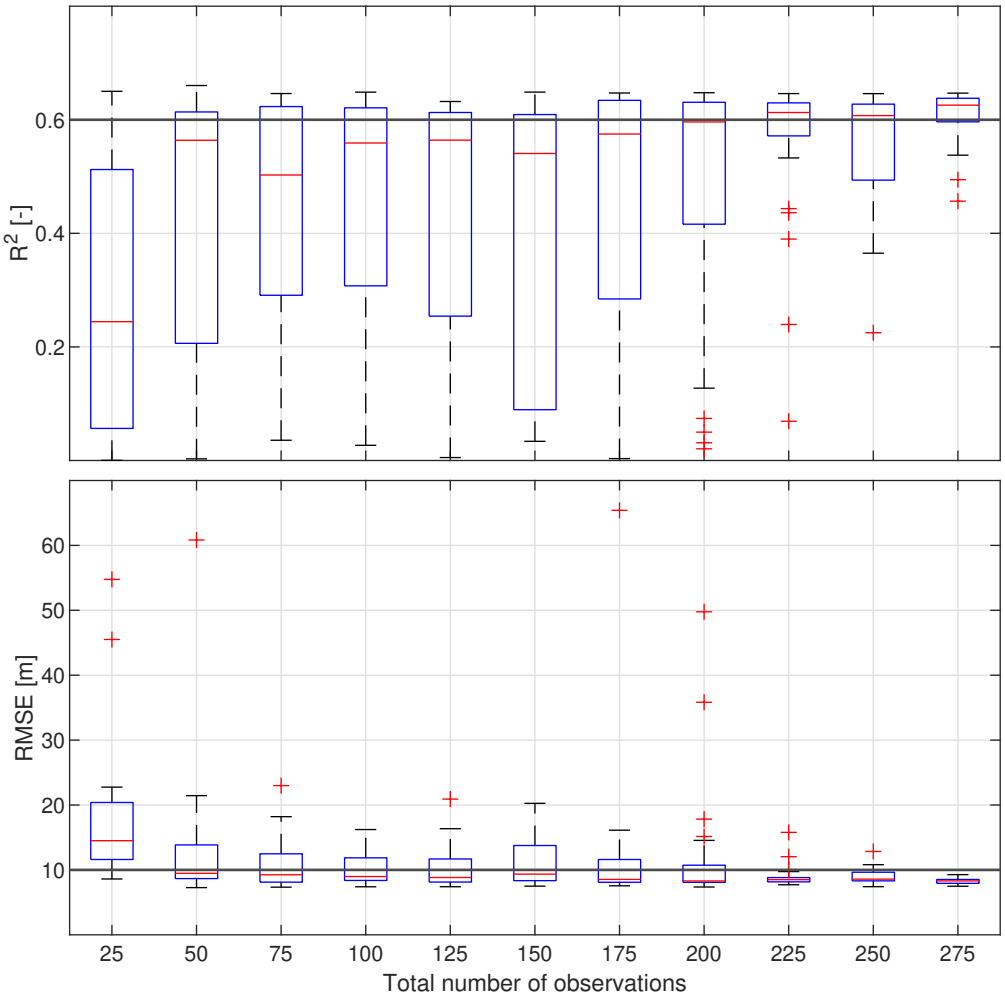

Figure 3.11: Performance indicators $RMSE$ and R^2 depicted in the lower and upper panel of the figure plotted against the number of data points used for the calibration. Each box corresponds to an ensemble of 30 simulations using N amount of data points randomly selected from the $\overline{W_S}$ dataset. The horizontal red line inside the boxes, indicates the median value and the top and bottom edges of the blue boxes indicate the 25th and 75th percentiles respectively. Maximum whisker length extends up to 1.5 times the interquantile range and any value outside this range is considered an outlier and depicted as a red cross.

3.5 Discussion

To the authors' knowledge the current study is the first ever successful use of uncorrected SDS data for the calibration of an equilibrium shoreline model in a high-energy, meso- macrotidal environment. Previous studies such as Castelle et al. (2014); Splinter et al. (2014) have used either data collected using traditional survey techniques such as GNSS or video-derived shorelines (e.g. Holman et al., 2003, ARGUS). Existing work using SDS observations in model calibration focused on microtidal environments (e.g. Alvarez-Cuesta et al., 2021a,b; Ibaceta et al., 2022), where SDS RMSE are on the order of 10 m. In their latest contribution Vitousek et al. (2023a) applied a SDS data assimilated shoreline model to hindcast and predict coastal change at the entire coast of California. They used almost exclusively SDS data for the calibration of the model, to which they applied water level corrections achieving a RMSE between SDS and in situ observations in the

order of 15 m.

There is a substantial amount of research aiming at reducing uncertainties and improving quality of SDS data (Castelle et al., 2021; Konstantinou et al., 2023). In the present application however the amount of data was found to be the most important parameter of the SDS dataset rather than the quality/accuracy of the shoreline position. Without applying any of the corrections proposed in Castelle et al. (2021), SDS data extracted in a meso- macrotidal, high-energy environment with a RMSE larger than 30 m, allowed skillful equilibrium shoreline model calibration. The calibrated model showed very good performance with a RMSE = 8.3 m and a strong correlation of R^2 = 0.63. This result was unexpected considering the large RMSE associated with the raw SDS data.

Recent research has increasingly focused on improving the accuracy and consistency of satellite-derived shorelines (SDS), recognising that the performance of extraction algorithms critically determines data quality. A comprehensive benchmark review by Vos et al. (2023a) summarised existing approaches and their relative strengths. Among these, normalized spectral indices such as the Normalized Difference Water Index (NDWI; McFeeters, 1996) and its variant, the Modified NDWI (MNDWI; Xu, 2006), remain widely used for their simplicity and robustness across sensors. The MNDWI, employed in the present work, enhances the land–water contrast in turbid or sediment-laden environments but can still misidentify the wet–dry sand limit instead of the true waterline under highly dynamic intertidal conditions. More recent developments, such as the Spectral Coastline Water Index (SCOWI; Bergsma et al., 2024), have demonstrated superior performance in such environments by optimally combining spectral bands to reduce sensitivity to moisture and illumination. At Truc Vert, SCOWI-derived shorelines exhibited greater temporal consistency and closer agreement with in-situ measurements compared to NDWI or MNDWI-based extractions. Continued improvements through adaptive thresholding, multi-spectral fusion, and uncertainty quantification offer promising pathways toward globally consistent, high quality SDS datasets.

The effect of noise in the datasets (both synthetic and observed) seems to be almost negligible as long as the sampling frequency is kept high (dt $\leq$ 30 days) and an adequate calibration period is considered. This observation stemming from the synthetic shoreline analysis experiment clearly explains why the worst model skill is obtained when the tide corrected dataset $\overline{S_{ST}}$ is used for calibration. The model seems to be sensitive to the period chosen for calibration as this would influence the shoreline trend as well as the phenomena included. Further analysis considering different calibration periods while maintaining the same duration should be performed to investigate this hypothesis.

It should be stated that the in situ data include a strong accretion spike in 2012 which is due to sandbar-welding and could only be captured at spring low tide which is when surveys take place at Truc Vert. This accretion signal is not as pronounced in the SDS datasets since the satellite flyover time does not necessarily coincide with spring low tide. Furthermore, as previously discussed the water level corrected datasets disregard low tide images, which results in smoothing of the

accretion spike. Such an event could not be captured by the physics of the model used, and is believed to have an impact in the performance of the model when calibrated with this period of the in-situ dataset. This could also be partly the reason for increasing model performance as the influence of 2012 gets smoothed with larger calibration period (see Figure 3.9).

The fact that the adopted methodology proved successful even in a very challenging site such as Truc Vert, is very encouraging for potential future applications of SDS data in equilibrium shoreline modelling even at sites where no in-situ data are available. The spatio-temporal coverage of freely available satellite imagery combined with the no a priori knowledge assumption adopted in the current study, hint that the proposed methodology could be universally applicable on cross-shore transport dominated coasts. The model used in the present work requires information about the median sediment grain size D_{50} of the simulated environment. Although this information is impossible to obtain via remote sensing, a reasonable guess would be sufficient as this would serve as a scaling factor that would be compensated by the calibration parameters.

Alongshore averaging was found to be the only necessary processing of the SDS data prior to their application in model calibration at Truc Vert. This can be explained by the presence of prominent mega-cusps, that typically form, migrate alongshore, and decay in time, which physics are not represented by an equilibrium model like Davidson et al. (2013). Therefore these features needed to be filtered out of the dataset, which was achieved by alongshore averaging over a window approximately 1.5 times the features wavelength. This approach does not violate the no a priori knowledge assumption adopted, since megacusp spacing can be estimated by simply studying the satellite images, and an averaging window of say 3-4 time this spacing be applied. Alternatively, filtering out megacusps, which are quite common on intermediate coastlines (Wright and Short, 1984), can be performed by applying a conservative alongshore window width in the order of a couple of km as Truc Vert shows larger rip spacing than most of the reported sandy beaches. Critically, our findings are in line with recent work suggesting that spacial averaging can reduce SDS noise (Castelle et al., 2022; Warrick et al., 2024), and demonstrate that global SDS datasets with transects spaced by 10s of kilometres are not relevant to address shoreline change on most coasts (Warrick et al., 2024).

A dataset covering 4 to 5 years with a monthly sampling frequency was found to be sufficient for the calibration of the model applied to hindcast $\sim$6 years of shoreline evolution in Truc Vert. This result, obtained with raw SDS data in a high energy, meso- macrotidal shoreline, is in line with the findings of Splinter et al. (2013) where they investigated the influence of noise, morphological sampling interval and dataset duration in equilibrium shoreline model calibration and the recent work of Alvarez-Cuesta et al. (2024) who performed a similar analysis on data assimilation. The fact that similar results with previous studies are obtained in the present work, further illustrates the strength of the simulated annealing algorithm considering that the investigated noise level in the synthetic time series is 4 times larger compared to previous studies (200% of the standard deviation) and so is the order of magnitude of the observation error ($O \sim 30$ m). It should be noted

that the SDS data after 2013, improve both in terms of image quality and sampling frequency. Therefore, the aforementioned result can be considered conservative and the models obtained using the methodology presented in this work are only expected to improve.

Our findings regarding the adequate sampling frequency indicate that even with as few as 25 points randomly spread over an 11 year period, the simulated annealing algorithm was able to find a very good solution. This is particularly encouraging for applications in higher latitudes where the amount of cloud-free satellite images are significantly reduced (Konstantinou et al., 2023). On average however, the performance of the models calibrated with the scarcely populated datasets ($N_{max} \leq 200$) is considered poor. Results could be significantly improved for all datasets by narrowing the range of investigated model free parameters which would guide the algorithm towards a desired solution.

The alongshore averaging window width and adequate spatiotemporal resolution of the SDS data, should be regarded as site specific variables. Given that Truc Vert is a challenging coastline, conservative estimates of these variables are provided in the current work. Exception would be high-latitude coastlines where cloud coverage can significantly affect the sampling frequency. The limited availability of cloud free satellite images that would significantly affect the temporal resolution could be addressed through an iterative approach. In addition larger waves associated with higher latitudes would influence the size of cusps and megacusps which in turn would control the width and spatial resolution of the alongshore window. The sufficient width and resolution of the alongshore window are not seen as limitations but rather as site-specific information readily available in the satellite imagery.

The present results suggest that the introduced methodology could be potentially applicable to any cross shore dominated sandy shoreline. To verify this hypothesis such approach should be applied to several diverse sites around the world investigating the influence of beach type, wave climate and tidal amplitude in model skill. Furthermore, applying such method to complex coasts where other processes (e.g. longshore sediment transport gradients) are at play should also be explored using one-line models. Finally applying the same approach to different model types would further challenge the findings of the present study. Although previous work using several models like Yates et al. (2009b); Splinter et al. (2014); Vitousek et al. (2017); D'Anna et al. (2022) suggest similar performance, further validation of the proposed methodology should be conducted.

The simulated annealing algorithm has proven to be a very useful tool, enabling the proposed methodology. The stochastic nature of the algorithm should be accounted for by repeating the experiment enough times such as to achieve convergence of the error statistics. Any application of the introduced methodology would require accurate inshore wave data (hindcast and /or forecast), that capture the wave climate variability (e.g. seasonal, interannual). Such data may be obtained from publicly available global wave hindcasts spanning over several decades such as Mentaschi et al. (2023); Hersbach et al. (2023a), and either used directly as a forcing or as a boundary condition to produce high resolution nearshore wave forcing for shoreline modelling.

3.6 Conclusion

The present work introduces a novel approach using uncorrected, noisy, SDS data for the calibration of equilibrium based shoreline models. The simulated annealing algorithm proposed by Bertsimas and Tsitsiklis (1993) guided by high quality wave forcing, extracts information from uncorrected noisy SDS data, even when assuming no a priori knowledge of the site. Rather than data quality, the amount of data (e.g sampling frequency) was found to be critical in the modelling application. The only required processing of the SDS data for the model calibration was alongshore averaging, while any other site-specific corrections did not significantly improve model skill. Though further validation is needed, our findings suggest that alongshore averaged uncorrected SDS extracted at any cross shore dominated coastline can be applied in the calibration of transect based equilibrium shoreline models. The present work opens new perspectives in modelling, understanding and predicting sandy shoreline change in sites lacking field data.

Chapter 4

Investigating the potential of time varying free parameters in equilibrium shoreline change models through data assimilation

Following the calibration experiments presented in Chapter 3, this chapter investigates whether allowing model free parameters to vary in time can capture non-stationary shoreline dynamics and improve predictive skill. Using a dual parameter–state data assimilation approach based on an ensemble Kalman filter, the analysis tests the hypothesis that temporal changes in calibrated parameters may reflect fluctuations in the local wave climate.

The experiments are conducted across multiple sites along the European Atlantic coast, enabling a comparative evaluation of the relationship between wave forcing, parameter variability, and model skill. The results show that while time-varying parameters sometimes enhance model performance—particularly at sites with high-quality observations—the relationship between parameter evolution and wave climate remains weak. These findings suggest that the apparent non-stationarity largely reflects unresolved local processes rather than climate-driven variability. This motivates a more flexible framework capable of integrating multiple process representations and complementary datasets. Chapter 4 responds to this challenge by introducing a hybrid modelling approach that couples distinct equilibrium formulations within a unified, data-assimilative system.

The present chapter has been accepted for publication with minor revisions in the peer review journal *Earth Surface Processes and Landorms*.

Azorakos, G., Castelle, B., Marieu, V., Idier, D, Ibaceta R., Splinter K.D., Bertin, S, Masselink G. & Scott T. (2025). Investigating the potential of time varying free parameters in equilibrium shoreline change models through data assimilation. *Earth Surface Processes and Landforms*, (Accepted with minor revisions).

4.1 Introduction

Responding to variable wave forcing, cross-shore sediment transport dominated shorelines constantly approach a dynamic equilibrium (Wright and Short, 1984). Models based on this equilibrium concept (Miller and Dean, 2004; Yates et al., 2009b; Davidson et al., 2013; Splinter et al., 2014) can effectively simulate sandy shoreline evolution over timescales ranging from days to decades (Wright et al., 1985; Splinter et al., 2013; Castelle et al., 2014; Montaño et al., 2020; Mao et al., 2025). Typically, time-invariant model free parameters are optimized over a calibration period using shoreline observations (Splinter et al., 2013, 2014), leading to shoreline predictions that can be biased by the phenomena present in the period used for model calibration (Splinter et al., 2017; D'Anna et al., 2020). Furthermore, shoreline change models with time-invariant best fit parameters may struggle to reproduce shoreline dynamics over time scales that differ from the calibration period (Splinter et al., 2013, 2017). Introducing time-varying model free parameters is hypothesized to make shoreline change models dynamic and adaptive, allowing them to better reflect the diversity of beach response and behaviour across different temporal scales.

Splinter et al. (2017) investigated the effect of changing storm seasonality on shoreline response and best-fit model free parameters at an open-coast beach exposed to a multi-modal wave climate on the east coast of Australia. They found that optimal model parameters varied by an order of magnitude following a shift of the incident wave climate, and of shoreline response from seasonal to episodic. Ibaceta et al. (2020); Alvarez-Cuesta et al. (2021a); Vitousek et al. (2023b) introduced data assimilation techniques to incorporate shoreline observations into their modeling applications. Ibaceta et al. (2022), working at the same site as Splinter et al. (2017), implemented a dual state/parameter ensemble Kalman filter (enKf) to track temporal variability in model free parameters, which they found to negatively correlate with incoming wave energy. Chen et al. (2025) explored the use of time varying model-free parameters and their relationship with environmental forcing at Hasaki Beach, Japan. They showed that changes in incoming wave energy positively correlate with changes in model free parameters which contradict the findings of Ibaceta et al. (2022).

Time varying parameters may compensate for missing processes in numerical models and should be interpreted cautiously, as site-specific links to environmental conditions may not generalize or accurately reflect system behaviour. To robustly test the hypothesis that variability in model free parameters could be linked to wave climate, it is necessary to examine multiple well-monitored cross shore sediment transport and wave dominated sites, exposed to similar wave climates. The present work seeks to address this gap by conducting such an investigation across three sites along the Atlantic coast of Europe. An enKf algorithm (Ibaceta et al., 2020) was applied to track temporal variability of the model free parameters in the Davidson et al. (2013) model. Improvement in model skill by the introduction of time varying model free parameters was quantified and links between parameter variability and environmental forcing were explored. The ability of

the enKf algorithm to track the non-stationarity of the system and the potential to improve shoreline prediction is thoroughly discussed. The study sites, data used, and adopted methodology are detailed in Section 4.2. The results are presented in Section 4.3 followed by a detailed discussion and conclusions in Sections 4.4 and 4.5.

4.2 Study sites, data & methodology

4.2.1 Study sites

Three study sites were selected along the west coast of Europe, namely Perranporth in SW England, Porsmilin in Brittany, NW France, and Truc Vert in Nouvelle-Aquitaine, SW France (Figure 4.1). All three sites are exposed to a wave climate generated in the north Atlantic ocean, consist of medium quartz sand ($0.32 \leq d_{50} \leq 0.35$ mm), and are predominantly cross-shore sediment transport dominated. Perranporth and Porsmilin are macrotidal beaches while Truc Vert is a meso-macrotidal beach with a spring tidal ranges of 6.3, 5.7 and 3.7 m respectively. Long-term monitoring programs have been in place at all three sites since between 2003 and 2006, with publicly available datasets described in detail in McCarroll et al. (2023); Bertin et al. (2022); Castelle et al. (2020).

4.2.2 Wave and shoreline data

The Perranporth wave timeseries (Figure 4.1, i) is recorded at 30-minute intervals by a Datawell Directional Waverider Mk III buoy moored at ∼18 m depth, offshore of the study site (50.352°N, -5.174°E). Gaps in the timeseries caused by failure of the buoy during extreme events are filled by the more reliable Bideford bay buoy located ∼100km up the coast (51.058°N, -4.277°E). Data and metadata reports are freely available through Southwest Coastal Monitoring (`https://southwest.coastalmonitoring.org/`). The Porsmilin wave timeseries (Figure 4.1, j) is extracted at hourly intervals from hindcasts produced using the Wavewatch III (WW3) model (version 4.11), at a depth of ∼14 m (48.347°N, -4.681°E). The timeseries is a product of two databases developed and curated by Ifremer, namely the HOMERE database (Accensi and Maisondieu, 2015) covering 1994 to 2023 and the NORGAS-UG database (Ardhuin and Accensi, 2012), which spans from 2008 to the present. The Truc Vert wave timeseries (Figure 4.1, k) is extracted at hourly intervals from the ERA5 global reanalysis dataset (Hersbach et al., 2023b) at a depth of ∼54 m (44.5°N, -1.5°E). The Truc Vert wave timeseries was shoaled and refracted to breaking wave conditions using the formula proposed by Larson et al. (2010).

For the three sites, shoreline position timeseries are obtained by topographic surveys performed during spring low tide, using an RTK-GNSS with a vertical accuracy between 3 and 10 cm in-

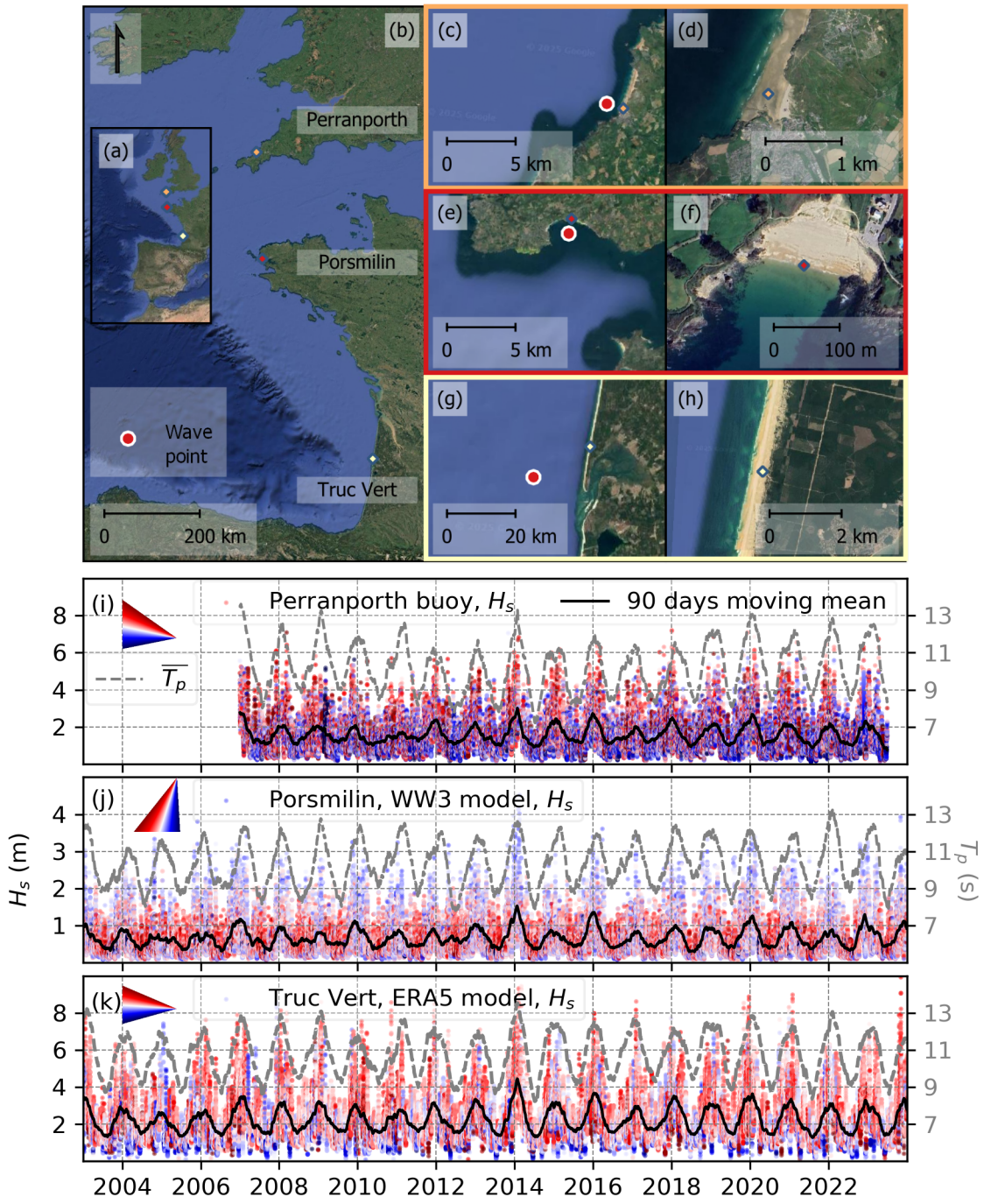

Figure 4.1: (a - b) Location of the three study sites along the west coast of Europe. (c) Perranporth beach and the wave buoy location (red dot). (d) Overview of the monitored area of Perranporth beach. (e) Porsmilin beach and the wave extraction grid point location (red dot). (f) Close-up view of Porsmilin beach. (g) Truc Vert beach and the wave extraction grid point location (red dot). (h) close-up view of the monitored area at Truc Vert. (i - k) Available wave conditions at the three sites. Wave height (H_s) measured/extracted is indicated by the coloured dots together with the three month moving mean $\overline{H_s}$ (black solid line) and $\overline{T_p}$ (grey dashed line, plotted in the right axis). Incoming wave direction is represented by colour, with the triangle indicating the mean incoming wave direction and the blue–red shading illustrating the directional spread around this mean.

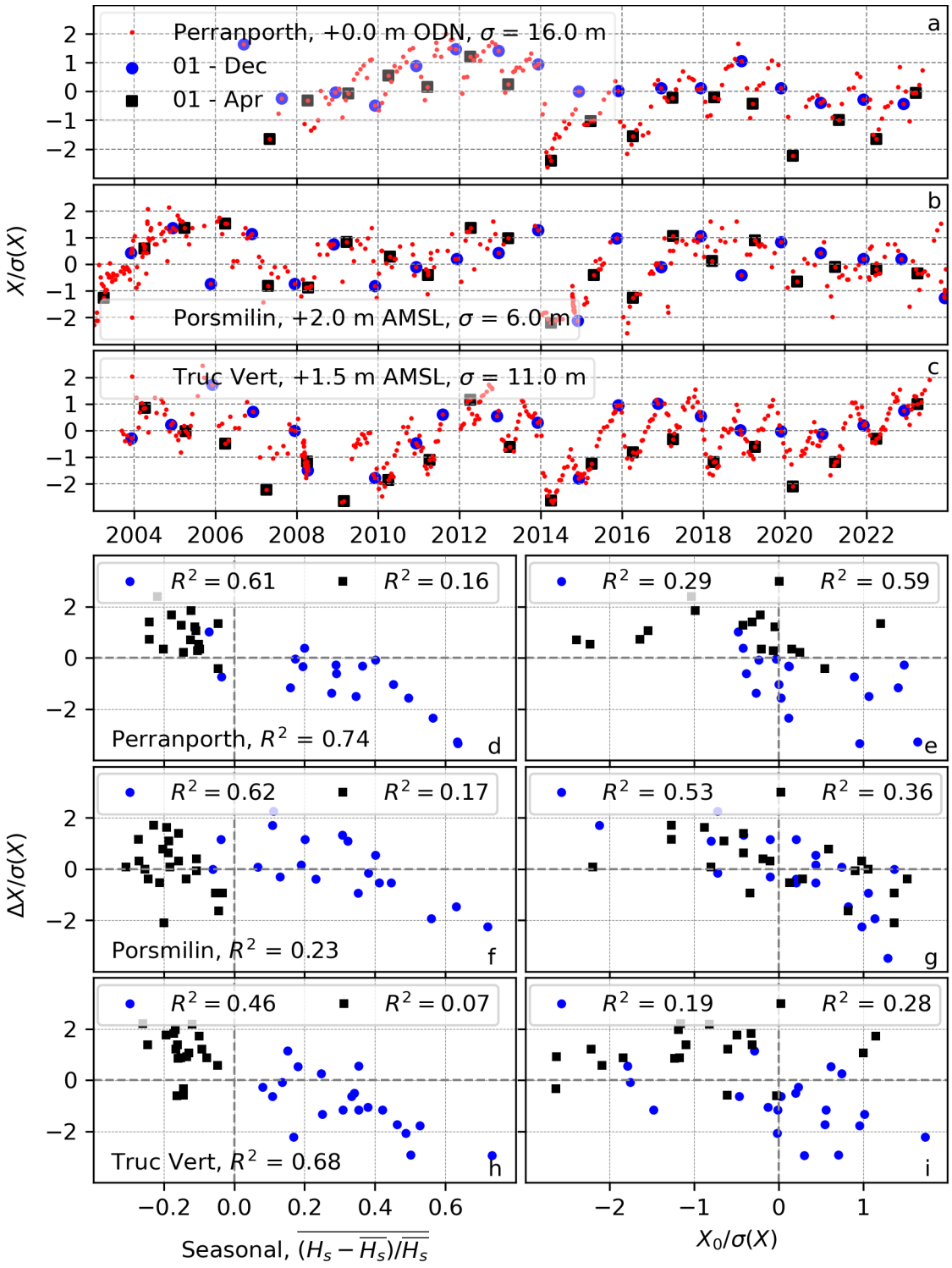

Figure 4.2: Normalized timeseries of shoreline fluctuation around the mean position $X/\sigma(X)$ in Perranporth (a), Porsmilin (b) and Truc Vert (c). The shoreline proxy, vertical datum used at each site, and standard deviation of shoreline position $\sigma(X)$, are indicated in the legend. The start of winter (1 December) and summer (1 April) are marked by blue circles and black squares on the nearest observations, respectively. (f) Normalized shoreline change $\Delta X/\sigma(X)$ in Perranporth versus seasonal normalized wave height fluctuations around the mean $(H_s - \overline{H_s})/H_s$ depicted in black squares and blue dots for summer and winter respectively. (e) Seasonal $\Delta X/\sigma(X)$ versus the shoreline position at the beginning of the season $X_0/\sigma(X)$ in Perranporth. (f - i) depict the same results for Porsmilin and Truc Vert. The seasonal and total coefficient of determination R^2 are indicated in each panel.

troducing a horizontal uncertainty between 3 and 10 m depending on beach slope. Shoreline proxies were defined as the horizontal position of the +0m elevation above Ordnance Datum Newlyn (ODN) in Perranporth, and the +2m and +1.5m elevation above Mean Sea Level (AMSL) in Porsmilin and Truc Vert, respectively. At Perranporth and Truc vert the beach profile is averaged alongshore to filter out three-dimensional beach features (e.g. cusps and megacusps). In contrast, a single profile at the center of the beach is monitored at Porsmilin. Prior to 2012 the alongshore extent surveyed at Truc Vert was less than 1000 m and varied between surveys. Fully filtering out megacusps at Truc Vert, however, requires a minimum alongshore extent of 1400 m (see Chapter 3). The shoreline positions X, normalized by the corresponding standard deviation $\sigma(X)$ of the timeseries are plotted in Figure 4.2 (a-c).

Throughout this work, winter and summer refer to the periods from December to March and April to November respectively. Figure 4.2(d-i) shows the seasonal shoreline change against the seasonal average wave forcing and shoreline position at the beginning of each season. To facilitate quantitative comparison between the three sites, wave height has been normalized. At Perranporth and Truc Vert seasonal shoreline changes are nearly identical and are strongly governed by the seasonal variations in wave forcing. Almost all winter/summer periods on record result in an erosion/accretion cycle. Porsmilin responds slightly differently, with mild winters occasionally leading to accretion and significant scatter during summer. This may partly reflect planform beach dynamics such as rotation and/or breathing considering a single profile is monitored. Nevertheless, the erosion/accretion cycle seems to be largely controlled by the shoreline position at the beginning of each season X_0, with accreted shorelines typically eroding and vice versa regardless of the season. Despite these site-specific differences, all three beaches respond similarly to high energy winters and have a nearly identical response to the extreme winter of 2013 - 2014. The present analysis confirms and extends previous studies investigating the influence of North Atlantic wave climate on beach response along the west coast of Europe (Castelle et al., 2017b; Dodet et al., 2019; Bertin et al., 2022; McCarroll et al., 2023; Masselink et al., 2023; Castelle et al., 2024). Wave conditions have been found to largely control shoreline change not only at the exposed beaches of Perranporth and Truc Vert as demonstrated by Masselink et al. (2023) but also at the sheltered Porsmilin beach. Furthermore, shoreline position at the beginning of each season was identified as an important factor influencing seasonal shoreline response (Dodet et al., 2019), particularly at Porsmilin.

4.2.3 Equilibrium shoreline model

In the present work the empirical equilibrium shoreline model ShoreFor developed by Davidson et al. (2013), presented in Section 2.5.1, was used to simulate shoreline evolution.

The original formulation by Davidson et al. (2013), and most subsequent variants, include a linear trend term b in equation 2.1. Given the absence of significant linear trends at all three sites, this

term was excluded under the assumption that the model's remaining free parameters—accretion/erosion rates $c^{\pm}$ and ϕ—can sufficiently represent the system dynamics.

For model calibration and quantitative comparison, the root mean square error RMSE, bias included, correlation R and standard deviation σ are integrated into the Loss function L, equation 4.2. Combining all three statistical parameters in one metric is believed to quantify model skill rather than just model error (Taylor, 2001; Mao et al., 2025), allowing for a more holistic approach in model calibration and comparison. RMSE and σ of the simulated shoreline are divided by the σ of the observation, ensuring that all three statistical parameters are normalized.

$$RMSE_{\text{norm}} = \frac{RMSE}{\sigma_{\text{Obs}}}, \sigma_{\text{norm}} = \frac{\sigma_{\text{Pred}}}{\sigma_{\text{Obs}}} \tag{4.1}$$

The loss function L is defined as:

$$L = \sqrt{RMSE_{\text{norm}}^2 + (1 - R)^2 + (1 - \sigma_{\text{norm}})^2} \tag{4.2}$$

Best-fit stationary model free parameters have been calibrated over a 12 year period (2012-2024) using a simulated annealing nonlinear optimization algorithm (Bertsimas and Tsitsiklis, 1993). A total of 10^6 iterations were performed to minimize the loss function. The process was repeated 10 times, resulting in an ensemble of simulated shorelines trajectories, to account for the stochastic nature of the calibration algorithm.

4.2.4 Data assimilation

The enKf algorithm of Ibaceta et al. (2020) breaks the data assimilation process in two steps, namely the parameter and state update. Using an initial set of model parameters an ensemble of simulated shorelines is calculated consisting of n = 500 members. At the first step (parameter update), the simulated shorelines are compared to the observation and if the error is larger than the observation uncertainty, the model parameters are adjusted in order to reduce it. At the second step (state update) a new ensemble of simulated shorelines is calculated using the updated parameters which is further corrected if the error between observed and simulated shoreline remains larger than the observation uncertainty. Throughout this work, observation uncertainty was set to 3 m for all three sites. A process noise magnitude is defined to inflate the parameters during the first step that can be considered as the "search step" within the "parameter space" and has been kept constant for all sites. Each model free parameter is inflated by a process noise in the order of $O(10^{-3})$ relative to the parameter magnitude. For a detailed description of the enKf algorithm implementation, the reader is referred to the work of Ibaceta et al. (2020). The time varying model free parameters obtained at the first step (parameter update), are referred to as the non-stationary

model throughout this work.

4.3 Results

In Figure 4.3(a-c), the simulated shorelines from both the stationary and non-stationary models denoted as S and NS, respectively, are compared with the observation for the 12-year period between 2012 and 2024. Shoreline data prior to 2012 were excluded from the modeling exercise due to the limited and variable alongshore extent of observation at Truc Vert. The poor model performance in Perranporth during winter 2013/2014 may stem from a buoy failure and subsequent substitution of the data with measurements from Bideford Bay. The introduction of non-stationary model parameters resulted in a significant improvement in model skill at Perranporth, had negligible impact at Truc Vert, and led to a deterioration in performance at Porsmilin. Adjusting the model free parameter value at each observation time step seems to only marginally improve model skill. The non-stationary model parameters are depicted in Figure 4.3 (e - g), normalized with the corresponding stationary value. In panel (h), to illustrate the wave climate variability, the wave height extracted from the ERA5 reanalysis dataset (Hersbach et al., 2023b) offshore of Truc Vert is depicted with the winter seasons indicated as shaded areas.

In Perranporth and Truc Vert all three non-stationary parameters seem to fluctuate around their stationary values. This is not the case for ϕ in Porsmilin however, especially between 2017 and 2021 when it drops to almost 10% of its stationary value ϕ_{ST}, which is in the order of 10^3 days in all three sites. ϕ exhibits the largest and most frequent fluctuations, hinting that there might be a seasonal/interannual signal. The accretion/erosion rates $c^{\pm}$ show smaller and longer fluctuations, suggesting that these might be affected by long-term patterns in the wave forcing and/or alongshore sediment transport processes. Some similarities in the temporal variability of all three parameters can be identified between the three sites. However, the correlation, although statistically significant, is very weak. For instance, the strongest correlation was found in the variability of the erosion rate c^{-} between Truc Vert and Porsmilin, with $R^2 = 0.3$ ($p \approx 0.00$). The high frequency fluctuations in ϕ and especially the response to high energy winters, prompted some further investigation into the drivers behind this variability. Changes in the normalized ϕ over the winter period have been calculated and compared with winter mean wave height (Figure 4.4), which seems to describe 37 to 58 % of winter $\Delta\phi$. There is some scatter during average winters ($\overline{(H_s - \overline{H_s})}/\overline{H_s} \approx 0.36$), while above average winters almost never result in a significant decrease of the parameter. All three sites respond similarly to the most and least energetic winters with a large increase and drop in ϕ, respectively.

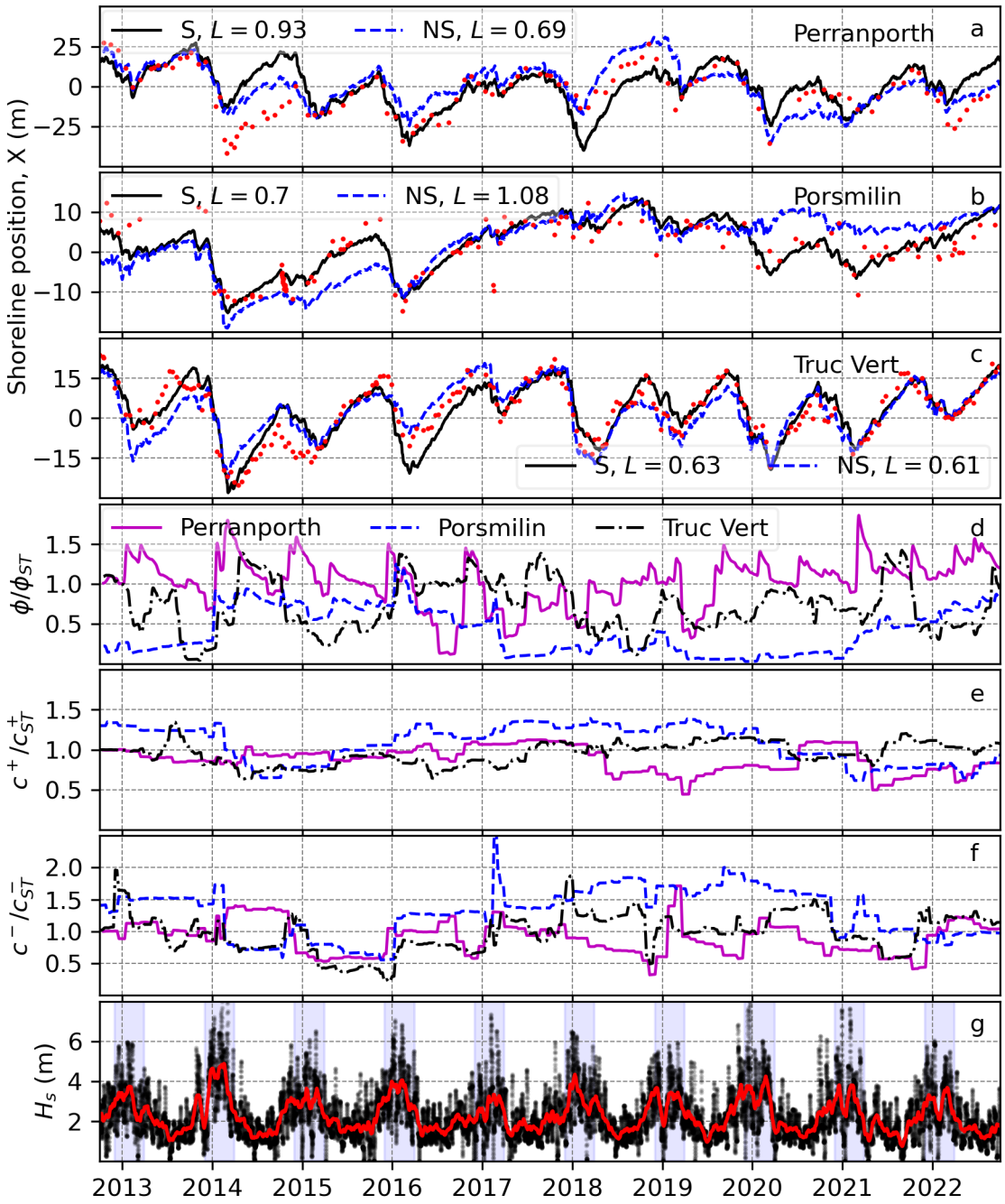

Figure 4.3: (a - c) simulated shoreline timeseries produced by the stationary S (solid black line) and non-stationary NS model (dashed blue line) depicted together with the shoreline observations (red dots) at all three sites. Model skill (loss function) is indicated in the legend as L. (e - g) time series of non-stationary model free parameters for Perranporth (magenta solid line), Porsmilin (blue dashed line) and Truc Vert (black dashed/dotted line). Non-stationary parameters have been normalized using the value of the corresponding stationary model free parameter. (h) ERA5 time-series of instantaneous (black dots) and monthly averaged (red line) H_s extracted offshore of Truc Vert. Winter period (December - March) is illustrated by the shaded background.

4.4 Discussion

To the best of the authors' knowledge, this is the first study to investigate whether temporal variability in model-free parameters across multiple sites exposed to similar wave climates reflects

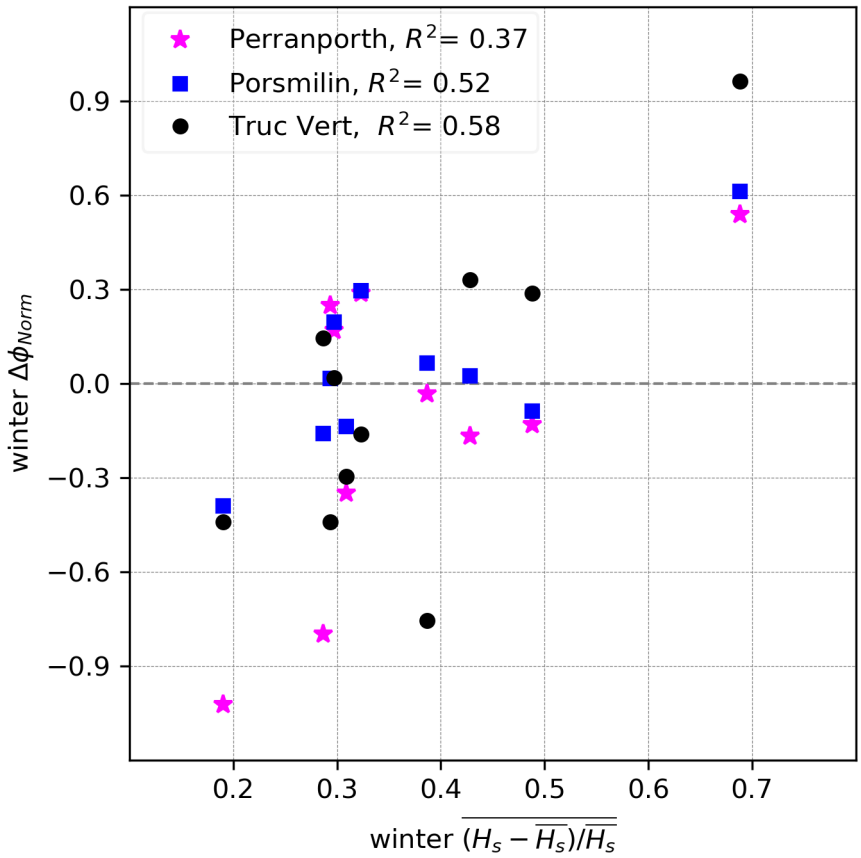

Figure 4.4: Changes in normalized beach memory ϕ/ϕ_{ST} between April and November plotted against winter normalized H_s.

changes in environmental forcing. Inter-site comparison of parameter variability reveals weak linear correlation, suggesting that subtle seasonal/inter annual wave climate fluctuations have minor impact and may not be the dominant mechanism along the Atlantic coast of Europe. At all sites, however, the ϕ parameter increased significantly in response to the most extreme winter on record (2013/2014). This aligns with (Splinter et al., 2017; Ibaceta et al., 2020) who showed that, at an open-coast beach exposed to a multi-modal wave climate and potential strong interannual storm regime shifts, notable changes in environmental forcing can impact best-fit model parameters, especially ϕ. Our results therefore highlight the potential of time-varying free parameters for improving model predictions of shoreline response during extreme events, a limitation that was emphasized in the benchmarking works of Montaño et al. (2020); Mao et al. (2025). It is also important to remember that the stationary models achieved skill levels among the highest reported in the literature for similar environments (Splinter et al., 2013, 2014; Montaño et al., 2020; Mao et al., 2025). Incorporating non-stationary model free parameters may offer limited benefit when baseline model performance is probably near its practical limits. Moreover, the ability of the enKf to match the performance of the stationary model suggests it may also serve as a viable alternative for model calibration (Alvarez-Cuesta et al., 2021a; Vitousek et al., 2023b).

The ability of the enKf algorithm to accurately track system non-stationarity, has been found to decline with increasing observation error and/or decreasing sampling frequency (Ibaceta et al.,

2020; Alvarez-Cuesta et al., 2024). The poor performance of the non-stationary model in Porsmilin may be partly attributed to the irregular observation frequency (Bertin et al., 2022). Additionally, unresolved 3D beach processes might further impact enKf performance in Porsmilin where only a single profile is measured (Bertin et al., 2022) and in Truc Vert prior to 2012 when spatial observation extent was small and inconsistent (Castelle et al., 2020). Pre-season beach state influences seasonal shoreline response at all sites - most notably in Porsmilin- while it's exclusion from the model likely contributes to the poor performance. The ability of the algorithm to track the non-stationarity of the system is highly dependent on the quality and properties of the dataset as well as the processes described by the model equations. Being that models constitute an incomplete description of a complicated physical system, non-stationary parameters should be interpreted with caution as they might be compensating for processes not included in the model structure. The correction step of the enKf algorithm always keeps the model within observation uncertainty, regardless of its ability to track non-stationarity. This feature of the algorithm allows us to keep models in track, compensating for cascading errors arising from simulated forcing conditions and the incomplete description of the system that can render long term shoreline predictions very unreliable.

4.5 Conclusions

Models with time invariant free-parameters demonstrate strong performance in sites exposed to seasonal, mostly unimodal, wave climate. Introducing time-varying free parameters shows great potential in improving prediction of extreme events in long term simulations and overall model performance at sites exposed to more complex wave conditions (Ibaceta et al., 2022). Links between free-parameter variability and wave forcing are more complex than expected, requiring accurate system representation for proper identification. Future research should consider multiple sites exposed to multimodal wave climates to further explore the relationship between environmental forcing and model free-parameter variability. Data assimilation applications can be very useful in keeping models aligned with observations and/or projected long term trends. Considering the computational efficiency, relatively easy implementation and ability to converge even with low quality datasets (Alvarez-Cuesta et al., 2024), the enKf algorithm is an efficient way to incorporate data in modeling applications. As coastal sciences are transformed to a data rich field of studies by the emergence of global datasets (Vitousek et al., 2023a; Calkoen et al., 2025), data assimilation becomes a necessary tool enabling the integration of data into our models, compensation for processes not accounted for and quantification of model error in real time.

Chapter 5

Blind testing of a hybrid equilibrium shoreline model

The limitations identified in Chapter 5 motivate the development of hybrid frameworks that merge complementary process representations to enhance both physical realism and predictive skill. This chapter presents such an approach, implemented and tested within the ShoreShop 2.0 international benchmarking experiment (Mao et al., 2025). The proposed hybrid model explicitly couples two equilibrium-based formulations: one representing shoreline rotation and another describing cross-shore sediment transport. These components are linked through a data assimilation scheme that integrates observed and projected shoreline data to keep the model on track with reality. In this configuration, the term hybrid refers not only to the combination of two distinct physical models, but also to the complementary use of calibration and assimilation, each compensating for the limitations of the other, to improve overall model performance.

The blind test context of ShoreShop 2.0 provides a unique opportunity to evaluate model performance under standardized conditions, independent of site-specific tuning and in line with the no a priori knowledge approach of Chapter 3. Results demonstrate that the coupled framework successfully reproduces multi-scale shoreline dynamics, showing strong predictive performance across both short- and medium-term timescales and ranking among the top-performing participants. Beyond its competitive outcome, this experiment underscores the value of integrating calibration and data assimilation within hybrid shoreline models to achieve greater stability, and reproducibility.

The results of the present chapter have been published in the peer review journal *Communications Earth & Environment*.

Mao, Y., Coco, G., Vitousek, S., Antolinez, J. A. A., Azorakos, G., Banno, M., Bouvier, C., Bryan, K. R., Cagigal, L., Calcraft, K., Castelle, B., Chen, X., D'Anna, M., de Freitas Pereira, L., de Santiago, I., Deshmukh, A. N., Dong, B., Elghandour, A., Gohari, A., de la Peña, E. G., Harley, M. D., Ibrahim, M., Idier, D., Cardona, C. J., Lim, C., Mingo, I., O'Grady, J., Pais, D.,

Repina, O., Robinet, A., Roelvink, D., Simmons, J., Sogut, E., Wilson, K. & Splinter, K. D. (2025). Benchmarking shoreline prediction models over multi-decadal timescales, *Communications Earth & Environment*, 6:581. https://doi.org/10.1038/s43247-025-02550-4

5.1 Introduction

Benchmarking model performance is central to model selection and to building confidence in predictions (Montaño et al., 2020; Repina et al., 2025; Mao et al., 2025). By enabling standardized and transparent comparisons of predictive accuracy, benchmarking highlights model strengths and limitations under consistent testing conditions (Repina et al., 2025). Although predictive skill is not the only consideration, since factors such as model complexity relative to scale, process representation, and data availability are also critical (Roelvink et al., 2016; Hunt et al., 2023), benchmarking provides an objective foundation for informed judgment. In shoreline modelling, the first dedicated benchmarking competition, ShoreShop, was held in 2018 (Montaño et al., 2020). ShoreShop demonstrated the value of benchmarking in fostering collaboration and provided the first unbiased assessment of shoreline model applicability to a wave-dominated beach.

The present chapter summarizes the hybrid modelling approach developed to participate in the international benchmarking competition ShoreShop 2.0 (Mao et al., 2025), which solicited model submissions from experts across the globe over a six-month period. The competition advanced the state-of-the-art assessment of shoreline models at a natural embayed beach (Figure 5.1) by testing their ability to incorporate spatio-temporal dynamics, leverage open-source datasets, and generate predictions across short-term (5-year) and medium-term (50-year) timescales via an open submission system on GitHub. A defining feature was its fully blind testing approach, as participants were not given the physical location of the study site. ShoreShop 2.0 demonstrated the applicability of shoreline models across diverse timescales, set a benchmark for inter-comparison, and promoted open science within the coastal research community. Results of the competition are reported in Mao et al. (2025), with all datasets and submissions publicly available on GitHub (https://github.com/ShoreShop).

5.2 Study site and data

The competition focused on Curl Curl Beach in New South Wales, Australia (Figure 5.1), which was presented to the participants as Beach X. The provided information, described an east-facing embayed sandy beach with median grain size of $D_{50} \approx 0.3$ mm, depth of closure of 11 m, and a slope of about 0.022 on the active beach profile. Nine shore-normal transects, spaced 100 m apart from north to south, were established to measure shoreline position. All coordinates were provided in a local system deliberately shifted but not distorted or rotated—and expressed in

easting (x) and northing (y) in meters.

For model calibration, participants were provided with 20 years of shoreline position data (1999–2018) shown in the calibration window of panel h in Figure 5.1, along with the shoreline position from 1951-05-01. Wave and sea-level data spanning 1940–2100 (panels d–g) were also supplied. Participants then submitted daily predictions of shoreline position at three time-scales, namely short-term (2019-01-01 to 2023-12-31), medium-term (1951-05-01 to 1998-12-31), and long-term (2019-01-01 to 2100-12-31). Predicted shoreline positions for all 9 transects had to be submitted, however model performance for the competition was evaluated on transects 2, 5 and 8 (see Figure 5.1).

Curl Curl Beach lies in a microtidal environment with a mean spring tidal range of $\sim$1.3 m (Turner et al., 2016b). The offshore wave climate in the Sydney region is characterized as moderate to high energy ($H_s \approx 1.6$ m, $T_p \approx 10$s) with pronounced seasonal and interannual variability. It is dominated by persistent long-period swell from the SSE and high-energy wind waves from the south (Figure 1, panel a) (Turner et al., 2016b). As waves propagate, shoaling and refraction modify their height and direction (Figure 1, panel c). At the 10-m depth contour near Curl Curl Beach, the mean H_s decreases to about 1.2 m (Figure 1, panel d), while refraction shifts the dominant wave approach to SE and ESE, averaging 114° and $\sim$85° relative to the shoreline (Figure 1, panel e).

Beyond cross-shore processes, Curl Curl also exhibits a strong rotational signal (Figure 5.1, panel g), a feature common among embayed beaches in New South Wales. This arises from the interaction of trapped longshore sediment transport within embayments and spatial variability in cross-shore processes (Harley et al., 2011, 2015).

5.3 Shoreline Variability

The shoreline variability of embayed beaches can be decomposed into three principal modes, namely cross-shore migration, beach rotation, and changes in beach planform (Jaramillo et al., 2021b). Cross-shore migration mostly reflects sediment transport along the beach profile driven by shore-normal wave energy (Yates et al., 2009b; Davidson et al., 2013). Beach rotation mostly arises from gradients in longshore sediment transport generated by obliquely incident waves relative to the beach orientation (Turki et al., 2013). Changes in beach curvature, often termed beach breathing, are controlled by variations in wave climate, headland–bay geometry (e.g., rock outcrops), and shifts between cross-shore and longshore transport regimes (Ratliff and Murray, 2014; Robinet et al., 2020). The relative influence of these three processes depends on local wave climate and position along the beach (Harley et al., 2011). Preliminary analysis of the provided shoreline transects indicated that rotation and cross-shore migration are the dominant modes in the present case, primarily driven by variation in incoming wave direction and energy.

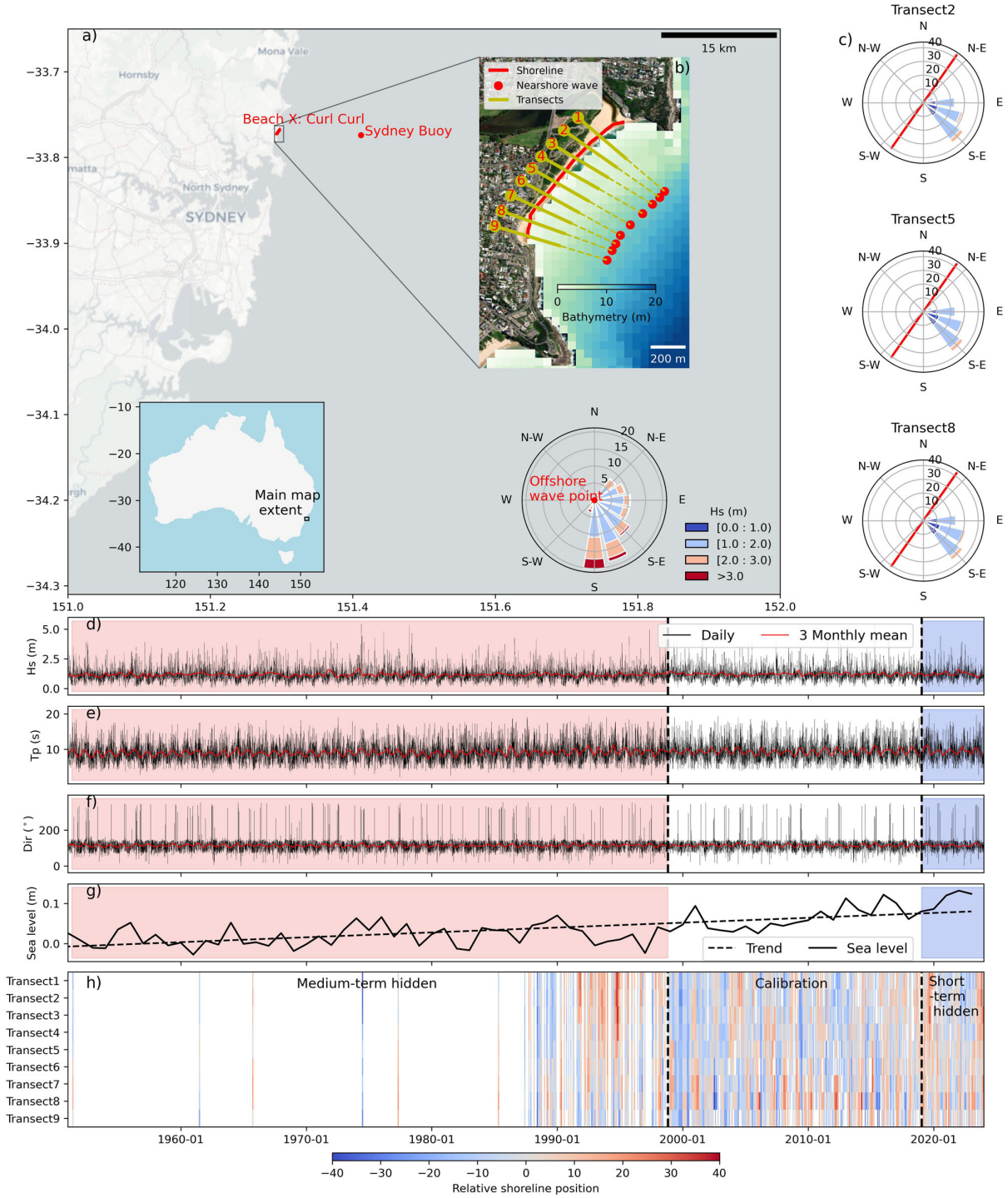

Figure 5.1: Study site and input data. (a) Location of BeachX. Inset wave rose shows the location and distribution of offshore waves from ERA5. (b) Detailed map of BeachX (Curl Curl Beach, New South Wales, Australia). The color gradient at the seaside indicates bathymetry. Yellow lines represent transects. Red dots show the location of nearshore waves. (c) Nearshore (depth = 10 m) wave roses for transects 2, 5 and 8. The red solid line represents the mean beach orientation. (d) Significant wave height H_s, (e) peak wave period T_p, (f) mean wave direction Dir, (g) annual mean sea level and its trend. (h) Spatio-temporal distribution of relative (de-meaned) shoreline position (blue/negative values indicating erosion and red/positive values indicating accretion). Basemaps: CartoDB Positron (©OpenStreetMap contributors) in panel a; Esri World Imagery (© Esri — Source: Esri, i-cubed, USDA, USGS, AEX, GeoEye, Getmapping, Aerogrid, IGN, IGP, UPR-EGP and the GIS User Community) in panel b. Basemap tiles are accessed via the Contextily Python package. The figure is borrowed from Mao et al. (2025)

To investigate the influence of the two dominant modes of shoreline evolution, a beach rotation analysis was undertaken. Shoreline observations at each transect over the calibration period are shown in Figure 5.2 (red points). The spatial variability in shoreline position indicates a rotational response with a pivot located near transect 3. Shoreline orientation (α_s) was quantified following the methodology of Turki et al. (2013) and Harley et al. (2015). At each observation time step, a linear regression was fitted to the shoreline positions. The dashed line in Figure 5.2 represents the regression at the initial observation. Orientation was then defined as the angle between the shore-normal to the regression line (red line in Figure 5.2) and geographic north.

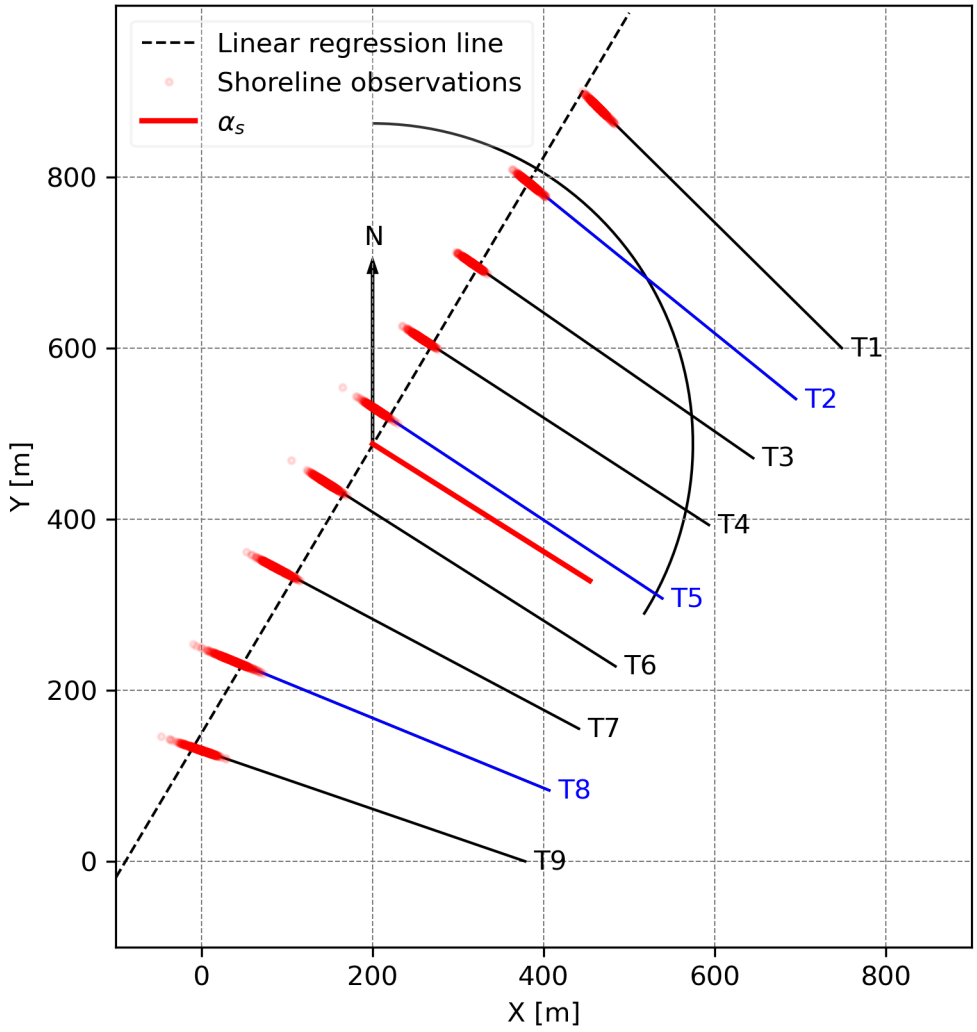

Figure 5.2: Shoreline transects T1 to T9 with the target transects plotted in blue. Shoreline observation are plotted as red points and a linear regression of the initial shoreline position at each transect is plotted as a dashed line. The red line indicates the orientation of the beach α_s relative to the north.

For each observation, the beach orientation index (BOI) was calculated using Equation 5.1 and is shown in the upper panel of Figure 5.3. The BOI is a widely used metric that describes beach orientation relative to its long-term average, with positive values indicating clockwise rotation (Harley et al., 2011; Jaramillo et al., 2021a; Abdulsalam et al., 2025). The lower panel of Figure

5.3 presents daily significant wave heights (points) and their mean values (black line), extracted from ERA5 at the offshore location of transect 2. Point colours represent the direction of incoming waves relative to north.

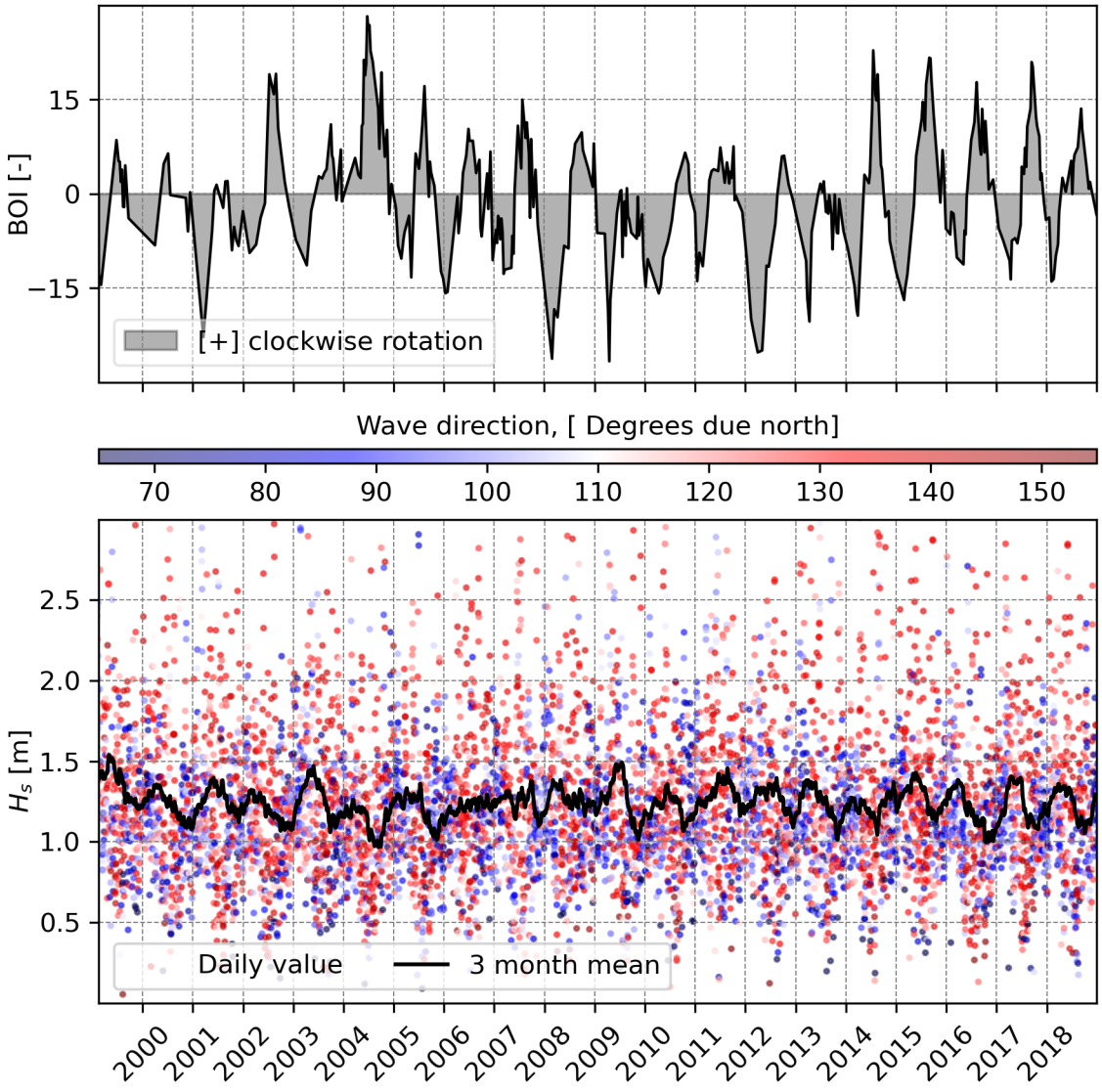

Figure 5.3: Upper panel: Beach orientation index (BOI) calculated using Equation 5.1. Lower panel: Significant wave height and direction plotted in colour of the incoming waves extracted at the offshore point of transect 2.

$$BOI = 10\frac{\alpha_s(t) - \overline{\alpha_s(t)}}{\sigma(\alpha_s(t))} \tag{5.1}$$

Where $\alpha_s(t)$ is the orientation of the shoreline at time t, $\overline{\alpha_s(t)}$ is the mean shoreline orientation and $\sigma(\alpha_s(t))$ is the standard deviation of the temporal variation in shoreline orientation.

5.4 Hybrid shoreline model

The natural variability of many beach parameters can be explored using simple equilibrium shoreline evolution models. Shoreline response to storms as well as seasonal and interannual fluctuations in wave conditions, can be modelled as perturbations around a static equilibrium. Changes in sea level and wave climate taking place over longer timescales, and tend to shift the response of beach systems around a dynamic equilibrium (Hunt et al., 2023). Conceptually, equilibrium models assume that shoreline parameters, mirror changes in antecedent wave conditions and environmental forcing. The adopted methodology assumes that total shoreline variability can be decomposed into two independent components, namely cross-shore translation of the profile and rotation associated with alongshore variations in beach planform. Rotation is thus treated as independent of cross-shore migration and beach breathing. The influence of varying water level shown in panel g of Figure 5.1 is not explicitly accounted for. Beach rotation is typically assumed to depend primarily on the power and directionality of incident waves (Jaramillo et al., 2021a). Equilibrium shoreline models, simulate cross shore erosion and accretion as mirroring the weighted moving average of the incoming wave timeseries (Vitousek et al., 2025).

For the purpose of ShoreShop 2.0 and based on a preliminary analysis of shoreline change at beach X to explore the expected drivers, I combined two cross-shore and rotation equilibrium shoreline models to simulate shoreline change at each transect. Beach rotation was modelled using the equilibrium-based approach of Jaramillo et al. (2021a) presented in Section 2.5.1, with cross-shore translation due to rotation estimated by calibrating the best-fit pivot arm for each transect. This calibrated rotational component was subtracted from each transect, with the residual change attributed to cross-shore sediment transport. Wave driven cross-shore erosion and accretion of the profile was simulated by the equilibrium model of Davidson et al. (2013) described in Section 2.5.1. Finally, the contributions of both components were calibrated and combined as a weighted sum, forming the final shoreline predictions submitted in Shoreshop 2.0 competition. A stepwise illustration of the adopted modelling approach is illustrated in Figure 5.4 using the middle transect 5 as an example.

5.4.1 Equilibrium based shoreline rotation model

The rate of beach rotation change $d\alpha_s/dt$ (degrees/s) is calculated based on the Jaramillo et al. (2021a) model. The rotation of the beach was translated into evolution of shoreline position at each transect by the following equation:

$$S_R(t) = f_T(\cos\alpha_s(t) - \overline{\cos\alpha_s(t)}) \tag{5.2}$$

where f_T (m) denotes the pivot arm at a given transect, calibrated independently for each transect.

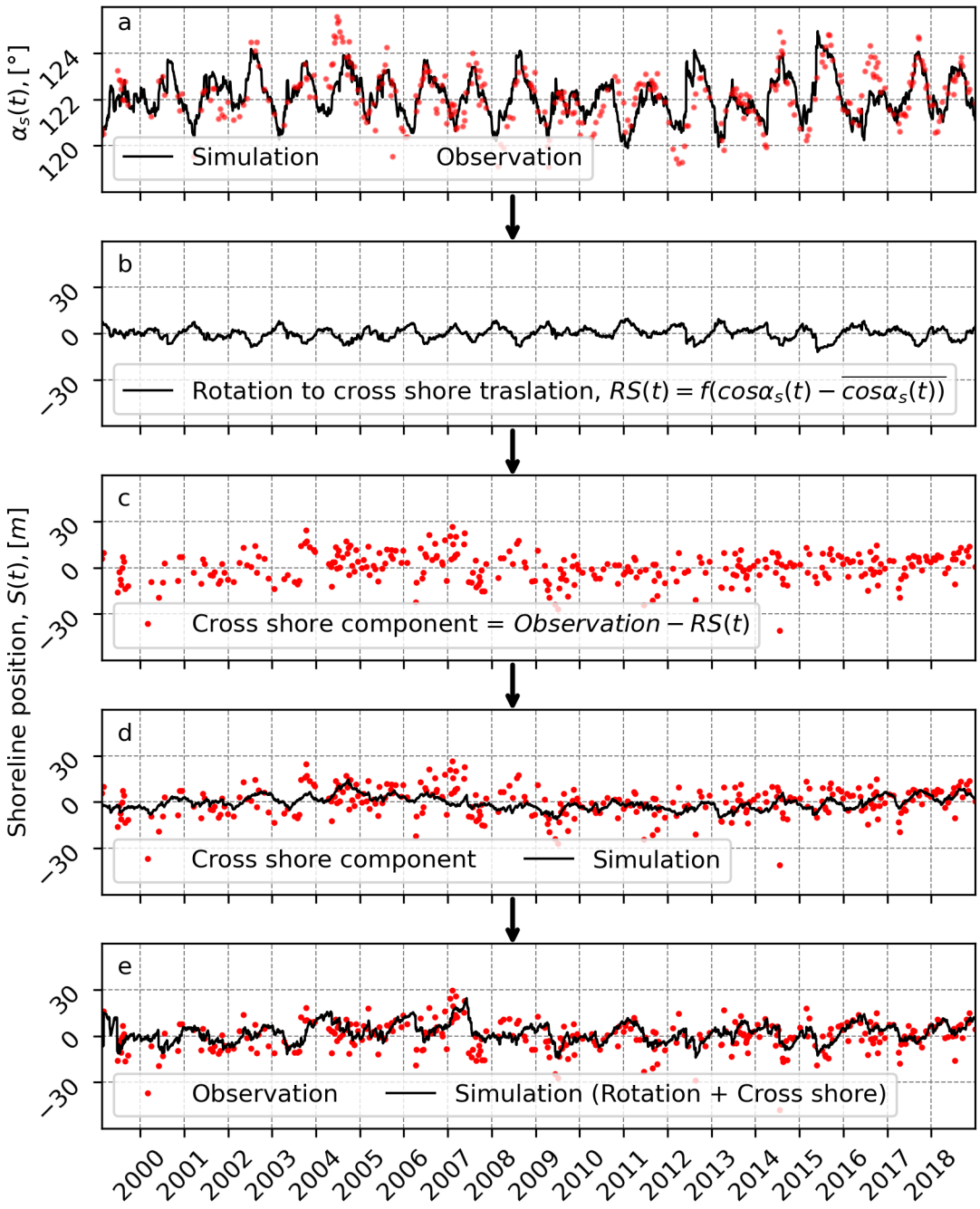

Figure 5.4: Panel a, observed and simulated beach rotation. Panel b, cross shoreline evolution of the profile due to beach rotation. Panel c, d cross shore component of shoreline evolution after modelled rotation influence has been subtracted. Panel e, observed and simulated shoreline evolution accounting for both rotation of the beach and cross shore sediment transport.

5.4.2 Equilibrium based cross shore transport model

The calibrated rotation component obtained from Equation 5.2, has been subtracted from the shoreline observation at each transect. The residual component was used to calibrate the equilibrium cross-shore transport model proposed by Davidson et al. (2013).

5.4.3 Model calibration

For model calibration and quantitative comparison, the Loss function, Equation 4.2, described in section 4.2.3 was used as this was defined as the official metric of the ShoreShop 2.0 competition.

Best-fit stationary model free parameters have been calibrated over the 20 year period using a simulated annealing non-linear optimization algorithm (Bertsimas and Tsitsiklis, 1993). A total of 10^6 iterations were performed to minimize the loss function Equation 4.2. The timeseries of the simulated shoreline positions at all three target transects during the calibration period (1999 - 2018) are depicted in Figure 5.5 together with the shoreline observations used for calibration. The value of the loss function calculated by Equation 4.2 at each transect is indicated in the legend of the figure. The calibrated model was then deployed to hindcast the position of the shoreline at all nine transects between 1951 and 2023, and complete the tasks of the ShoreShop 2.0 competition.

5.4.4 Model guidance through data assimilation

The calibrated model produced reliable predictions for the short-term (1999–2023) and medium-term (1979–1990) periods (black dashed line in Figure 5.6). However, predictions prior to 1979 exhibited a pronounced and unrealistic divergence from observed shoreline trends. To address this, a data assimilation approach was implemented to guide the model using trends derived from the calibration period. A synthetic dataset of biannual shoreline observations (1951–1999) was generated based on the calculated shoreline trend, and the dual state–parameter ensemble Kalman filter algorithm of Ibaceta et al. (2020) was applied to maintain model stability.

The data assimilation algorithm of Ibaceta et al. (2020), calculates a model ensemble of N members by slightly inflating model parameters at every timestep it encounters an observation. If the standard deviation of the ensemble (grey area in Figure 5.6) is larger than the uncertainty of the observation, then the algorithm favours the observed instead of the simulated value. The data assimilation algorithm was deployed based on the calibrated model allowing, for small variability in model free parameters, to ensure stability. A large error of R = 120 m was assigned to the synthetic datasets, corresponding to an order of magnitude greater than the standard deviation of the observed shoreline positions in the calibrated period. The magnitude of the assigned error can be interpreted as the level of freedom assigned to the model. The guided model submitted to the modelling competition was calculated as the mean of an ensemble with N = 500 members at each transect separately. An example of the guided model application at transect 2 is shown as a blue solid line in Figure 5.6.

The performance metrics, including normalized centred root mean squared error CRMSE (bias excluded), correlation coefficient and normalized standard deviation, of the submitted shoreline

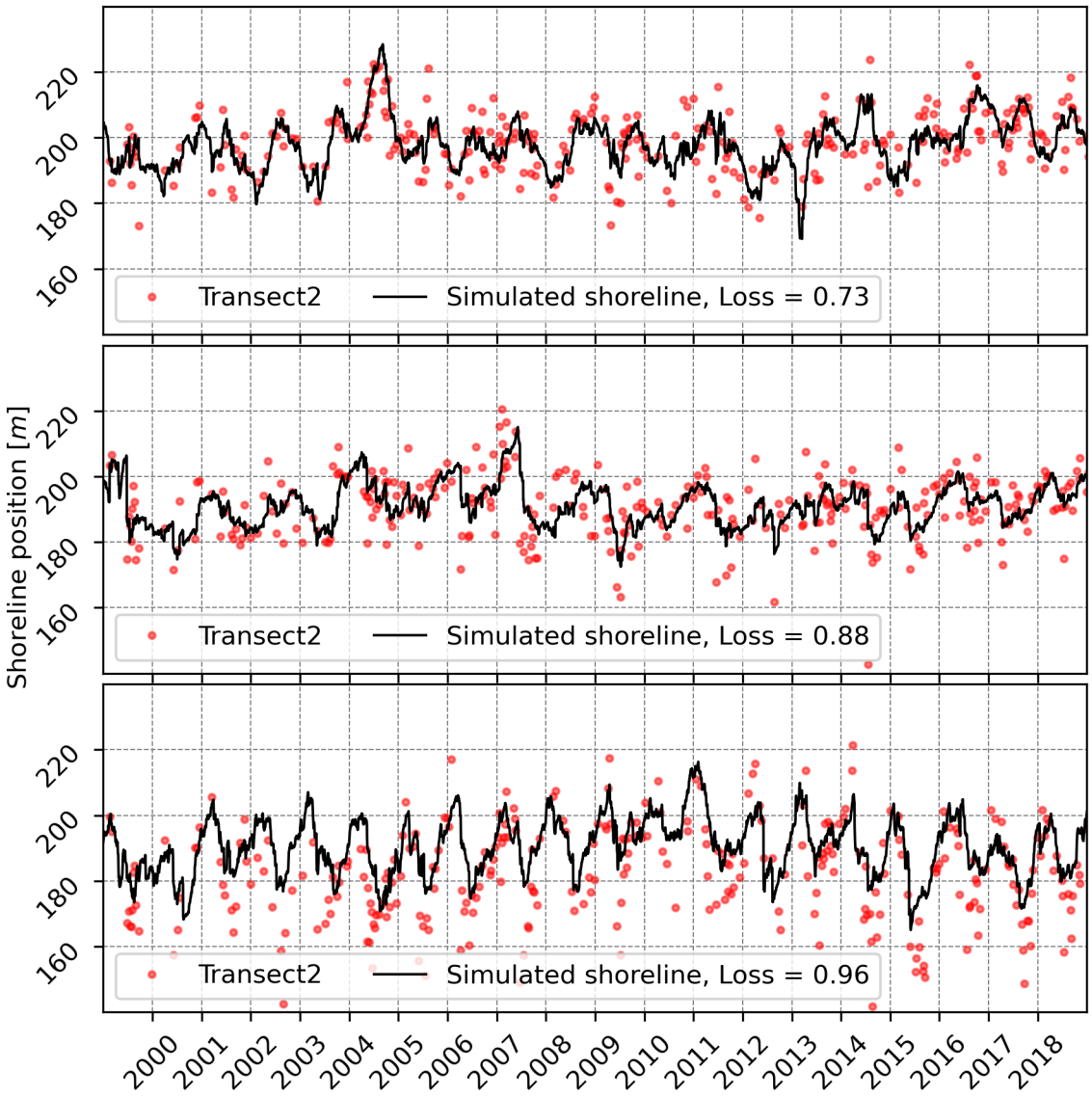

Figure 5.5: Observed (red dots) and simulated (black line) shoreline position timeseries during the calibration period for all three target transects. The value of the loss function for the calibrated models, is indicated in the legend.

predictions to Shoreshop 2.0 are summarized in Figure 5.7. Each of the target transects is plotted in a different colour, while the calibration period, short term, and medium term post, and pre 1986 predictions are illustrated as stars, circles, squares and diamonds respectively. The average loss across all target transects served as the final metric for ranking the model performance and is shown in the legend of Figure 5.7. Please note that due to the difference between CRMSE and RMSE, the Loss is indicative of, but not identical to, the distance between the model points and the target point (the black triangle) in the Taylor diagram (Figure 5.7).

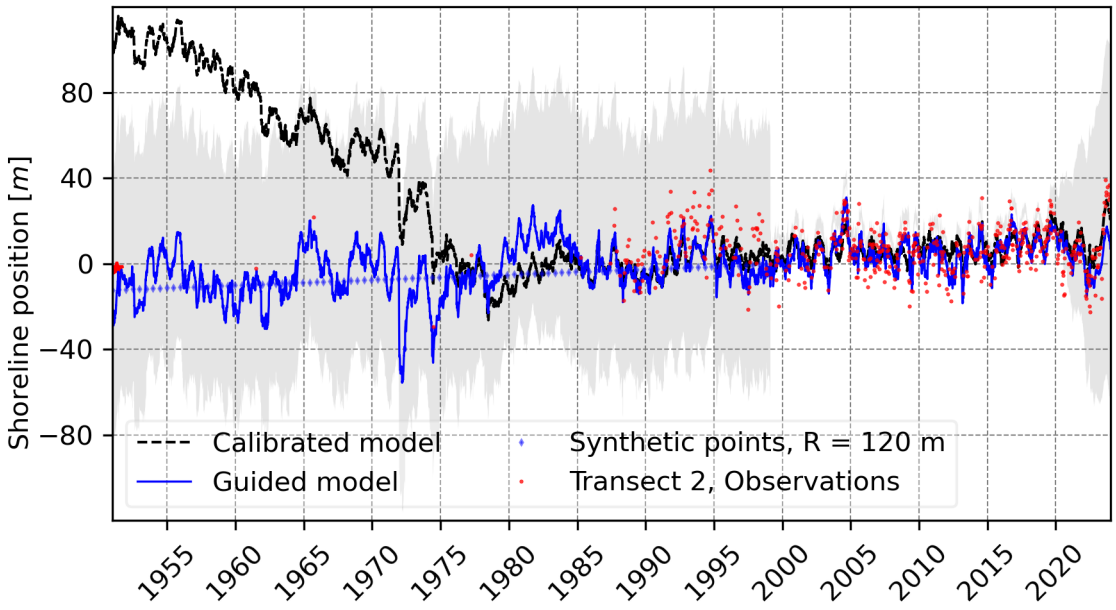

Figure 5.6: Shoreline observations (red dots) and predictions for the entire period (calibration and hindcast) obtained by the calibrated (black dashed line) and guided model (blue solid line) at transect 2. Synthetic shoreline positions used to guide the model are also depicted.

5.5 Discussion

Coupling shoreline models has become a widely used approach, allowing multiple processes and environmental drivers of shoreline change to be represented within a single framework (Vitousek et al., 2017; Robinet et al., 2018; Antolínez et al., 2019). In the present work a model application is developed, accounting for the combined effect of beach rotation and cross-shore sediment transport along the beach profile, aiming to hindcast alongshore variable shoreline change across 9 transects at an undisclosed east-facing embayed beach. Linear decomposition of the shoreline signal proved to be a valid assumption as the influence of the two components driving shoreline change and their alongshore variability were calibrated independently and combined to produce shoreline predictions extending from 1950 to 2023. Excluding medium term predictions for transect 5 prior to 1986, the adopted hybrid modelling approach managed to produce shoreline observations within the accuracy of the observations and ranked at the top one third of model submissions.

Shoreshop 2.0 solicited 41 different submissions of shoreline predictions, the majority of which managed to compare quite well with the observations, producing a relatively narrow ensemble (Mao et al., 2025). Modelling applications that used a ShoreFor (Davidson et al., 2013; Splinter et al., 2014) type model to simulate the cross shore sediment transport component yielded large, unrealistic shoreline trends prior to ≈1979. ShoreFor based models, tend to exhibit larger fluctuations of the shoreline position compared to other cross-shore sediment transport equilibrium based shoreline models such as Yates et al. (2009b) (Davidson et al., 2013; Splinter et al., 2014). ShoreFor type models are shoreline position independent, allowing them to completely mirror the

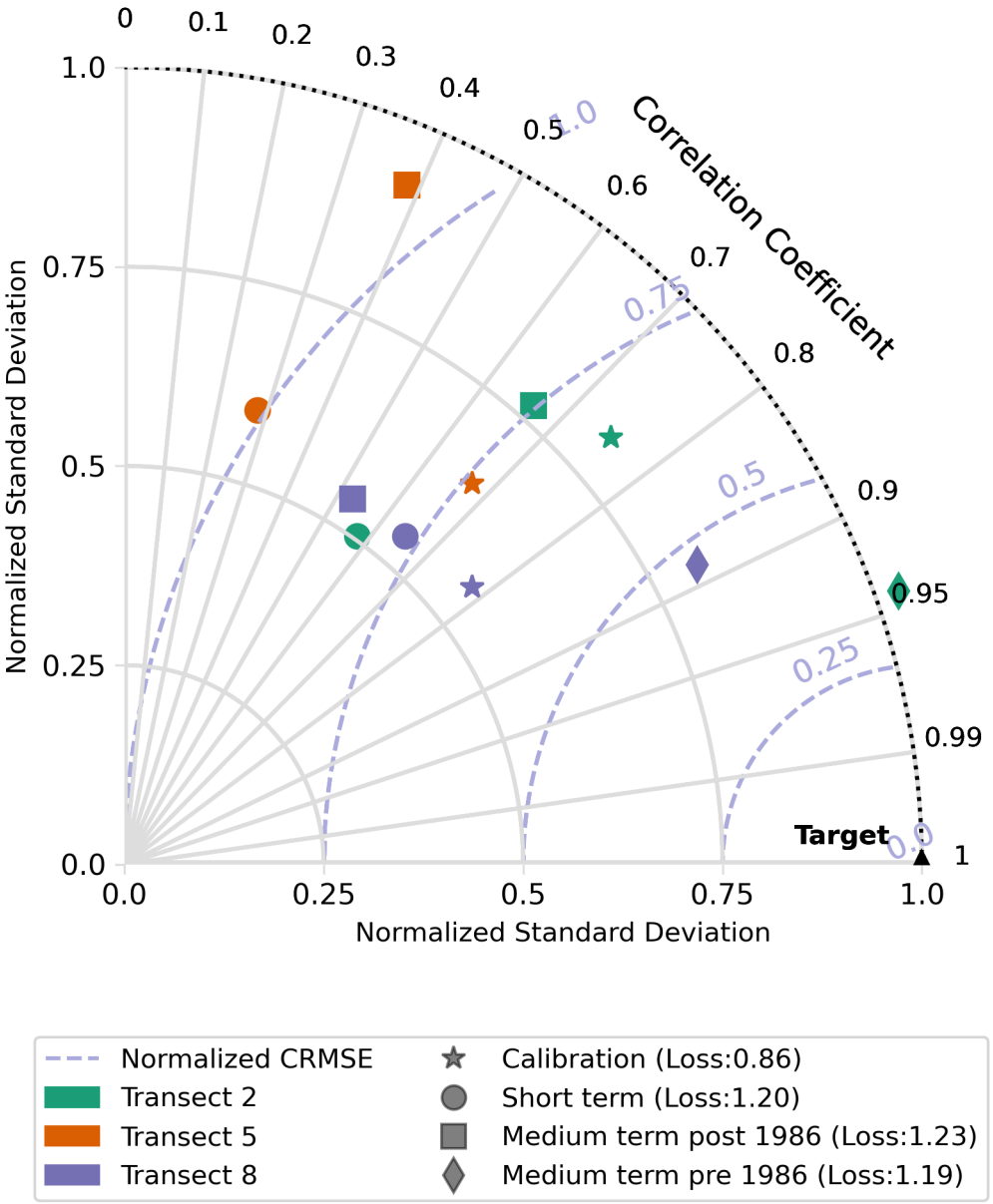

Figure 5.7: Taylor diagram for all transects and timescales. The figure shows the normalized standard deviation (radial - x and y-axis), correlation coefficient (curved axes along the circumference of the circle), and normalized centred root mean square error (CRMSE, concentric dashed arcs). Stars, circles, squares and diamonds represent the different timescales and periods, calibration, short term, medium term post and pre 1986 respectively. The black triangle (Target) shows the observed data in a Taylor diagram with zero error. The model performance is indicated by the distance of scatter points of model predictions to the observed. The average Loss of the three transects calculated by Equation 4.2 is displayed in the legend for all timescales.

weighted average of the antecedent wave conditions without any spatial restriction, making them particularly sensitive to changes in the wave conditions (Davidson et al., 2013; Splinter et al., 2014; Ibaceta et al., 2022). Vitousek et al. (2025) suggested that equilibrium shoreline models are mathematically equivalent to discrete convolutions. Thus, for an equilibrium shoreline model to produce a shoreline trend, a trend has to exist in the forcing as well. As the hindcast wave data uses different observations for data assimilation pre and post 1979 (Hersbach et al., 2020; Bell et al., 2021), the wave climate changes slightly around 1979. This minor change in the distribution of waves is suspected to lead to the large long-term divergence of the ShoreFor-based models.

The ensemble Kalman filter data assimilation algorithm, developed by Ibaceta et al. (2020) to track temporal variability in model free parameters, was successfully implemented to apply a spatial restriction to a shoreline position independent model. The data assimilation algorithm restricted the model within a specified standard deviation from the projected shoreline position. Splinter et al. (2017) and Ibaceta et al. (2020) demonstrated that medium term shoreline change simulations on beaches exposed to multimodal wave climate can benefit from non-stationary model free parameters. Equilibrium shoreline models can yield erroneous predictions of shoreline evolution for a number of reasons, like cascading errors stemming from erroneous boundary conditions and forcing, and incomplete description of the system (Hunt et al., 2023). Exploring non-stationarity in model free parameters and ensemble methods to account for the uncertainties in the modelling process is a very promising tool in shoreline change modelling (D'Anna et al., 2020, 2021, 2022; Ibaceta et al., 2022). A sequential data assimilation approach introducing non-stationary model free parameters, based on projected shoreline positions, effectively compensated for model errors, primarily arising from inaccuracies in the wave forcing (Bell et al., 2021).

Chapter 6

2D Satellite-derived data assimilation in LX-Shore model. Investigation on the Sacalin spit, in The Danube Delta.

Expanding upon the hybrid and assimilation frameworks developed in Chapters 4 and 5, this chapter introduces a quasi-two-dimensional (2D) implementation of data assimilation within the LX-Shore model (Robinet et al., 2018). The objective is to move beyond alongshore-averaged representations toward a grid-based formulation that integrates spatially distributed satellite observations. The method applies a spatial nudging scheme to assimilate land–water classifications directly derived from optical satellite imagery, enabling the model to reproduce observed shoreline dynamics across a 2D grid.

The application focuses on the Sacalin Spit, a highly dynamic system in the southern Danube Delta where multiple interacting processes—fluvial inputs, overwash, and barrier migration—challenge traditional one-dimensional modelling. The site was intentionally selected as a test case despite the known limitations of LX-Shore in representing such complex processes, providing a rigorous environment for evaluating the capacity of data assimilation to compensate for missing dynamics. This work was conducted within the collaborative framework of the SHORMOSAT consortium, fostering exchange between complementary expertise in modelling and Earth observation.

The results show that even within this simplified morphodynamic configuration, the assimilation scheme effectively constrains model evolution and compensates for unrepresented processes. This chapter therefore represents a key step toward fully two-dimensional, observation-driven shoreline modelling frameworks capable of exploiting the increasing availability of global satellite archives. The broader implications and prospective developments emerging from this progression are discussed in Chapter 7.

The work presented in this chapter will be submitted to a peer reviewed journal for publication.

6.1 Introduction

Data assimilation techniques are particularly well suited for morphological simulations, where numerous tunable parameters and empirical coefficients require calibration. Existing models inevitably neglect certain physical processes, either by design in reduced-complexity or data-driven approaches, or due to incomplete initial and boundary conditions in physics-based models, limiting their ability to reproduce shoreline dynamics with the fidelity of direct observations (Hunt et al., 2023; Vitousek et al., 2023a). By systematically integrating observations into model simulations, data assimilation enhances predictive skill and enables models to better capture real-world dynamics (Vitousek et al., 2023a).

Hybrid modelling frameworks, which combine multiple reduced-complexity or semi-empirical approaches, allow interactions between different drivers of shoreline change while maintaining computational efficiency (Vitousek et al., 2017; Robinet et al., 2018; Antolínez et al., 2019; Alvarez-Cuesta et al., 2021a; de Santiago et al., 2021; Jaramillo et al., 2021b). These frameworks provide a natural platform for data assimilation, enabling dynamic calibration, tracking of system non-stationarity, and improved predictive skill across coupled processes. To date, most applications have relied on sequential approaches such as Kalman filters (e.g., Kalman, 1960; Evensen, 2009), often implemented in transect-based models to implicitly account for processes missing from the model architecture. Early examples include Long and Plant (2012), who coupled an extended Kalman filter with a cross-shore model, and Vitousek et al. (2017), who assimilated low-frequency LiDAR observations in the CoSMoS-COAST hybrid model using an ensemble Kalman filter. More recent studies have applied EnKF methods to video- and satellite-derived shorelines, quantifying prediction uncertainties and tracking temporal variability in model parameters (Ibaceta et al., 2020, 2022; Alvarez-Cuesta et al., 2021a; Vitousek et al., 2021, 2023b).

Assimilating gridded land–water data provides a key advantage as it represents the coastal system natively, without the intermediate processing steps required for extracting satellite-derived shorelines, each of which introduces additional uncertainty. The 2D, grid-based architecture of the LX-Shore model (Robinet et al., 2018) allows for the direct integration of satellite-derived observations into the model framework, establishing a seamless satellite-to-model workflow. This configuration leverages LX-Shore's capacity to represent complex coastal geometries and shoreline instabilities that transect-based models cannot, while also supporting spatially distributed data assimilation. The approach facilitates quantifying model errors in space and time, and ultimately improving understanding of regional-scale coastal morphodynamics.

This study focuses on the Sacalin Spit, situated on the southern lobe of the Danube Delta along the Black Sea coast. The site was selected as a challenging test case where key morphodynamic processes—such as overwash, breaching, and barrier migration—are not explicitly represented in the model structure, offering an opportunity to evaluate the added value of the data assimilation framework. Its inclusion also stems from the collaborative efforts within the SHORMOSAT

consortium, which aims to advance satellite-based coastal monitoring and modelling. A 40-year dataset of publicly available satellite imagery, cropped and downloaded from the Sentinel-2 and Landsat collections via Google Earth Engine (Gorelick et al., 2017), was used to investigate the long-term morphological evolution of the area. By relying exclusively on satellite-derived observations, this work establishes a fully two-dimensional assessment and numerical modelling framework that integrates these data directly into a grid-based model. The study serves as a proof of concept for two-dimensional data assimilation within the cell-based LX-Shore model, demonstrating how satellite observations can constrain model evolution and quantify model errors in space and time.

The developed methodology including the data assimilation approach, data curation and model are presented in detail in Section 6.2, while the study site, data used and model setup are detailed in Section 6.3. Finally the results of the data assimilation simulation are presented in Section 6.4, followed by a detailed discussion in Section 6.5. Finally the main conclusions of the present work are summarized in Section 6.6.

6.2 Methodology

The cell-based structure of LX-Shore naturally supports the direct integration of satellite-derived gridded data with minimal preprocessing, as both share a compatible spatial architecture. In most cases, only local reprojection and, where necessary, resampling are required to match the model resolution. A semi-automated satellite-to-model workflow, described in Section 6.2.1, was developed to generate initial conditions for LX-Shore simulations.

Multi-band satellite images were converted into binary land–water grids consistent with the LX-Shore format, then locally reprojected and downsampled to the model resolution. These processed observations were subsequently assimilated into LX-Shore to constrain model evolution and compensate for processes not explicitly resolved within the model formulation.

The proposed satellite-to-model workflow reduces subjectivity in shoreline definition, ensures temporal consistency across long-term datasets, and enables complex morphologies—such as spits and lagoons—to be more faithfully represented during model initialization. By facilitating the direct assimilation of satellite-derived observations, it strengthens the connection between Earth observation and process-based coastal morphodynamic modelling.

6.2.1 Satellite derived sediment fraction grid

The proposed satellite-to-model workflow is designed to leverage publicly available satellite imagery from the Landsat and Sentinel missions, which offer spatial resolutions of 30 m and

10 m, respectively. These datasets can be efficiently cropped to the area and spectral bands of interest and downloaded directly from Google Earth Engine (Gorelick et al., 2017). Together, they provide a continuous temporal record of coastal evolution spanning from 1984 to the present, offering a valuable long-term observational archive for model initialization, calibration, and data assimilation.

The developed workflow builds upon the CoastSat shoreline extraction algorithm (Vos et al., 2019b) to automate the identification, cropping, and downloading of satellite frames over the study area. Images are filtered according to user-defined thresholds for georeferencing error and cloud coverage, ensuring that only high-quality scenes are retained. The selected frames then undergo manual quality control to exclude images unsuitable for analysis (e.g., those affected by extensive cloud cover or sensor noise).

Following quality control, the retained images are processed automatically following the workflow illustrated in Figure 6.1, resulting in a binary grid of land and water cells with a smoothed land–water interface for each acquisition date.

The multiband satellite images consist of red (R), green (G), blue (B) and short wave infrared (SWIR) bands. An example image is plotted in panel a of Figure 6.1. As a first processing step, the modified normalized difference water index (MNDWI) was applied to each of the images calculated based on Xu (2006) as:

$$MNDWI = \frac{SWIR - G}{SWIR + G} \tag{6.1}$$

where SWIR and G are the pixel intensities in the short-wave infrared and green bands, respectively, the MNDWI values plotted in panel b of Figure 6.1 range between –1 and 1, corresponding to water and land, respectively. A histogram of MNDWI values is then constructed using all labelled pixels within the image. In this histogram, the probability density functions (PDFs) and the MNDWI values for land and water pixels are depicted, typically centred around positive and negative values, respectively. The land–water threshold is subsequently computed by applying a minimum thresholding algorithm that identifies the MNDWI value maximizing inter-class variance between the land and water distributions, as illustrated in the right panel of Figure 6.1. This procedure produces a binary segmented image of land and water pixels (panel c, Figure 6.1).

Finally, a dilation–erosion morphological filtering operation was applied to smooth the land–water interface and mitigate noise in the satellite imagery caused by shallow water areas and features like coastal vegetation. Dilation and erosion are fundamental image-processing techniques that respectively expand or contract image regions based on a defined structuring element, allowing for effective noise reduction, feature enhancement, and shape regularization (Soille, 2004). In the context of coastal satellite imagery, the application of dilation–erosion filtering helps incorporate small island- and lagoon-like features into the surrounding environment, producing a cleaner and more coherent land–water mask. This step also facilitates consistent rescaling of the satellite-derived

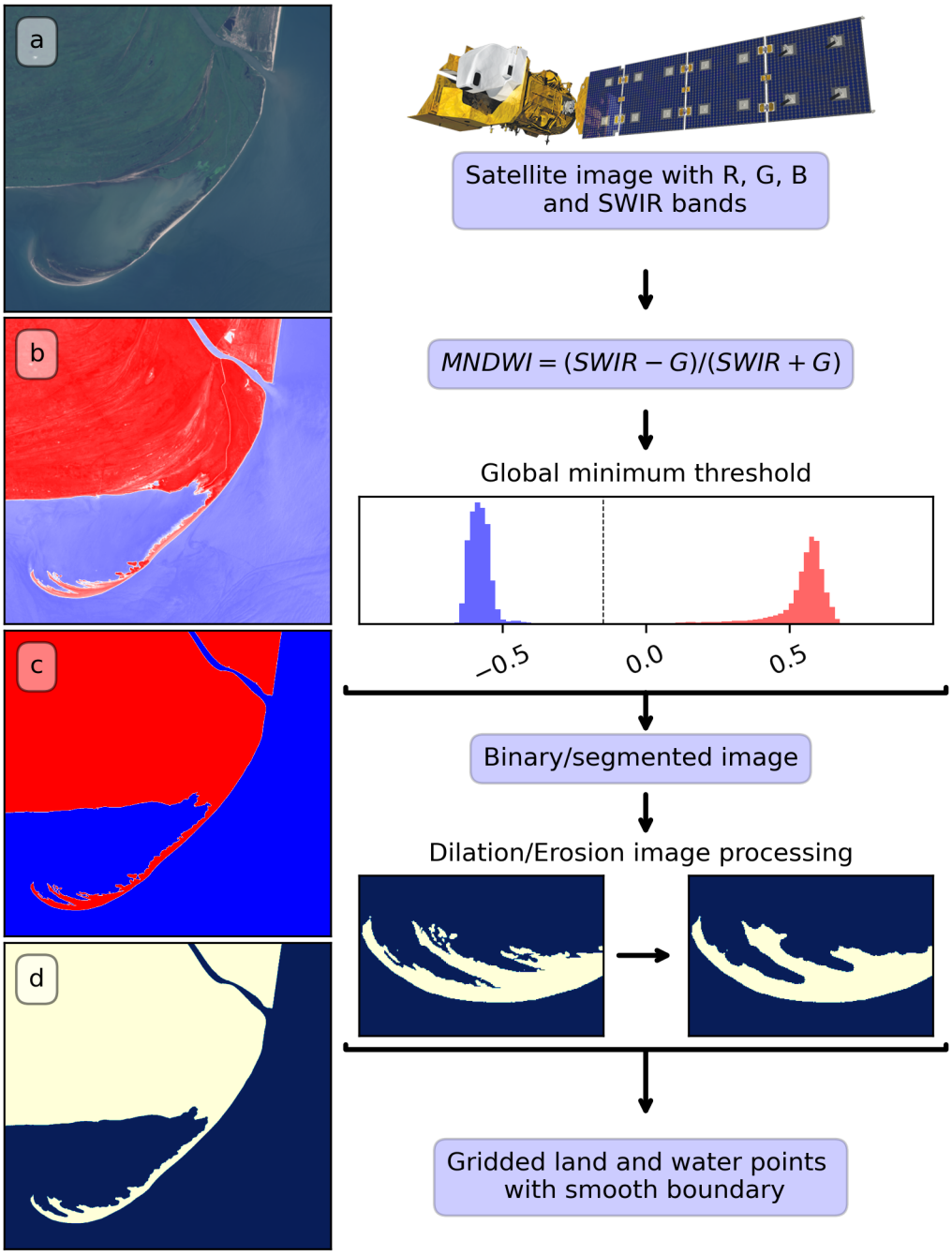

Figure 6.1: Panel a, Satellite image including R, G, B and SWIR bands cropped and downloaded from Google Eart Engine (Gorelick et al., 2017). Panel b, calculated MNDWI index from the multi band satellite image. Panel c, binary segmented image of land and water regions. Panel d, Grid of land and water points with a smoothed interface. The right column of the figure illustrates the workflow followed to transform the satellite images to gridded data with a smooth land-water interface.

grid to match the model resolution, ensuring a smooth integration into the LX-Shore framework. The resulting dataset is natively compatible with the LX-Shore grid structure and suitable for direct assimilation into the model framework.

6.2.2 LX-Shore model

The reduced-complexity LX-Shore model developed by Robinet et al. (2018) is a cellular-based one-line model that represents the active coastal zone through fractional sediment values (F) ranging from 0 to 1, where $F = 0$ denotes fully submerged (water) cells and $F = 1$ indicates fully emerged (land or subaerial beach) cells. At each time step, the fractional sediment content of shoreline cells is updated according to the net sediment flux into or out of each cell, while non-erodible cells can also be specified. This cellular representation facilitates the simulation of longshore-transport–driven shoreline dynamics in complex morphologies, such as spits, barrier islands, and enclosed lagoons. A schematic overview of the LX-Shore model and the integrated processes is presented in Figure 6.2. For sediment flux calculations, LX-Shore integrates the longshore transport formulation of Kamphuis (1991) with the cross-shore transport model of Davidson et al. (2013). The resulting framework dynamically couples shoreline change with the nearshore wave field, which can be provided either by coupling with a spectral wave model (Booij et al., 1999) or estimated using the formulation of Larson et al. (2010). The Larson et al. (2010) formula is complimented by the shadowing procedure described in Ashton and Murray (2006), whereby no sediment transport or wave computations are performed in areas shielded from incoming wave energy (shadow zones).

Originally LX- Shore as proposed by Robinet et al. (2018), is initialized by defining a shoreline and a grid, from which the 2D grid of cells containing the fractional sediment value F is constructed. In the present work, a modified initialization approach was adopted, to facilitate the assimilation of the satellite derived sediment fraction grids obtained by the workflow described in Section 6.2.1 into the model framework using a hotstart functionality to skip the initialization step and directly read the sediment fraction matrix F. A schematic representation of the model architecture is illustrated in Figure 6.3 while a full description and validation of the model can be found in Robinet et al. (2018).

The model bathymetry, is defined by projecting the shoreline over the hydrodynamic grid using a beach profile following a power law, similar to the equilibrium profile defined by Dean (1991),

$$depth = \alpha d_{SL}^{\beta} \tag{6.2}$$

where d_{SL} is the shore normal distance to the shoreline, and α and β are profile shape parameters that can be defined as model inputs.

The longshore sediment transport component can be estimated using the empirical formulations proposed by USACE (1984) or Kamphuis (1991). A sensitivity analysis indicates that the latter yields longshore sediment transport rates approximately twice as large. Accordingly, the

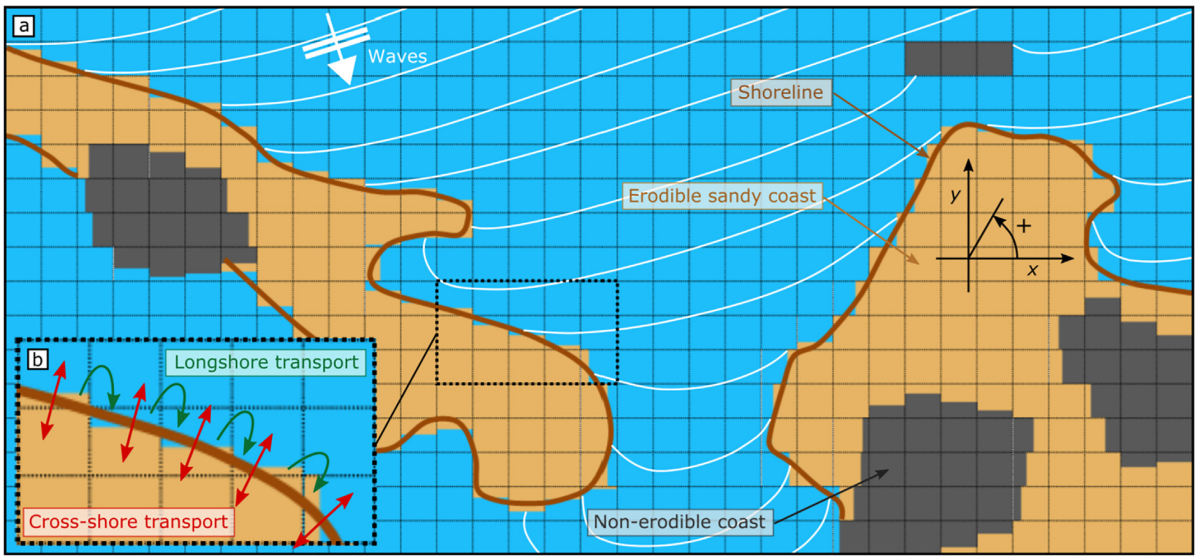

Figure 6.2: Overview of the features and processes integrated in the LX-Shore model. Panel a, example of a plan-view coastal area used in the model. Panel b, example of the longshore and cross-shore sediment transports rate calculations. Figure is borrowed from Robinet et al. (2018).

formulation of Kamphuis (1991) has been adopted in this work.

$$Q_l = QF \times \frac{2.27 H_{s,b}^2 T_p^{1.5} m_b^{0.75} d_{50}^{-0.25}}{(\rho_s - \rho)(1-p)} \sin^{0.6}(2\theta_b) \tag{6.3}$$

where $H_{s,b}$ is the significant wave height at breaking, θ_b is the incident wave direction relative to the beach, at breaking, and T_p is the peak wave period. m_b is the slope of the beach, d_{50} is the median grain diameter of the sediment on the beach, while ρ_s and ρ are the density of sediment and water respectively, and p is the bed porosity. The QF parameter in front of Equation 6.3, is the only free parameter in the model and acts as a constant scaling factor for the computed littoral drift. The USACE (1984) formula can alo be ued to calculate the longhore ediement tranport

The model developed by Davidson et al. (2013) used to calculate the cross shore sediment transport component is described in Section 2.5.1.

6.2.3 Data assimilation method

Data assimilation was implemented by periodically updating the modelled grid of fractional sediment values (F) with satellite-derived datasets. The assimilation frequency was determined by the temporal availability of quality-controlled satellite imagery, while a relaxation parameter governed the magnitude of the imposed correction to ensure physically consistent shoreline evolution.

The matrices of satellite-derived and simulated sediment fractions, denoted $\mathbf{F}_{\text{sat}}$ and $\mathbf{F}_{\text{sim}}$ respectively, were combined at each assimilation step as

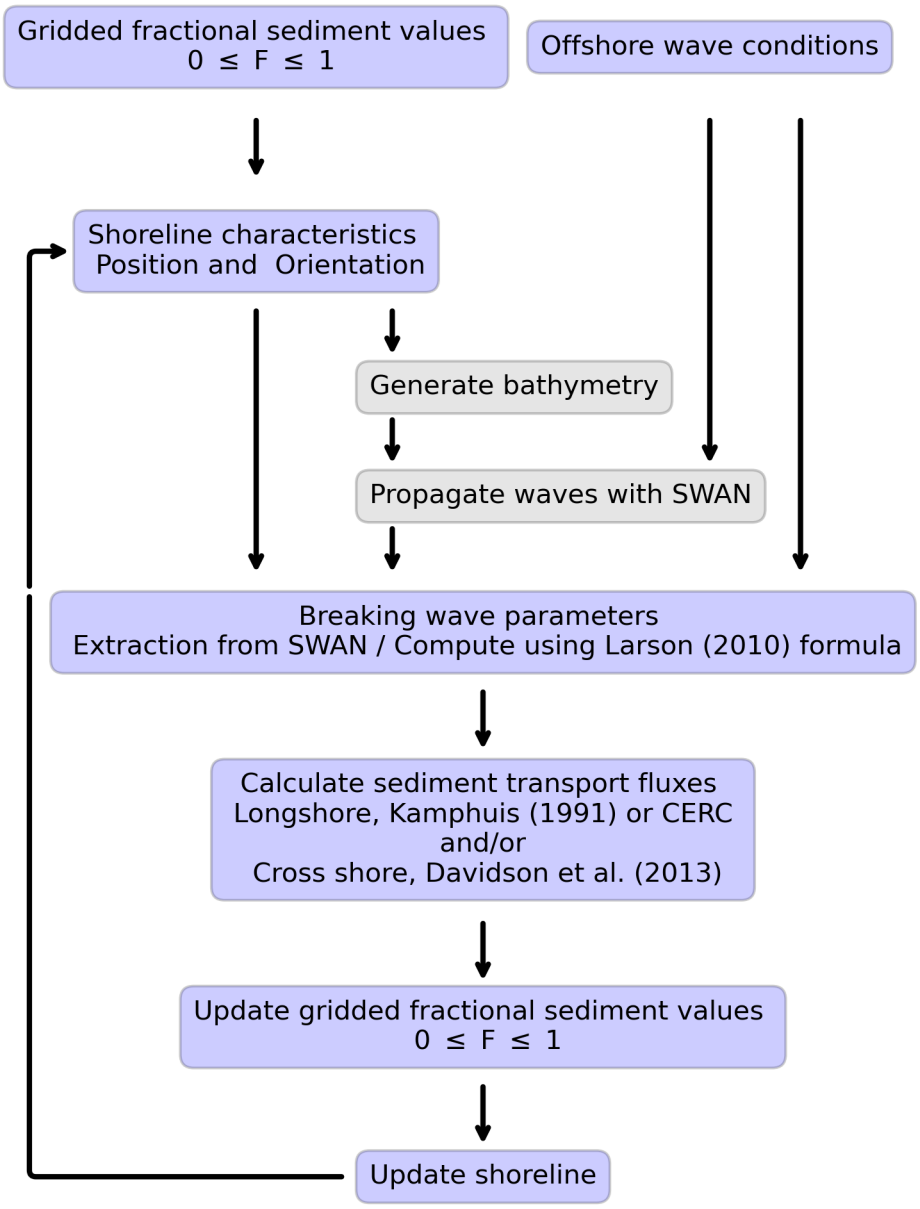

Figure 6.3: LX-Shore model architecture for both wave options, namely computing nearshore waves using SWAN (Booij et al., 1999) or the Larson et al. (2010) formula.

$$\mathbf{F} = w_{\text{sat}} \times \mathbf{F}_{\text{sat}} + w_{\text{sim}} \times \mathbf{F}_{\text{sim}}, \tag{6.4}$$

where $\mathbf{F}$ represents the updated matrix of fractional sediment values. The weighting coefficients w_{sat} and w_{sim} satisfy $w_{\text{sim}} = 1 - w_{\text{sat}}$, with w_{sat} ranging between 0 and 1. This relaxation parameter defines the relative influence of the observations and the model predictions, effectively guiding the assimilation step toward either the satellite-derived or simulated state, depending on data confidence and model stability. A dedicated Python routine was developed to automate the assimilation of satellite-derived gridded sediment fractions.

This approach can be viewed as a simplified form of data assimilation, analogous to the direct insertion or nudging methods commonly used in geophysical and oceanographic modelling (Lakshmivarahan and Lewis, 2013). Unlike more computationally intensive ensemble-based or variational schemes (Alvarez-Cuesta et al., 2024), this relaxation-based formulation provides a flexible and efficient mechanism for incorporating observational information into reduced-complexity morphodynamic models while maintaining numerical stability and physical coherence.

6.3 Study site, datasets and model setup

Building on the satellite-to-model framework introduced in Section 6.2, this section focuses on the application to the Sacalin spit—one of the most dynamic coastal features of the Danube Delta. The following subsections first introduce the physical setting and key characteristics of the study site, then describe the satellite datasets and derived products used for model initialization and validation. A preliminary analysis of the observed shoreline evolution provides the context for configuring and testing the LX-Shore model under realistic forcing conditions.

6.3.1 Study site

The Danube Delta is one of the few large deltas worldwide whose evolution has been governed by a complex interplay of riverine sediment supply, longshore sediment transport, marine dispersal forces, vertical movements (including neotectonics and sediment compaction), and sea-level fluctuations. This interaction has generated a highly diverse morphology, encompassing a labyrinthine network of channels and lakes (fluvial delta), extensive reed marshes, large barrier-divided lagoons, and beach-ridge plains supporting expansive transgressive dunefields (maritime delta) (Vespremeanu-Stroe et al., 2017). The modern Sfântu Gheorghe deltaic lobe, the southernmost of the three distributaries (Figure 6.4), developed through the accumulation of both fluvial and marine sediments at the mouth of its branch.

The Danube River is 2,870 km long and drains an area of approximately 817,000 km^2. Near the apex of the Danube Delta, mean water discharge is about 6,500 m^3/s (AD 1840–2013). The present suspended sediment flux to the Black Sea is estimated at $\sim$12.4 $\times$ 10^6 m^3/year for the period 1985–2013, based on data from the National Institute of Hydrology and Water Management (NIHWM) (Preoteasa et al., 2016). At present, the Danube enters the Black Sea through three main distributaries—Chilia, Sulina, and Sfântu Gheorghe (north to south)—which carry $\sim$58%, $\sim$19%, and $\sim$23% of the total discharge, respectively (Bondar and Panin, 2001).

The present work focuses on the Sacalin Spit, which first emerged as a barrier island in the 1890s (Zăinescu et al., 2019), at the mouth of the Sfântu Gheorghe distributary (Figure 6.4). Since the 1960s, the spit has evolved into three morphodynamically distinct sectors. The northernmost

sector, located immediately south of the Sfântu Gheorghe river mouth, forms a barrier attached to the delta plain. The central sector forms a barrier island backed by a lagoon, while the southernmost tip, started forming in the 1960s, and consists of a series of beach ridges prograding into the Black Sea (Zăinescu et al., 2019).

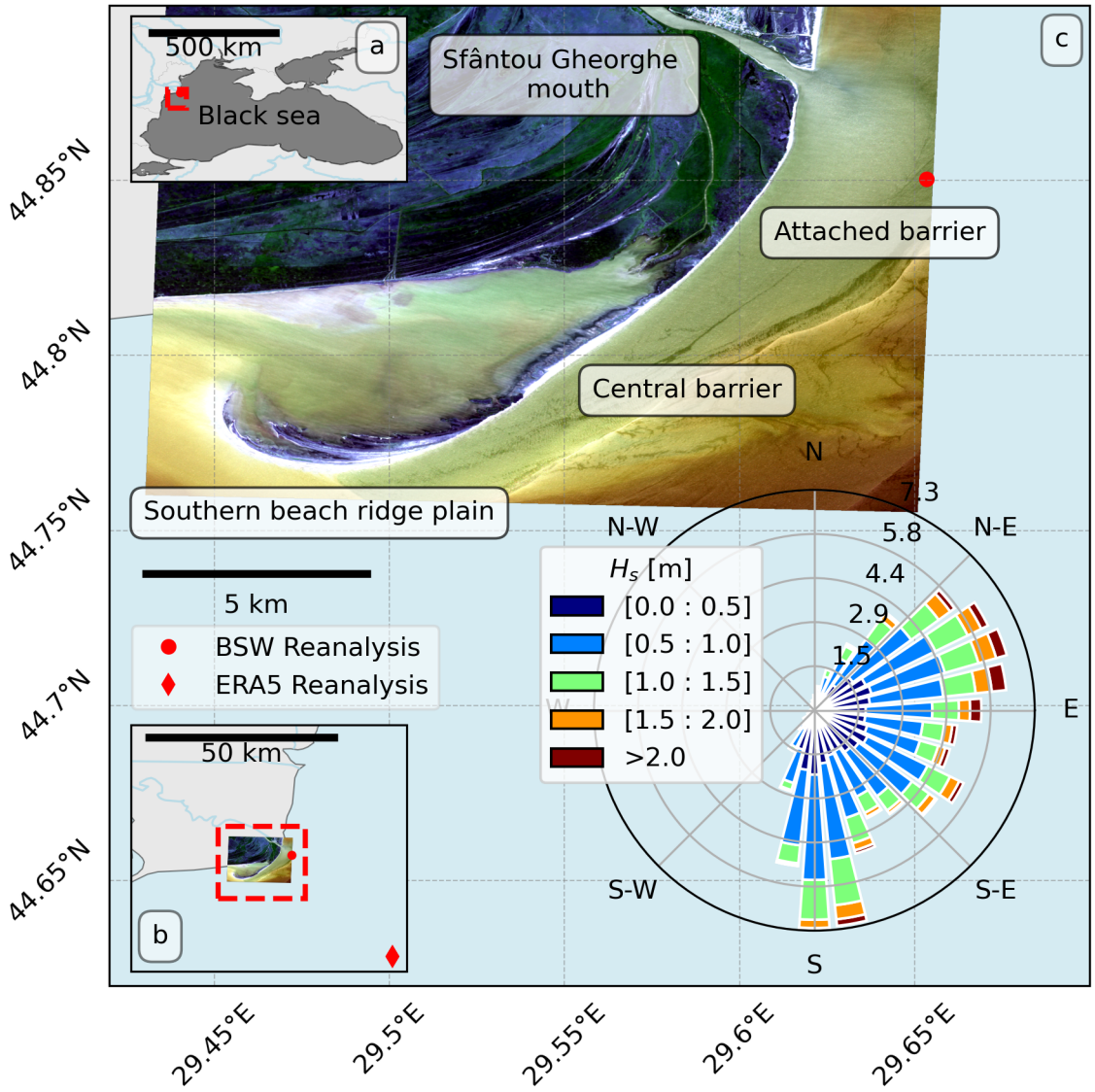

Figure 6.4: Panel a, location of the Danube delta on the Black Sea coast. Panel b Location of the Sfantu Gheorghe lobe of the Danube delta. Panel c, the Sacalin spit, subdivided into three distinct areas based on morphological characteristics. The wave rose consists of a 40 year timeseries (1984 - 2024), extracted from the Black sea wave reanalysis dataset (Staneva et al., 2022), produced by the Copernicus Black Sea operational wave model (Ricker et al., 2024). An offshore wave point was extracted from the ERA5 reanalysis dataset (Hersbach et al., 2023b). The overlayed image is captured by Sentinel-2 satellite at 21/05/2025, and is downloaded from Google Earth Engine (Gorelick et al., 2017).

The central barrier consists of a quasi-continuous, low-lying, narrow washover berm, with a maximum elevation of about 1 m and a width of up to 100 m and is retreating at a rate of $\sim$20 m/yr since 1984. This berm is backed by a gently sloping platform created during past breaching events, supporting marshes mostly colonized by reeds (Zăinescu et al., 2019). Further south, an elongated beach-ridge plain extends for approximately 6 km, formed by sediment deposition at the

downdrift tip of the spit. The prograding barrier is characterized by low, parallel foredune ridges, while the downdrift tip displays multiple recurves since its emergence, indicating cyclicity in the elongation process (Vespremeanu-Stroe et al., 2017).

The shoreface fronting the northern and central sectors of the spit is convex–concave, with long-term erosional trends and a lower-sloping platform at around 6 m depth (Preoteasa et al., 2016; Zăinescu et al., 2019). Past surveys have indicated transverse nearshore bars, spaced several hundred meters apart, extending to depths of 8 m (Zăinescu et al., 2019). In contrast, the southern beach-ridge plain is fronted by a linear, gently sloping profile characteristic of a depositional environment (Zăinescu et al., 2019). The back-barrier lagoon evolves alongside the elongation and narrowing of the retreating Sacalin barrier. It overlies mouth-bar deposits formed by sediment settling from fluvial jet expansion at the Sfântu Gheorghe mouth, predating the emergence of the Sacalin spit (Zăinescu et al., 2019). Progressive infilling occurs from north to south through the formation of a bayhead delta supplied by a secondary Sfântu Gheorghe distributary (see Figure 6.4) (Preoteasa et al., 2016).

A 40-year wave time series (1984–2024) was extracted from the Black Sea wave dataset (Staneva et al., 2022) at 15 m depth, offshore of the Sfântu Gheorghe river mouth (red point in Figure 6.4). Generated by the Copernicus Black Sea operational wave model (Ricker et al., 2024), this record shows that the wave climate along the Danube Delta coast is generally of low to moderate energy, with a mean significant wave height of 0.8 m and a mean period of 4.6 s. Wave energy is predominantly from the northeast, while extreme events can produce waves with significant wave height exceeding 3 m several times per year and may reach up to 4 m with a return period of 10 years.

At the Sfântu Gheorghe mouth, these dominant northeasterly waves can drive an estimated net longshore sediment transport rate of $\sim$0.9 to 1 $\times$ 10^6 m^3/yr (Dan et al., 2007), with maximum values reaching up to 1.6 $\times$ 10^6 m^3/yr along the central Sacalin barrier (Dan et al., 2011). Bathymetric measurements suggest that these rates may be underestimated, as silts and muds dominate at greater depths, and interannual variability is high (Zăinescu et al., 2019). Nevertheless, these values provide a first-order estimate of the potential sand supply to the Sacalin spit through wave-induced transport from updrift sources. By comparison, cross-shore transport rates between the upper and lower shoreface range from $\sim$0.05 $\times$ 10^6 m^3/yr along the relatively stable Sfântu Gheorghe beach to $\sim$0.17 $\times$ 10^6 m^3/yr along the eroding Sulina–Sfântu Gheorghe sector further north (Tătui and Vespremeanu-Stroe, 2017).

The Black Sea is virtually tideless, with a maximum spring-tide range of 0.12 m (Bondar and Panin, 2001). Long-term records from the Sulina tide gauge, located 30 km north of the Sfântu Gheorghe mouth, indicate a relative sea-level rise (SLR) rate of 2.5 mm/yr since 1858 (Zăinescu et al., 2019). The impact of SLR on the coastal dynamics of the Danube Delta is therefore considered negligible in comparison with the high rates of shoreline retreat. Beaches along the Sacalin spit are composed of fine sands with grain sizes of 0.19–0.20 mm. The upper shoreface is dom-

inated by fine sands to depths of 8–10 m, whereas the lower shoreface consists primarily of silts and muds (Zăinescu et al., 2019).

6.3.2 Satellite derived observations

In the present work, a 40-year dataset of publicly available satellite imagery, cropped and downloaded from the Sentinel-2 and Landsat collections using Google Earth Engine (Gorelick et al., 2017), was used to investigate the morphological evolution of the Sacalin spit. This sandy barrier extends approximately 20 km south of the Sfântu Gheorghe river mouth, located on the southern lobe of the Danube Delta in the Black Sea. The analysis relied exclusively on satellite-derived observations to conduct a two-dimensional (planform) assessment and numerical modelling of the spit's long-term morphological development.

The obtained timeseries of satellite derived gridded data of land/water coverage within the study area is depicted in Figure 6.5. Panels a–f illustrate six snapshots of the Sacalin spit at approximately 8-year intervals between 1984 and 2025, highlighting its morphological evolution. Panel g presents the cumulative distribution of all accepted satellite observations used in the analysis, while panel h shows the time intervals (in days) between successive observations. A data gap between 2012 and 2014 results from the decommissioning of Landsat 5 in 2012 and the launch of Landsat 8 in 2013. Although Landsat 7 operated during this period, its images were unsuitable for analysis due to the Scan Line Corrector (SLC) failure in 2003. Finally, panel i depicts the annual distribution of observations across the full period, which are predominantly concentrated in summer months, as winter imagery is more frequently affected by cloud cover.

The time series of satellite-derived observations was used to investigate the morphodynamic evolution of the area covered by the Sacalin spit over the 40-year period from 1984 to 2025. This timeframe was selected based on the availability of publicly available satellite imagery. A total of 2,983 images from the Landsat and Sentinel collections were retrieved for the study area, of which 821 (27%) passed quality control. Due to persistent georeferencing issues, Sentinel-2 images collected through the Google Earth engine, were discarded, resulting in a reduced dataset of 593 usable Landsat-derived observations. With appropriate preprocessing, Sentinel-2 imagery could be incorporated in future analyses to improve temporal resolution. The accepted observations were used as initial conditions in the hybrid LX-Shore model (Robinet et al., 2016), which was applied to simulate the complex morphodynamic behaviour of the Sacalin spit. Finally, the observations were assimilated into LX-Shore to constrain the model trajectory compensate for processes not explicitly represented within the model structure.

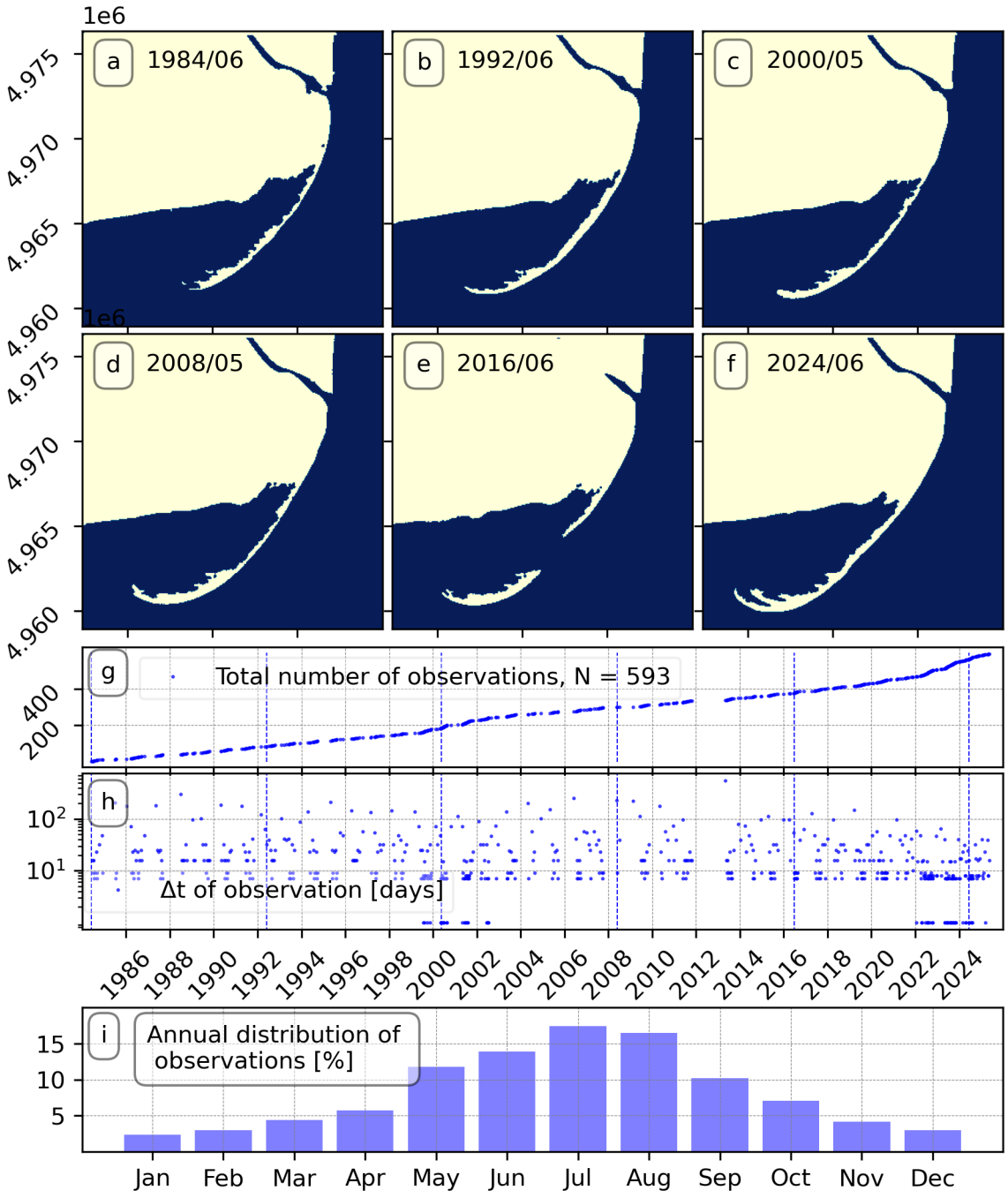

Figure 6.5: Panels a-f, land-water binary grid produced from the satellite images spanning the entire period of available data. Panel g, Cumulative distribution of accepted satellite observations used in the analysis. Panel h, interval between successive observations in days. The dashed vertical lines in panels g and h indicate the instance of observations depicted in panels a to f. Panel i, annual distribution of observations.

6.3.3 Preliminary analysis of the satellite-derived observations: evolution of the Sacalin spit

In the upper panel of Figure 6.6, the areas covered by the spit in May 1984 and May 2025 are overlaid, highlighting the morphological evolution of the Sacalin spit over the study period. The three distinct regions of the spit, namely the attached barrier in the north, the central barrier, and

the southern spit that formed during the study period, are delineated within red polygons. At each observation, the total area of the Sacalin spit is defined as the sum of the land areas within these polygons. The lower panel of Figure 6.6 shows the evolution of the observed spit area relative to the initial observation in May 1984 (Obs(i) – Obs(0)), plotted as blue squares, together with a seasonal mean calculated as a moving average with a 3-month backward-facing window. The initial area in May 1984 was 6.8×10^6 m^2. Over the 42-year period, the spit area fluctuates around this initial value but shows an abrupt increase of $\sim 2 \times 10^6$ m^2 in 2016, after which it continues to fluctuate around this value with a seasonal variability.

In Figure 6.7, the morphological evolution of the Sacalin spit is shown in six snapshots spanning the entire study period. For reference, the initial area covered by the spit in May 1984 (observed by Landsat 5) is outlined in red in all panels. During the first decade (1984–1994; panel a), the attached barrier underwent uniform erosion extending southward to the northern limit of the central barrier, while the spit tip elongated by $\sim$2 km. Over the following period (panel b), erosion of the attached barrier continued, and the central barrier retreated landward into the lagoon. The retreat rate decreased southward, while the spit tip experienced further deposition, resulting in widening rather than elongation. This behaviour persisted until 2007 (panel c), with the retreat zone of the central barrier extending even further southward and the overall shoreline reorienting from its convex 1984 outline to a more uniform southeast-facing alignment. Meanwhile, sand accumulation at the southern end produced elongation, widening, and a northward rotation of the tip.

A major breach developed in the central barrier in 2011 (Zăinescu et al., 2019), reaching its maximum extent by May 2013 (panel d), while the attached barrier and southern tip continued to erode and accrete, respectively. By May 2018, the central barrier had "re-emerged" $\sim$400 m further east as sediment was transported across the submerged breach platform, forming terraces and bars on the lagoon side probably stabilized by vegetation. At the same time, continued deposition at the southern tip led to the formation of a new protrusion. In the most recent period (2018–present; panels e–f), the central barrier has widened, likely due to overwash deposition creating lagoon-side terraces, while the attached barrier in the north continued its long-term erosion, with the erosion area progressively shrinking toward the immediate vicinity of the Sfântu Gheorghe river mouth. The southern tip remains the main zone of sediment accumulation, displaying multiple recurves as deposition extends the spit southward and westward. Notably, as the spit evolves, the locus of erosion has shifted progressively from north to south, with the former 1984 spit tip experiencing erosion for the first time in nearly 40 years (panels e-f in Figure 6.7).

In Figure 6.8, the temporal evolution of the area of each distinct part of the spit relative to the initial observation in May 1984 (Obs(i) – Obs(0)) is shown. The areas considered in the land–cover calculations correspond to the red polygons outlined in the upper panel of Figure 6.6, as well as the inset in the lower-left corner of Figure 6.8. The attached barrier in the north shows a continuous reduction in area, eroding at a rate of $\sim 0.1 \times 10^6$ m^2/yr until about 1999. After this point, the

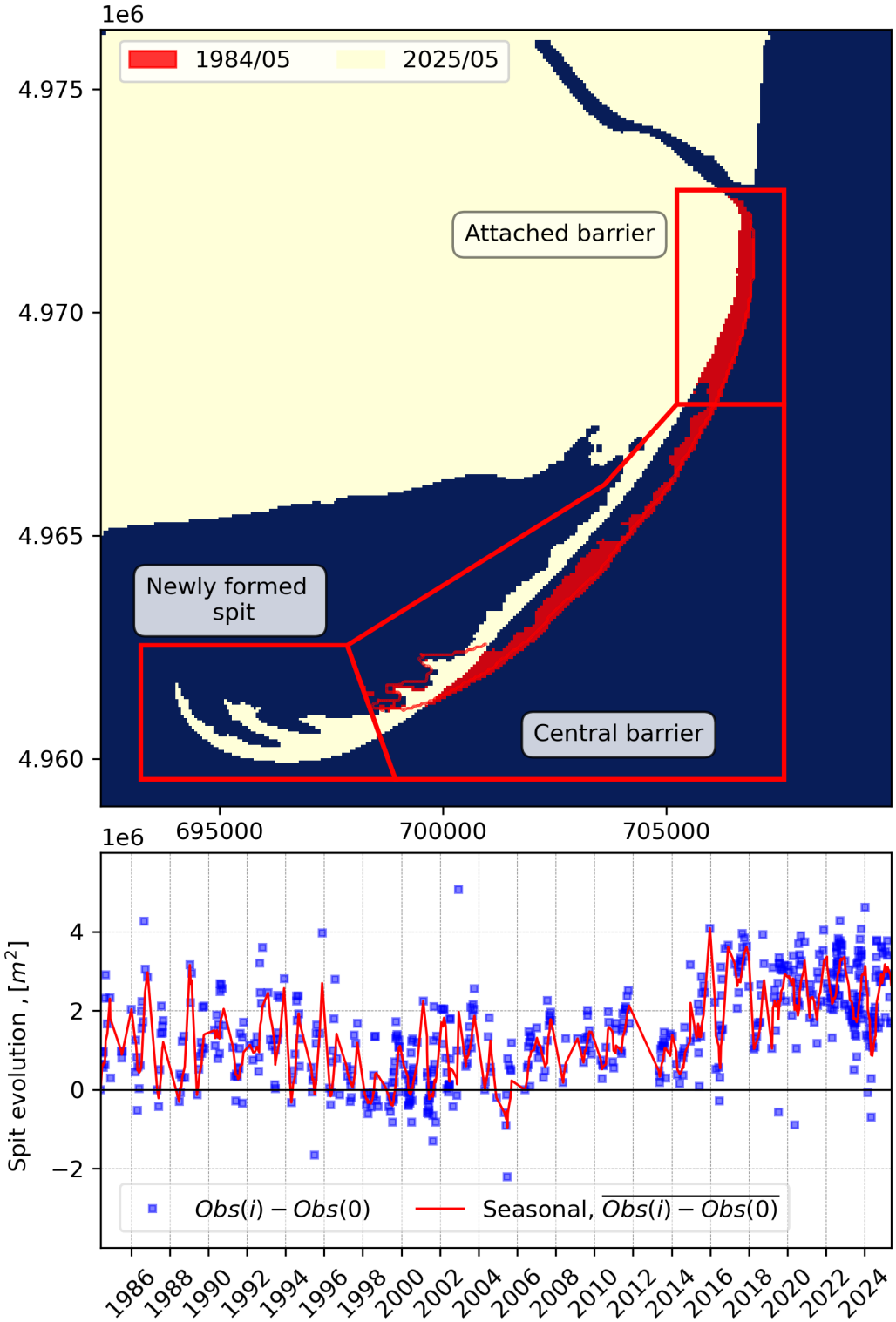

Figure 6.6: Upper panel: Overlayed satellite derived observations of the area covered by the Sacalin spit in May 1986 and 2025. The three distinct areas of the spit are separated by red polygons. Lower panel Observed evolution of the area covered by the Sacalin spit with reference to the initial observation Obs(0) captured in May 1984 plotted as blue squares and a seasonal (3 month backwards facing window) moving average is plotted as a red solid line.

erosion rate decreases by roughly an order of magnitude to $\sim 0.4 \times 10^5$ m^2/yr. A similar but opposite behaviour is observed in the newly formed tip of the spit in the south west corner of the domain. As this part of the spit did not exist in the 1984, the land areaage is constantly increasing

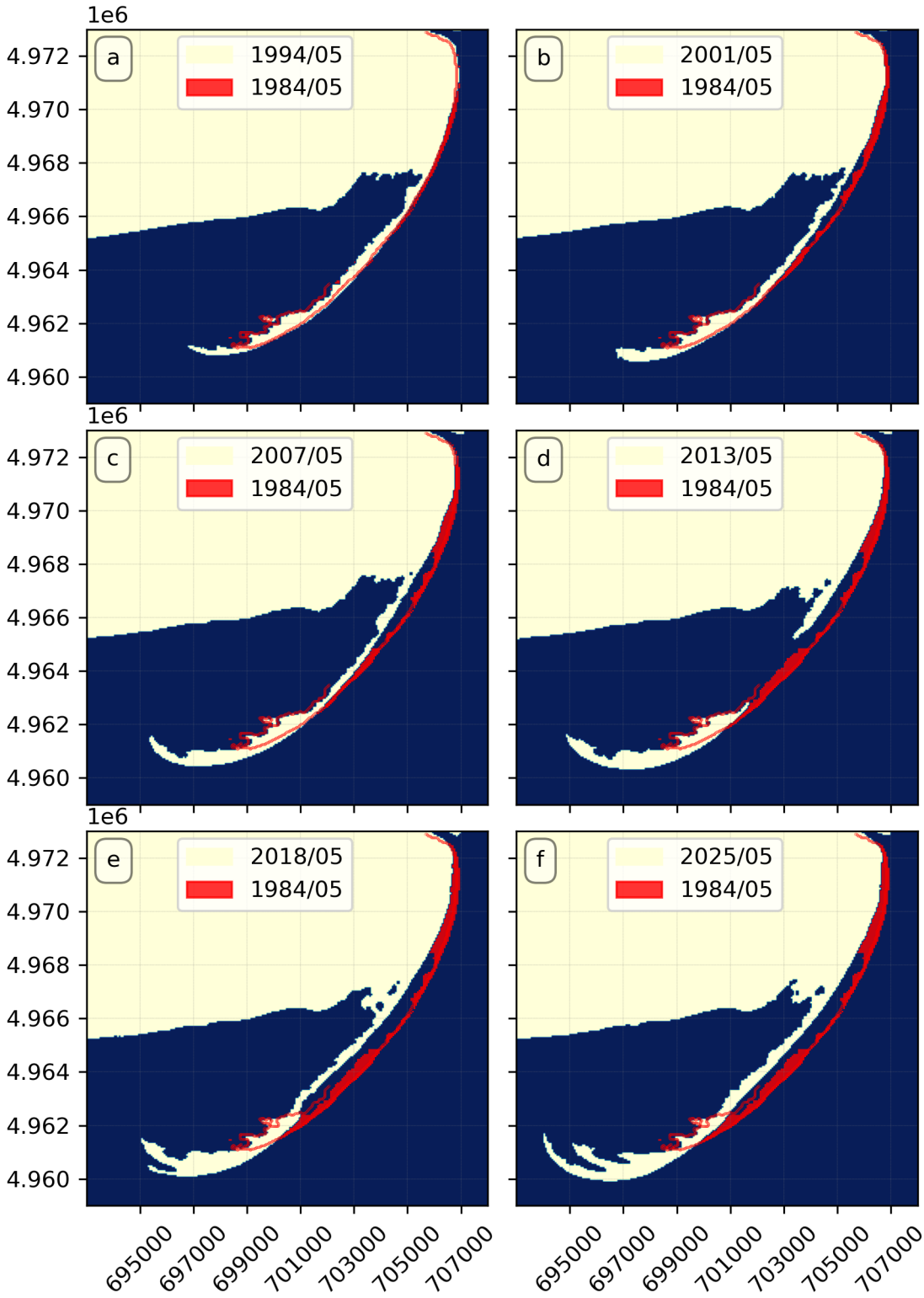

Figure 6.7: Binary grid of land-water values covering the Sacalin spit produced from the Landsat satellite images, spanning the entire period of available data. The area covered by the spit at the first observation in May 1985 is depicted with red in all panels.

during the study period at a rate of $\sim 0.45 \times 10^5$ m^2/yr until about 1999. After this point the rate almost doubles in magnitude and the tip of the spit seems to gain $\sim 0.87 \times 10^5$ m^2/yr. This change in slope to the rate of change in land areaage, coincides with a clockwise reorientation of

the attached and central barriers of the Sacalin spit, aligning with the present-day orientation (see panels a–f in Figure 6.5).

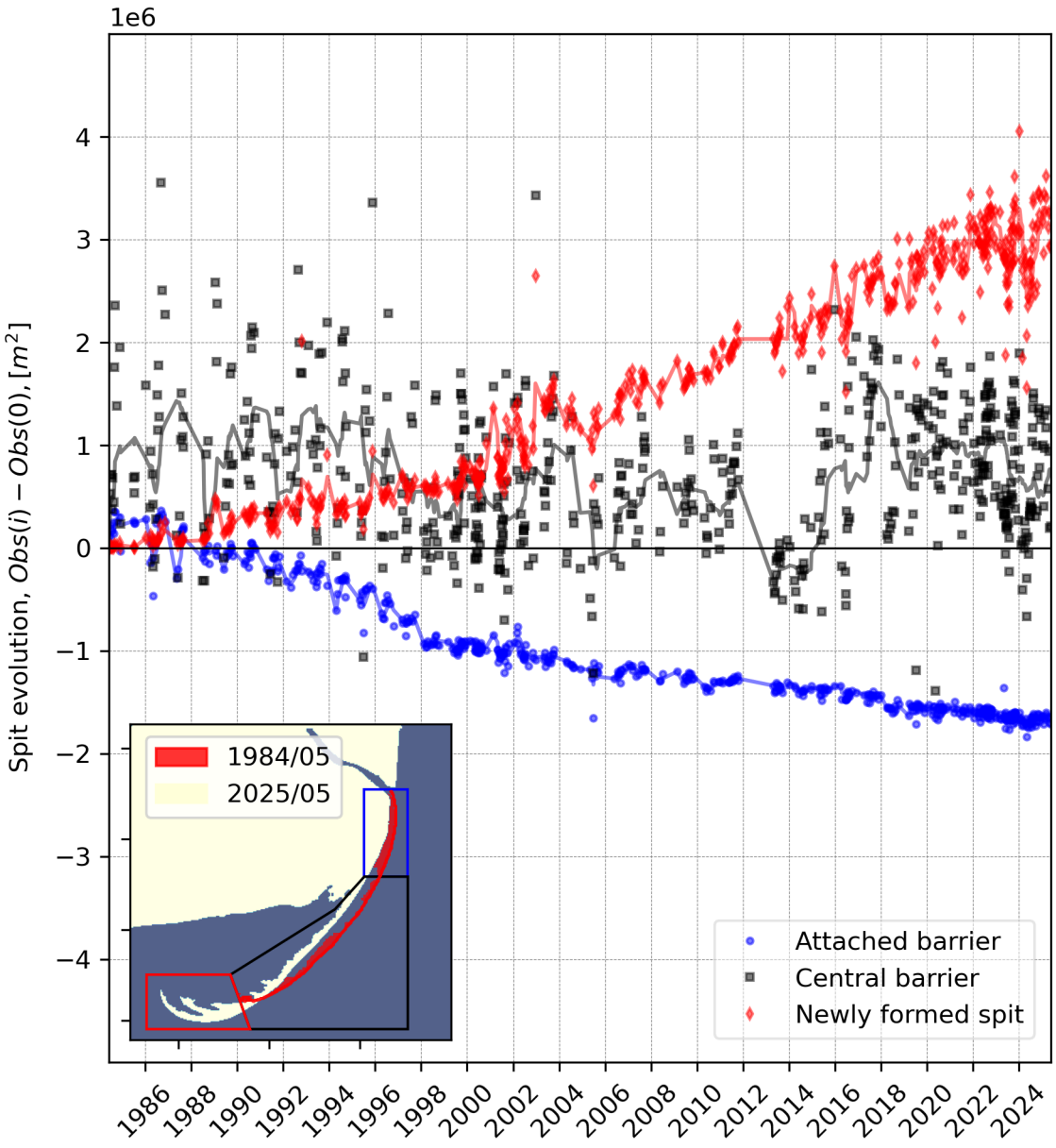

Figure 6.8: Observed evolution of the area covered by each distinct area of the Sacalin spit with reference to the initial observation Obs(0) captured in May 1984 plotted as blue circles (Attached barrier), black squares (Central barrier) and red diamonds (Newly formed spit). The three partitions over which area calculations have been performed are indicated in the snippet on the lower left corner of the figure.

The evolution of the area in the central barrier, plotted as black squares in Figure 6.8, shows the largest fluctuations, with a standard deviation of $\sim 0.7 \times 10^6$ m^2 and seems to have gained $\sim 1 \times 10^6$ m^2 over the course of the 40 year study period. Fluctuations at this part of the spit should be carefully interpreted, as this area is backed by a very shallow lagoon that is slowly filling supplied

by fluvial sediment and small variations in water level might be easily confused as land gain. Furthermore the barrier is retreating at an average rate of 20 m/yr due to frequent overwashing and breaching events, creating a shallow platform on the Black Sea side (Zăinescu et al., 2019). There is a decrease in the order of 0.5×10^6 m^2 around 1999, coinciding with the change in rates observed in the two extremities of the spit. The area seems to fluctuate around a steady value without any obvious trend until a significant drop in land areaage in 2013, followed by an abrupt increased by 2018, seemingly gaining more than $\sim 1 \times 10^6$ m^2. The loss in area observed in 2013 is due to a big breaching event that was initiated during the winter of 2011/2012 and reached a maximum extent of 3 km in May of 2013 (Zăinescu et al., 2019). The barrier started slowly recovering in 2014, forming a wide ($\sim$ 0.5 km) submerged breach platform on the lagoon side and by the summer of 2016 emerging washover terraces and bars completely closed the breach (Zăinescu et al., 2019).

6.3.4 LX-Shore model setup

The evolution of the Sacalin spit was simulated using the LX-Shore model configuration described in Section 6.2.2, initialized with the satellite-derived grid from May 1984, interpolated onto a 60 m × 60 m grid. Prior to selecting the final wave forcing dataset, an initial set of simulations was carried out using both the ERA5 reanalysis (Hersbach et al., 2023b) and the regional Black Sea wave (BLW) reanalysis dataset (Staneva et al., 2022) to evaluate their respective suitability for nearshore modelling at the site (see Figure 6.9). The ERA5 data, extracted further offshore and based on a coarser model grid, produced unrealistic shoreline evolution patterns, with alternating zones of erosion and deposition that were inconsistent with observed trends. These artefacts are likely a consequence of the simplified nearshore bathymetry representation and the model's refraction scheme.

In contrast, simulations forced with the BLW dataset—generated by the Copernicus Black Sea operational wave model (Ricker et al., 2024) at 0.025° resolution—yielded more coherent and physically plausible shoreline changes, better aligned with the expected morphodynamic behaviour of the Sacalin spit. Consequently, the BLW dataset was selected for all subsequent analyses. The 40-year wave time series (1984–2024), extracted at 15 m depth offshore of the Sfântu Gheorghe river mouth (red point in Figure 6.4), was used to drive the LX-Shore simulations. Wave transformation followed the formulation proposed by Larson et al. (2010), complemented by the shadowing procedure of Ashton and Murray (2006), whereby sediment transport and wave computations were omitted in areas shielded from incoming wave energy. Only the longshore sediment transport component, calculated following Larson et al. (2010), was included in the present work. Although the morphodynamic behaviour of the site is far more complex than can be captured by gradients in longshore sediment transport alone, this simplified approach was deliberately adopted to maintain focus on evaluating the data assimilation methodology.

To establish a reference for model performance, a series of baseline simulations was conducted

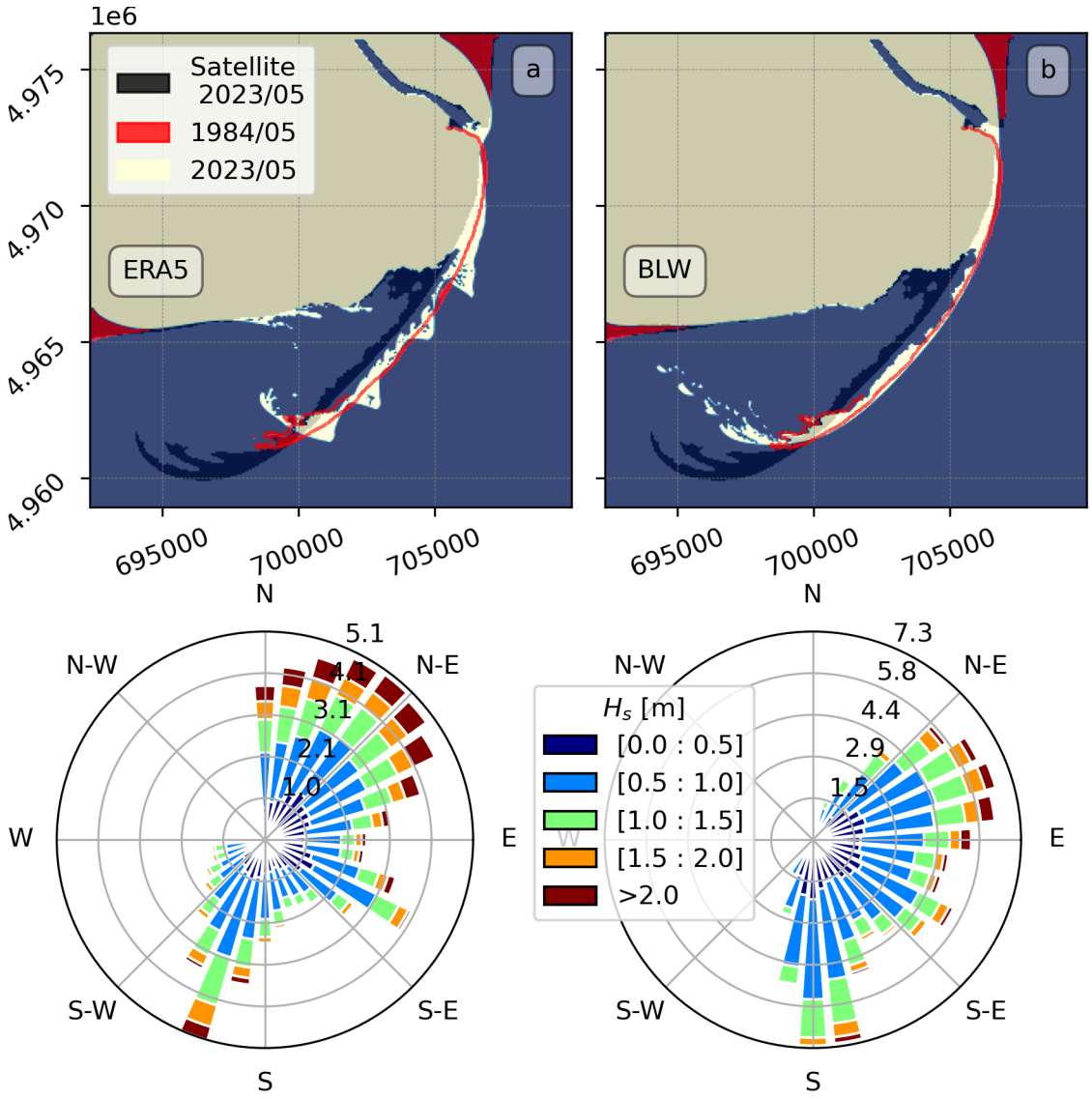

Figure 6.9: Simulated evolution of the Sfântu Gheorghe river mouth and the Sacalin spit forced by the waves from the ERA 5 reanalysis dataset (Hersbach et al., 2023b) (left panels) and the Black Sea Wave reanalysis (Staneva et al., 2022) (right panels).

without data assimilation, allowing the system to evolve freely under wave forcing and to assess the sensitivity of shoreline change to the littoral drift calibration factor QF. The value of QF was progressively increased until the model became unstable due to unrealistically large longshore sediment transport rates, which occurred for QF values greater than 12 Figure 6.10 shows the simulated sediment fraction F at the final timestep, illustrating the extent of the Sacalin spit after 40 years of simulation. The initial shoreline from May 1984 is shown in red, while the model results are overlaid with the corresponding satellite-derived observation at the final timestep in black. Panels (a)–(f) in Figure 6.10 correspond to different values of the littoral drift calibration factor QF, ranging from 1 to 12.

Across all simulations, longshore sediment transport was sufficient to close the Sfântu Gheorghe river mouth, while values of QF $\approx$ 10 were required to drive sediment accumulation at the southern tip of the spit. The model did not reproduce the erosion of the attached barrier south

of the mouth, likely due to excess sediment supply from unrealistic erosion of the beach north of the river mouth. Runs with QF ≥ 6 performed better in the attached barrier region, suggesting that faster erosion of the northern part, limited sediment availability and gradually shifted erosion southward. The breaching and retreat of the central barrier were not captured, as these processes result from overwash and breaching dynamics not represented in LX-Shore.

Figure 6.11 presents the temporal evolution of the absolute difference in area between the simulated and observed Sacalin spit for all six scenarios shown in Figure 6.10. The region used for the area calculation is indicated in the inset located in the lower right corner of the figure. The absolute error in the area covered by the spit increases progressively throughout the simulation period, reflecting the limited spatial agreement between the modelled and observed shorelines. By the end of the simulation, the absolute error exceeds the total observed area of the spit, estimated at approximately 0.9×10^7 m^2. The similarity of the error curves across all tested values of the littoral drift calibration factor (QF) suggests that the model response is largely insensitive to the parameter in the absence of data assimilation. However, during the last decade of the simulation (after 2014), a slight divergence among the curves becomes apparent, suggesting that the enhanced erosion of the attached barrier and the increased accretion at the spit tip obtained with higher QF values begin to influence the overall area of the simulated Sacalin spit.

To better understand the system's behaviour and compare model results with the morphodynamic evolution of the Sacalin spit, the study area was subdivided into three distinct regions described in Section 6.3.3, namely the attached barrier, the central barrier, and the tip of the spit. The temporal evolution of the absolute error between simulated and observed land area within each subregion is shown in Figure 6.12, expressed as a percentage of the observed area at each comparison timestep for all six values of the littoral drift calibration factor (QF). The error corresponding to the attached barrier, located immediately south of the Sfântu Gheorghe river mouth, is shown in panel (a), while panels (b) and (c) illustrate the error evolution for the central barrier and the spit tip, respectively. The specific region considered in each case is highlighted by the coloured inset within each panel.

At the attached barrier (panel a), the absolute error exhibits a clear negative correlation with the littoral drift factor. Higher QF values lead to increased erosion of this region, which more closely reflects the observed morphological behaviour of the system. The inflection point observed in all curves in panel (a) of Figure 6.10 coincides with the shift in slope in the observed area evolution (Figure 6.8) discussed in Section 6.3.3. The model captures the reduction in erosion rates after 1998 more accurately when QF ≥ 10, as indicated by the stabilisation of the relative error during this period.

In contrast, the littoral drift factor appears to have little influence on the central barrier, where all six curves in panel (b) of Figure 6.10 are nearly identical, indicating a consistent model– observation discrepancy across QF values. For the tip of the spit (panel c), the relative error increases rapidly at the beginning of the simulation—reaching values comparable to the total ob-

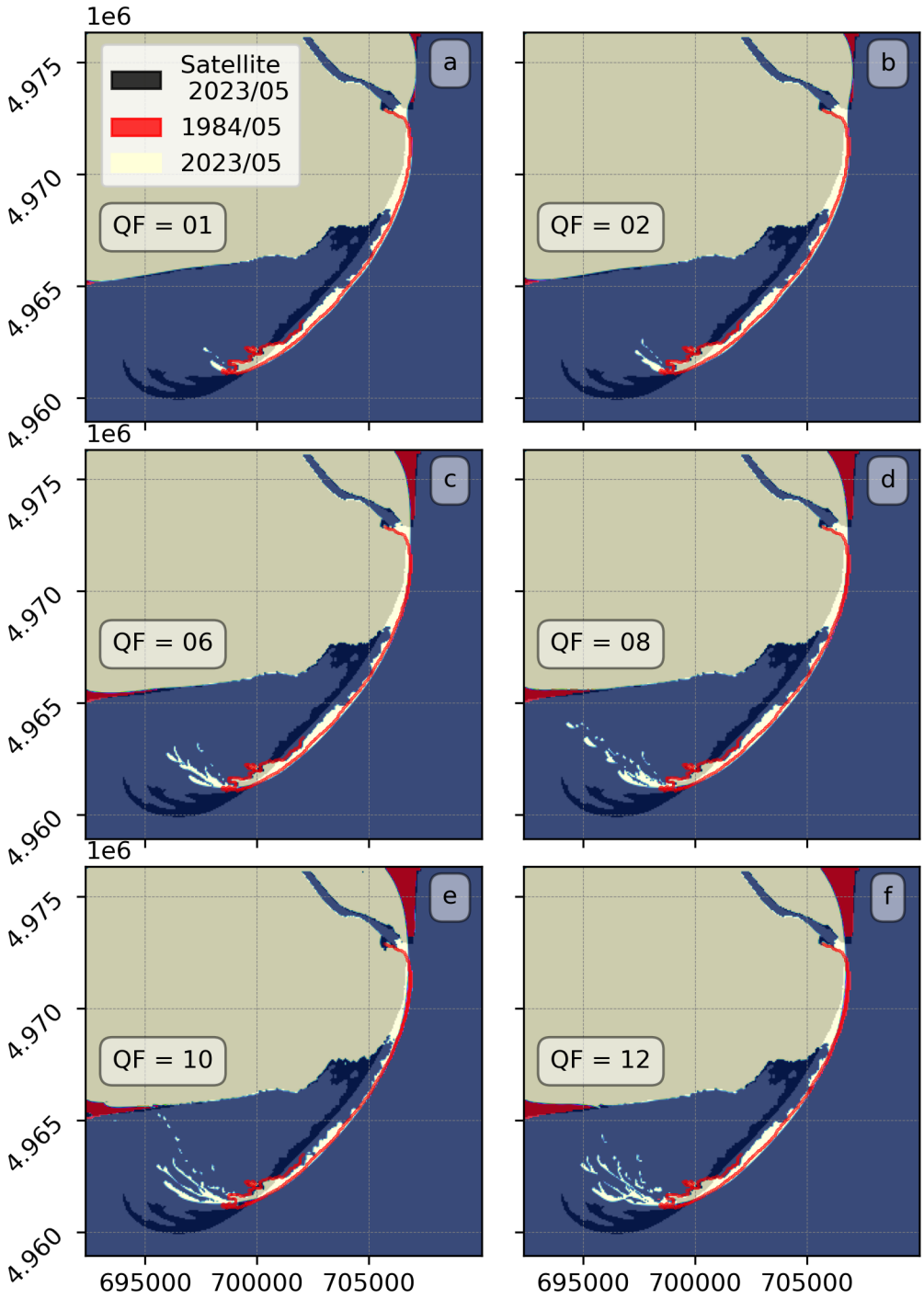

Figure 6.10: Simulated evolution of the Sfântu Gheorghe river mouth and the Sacalin spit for different values of the littoral drift calibration factor QF in Equation 6.3. The sediment fraction F at the initial and final timesteps of the simulation is shown in red and sand, respectively, while the satellite-derived observation corresponding to the final timestep is shown in black.

served area—before stabilising and slowly converging across QF values. This early rapid increase likely reflects the small initial extent of the spit prior to 1988. Increasing the littoral drift factor tends to amplify errors in this region, as higher QF values promote excessive sediment transport toward the spit tip. However, due to the simplified bathymetry and inaccuracies in wave refrac-

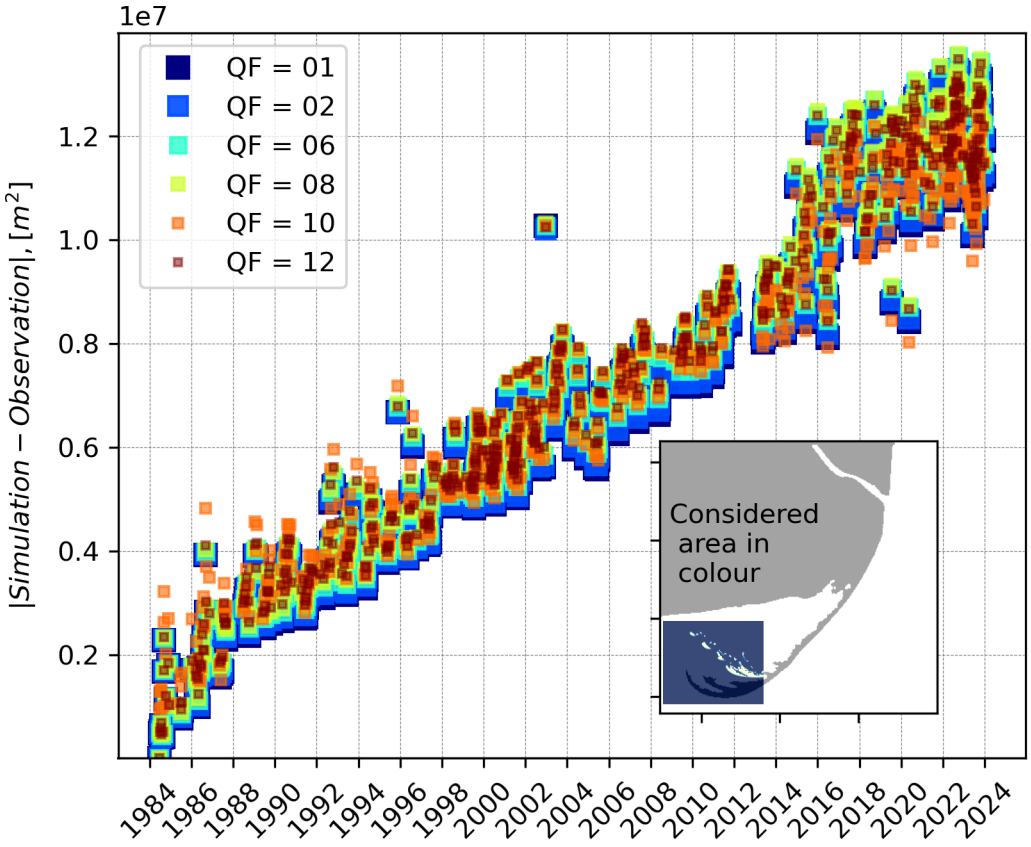

Figure 6.11: Temporal evolution of the absolute difference in the area covered by the Sacalin spit between simulations and observations, computed within the region shown in the inset, for all simulations presented in Figure 6.10.

tion and shoaling representation, this sediment is often misplaced, leading to larger discrepancies compared to lower-QF simulations that fail to deliver sediment to the tip altogether.

Figure 6.13 illustrates the percentage of time each grid cell differs from the corresponding satellite-derived observation throughout the simulation period, for the scenario with a littoral drift calibration factor of QF = 8 (panel d in Figure 6.10). The configuration with QF = 8 was selected as the reference setup for subsequent analyses, representing an optimal balance between reproducing realistic shoreline morphology and maintaining physically consistent sediment transport rates. The model is constantly wrong on the boundaries of the domain due to zero sediment flux boundary conditions and similarly at the Sfanthu Gheorghe river mouth where normally river flow would keep the channel open. The model performed best at the northern end of the attached barrier, immediately south of the river mouth.

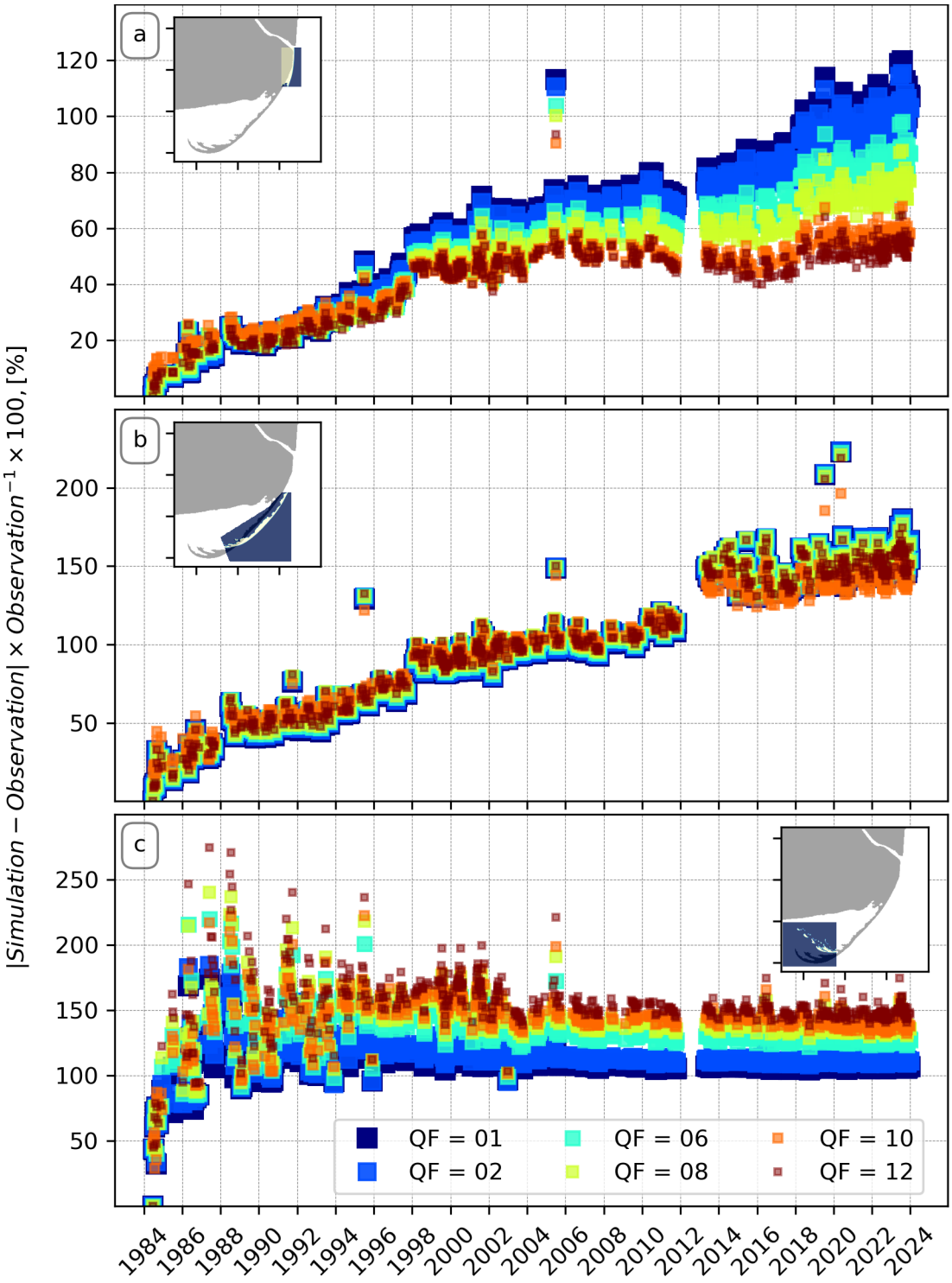

Figure 6.12: Temporal evolution of the absolute difference between simulated and observed land area within the three defined sectors of the Sacalin spit. The areas considered in the land area analysis are outlined in the insets of each panel, while the applied littoral drift factor QF is indicated in the legend of panel (c). The error is expressed as a percentage of the total observed spit area at each comparison time and is shown for all simulations presented in Figure 6.10.

6.4 Results

Building on the insights from the baseline simulations, a second set of experiments was performed incorporating data assimilation to constrain model evolution and enhance agreement with

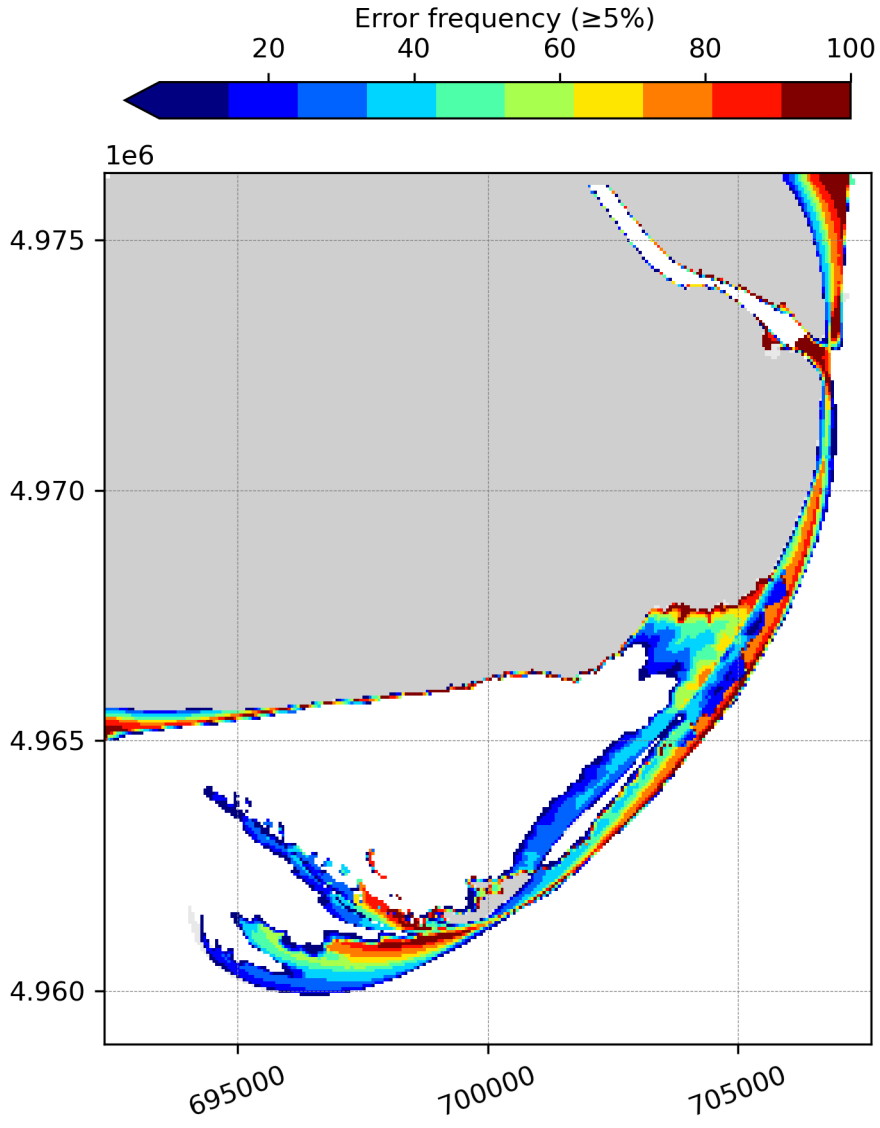

Figure 6.13: Percentage of timesteps each cell was found to differ from the observation for the simulation with a QF = 8 panel d in Figure 6.10. The initial and final satellite data are overlayed as grey transparent areas for reference.

observed shoreline changes. The model was initialized using the same initial conditions as in the baseline simulations, with a littoral drift calibration factor of QF = 8 selected as the optimal compromise between realistic morphological behaviour, quantitative performance, and numerical stability. A satellite derived observation was assimilated almost every year around July, between 1984 and 2024. The assimilation period was chosen based on consistency of observation during the entire period, as the annual distribution of suitable satellite derived observations is centred around July (panel i in Figure 6.5). A relaxation parameter of w_{sat} = 0.9 was implemented to control the magnitude of the imposed correction at each assimilation timestep, nudging the model

results towards the observations while ensuring physically consistent morphological evolution of the Sacalin spit.

6.4.1 Data assimilation in LX-Shore

Figure 6.14 presents the temporal evolution of the absolute error between the simulated and observed area covered by the Sacalin spit. The error time series, computed within the area indicated in the inset, is shown as blue squares, while the assimilation timesteps are marked by black diamonds along the time axis. Model performance is clearly improved through the introduction of data assimilation, with the error remaining on average within 15% of the total spit area—approximately 10 km^2—by the end of the simulation period. The error tends to increase progressively following each assimilation event, typically around July, reaching a maximum toward December before decreasing again, suggesting a seasonal pattern in the model–observation discrepancies.

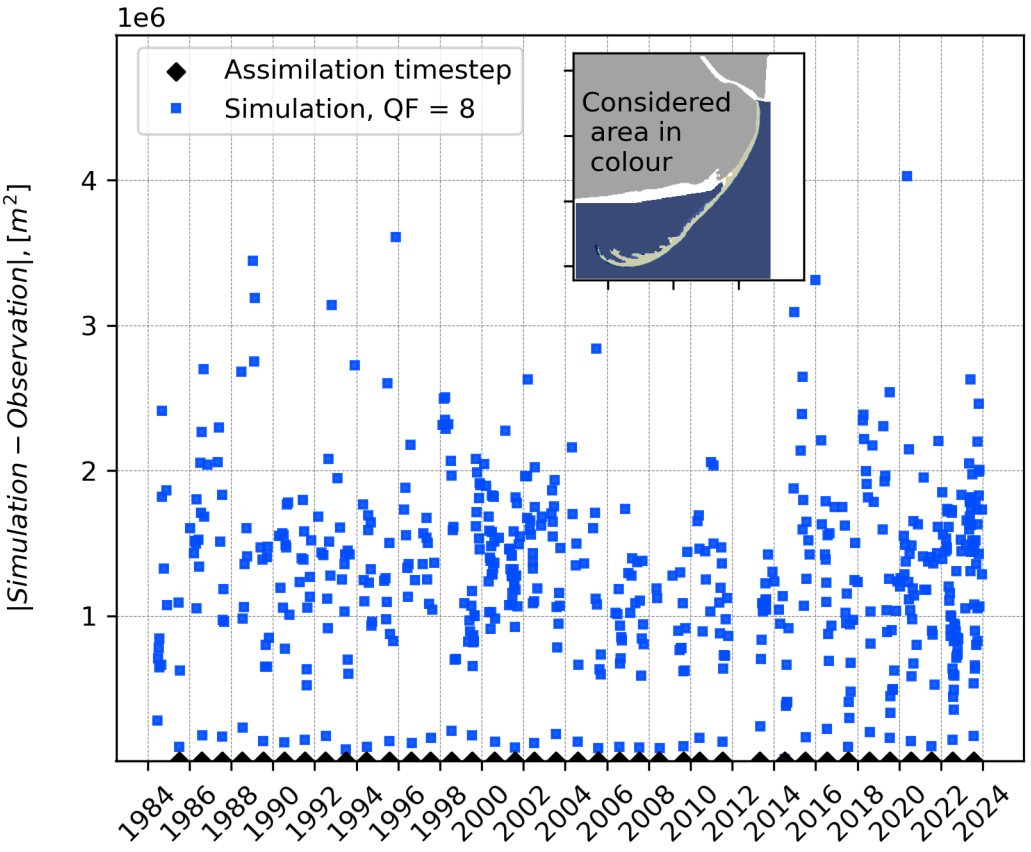

Figure 6.14: Temporal evolution of the absolute difference in the area covered by the Sacalin spit between the simulation assimilating a satellite observation annually and the satellite derived observations. The error is computed within the region shown in the inset. The assimilation timesteps are indicated by the black diamonds along the time axis.

The temporal evolution of the absolute error between simulated and observed land area within each subregion is shown in Figure 6.15, expressed as a percentage of the observed area at each comparison timestep and is shown as blue squares, while the assimilation timesteps are marked

by black diamonds along the time axis. The error corresponding to the attached barrier, located immediately south of the Sfântu Gheorghe river mouth, is shown in panel (a), while panels (b) and (c) illustrate the error evolution for the central barrier and the spit tip, respectively. The specific region considered in each case is highlighted by the inset within each panel.

In the attached barrier region (panel a), the absolute error exceeds 10% almost annually during the first part of the simulation, up to approximately 1998, with mean values fluctuating between 5% and 10%. After 1998, the error appears to decrease slightly and stabilise, only rarely exceeding 10% and maintaining a mean value of around 5%. This shift in the error pattern coincides temporally with the change in slope observed in the evolution of the spit area (Figure 6.8), as discussed in Section 6.3.3.

The error in the central barrier region, shown in panel b of Figure 6.15, is slightly higher than that observed in the attached barrier area. This can be partly attributed to fluctuations in land area along the low-lying lagoon side of the barrier, as well as to the expansion of the newly formed delta at the northeastern end of the lagoon. Despite its larger magnitude, the error displays a similar yet slightly delayed temporal pattern compared to the attached barrier. It fluctuates around a mean value slightly above 20% until approximately 2002, after which the mean error decreases below 20%. During the final decade of the simulation, the error exhibits distinct peaks between 2015 and 2018, likely associated with the "re-emergence" of the breached area, that occurred during this period.

The error at the tip of the spit, shown in panel c of Figure 6.15, is substantially larger than in the other regions during the early phase of the simulation. This is primarily due to the very limited sand-covered area in 1984, which leads to small denominator values and consequently inflates the percentage error. The error decreases asymptotically to a mean value below 25% around 2006 and further drops to approximately 10% towards the end of the simulation. The error in all three areas exhibits a seasonality with larger values normally associated with the winter period.

To further explore the seasonality of the error between the simulated and observed area covered by the Sacalin spit, a statistical analysis of the monthly error spanning the entire duration of the simulation was performed. Quantiles of the absolute error for each calendar month have been calculated and are depicted in panel a of Figure 6.16. Logically the smallest values of the error fall within or follow immediately after the assimilation period when the model is reset with an observation. A gradual increase is seen following the assimilation period with peak error values being observed during the winter (between December and April). Subsequently the error is decreasing during the spring and summer period suggesting seasonal dependencies in model performance. Quantiles of the wave energy flux calculated by Equation 6.5 and observation counts of all available images used in the present work for each calendar month during the 40 years between mid 1984 and mid 2024 are depicted in panels b and c of Figure 6.16 respectively. The correlation r and significance p of each variable with the median value of the absolute observation error for each month are indicated in the respective panels of the figure. The seasonality in the absolute

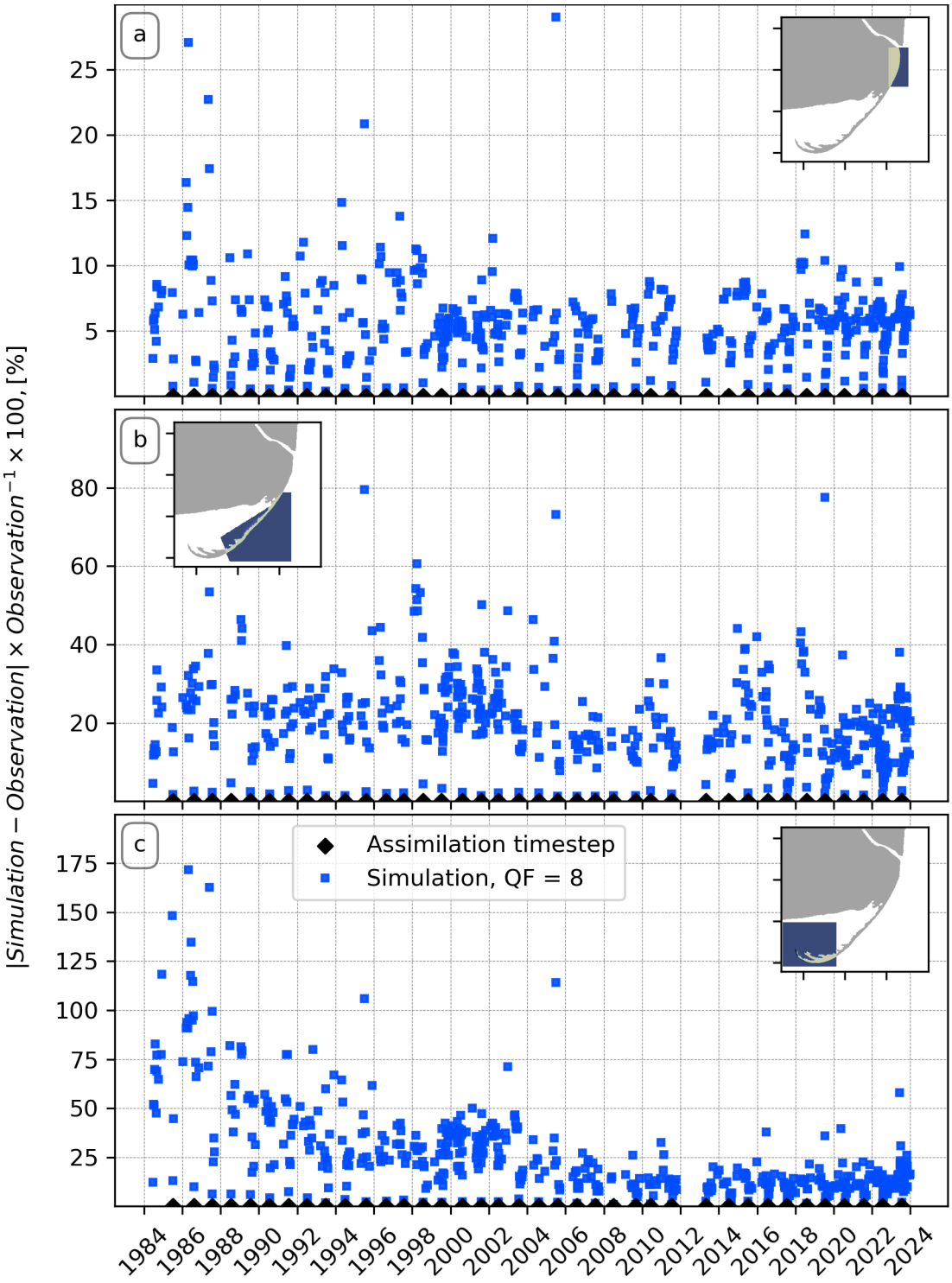

Figure 6.15: Temporal evolution of the absolute difference between simulated and observed land area within the three defined sectors of the Sacalin spit. The areas considered in the land area analysis are outlined in the insets of each panel. The error is expressed as a percentage of the total observed spit area at each comparison time, while the assimilation timesteps are indicated by the black diamonds along the time axis.

observation error has a positive and negative correlation with the seasonal wave energy and the annual distribution of observations, respectively.

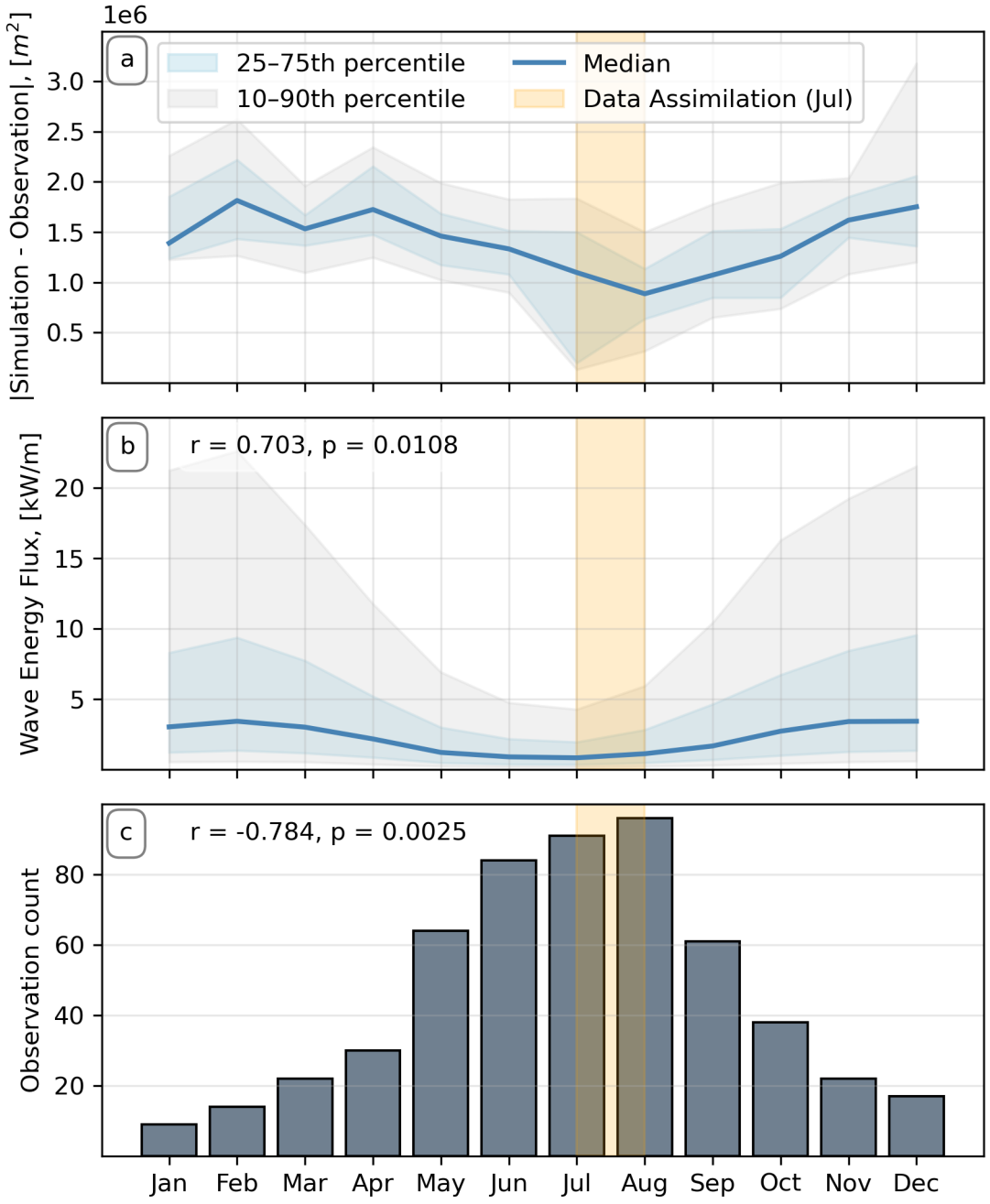

Figure 6.16: (Panel a, b) Absolute simulation error and wave energy flux quantiles per calendar month(10th–90th percentile shading, median line). (Panel c) Observation count per calendar month of all available images used in the present work (see Figure 6.5). The correlation and p value of the monthly statistics presented in each panel with the monthly median absolute error are indicated in the respective panel. The orange-shaded region marks the assimilation period.

The wave energy flux E_f shown in panel b of Figure 6.16, also known as wave power per unit crest length expressed in W/m, in arbitrary depths can be calculated as:

$$E_f = \frac{1}{16}\rho g H_s^2 \frac{\omega}{k}\left(1 + \frac{2kh}{\tanh(2kh)}\right) \tag{6.5}$$

where ρ is the water density in kg/m^3, g is the acceleration of gravity in m/s^2, H_s is the wave

height in m, ω is the wave angular frequency in rad/s, calculated by $\omega = 2\pi/T_p$, where T_p is the peak period of the incoming wave, k is the wave number with units 1/m calculated by numerically solving the linear dispersion relation $\omega^2 = gk\tanh(kh)$ and h is the water depth in m.

Figure 6.17 illustrates the percentage of time each grid cell differs from the corresponding satellite-derived observation over the simulation period. Consistent with the baseline simulations, the model exhibits persistent errors along the domain boundaries due to zero sediment flux boundary conditions, and at the Sfântu Gheorghe river mouth, where natural river flow would normally maintain an open channel. Within the lagoon, error frequencies exceed 15%, reflecting unrepresented processes in LX-Shore. In contrast, along the east coast of the Sacalin spit, exposed to the Black Sea, the model agrees with observations nearly 80% of the time, indicating that dominant shoreline-change processes driven by longshore sediment transport are well captured by the model between successive assimilation steps.

6.5 Discussion

The results of this study demonstrate the potential of combining satellite-derived shoreline observations with process-based morphodynamic modelling to investigate the long-term evolution of complex coastal systems such as the Sacalin spit. The preliminary analysis of the 40-year satellite record revealed distinct morphodynamic phases and spatial variability in erosion and accretion patterns across the three characteristic zones of the system — the attached barrier, the central barrier, and the tip of the spit — providing essential context for model configuration and interpretation. By integrating these remotely sensed observations with the LX-Shore model, the study successfully captured key patterns of sediment redistribution and shoreline change driven by wave forcing along the Danube Delta's southern lobe. The baseline simulations provided valuable insights into the dominant sediment transport pathways and the sensitivity of the system to the littoral drift calibration factor, while the subsequent data assimilation experiments significantly improved the agreement between simulated and observed shoreline evolution. Despite these improvements, some discrepancies remained — particularly in regions affected by processes not explicitly represented in the model, such as overwash, breaching, lagoon sediment dynamics, sediment supply in the domain as well as fluvial hydrodynamics and sediment transport. These findings highlight both the strengths and current limitations of hybrid satellite–model approaches for reconstructing and predicting coastal morphodynamics at decadal timescales.

Satellite-based remote sensing offers unprecedented opportunities for monitoring coastal dynamics across large spatial and temporal scales, particularly in remote or data-scarce regions, through various proxies such as shoreline position (Graffin et al., 2025b). Nevertheless, several limitations affect the reliability and consistency of satellite-derived observations. Since images are acquired by different satellite missions, variations in sensor characteristics can introduce inconsistencies in long-term time series spanning the 40 years of available data (Vitousek et al., 2023a).

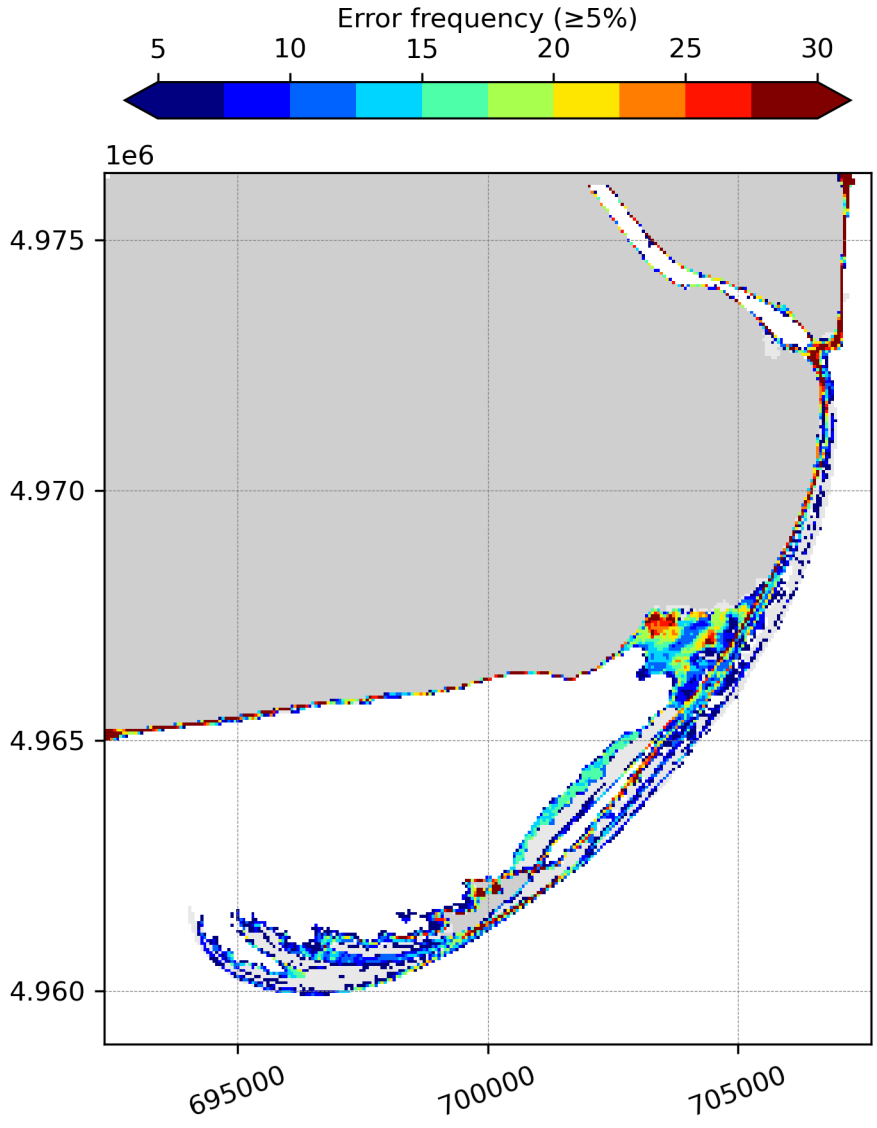

Figure 6.17: Percentage of timesteps each cell was found to differ from the observation for the simulation assimilating observations annually.

Additional discrepancies may arise from differences in post-processing procedures, such as geo-referencing accuracy and map projection methods, which can further affect the spatio-temporal consistency of the dataset. As optical observations, satellite images are also highly sensitive to cloud coverage—a limitation present across most regions of the globe and particularly pronounced at higher latitudes. Cloud obstruction, more frequent during winter months, introduces seasonal variability in observation frequency, resulting in irregular temporal sampling and potentially biasing the captured shoreline dynamics (Konstantinou et al., 2023).

In the present study, only 27% of the available satellite images were deemed suitable for mor-

phological analysis and assimilation in the modelling workflow, meaning that more than two-thirds of the data had to be discarded. This underscores the importance of rigorous quality control and consistent processing workflows to ensure dataset reliability. Manual inspection, combined with a standardized and reproducible image-processing pipeline such as the one implemented in this work (Figure 6.1), can substantially mitigate these limitations and help extract the most accurate and consistent shoreline information from long-term satellite archives.

The findings of the morphological analysis (based solely on the the satellite-derived observations) are consistent with previous research on the Sacalin spit based on in-situ observations and detailed knowledge of local coastal dynamics (e.g., Zăinescu et al., 2019). The Sacalin spit and the broader Danube Delta region represent a highly dynamic coastal environment, where multiple physical processes—such as wave-driven cross-shore and longshore sediment transport, fluvial sediment input, overwash, and barrier island breaching—interact in complex and highly nonlinear ways. The sole satellite-derived observations allowed to capture the major morphological trends and transitions of the system. The analysis successfully identified distinct morphodynamic phases and revealed the spatio-temporal patterns of erosion and accretion that characterize the long-term evolution of the Sacalin spit.

The LX-Shore model has been successfully applied to simulate shoreline instabilities and complex coastal geometries (Robinet et al., 2018). However, it does not explicitly account for key physical processes such as overwash events, fluvial hydro-sedimentary dynamics, and the influence of coastal vegetation. These processes play a crucial role in the Sacalin spit system and represent significant challenges for accurately modelling its morphological evolution. Despite these limitations, the baseline simulations—initialized directly from satellite-derived fractional sediment grids—provided valuable insights into the dominant processes shaping different sectors of the spit. When used not as a purely predictive tool but rather as a framework for interpreting observations in conjunction with environmental forcing, LX-Shore simulations offered an effective means of improving our understanding of the morphodynamic behaviour of the Sacalin spit.

During the preliminary analysis, baseline simulations of the Sacalin spit were forced with the ERA5 wave reanalysis dataset (Hersbach et al., 2023b), which has a coarser spatial resolution and is extracted further offshore compared to the nearshore Black Sea wave reanalysis time series (Staneva et al., 2022). These tests highlighted the critical importance of accurately representing the nearshore wave field to reproduce the morphodynamic evolution of the coastline. When forced with the offshore ERA5 data, the relatively short Black Sea wave periods resulted in highly oblique nearshore incidence angles. Because shorter waves undergo limited refraction, this—combined with the simplified bathymetric representation in the model—produced an unrealistic nearshore wave field, which subsequently yielded unphysical morphodynamic patterns, including wave-like spurious depositional and erosional features along the Sacalin coastline. These findings underscore the importance of accurate nearshore wave forcing for reliable morphodynamic simulations. A dynamic coupling of LX-Shore with the spectral wave model SWAN (Booij et al., 1999), already

implemented and tested by Robinet et al. (2018), could substantially improve model performance, albeit at increased computational cost.

Assimilating satellite-derived fractional sediment grids into LX-Shore at a quasi-annual frequency, using an appropriate relaxation parameter, effectively kept the model on track by implicitly accounting for processes not represented within its physical framework. Although LX-Shore considers only longshore sediment transport, the model successfully reproduced the large-scale morphological evolution of a highly dynamic and complex coastal system between assimilation steps. Analysis of the spatio-temporal evolution of model error provided valuable insights into system behaviour and the dominant drivers of morphodynamic variability across the Sacalin spit and its surrounding area. Seasonal fluctuations in model error were found to correlate positively with incoming wave energy, suggesting that high-energy conditions are associated with reduced model performance. Winter periods, characterized by increased river discharge, elevated water levels, and more frequent storm surges, likely influence the extent of the submerged area in the shallow and low-lying nearshore region, further affecting model accuracy.

The satellite-derived observations themselves are based on pixel colour classification, which can be influenced by seasonal variations in vegetation, thereby increasing observational uncertainty. As the model is initialized and assimilates data primarily acquired during the summer months, this seasonal bias may amplify discrepancies between simulated and observed areas. Furthermore, the seasonal fluctuations of the model's absolute error display a negative correlation with the temporal distribution of available satellite observations. While correlation does not necessarily imply causation, this pattern suggests that periods of reduced observation frequency may contribute additional uncertainty, negatively impacting the model–observation comparison.

Overall, these findings underscore the importance of frequent, seasonally distributed observations for effectively constraining morphodynamic models and highlight the potential of satellite-derived data to improve understanding and prediction of complex coastal evolution when integrated thoughtfully with process-based modelling.

6.6 Conclusions

In the present work, we provided a proof of concept for assimilating two-dimensional, satellite-derived shoreline data within a grid-based model framework. The implementation of 2D data assimilation in the LX-Shore model demonstrates a robust approach for integrating long-term observations into coastal morphodynamic simulations. By assimilating a 40-year dataset, the method constrained model evolution across the full 2D grid, implicitly accounting for unresolved processes and improving agreement with observed shoreline changes. Applied to the Sacalin spit, this framework enabled the identification of distinct morphodynamic phases, spatial patterns of erosion and accretion, and variability across seasonal, interannual, and decadal timescales, highlighting

the value of combining observational datasets with dynamic modelling to understand and predict complex shoreline evolution. Baseline simulations demonstrated the dominant role of longshore sediment transport while highlighted the effect of not accounting for overwash processes, barrier breaching, and fluvial sediment dynamics in the shoreline model. Analysis of the spatio-temporal error of the assimilated simulations, further revealed the influence of wave energy, water level fluctuations, and observational variability on model performance. These results demonstrate the value of integrating remote sensing with hybrid modelling approaches to advance the understanding of complex coastal systems.

Chapter 7

Conclusion and future perspectives

7.1 Conclusions

The present work focuses on advancing the understanding and prediction of contemporary shoreline evolution under a changing climate. It integrates data from multiple publicly available sources—including satellite-derived shorelines, in situ measurements, and publicly available wave forcing from global and regional models—within hybrid modelling frameworks. A central objective is to generate long-term, consistent, and physically informed datasets of waterlines and shoreline positions, alongside complementary products that support coastal morphodynamic analysis and modelling over periods exceeding four decades (1984–present). This effort also aims to establish robust satellite-to-model workflows that emphasize a clear and objective definition of the shoreline, careful selection of proxies, and methodological repeatability, enabling consistent application across diverse coastal settings and advancing progress toward a universal approach.

Building on this foundation, the work introduces a novel approach for calibrating equilibrium-based shoreline models (e.g. Davidson et al., 2013) using uncorrected, noisy satellite-derived shoreline (SDS) data. The study was conducted at Truc Vert beach, a fully exposed, wave-dominated sandy coastline on the Atlantic coast of France, deliberately selected for its high-energy waves, extensive tidal range, multiple nearshore bar systems, and gently sloping beachface. These conditions amplify uncertainties in satellite-derived shorelines due to wave run-up, tidal aliasing, and intertidal variability, making Truc Vert an ideal testbed for assessing the lower limits of SDS usability. Despite the low signal-to-noise ratio, model calibration guided by high-quality wave forcing (Hersbach et al., 2020) and optimized through a simulated annealing algorithm (Bertsimas and Tsitsiklis, 1993) produced robust and physically consistent results. Notably, the performance of models calibrated with raw SDS data was comparable to that of models using higher-quality, corrected SDS or in situ observations. While corrected datasets offer improved precision, they often provide lower temporal density, whereas the uncorrected SDS offered higher observation frequency, which proved critical for successful calibration. Alongshore averaging alone was suf-

ficient for preprocessing, while additional site-specific corrections did not systematically enhance model skill. These findings demonstrate that valuable information can be extracted from uncorrected SDS without prior knowledge of local hydrodynamic or morphodynamic conditions, providing a conservative assessment of their potential and supporting broad applicability in other sites where model physics capture the dominant processes.

While the successful calibration of 1D equilibrium models confirms the robustness of the approach, applying uncorrected SDS directly in sequential data assimilation frameworks proved more challenging (Ibaceta et al., 2020). High noise levels and uncertainties hindered the ability of the algorithms to track system non-stationarity reliably, limiting their effectiveness for dynamically updating model free parameters. To address this, in situ observations were used to investigate whether temporal variability in model free parameters could be linked to changes in wave climate and whether implementing temporally varying parameters via data assimilation could enhance predictive skill of the model (Davidson et al., 2013). Analyses across multiple sites along the European Atlantic coast revealed that the connection between parameter variability and regional climate forcing was weak or absent, suggesting that observed non-stationarity might primarily reflect local morphodynamic adjustments rather than direct climate controls.

Models with non-stationary free parameters, which allow temporal variation, provided additional insights into shoreline dynamics. Across the sites considered, the introduction of time-varying parameters led to slightly improved predictive performance at some locations, whereas skill was reduced at others, suggesting that the benefits of non-stationarity depend on both site characteristics and the quality of the observational record. In particular, sites with higher-quality in situ data tended to benefit more from temporally varying parameters, reflecting the greater ability of the assimilation framework to detect meaningful trends when observation noise is limited (Alvarez-Cuesta et al., 2024). Importantly, non-stationary models were particularly effective at capturing extreme erosion events, which are typically associated with forcing conditions far from the mean, highlighting their potential for understanding and forecasting rare but significant coastal changes. At the investigated sites, improvements remained limited, likely because the wave climate is primarily seasonal and unimodal, with relatively small deviations from the mean. Greater benefits from non-stationary parameterizations would be expected in regions exposed to multimodal wave climates, where distinct variability in forcing provides stronger signals for adaptive parameter adjustments (Splinter et al., 2017; Ibaceta et al., 2022).

Building on these insights, an ad hoc hybrid framework was developed to couple two equilibrium-based models, explicitly representing both cross-shore and longshore sediment transport (Davidson et al., 2013; Jaramillo et al., 2021a). Non-linear calibration was used to determine best-fit model free parameters (Bertsimas and Tsitsiklis, 1993), while sequential assimilation (Ibaceta et al., 2020) of projected shoreline trends compensated for cascading errors arising from imperfect wave forcing (Bell et al., 2021). This combined approach successfully simulated shoreline evolution over temporal scales from a few years to up to a century. Application to a multi-transect site allowed linear

decomposition of shoreline signals into rotational and cross-shore components, each independently calibrated and then recombined to produce continuous shoreline predictions. The methodology reproduced observed positions within measurement accuracy and performed comparably to the top submissions in the Shoreshop 2.0 international benchmark (Mao et al., 2025), demonstrating its capacity to resolve alongshore variability, multi-scale dynamics, and mitigate the limitations of traditional equilibrium-type models that are shoreline-position independent.

Finally, the work provides a proof of concept for quasi-2D assimilation of satellite-derived shoreline data within a grid-based framework using LX-Shore (Robinet et al., 2018). The Sacalin Spit in the southern lobe of the Danube Delta was chosen for this application due to its highly dynamic behaviour and dominant local processes—such as overwash, barrier breaching, and fluvial sediment dynamics—not explicitly represented in the model. This challenging setting provided a rigorous test for the ability of data assimilation to account for unresolved processes and constrain model evolution across the 2D grid. In this application, the assimilation approach was implemented as a nudging scheme rather than a filtering algorithm, progressively adjusting modelled shoreline positions toward observations without explicitly updating model free parameters. Assimilation of a 40-year SDS dataset improved agreement with observations, enabled identification of distinct morphodynamic phases, spatial patterns of erosion and accretion, and variability across seasonal, interannual, and decadal timescales. Baseline simulations highlighted the predominant influence of longshore sediment transport while revealing the limitations of neglecting other key processes. Spatio-temporal error analysis further illuminated the influence of wave energy, water level fluctuations, and observational uncertainty on model performance. Collectively, these results demonstrate the potential of quasi-2D data assimilation to compensate for unresolved processes, constrain model dynamics, and provide valuable insight into the spatiotemporal structure of model error, reinforcing the broader conclusion that integrating remote sensing with hybrid modelling and data assimilation is a powerful approach for understanding and predicting shoreline evolution in morphodynamically complex systems.

7.2 Future perspectives

Building on the findings of the present work, future research should focus on extending the application of satellite-derived shorelines (SDS) to a broader range of coastal environments. To achieve this objective, a first perspective focuses on incorporating the satellite data into shoreline change models. While current analyses primarily rely on optical sensors such as Landsat and Sentinel-2 (Vitousek et al., 2023a), the inclusion of complementary datasets from alternative missions can improve both spatial and temporal coverage and provide richer insights into coastal processes. High-resolution constellations such as PlanetScope offer near-daily observations that capture short-term shoreline responses to storms and other extreme events (Doherty et al., 2022), while radar-based datasets such as Sentinel-1 enable all-weather, day-and-night monitoring, partic-

ularly valuable in regions with frequent cloud cover or seasonal variability in illumination. Emerging missions such as SWOT (Fu et al., 2024) provide the opportunity to study inundation dynamics, fluvial–coastal interactions, and transient hydromorphological processes, especially in low-lying deltaic environments where water and sediment exchange critically influences shoreline evolution. Figure 7.1 shows a diagram illustrating the swaths of data that SWOT satellite collects while orbiting the earth.

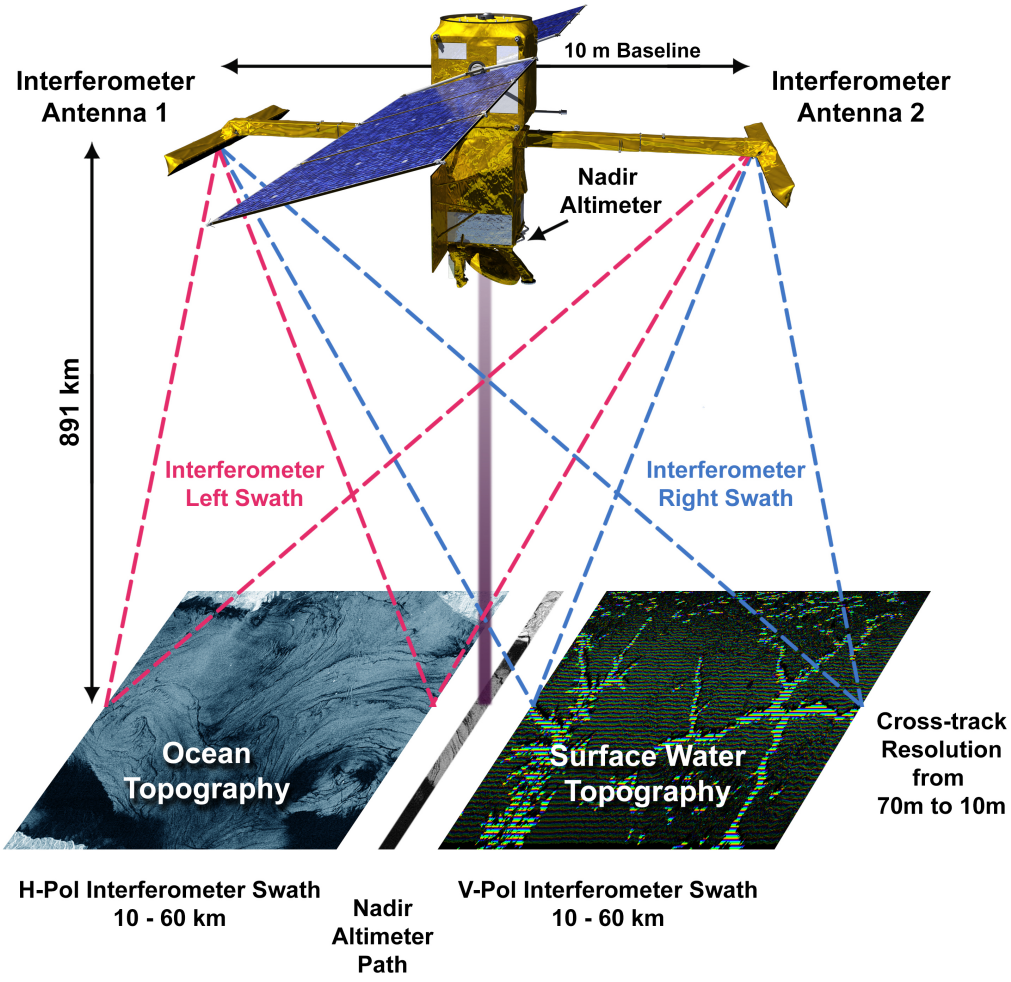

Figure 7.1: A diagram illustrating the swaths of data that SWOT collects. The interferometer will produce two parallel tracks, with a Nadir track from a traditional altimeter in the gap between the swaths. The overall width of the swaths is approximately 120 km. The diagram is downloaded from `https://swot.jpl.nasa.gov/resources/104/diagram-of-swot-data-collection/`

The integration of these diverse observation types through multi-source data assimilation represents a key next step. Combining optical, radar, and altimetric datasets within hybrid modelling frameworks such as LX-Shore would enable a more comprehensive representation of subaerial and subaqueous morphodynamic processes and their interactions across different scales. This approach also provides a mechanism to constrain model uncertainty by capturing complementary aspects of coastal change, for example using optical data for shoreline delineation, radar for inundation ex-

tent, and SWOT-derived elevation changes to infer water storage and exchange patterns. Extending the SDS database to include a larger and more diverse set of sites is essential for developing generalized model parameterizations and adaptive data assimilation schemes, allowing for systematic evaluation of model behaviour under varying morphodynamic and climatic conditions.

Further methodological development should focus on robust, transferable data assimilation workflows that can account for missing processes, parameter uncertainty, and site-specific variability, moving toward a universal modelling framework. Standardizing workflows for shoreline extraction, proxy selection, and model integration will facilitate repeatable and transferable procedures applicable across diverse coastlines. Large-scale applications of the model-calibration framework, based on uncorrected SDS and non-supervised optimization, could be applied over extended coastal regions, generating spatially continuous model ensembles with no a priori site-specific knowledge. Such analyses would enable the mapping of regional distributions of free model parameters, identification of systematic relationships between parameter variability and environmental forcing, and classification of coastal sectors according to dominant processes (e.g., cross-shore, longshore, or mixed transport regimes).

A central aspect of future work is the exploration of spatiotemporal variability in model free parameters, in order to better understand system and model behaviour and ultimately improve the model's predictive skill. Both sequential and variational data assimilation approaches should be applied to examine how parameters evolve in space and time in response to environmental forcing such as wave energy and water-level variability (Alvarez-Cuesta et al., 2024; Douglas et al., 2025). Ensemble-based and probabilistic methods, including Ensemble Kalman Filters (EnKF), Particle Filters (PF), and hybrid ensemble–variational approaches, provide complementary pathways for quantifying uncertainty (Mattern et al., 2013; Miller and Ehret, 2014; Ibaceta et al., 2020; Alvarez-Cuesta et al., 2024; Douglas et al., 2025). EnKF offers computational efficiency and works well under moderate uncertainties with approximately Gaussian dynamics, making it suitable for large 2D domains where processes are relatively linear (e.g., Almeida et al., 2015; Vitousek et al., 2017; Ibaceta et al., 2020; Alvarez-Cuesta et al., 2021a). PF, by contrast, allows the full representation of non-Gaussian, nonlinear system behaviour, such as abrupt barrier breaching, storm-induced erosion, or river mouth migration (e.g., Mattern et al., 2013; Miller and Ehret, 2014). Hybrid approaches that combine EnKF and PF can leverage the efficiency of EnKF while capturing extreme, nonlinear dynamics, offering a flexible toolset for robust 2D assimilation of heterogeneous observations, including multi-source satellite and in situ datasets.

Another key perspective in terms of development is 2D assimilation. Indeed, the present work implemented a quasi-2D approach, where each grid point in the model was assimilated independently with the corresponding observation point, without accounting for interactions with neighbouring grid cells. While effective, proper 2D assimilation, which explicitly considers spatial correlations between adjacent grid points, could better capture the propagation of morphodynamic signals, local coherence, and cross-shore/alongshore feedbacks. Future research should investi-

gate the benefits of fully 2D assimilation schemes, comparing them against quasi-2D approaches to quantify improvements in model skill, uncertainty representation, and predictive reliability.

Integration of multiple data types—including SDS, radar, altimetry, and in situ measurements such as wave buoys, tide gauges, and lidar—will enhance predictive skill, enable cross-validation, and provide a comprehensive assessment of model performance (Vitousek et al., 2023a). Within 2D assimilation frameworks such as LX-Shore, ensemble-based and probabilistic approaches will allow explicit quantification of parameter and state uncertainties, assessment of local sensitivities, evaluation of spatial coherence, and propagation of uncertainty through the model domain. This capability is crucial for developing physically grounded, adaptive parameter schemes that respond dynamically to environmental forcing rather than relying solely on empirical calibration.

Finally, to increase our understanding in shoreline dynamics, these methodological advancements should be coupled with expansion in spatial and temporal scales. Applying SDS-based calibration and assimilation across regional or global coastlines would facilitate large-scale meta-analyses, enabling the identification of universal patterns in shoreline behaviour and process-dominated domains. Such approaches would allow direct comparison of coastal types, linking free-parameter variability to environmental forcing, and informing adaptive, scalable modelling frameworks. By integrating multi-source observations, probabilistic assimilation techniques, and standardized workflows, future research can move toward universal, data-driven shoreline models capable of accurately representing the non-stationary, complex dynamics of coastal systems under evolving climate conditions.

Bibliography

Aagaard, T., Davidson-Arnott, R., Greenwood, B., and Nielsen, J. (2004). Sediment supply from shoreface to dunes: Linking sediment transport measurements and long-term morphological evolution. *Geomorphology*, 60:205–224.

Aagaard, T. and Holm, J. (1989). Digitization of wave run-up using video records. *Journal of Coastal Research*, 5(3):547–551.

Aarninkhof, S. and Holman, R. (1999). Monitoring the nearshore with video. *Backscatter*, 10(2):8–11.

Aarninkhof, S. G., Turner, I. L., Dronkers, T. D., Caljouw, M., and Nipius, L. (2003). A video-based technique for mapping intertidal beach bathymetry. *Coastal Engineering*, 49:275–289.

Abdulsalam, M. B., Jaramillo, C., de Freitas, L., González, M., and Antolínez, J. A. (2025). Assessing shoreline orientation variation across diverse coastal environments. *Coastal Engineering*, 200.

Accensi, M. and Maisondieu, C. (2015). Homere. Technical report, Ifremer - Laboratoire Comportement des Structures en Mer, Ifremer - Laboratoire Spatial et Interfaces Air-Mer.

Aleman, N., Robin, N., Certain, R., Anthony, E. J., and Barusseau, J. P. (2015). Longshore variability of beach states and bar types in a microtidal, storm-influenced, low-energy environment. *Geomorphology*, 241:175–191.

Almar, R., Boucharel, J., Graffin, M., Abessolo, G. O., Thoumyre, G., Papa, F., Ranasinghe, R., Montano, J., Bergsma, E. W., Baba, M. W., and Jin, F. F. (2023). Influence of el niño on the variability of global shoreline position. *Nature Communications*, 14.

Almar, R., Coco, G., Bryan, K. R., Huntley, D. A., Short, A. D., and Senechal, N. (2008). Video observations of beach cusp morphodynamics. *Marine Geology*, 254:216–223.

Almar, R., Ranasinghe, R., Snchal, N., Bonneton, P., Roelvink, D., Bryan, K. R., Marieu, V., and Parisot, J. P. (2012). Video-based detection of shorelines at complex mesomacro tidal beaches. *Journal of Coastal Research*, 28:1040–1048.

Almeida, L. P., de Oliveira, I. E., Lyra, R., Dazzi, R. L. S., Martins, V. G., and da Fontoura Klein, A. H. (2021). Coastal analyst system from space imagery engine (cassie): Shoreline management module. *Environmental Modelling and Software*, 140.

Almeida, L. P., Masselink, G., Russell, P. E., and Davidson, M. A. (2015). Observations of gravel beach dynamics during high energy wave conditions using a laser scanner. *Geomorphology*, 228:15–27.

Almonacid-Caballer, J., Pardo-Pascual, J. E., and Ruiz, L. A. (2017). Evaluating fourier cross-correlation sub-pixel registration in landsat images. *Remote Sensing*, 9.

Alvarez-Cuesta, M., Toimil, A., and Losada, I. J. (2021a). Modelling long-term shoreline evolution in highly anthropized coastal areas. part 1: Model description and validation. *Coastal Engineering*, 169.

Alvarez-Cuesta, M., Toimil, A., and Losada, I. J. (2021b). Modelling long-term shoreline evolution in highly anthropized coastal areas. part 2: Assessing the response to climate change. *Coastal Engineering*, 168.

Alvarez-Cuesta, M., Toimil, A., and Losada, I. J. (2024). Which data assimilation method to use and when: unlocking the potential of observations in shoreline modelling. *Environmental Research Letters*, 19.

Anders, F. J. and Byrnes, M. R. (1991). Accuracy of shoreline change rates as determined from maps and aerial photographs. *Shore & Beach*, 59(2):17–26.

Andrews, B. D., Gares, P. A., and Colby, J. D. (2002). Techniques for gis modeling of coastal dunes. *Geomorphology*, 48:289–308.

Antolínez, J. A., Méndez, F. J., Anderson, D., Ruggiero, P., and Kaminsky, G. M. (2019). Predicting climate-driven coastlines with a simple and efficient multiscale model. *Journal of Geophysical Research: Earth Surface*, 124:1596–1624.

Ardhuin, F. and Accensi, M. (2012). Prévisions de vagues (ww3) pour la façade golfe de gascogne / nord atlantique (grille non structurée - ww3- norgas-ug). Technical report, CNRS, Ifremer.

Ashton, A. D. and Murray, A. B. (2006). High-angle wave instability and emergent shoreline shapes: 1. modeling of sand waves, flying spits, and capes. *Journal of Geophysical Research: Earth Surface*, 111.

Azorakos, G., Castelle, B., Marieu, V., and Idier, D. (2024). Satellite-derived equilibrium shoreline modelling at a high-energy meso-macrotidal beach. *Coastal Engineering*, 191:104536.

Baily, B. and Nowell, D. (1996). Techniques for monitoring coastal change: a review and case study. *Ocean & Coastal Management*, 32:85–95.

Banno, M., Nakamura, S., Kosako, T., Nakagawa, Y., Yanagishima, S. I., and Kuriyama, Y. (2020). Long-term observations of beach variability at hasaki, japan. *Journal of Marine Science and Engineering*, 8:1–17.

Barbier, E. B., Hacker, S. D., Kennedy, C., Koch, E. W., Stier, A. C., and Silliman, B. R. (2011). The value of estuarine and coastal ecosystem services. *Ecological Monographs*, 81:169–193.

Barnard, P. L., Dugan, J. E., Page, H. M., Wood, N. J., Hart, J. A., Cayan, D. R., Erikson, L. H., Hubbard, D. M., Myers, M. R., Melack, J. M., and Iacobellis, S. F. (2021). Multiple climate change-driven tipping points for coastal systems. *Scientific Reports*, 11.

Barnard, P. L., Short, A. D., Harley, M. D., Splinter, K. D., Vitousek, S., Turner, I. L., Allan, J., Banno, M., Bryan, K. R., Doria, A., Hansen, J. E., Kato, S., Kuriyama, Y., Randall-Goodwin, E., Ruggiero, P., Walker, I. J., and Heathfield, D. K. (2015). Coastal vulnerability across the pacific dominated by el niño/southern oscillation. *Nature Geoscience*, 8:801–807.

Bayram, B., Acar, U., Seker, D., and Ari, A. (2008). A novel algorithm for coastline fitting through a case study over the bosphorus. *Journal of Coastal Research*, 24(4):983–991.

Bell, B., Hersbach, H., Simmons, A., Berrisford, P., Dahlgren, P., Horányi, A., Muñoz-Sabater, J., Nicolas, J., Radu, R., Schepers, D., Soci, C., Villaume, S., Bidlot, J. R., Haimberger, L., Woollen, J., Buontempo, C., and Thépaut, J. N. (2021). The era5 global reanalysis: Preliminary extension to 1950. *Quarterly Journal of the Royal Meteorological Society*, 147:4186–4227.

Belward, A. S. and Skøien, J. O. (2015). Who launched what, when and why; trends in global land-cover observation capacity from civilian earth observation satellites. *ISPRS Journal of Photogrammetry and Remote Sensing*, 103:115–128.

Bergsma, E. W. and Almar, R. (2018). Video-based depth inversion techniques, a method comparison with synthetic cases. *Coastal Engineering*, 138:199–209.

Bergsma, E. W., Conley, D. C., Davidson, M. A., and O'Hare, T. J. (2016). Video-based nearshore bathymetry estimation in macro-tidal environments. *Marine Geology*, 374:31–41.

Bergsma, E. W., Klotz, A. N., Artigues, S., Graffin, M., Prenowitz, A., Delvit, J. M., and Almar, R. (2024). Shoreliner: A sub-pixel coastal waterline extraction pipeline for multi-spectral satellite optical imagery. *Remote Sensing*, 16.

Bertin, S., Floc'h, F., Dantec, N. L., Jaud, M., Cancouët, R., Franzetti, M., Cuq, V., Prunier, C., Ammann, J., Augereau, E., Lamarche, S., Belleney, D., Rouan, M., David, L., Deschamps, A., Delacourt, C., and Suanez, S. (2022). A long-term dataset of topography and nearshore bathymetry at the macrotidal pocket beach of porsmilin, france. *Scientific Data*, 9.

Bertsimas, D. and Tsitsiklis, J. (1993). Simulated annealing. *Statistical Science*, 8:10–15.

Bijker, E. W. (1971). Longshore transport computations. *Journal of the Waterways, Harbors and Coastal Engineering Division*, 97(4):687–701.

Birrien, F., Castelle, B., Marieu, V., and Dubarbier, B. (2013). On a data-model assimilation method to inverse wave-dominated beach bathymetry using heterogeneous video-derived observations. *Ocean Engineering*, 73:126–138.

Bishop-Taylor, R., Nanson, R., Sagar, S., and Lymburner, L. (2021). Mapping australia's dynamic coastline at mean sea level using three decades of landsat imagery. *Remote Sensing of Environment*, 267.

Blenkinsopp, C. E., Mole, M. A., Turner, I. L., and Peirson, W. L. (2010). Measurements of the time-varying free-surface profile across the swash zone obtained using an industrial lidar. *Coastal Engineering*, 57:1059–1065.

Blenkinsopp, C. E., Turner, I. L., Allis, M. J., Peirson, W. L., and Garden, L. E. (2012). Application of lidar technology for measurement of time-varying free-surface profiles in a laboratory wave flume. *Coastal Engineering*, 68:1–5.

Blodget, H. W., Taylor, P. T., and Roark, J. H. (1991). Shoreline changes along the rosetta-nile promontory: Monitoring with satellite observations. *Marine Geology*, 99:67–77.

Boak, E. H. and Turner, I. L. (2005). Shoreline definition and detection: A review. *Journal of Coastal Research*, 21:688–703.

Bondar, C. and Panin, N. (2001). The danube delta hydrologic database and modelling. *Geo-Eco-Marina*, 5(6):5–52.

Booij, N., Ris, R. C., and Holthuijsen, L. H. (1999). A third-generation wave model for coastal regions: 1. model description and validation. *Journal of Geophysical Research*, 104:7649–7666.

Boudière, E., Maisondieu, C., Ardhuin, F., Accensi, M., Pineau-Guillou, L., and Lepesqueur, J. (2013). A suitable metocean hindcast database for the design of marine energy converters. *International Journal of Marine Energy*, 3-4.

Bracs, M. A., Turner, I. L., and Short, A. (2015). Evaluation of opportunistic shoreline monitoring capability utilizing existing "surfcam" infrastructure. *Journal of Coastal Research*.

Brodie, K. L., Raubenheimer, B., Elgar, S., Slocum, R. K., and McNinch, J. E. (2015). Lidar and pressure measurements of inner-surfzone waves and setup. *Journal of Atmospheric and Oceanic Technology*, 32:1945–1959.

Broecker, W. S. (1975). Climatic change: Are we on the brink of a pronounced global warming? *Science*, 189(4201):460–463.

Bruun, P. (1962). Sea-level rise as a cause of shore erosion. *Journal of the Waterways and Harbors Division*, 88(1):117–132.

Burvingt, O., Masselink, G., Russell, P., and Scott, T. (2017). Classification of beach response to extreme storms. *Geomorphology*, 295:722–737.

Burvingt, O., Masselink, G., Scott, T., Davidson, M., and Russell, P. (2018). Climate forcing of regionally-coherent extreme storm impact and recovery on embayed beaches. *Marine Geology*, 401:112–128.

Cabezas-Rabadán, C., Pardo-Pascual, J. E., Almonacid-Caballer, J., and Rodilla, M. (2019). Detecting problematic beach widths for the recreational function along the gulf of valencia (spain) from landsat 8 subpixel shorelines. *Applied Geography*, 110.

Calcraft, K., Simmons, J. A., Marshall, L. A., and Splinter, K. D. (2025a). A mixture of experts approach to sandy shoreline modelling in storm dominated systems. *Coastal Engineering*, 201.

Calcraft, K., Splinter, K. D., Simmons, J. A., and Marshall, L. A. (2025b). Do lstm memory states reflect the relationships in reduced-complexity sandy shoreline models. *Environmental Modelling and Software*, 183.

Calkoen, F. R., Luijendijk, A. P., Vos, K., Kras, E., and Baart, F. (2025). Enabling coastal analytics at planetary scale. *Environmental Modelling and Software*, 183.

Carr, A. P. (1962). Cartographie record and historical accuracy. *Source: Geography*, 47:135–144.

Carvalho, R. C., Kennedy, D. M., Niyazi, Y., Leach, C., Konlechner, T. M., and Ierodiaconou, D. (2020). Structure-from-motion photogrammetry analysis of historical aerial photography: Determining beach volumetric change over decadal scales. *Earth Surface Processes and Landforms*, 45:2540–2555.

Castelle, B., Bujan, S., Ferreira, S., and Dodet, G. (2017a). Foredune morphological changes and beach recovery from the extreme 2013/2014 winter at a high-energy sandy coast. *Marine Geology*, 385:41–55.

Castelle, B., Bujan, S., Ferreira, S., and Dodet, G. (2017b). Foredune morphological changes and beach recovery from the extreme 2013/2014 winter at a high-energy sandy coast. *Marine Geology*, 385:41–55.

Castelle, B., Bujan, S., Marieu, V., and Ferreira, S. (2020). 16 years of topographic surveys of rip-channelled high-energy meso-macrotidal sandy beach. *Scientific Data*, 7.

Castelle, B., Dodet, G., Masselink, G., and Scott, T. (2018a). Increased winter-mean wave height, variability, and periodicity in the northeast atlantic over 1949–2017. *Geophysical Research Letters*, 45:3586–3596.

Castelle, B., Guillot, B., Marieu, V., Chaumillon, E., Hanquiez, V., Bujan, S., and Poppeschi, C. (2018b). Spatial and temporal patterns of shoreline change of a 280-km high-energy disrupted sandy coast from 1950 to 2014: Sw france. *Estuarine, Coastal and Shelf Science*, 200:212–223.

Castelle, B., Guillot, B., Marieu, V., Chaumillon, E., Hanquiez, V., Bujan, S., and Poppeschi, C. (2018c). Spatial and temporal patterns of shoreline change of a 280-km high-energy disrupted sandy coast from 1950 to 2014: Sw france. *Estuarine, Coastal and Shelf Science*, 200:212–223.

Castelle, B., Kras, E., Masselink, G., Scott, T., Konstantinou, A., and Luijendijk, A. (2024). Satellite-derived sandy shoreline trends and interannual variability along the atlantic coast of europe. *Scientific Reports*, 14.

Castelle, B., Marieu, V., and Bujan, S. (2019a). Alongshore-variable beach and dune changes on the timescales from days (storms) to decades along the rip-dominated beaches of the gironde coast, sw france. *Journal of Coastal Research*, 88:157–171.

Castelle, B., Marieu, V., and Bujan, S. (2019b). Alongshore-variable beach and dune changes on the timescales from days (storms) to decades along the rip-dominated beaches of the gironde coast, sw france. *Journal of Coastal Research*, 88:157–171.

Castelle, B., Marieu, V., Bujan, S., Ferreira, S., Parisot, J. P., Capo, S., Sénéchal, N., and Chouzenoux, T. (2014). Equilibrium shoreline modelling of a high-energy meso-macrotidal multiple-barred beach. *Marine Geology*, 347:85–94.

Castelle, B., Marieu, V., Bujan, S., Splinter, K. D., Robinet, A., Sénéchal, N., and Ferreira, S. (2015). Impact of the winter 2013-2014 series of severe western europe storms on a double-barred sandy coast: Beach and dune erosion and megacusp embayments. *Geomorphology*, 238:135–148.

Castelle, B. and Masselink, G. (2023). Morphodynamics of wave-dominated beaches. *Cambridge Prisms: Coastal Futures*, 1:e1.

Castelle, B., Masselink, G., Scott, T., Stokes, C., Konstantinou, A., Marieu, V., and Bujan, S. (2021). Satellite-derived shoreline detection at a high-energy meso-macrotidal beach. *Geomorphology*, 383.

Castelle, B., Ritz, A., Marieu, V., Lerma, A. N., and Vandenhove, M. (2022). Primary drivers of multidecadal spatial and temporal patterns of shoreline change derived from optical satellite imagery. *Geomorphology*, 413.

Chaaban, F., Darwishe, H., Battiau-Queney, Y., Louche, B., Masson, E., Khattabi, J. E., and Carlier, E. (2012). Using ArcGIS® Modelbuilder and Aerial Photographs to Measure Coastline Retreat and Advance: North of France. *Journal of Coastal Research*, 28(6):1567 – 1579.

Chen, X., Banno, M., and Mori, N. (2025). Equilibrium shoreline change model with non-stationary free parameters at hasaki beach, japan. *Coastal Engineering*, 200.

Cipolletti, M. P., Delrieux, C. A., Perillo, G. M., and Piccolo, M. C. (2012). Superresolution border segmentation and measurement in remote sensing images. *Computers and Geosciences*, 40:87–96.

Clarkson, C., Jacobs, Z., Marwick, B., Fullagar, R., Wallis, L., Smith, M., Roberts, R. G., Hayes, E., Lowe, K., Carah, X., Florin, S. A., McNeil, J., Cox, D., Arnold, L. J., Hua, Q., Huntley, J., Brand, H. E., Manne, T., Fairbairn, A., Shulmeister, J., Lyle, L., Salinas, M., Page, M., Connell,

K., Park, G., Norman, K., Murphy, T., and Pardoe, C. (2017). Human occupation of northern australia by 65,000 years ago. *Nature*, 547:306–310.

Cobos, R. (2008). *Seaports of the Maya*, pages 1989–1992. Springer Netherlands, Dordrecht.

Coco, G. and Murray, A. B. (2007). Patterns in the sand: From forcing templates to self-organization. *Geomorphology*, 91:271–290.

Coco, G., Senechal, N., Rejas, A., Bryan, K. R., Capo, S., Parisot, J. P., Brown, J. A., and MacMahan, J. H. (2014). Beach response to a sequence of extreme storms. *Geomorphology*, 204:493–501.

Conti, S., Splinter, K. D., Booth, E., Djadjiguna, D., and Turner, I. L. (2024). Observations on the role of internal sand moisture dynamics in wave-driven dune face erosion. *Geomorphology*, 462.

Conti, S., Splinter, K. D., and Turner, I. L. (2025). Controlled laboratory measurements of dune erosion under variable waves, water levels and dune pore-moisture. *Scientific Data*, 12:1648.

Cooper, J. A. G., Masselink, G., Coco, G., Short, A. D., Castelle, B., Rogers, K., Anthony, E. J., Green, A. N., Kelley, J. T., Pilkey, O. H., and Jackson, D. W. T. (2020). Sandy beaches can survive sea-level rise. *Nature Climate Change*, 10:993 – 995.

Cosby, A. G., Lebakula, V., Smith, C. N., Wanik, D. W., Bergene, K., Rose, A. N., Swanson, D., and Bloom, D. E. (2024). Accelerating growth of human coastal populations at the global and continent levels: 2000–2018. *Scientific Reports*, 14.

Cozannet, G. L., Bulteau, T., Castelle, B., Ranasinghe, R., Wöppelmann, G., Rohmer, J., Bernon, N., Idier, D., Louisor, J., and y Mélia, D. S. (2019). Quantifying uncertainties of sandy shoreline change projections as sea level rises. *Scientific Reports*, 9.

Crowell, M., Douglas, B. C., and Leatherman, S. P. (1997). On forecasting future u.s. shoreline positions: A test of algorithms. *Journal of Coastal Research*, 13(4):1245–1255.

Crowell, M., Leatherman, S. P., and Buckley, M. K. (1991). Historical shoreline change: error analysis and mapping accuracy. *Journal of Coastal Research*, 7(3):839–852.

Dan, S., Stive, M., and Westhuysen, A. (2007). Alongshore sediment transport capacity computation on the coastal zone of the danube delta using a simulated wave climate. *GeoEcoMarina*, 13:21–30.

Dan, S., Walstra, D. J. R., Stive, M. J., and Panin, N. (2011). Processes controlling the development of a river mouth spit. *Marine Geology*, 280:116–129.

D'Anna, M., Castelle, B., Idier, D., Rohmer, J., Cozannet, G. L., Thieblemont, R., and Bricheno, L. (2021). Uncertainties in shoreline projections to 2100 at truc vert beach (france): Role of sea-level rise and equilibrium model assumptions. *Journal of Geophysical Research: Earth Surface*, 126.

D'Anna, M., Idier, D., Castelle, B., Cozannet, G. L., Rohmer, J., and Robinet, A. (2020). Impact of model free parameters and sea-level rise uncertainties on 20-years shoreline hindcast: the case of truc vert beach (sw france). *Earth Surface Processes and Landforms*, 45:1895–1907.

D'Anna, M., Idier, D., Castelle, B., Rohmer, J., Cagigal, L., and Mendez, F. J. (2022). Effects of stochastic wave forcing on probabilistic equilibrium shoreline response across the 21st century including sea-level rise. *Coastal Engineering*, 175.

Davidson, M. (2021). Forecasting coastal evolution on time-scales of days to decades. *Coastal Engineering*, 168.

Davidson, M., Koningsveld, M. V., de Kruif, A., Rawson, J., Holman, R., Lamberti, A., Medina, R., Kroon, A., and Aarninkhof, S. (2007). The coastview project: Developing video-derived coastal state indicators in support of coastal zone management. *Coastal Engineering*, 54:463–475.

Davidson, M. A., Splinter, K. D., and Turner, I. L. (2013). A simple equilibrium model for predicting shoreline change. *Coastal Engineering*, 73:191–202.

Davidson, M. A. and Turner, I. L. (2009). A behavioral template beach profile model for predicting seasonal to interannual shoreline evolution. *Journal of Geophysical Research: Earth Surface*, 114.

de Santiago, I., Camus, P., González, M., Liria, P., Epelde, I., Chust, G., del Campo, A., and Uriarte, A. (2021). Impact of climate change on beach erosion in the basque coast (ne spain). *Coastal Engineering*, 167.

de Vries, S., Hill, D. F., de Schipper, M. A., and Stive, M. J. (2011). Remote sensing of surf zone waves using stereo imaging. *Coastal Engineering*, 58:239–250.

Dean, J. and Ghemawat, S. (2008). Mapreduce: Simplified data processing on large clusters. *Communications of the ACM*, 51:107–113.

Dean, R. G. (1991). Equilibrium beach profiles: Characteristics and applications. *Journal of Coastal Research*, 7(1):53–84.

Deigaard, R., Fredsøe, J., and Hedegaard, I. B. (1986). Mathematical model for littoral drift. *Journal of Waterway, Port, Coastal, and Ocean Engineering*, 112(3):351–369.

Dewi, R. S., Bijker, W., Stein, A., and Marfai, M. A. (2018). Transferability and upscaling of fuzzy classification for shoreline change over 30 years. *Remote Sensing*, 10.

Dillehay, T. D., Bonavia, D., Goodbred, S. L., Pino, M., Vásquez, V., and Tham, T. R. (2012). A late pleistocene human presence at huaca prieta, peru, and early pacific coastal adaptations. *Quaternary Research*, 77:418–423.

Dodet, G., Castelle, B., Masselink, G., Scott, T., Davidson, M., Floc, F., Jackson, D., and Suanez, S. S. (2019). Beach recovery from extreme storm activity during the 2013/14 winter along the atlantic coast of europe. *Earth Surface Processes and Landforms*, 44.

Doherty, Y., Harley, M. D., Vos, K., and Splinter, K. D. (2022). A python toolkit to monitor sandy shoreline change using high-resolution planetscope cubesats. *Environmental Modelling and Software*, 157.

Donchyts, G., Baart, F., Winsemius, H., Gorelick, N., Kwadijk, J., and Giesen, N. V. D. (2016). Earth's surface water change over the past 30 years. *Nature Climate Change*, 6:810–813.

Douglas, N., Quaife, T., and Bannister, R. (2025). Exploring a hybrid ensemble–variational data assimilation technique (4denvar) with a simple ecosystem carbon model. *Environmental Modelling and Software*, 186.

Durand, E., Castelle, B., Idier, D., Marieu, V., Robinet, A., and Guérin, T. (2024). Influence of rocky obstacle sand bypassing on embayed beach dynamics using a reduced-complexity shoreline model. *Journal of Marine Science and Engineering*, 12.

Elfrink, B. and Baldock, T. (2002). Hydrodynamics and sediment transport in the swash zone: a review and perspectives. *Coastal Engineering*, 45:149–167.

Emery, K. O. (1961). A simple method of measuring beach profiles. *Limnology and Oceanography*, 6:90–93.

Evensen, G. (2009). The ensemble kalman filter for combined state and parameter estimation: Monte carlo techniques for data assimilation in large systems. *IEEE Control Systems*, 29:83–104.

Fernández-Mora, A., Criado-Sudau, F. F., Gómez-Pujol, L., Tintoré, J., and Orfila, A. (2023). Ten years of morphodynamic data at a micro-tidal urban beach: Cala millor (western mediterranean sea). *Scientific Data*, 10.

Fletcher, S. J. (2017). *Chapter 1 - Introduction*. Elsevier.

Foody, G. M., Muslim, A. M., and Atkinson, P. M. (2005). Super-resolution mapping of the waterline from remotely sensed data. *International Journal of Remote Sensing*, 26(24):5381–5392.

Ford, M. (2013). Shoreline changes interpreted from multi-temporal aerial photographs and high resolution satellite images: Wotje atoll, marshall islands. *Remote Sensing of Environment*, 135:130–140.

Fredsøe, J. and Deigaard, R. (1992). *Mechanics of coastal sediment transport*. World Scientific.

Frihy, O. E. (1988). Nile delta shoreline changes: Aerial photographic study of a 28-year period. *Journal of Coastal Research*, 4(4):597–606.

Fu, L. L., Pavelsky, T., Cretaux, J. F., Morrow, R., Farrar, J. T., Vaze, P., Sengenes, P., Vinogradova-Shiffer, N., Sylvestre-Baron, A., Picot, N., and Dibarboure, G. (2024). The surface water and ocean topography mission: A breakthrough in radar remote sensing of the ocean and land surface water. *Geophysical Research Letters*, 51.

Gallagher, E. L., MacMahan, J., Reniers, A., Brown, J., and Thornton, E. B. (2011). Grain size variability on a rip-channeled beach. *Marine Geology*, 287(1-4):43 – 53.

García-Rubio, G., Huntley, D., and Russell, P. (2015). Evaluating shoreline identification using optical satellite images. *Marine Geology*, 359:96–105.

Ghermandi, A. and Nunes, P. A. (2013). A global map of coastal recreation values: Results from a spatially explicit meta-analysis. *Ecological Economics*, 86:1–15.

Gorelick, N., Hancher, M., Dixon, M., Ilyushchenko, S., Thau, D., and Moore, R. (2017). Google earth engine: Planetary-scale geospatial analysis for everyone. *Remote Sensing of Environment*, 202:18–27.

Graffin, M., Almar, R., Bergsma, E. W., Boucharel, J., Vitousek, S., Taherkhani, M., and Ruggiero, P. (2025a). Waterline responses to climate forcing along the north american west coast. *Communications Earth and Environment*, 6.

Graffin, M., Taherkhani, M., Leung, M., Vitousek, S., Kaminsky, G., and Ruggiero, P. (2023). Monitoring interdecadal coastal change along dissipative beaches via satellite imagery at regional scale. *Cambridge Prisms: Coastal Futures*, 1.

Graffin, M., Touzé, T., Bergsma, E. W., and Almar, R. (2025b). Towards a global assessment of sandy shorelines: Systematic extraction and validation of optical satellite-derived coastal indicators at various sites. *Remote Sensing of Environment*, 331:115033.

Gupta, E., Prabhakar, V. N., and Jain, V. (2024). Sabarmati and its connection with the harappan port lothal and the nal corridor: A study using multi-sensor data, cloud-computing and multi-platforms. *Journal of Archaeological Science*, 170.

Hagenaars, G., de Vries, S., Luijendijk, A. P., de Boer, W. P., and Reniers, A. J. (2018). On the accuracy of automated shoreline detection derived from satellite imagery: A case study of the sand motor mega-scale nourishment. *Coastal Engineering*, 133:113–125.

Hanson, H. (1989). Genesis: A generalized shoreline change numerical model. *Journal of Coastal Research*, 5(1):1–27.

Harley, M. D., Kinsela, M. A., Sánchez-García, E., and Vos, K. (2019). Shoreline change mapping using crowd-sourced smartphone images. *Coastal Engineering*, 150:175–189.

Harley, M. D., Turner, I. L., Kinsela, M. A., Middleton, J. H., Mumford, P. J., Splinter, K. D., Phillips, M. S., Simmons, J. A., Hanslow, D. J., and Short, A. D. (2017). Extreme coastal erosion enhanced by anomalous extratropical storm wave direction. *Scientific Reports*, 7:1–9.

Harley, M. D., Turner, I. L., and Short, A. D. (2015). New insights into embayed beach rotation: The importance of wave exposure and cross-shore processes. *Journal of Geophysical Research: Earth Surface*, 120:1470–1484.

Harley, M. D., Turner, I. L., Short, A. D., and Ranasinghe, R. (2011). Assessment and integration of conventional, rtk-gps and image-derived beach survey methods for daily to decadal coastal monitoring. *Coastal Engineering*, 58:194–205.

Hayes, M. O. (1967). Marine geology-elsevier publishing company, amsterdam-printed in the netherlands relationship between coastal climate and bottom sediment type on the inner continental shelf. *Marine Geol*, 5:111–132.

Hersbach, Bell, B., Berrisford, P., Biavati, G., Horányi, A., Sabater, J. M., Nicolas, J., Peubey, C., Radu, R., Rozum, I., Schepers, D., Simmons, A., Soci, C., Dee, D., and Thépaut, J.-N. (2023a). Era5 hourly data on single levels from 1940 to present. *Copernicus Climate Change Service (C3S) Climate Data Store (CDS)*, (Accessed on 16-Oct-2023).

Hersbach, H., Bell, B., Berrisford, P., Hirahara, S., Horányi, A., Muñoz-Sabater, J., Nicolas, J., Peubey, C., Radu, R., Schepers, D., Simmons, A., Soci, C., Abdalla, S., Abellan, X., Balsamo, G., Bechtold, P., Biavati, G., Bidlot, J., Bonavita, M., Chiara, G. D., Dahlgren, P., Dee, D., Diamantakis, M., Dragani, R., Flemming, J., Forbes, R., Fuentes, M., Geer, A., Haimberger, L., Healy, S., Hogan, R. J., Hólm, E., Janisková, M., Keeley, S., Laloyaux, P., Lopez, P., Lupu, C., Radnoti, G., de Rosnay, P., Rozum, I., Vamborg, F., Villaume, S., and Thépaut, J. N. (2023b). Era5 hourly data on single levels from 1940 to present. Technical report, Copernicus Climate Change Service (C3S), Climate Data Store (CDS). Accessed on 02-May-2025.

Hersbach, H., Bell, B., Berrisford, P., Hirahara, S., Horányi, A., Muñoz-Sabater, J., Nicolas, J., Peubey, C., Radu, R., Schepers, D., Simmons, A., Soci, C., Abdalla, S., Abellan, X., Balsamo, G., Bechtold, P., Biavati, G., Bidlot, J., Bonavita, M., Chiara, G. D., Dahlgren, P., Dee, D., Diamantakis, M., Dragani, R., Flemming, J., Forbes, R., Fuentes, M., Geer, A., Haimberger, L., Healy, S., Hogan, R. J., Hólm, E., Janisková, M., Keeley, S., Laloyaux, P., Lopez, P., Lupu, C., Radnoti, G., de Rosnay, P., Rozum, I., Vamborg, F., Villaume, S., and Thépaut, J. N. (2020). The era5 global reanalysis. *Quarterly Journal of the Royal Meteorological Society*, 146:1999–2049.

Hofland, B., Diamantidou, E., van Steeg, P., and Meys, P. (2015). Wave runup and wave overtopping measurements using a laser scanner. *Coastal Engineering*, 106:20–29.

Holland, K. T. and Holman, R. A. (1999). Wavenumber-frequency structure of infragravity swash motions. *Journal of Geophysical Research: Oceans*, 104:13479–13488.

Holman, R. and Haller, M. C. (2013). Remote sensing of the nearshore. *Annual Review of Marine Science*, 5:95–113.

Holman, R., Plant, N., and Holland, T. (2013). Cbathy: A robust algorithm for estimating nearshore bathymetry. *Journal of Geophysical Research: Oceans*, 118:2595–2609.

Holman, R., Stanley, J., and Ozkan-Haller, T. (2003). Applying video sensor networks to nearshore environment monitoring. *IEEE Pervasive Computing*, 2(4):14–21.

Holman, R. A. and Guza, R. T. (1984). Measuring run-up on a natural beach. *Coastal Engineering*, 8:129–140.

Holman, R. A. and Stanley, J. (2007). The history and technical capabilities of argus. *Coastal Engineering*, 54:477–491.

Holthuijsen, L. H. (2007). *Waves in Oceanic and Coastal Waters*. Cambridge University Press.

Hotta, S., Mizuguchi, M., and Isobe, M. (1981). Observations of long period waves in the nearshore zone. *Coastal Engineering in Japan*, 24(1):41–76.

Hunt, E., Davidson, M., Steele, E. C., Amies, J. D., Scott, T., and Russell, P. (2023). Shoreline modelling on timescales of days to decades. *Cambridge Prisms: Coastal Futures*, 1.

Ibaceta, R., Splinter, K. D., Harley, M. D., and Turner, I. L. (2020). Enhanced coastal shoreline modeling using an ensemble kalman filter to include nonstationarity in future wave climates. *Geophysical Research Letters*, 47.

Ibaceta, R., Splinter, K. D., Harley, M. D., and Turner, I. L. (2022). Improving multi-decadal coastal shoreline change predictions by including model parameter non-stationarity. *Frontiers in Marine Science*, 9.

Irish, J. L. and White, T. E. (1998). Coastal engineering applications of high-resolution lidar bathymetry. *Coastal Engineering*, 35:47–71.

Jaramillo, C., González, M., Medina, R., and Turki, I. (2021a). An equilibrium-based shoreline rotation model. *Coastal Engineering*, 163.

Jaramillo, C., Jara, M. S., González, M., and Medina, R. (2021b). A shoreline evolution model for embayed beaches based on cross-shore, planform and rotation equilibrium models. *Coastal Engineering*, 169.

Jaud, M., Augereau, E., Saint-Cyr, T., Dantec, N. L., and Delacourt, C. (2025). Variance-based shoreline extraction from nearshore video monitoring systems. *Earth Surface Processes and Landforms*, 50.

Jiménez, J. A., Sánchez-Arcilla, A., Bou, J., and Ortiz, M. A. (1997). Analysing short-term shoreline changes along the ebro delta (spain) using aerial photographs. *Journal of Coastal Research*, 13(4):1256–1266.

Johnson, J. W., editor (1950). *Proceedings of the first conference in coastal engineering*.

Kaergaard, K. and Fredsoe, J. (2013). A numerical shoreline model for shorelines with large curvature. *Coastal Engineering*, 74:19–32.

Kalman, R. E. (1960). A new approach to linear filtering and prediction problems. *Journal of Basic Engineering*, 82:35–45.

Kalnay, E., Li, H., Miyoshi, T., Yang, S. C., and Ballabrera-Poy, J. (2007). 4-d-var or ensemble kalman filter? *Tellus, Series A: Dynamic Meteorology and Oceanography*, 59:758–773.

Kamphuis, J. W. (1991). Alongshore sediment transport rate. *Journal of Waterway, Port, Coastal, and Ocean Engineering*, 117(6):624–640.

Kamphuis, J. W. (2006). Coastal engineering - quo vadis? *Coastal Engineering*, 53:133–140.

Kamphuis, J. W., Davies, M. H., Nairn, R. B., and Sayao, O. J. (1986). Calculation of littoral sand transport rate. *Coastal engineering*, 10(1):1–22.

Konstantinou, A., Scott, T., Masselink, G., Stokes, K., Conley, D., and Castelle, B. (2023). Satellite-based shoreline detection along high-energy macrotidal coasts and influence of beach state. *Marine Geology*, 462:107082.

Kraus, N. C. (2018). *History and Heritage of Coastal Engineering*. American Society of Civil Engineers.

Kristensen, S. E., Drønen, N., Deigaard, R., and Fredsoe, J. (2016). Impact of groyne fields on the littoral drift: A hybrid morphological modelling study. *Coastal Engineering*, 111:13–22.

Kuleli, T., Guneroglu, A., Karsli, F., and Dihkan, M. (2011). Automatic detection of shoreline change on coastal ramsar wetlands of turkey. *Ocean Engineering*, 38:1141–1149.

Labarthe, C., Castelle, B., Marieu, V., Garlan, T., and Bujan, S. (2023). Observation and modeling of the equilibrium slope response of a high-energy meso-macrotidal sandy beach. *Journal of Marine Science and Engineering*, 11:584.

Lahoz, W. A. and Schneider, P. (2014). Data assimilation: Making sense of earth observation. *Frontiers in Environmental Science*, 2.

Lakshmivarahan, S. and Lewis, J. M. (2013). *Nudging Methods: A Critical Overview*, pages 27–57. Springer Berlin Heidelberg, Berlin, Heidelberg.

Laporte-Fauret, Q., Castelle, B., Marieu, V., Nicolae-Lerma, A., and Rosebery, D. (2022). Foredune blowout formation and subsequent evolution along a chronically eroding high-energy coast. *Geomorphology*, 414.

Laporte-Fauret, Q., Lubac, B., Castelle, B., Michalet, R., Marieu, V., Bombrun, L., Launeau, P., Giraud, M., Normandin, C., and Rosebery, D. (2020). Classification of atlantic coastal sand dune vegetation using in situ, uav, and airborne hyperspectral data. *Remote Sensing*, 12.

Larson, M. (1989). Sbeach: Numerical model for simulating storm-induced beach change. report 1. empirical foundation and model development. Technical report, Vicksburg, Miss, Dept. of the Army, Waterways Experiment Station, United States Army Corps of Engineers, Coastal Engineering Research Center, 1984.

Larson, M. and Kraus, N. C. (1994). Temporal and spatial scales of beach profile change, duck, north carolina. *Marine Geology*, 117:75–94.

Larson, M. and Kraus, N. C. (1995). Prediction of cross-shore sediment transport and temporal scales at different spatial. *Marine Geology*, 126:11–127.

Larson, M., Le, X. H., and Hanson, H. (2010). Direct formula to compute wave height and angle at incipient breaking. *Journal of Waterway, Port, Coastal, and Ocean Engineering*, 136:119–122.

Leatherman, S. P. and Pajak, M. J. (2002). The high water line as shoreline indicator. *Article in Journal of Coastal Research*, pages 329–337.

Lerma, A. N., Ayache, B., Ulvoas, B., Paris, F., Bernon, N., Bulteau, T., and Mallet, C. (2019). Pluriannual beach-dune evolutions at regional scale: Erosion and recovery sequences analysis along the aquitaine coast based on airborne lidar data. *Continental Shelf Research*, 189.

Levallois, J. J. (1988). *Mesurer la Terre. 300 Ans de Géodésie Française, Presses Ponts et Chaussées*. Presses de l'Ecole nationale des ponts et chaussées ; 136 bis rue de Grenelle : Association française de topographie.

Lippmann, T. C. and Holman, R. A. (1989). Quantification of sand bar morphology: a video technique based on wave dissipation. *Journal of Geophysical Research*, 94:995–1011.

Lippmann, T. C. and Holman, R. A. (1990). The spatial and temporal variability of sand bar morphology. *Journal of Geophysical Research*, 95.

Liu, Q., Trinder, J. C., and Turner, I. L. (2017). Automatic super-resolution shoreline change monitoring using Landsat archival data: a case study at Narrabeen–Collaroy Beach, Australia. *Journal of Applied Remote Sensing*, 11(1):016036.

Long, J. W. and Plant, N. G. (2012). Extended kalman filter framework for forecasting shoreline evolution. *Geophysical Research Letters*, 39.

Ludka, B. C., Guza, R. T., O'Reilly, W. C., Merrifield, M. A., Flick, R. E., Bak, A. S., Hesser, T., Bucciarelli, R., Olfe, C., Woodward, B., Boyd, W., Smith, K., Okihiro, M., Grenzeback, R., Parry, L., and Boyd, G. (2019). Sixteen years of bathymetry and waves at san diego beaches. *Scientific Data*, 6.

Luijendijk, A., Hagenaars, G., Ranasinghe, R., Baart, F., Donchyts, G., and Aarninkhof, S. (2018). The state of the world's beaches. *Scientific Reports*, 8.

Maiti, S. and Bhattacharya, A. K. (2009). Shoreline change analysis and its application to prediction: A remote sensing and statistics based approach. *Marine Geology*, 257:11–23.

Mao, Y., Coco, G., Vitousek, S., Antolinez, J. A. A., Azorakos, G., Banno, M., Bouvier, C., Bryan, K. R., Cagigal, L., Calcraft, K., Castelle, B., Chen, X., D'Anna, M., de Freitas Pereira, L., de Santiago, I., Deshmukh, A. N., Dong, B., Elghandour, A., Gohari, A., de la Peña, E. G., Harley, M. D., Ibrahim, M., Idier, D., Cardona, C. J., Lim, C., Mingo, I., O'Grady, J., Pais, D., Repina, O., Robinet, A., Roelvink, D., Simmons, J., Sogut, E., Wilson, K., and Splinter, K. D. (2025). Benchmarking shoreline prediction models over multi-decadal timescales. *Communications Earth & Environment*, 6:581.

Mao, Y., Harris, D. L., Xie, Z., and Phinn, S. (2021). Efficient measurement of large-scale decadal shoreline change with increased accuracy in tide-dominated coastal environments with google earth engine. *ISPRS Journal of Photogrammetry and Remote Sensing*, 181:385–399.

Marean, C. W. (2010). Pinnacle point cave 13b (western cape province, south africa) in context: The cape floral kingdom, shellfish, and modern human origins. *Journal of Human Evolution*, 59:425–443.

Marean, C. W. (2014). The origins and significance of coastal resource use in africa and western eurasia. *Journal of Human Evolution*, 77:17–40.

Marriner, N., Morhange, C., Flaux, C., and Carayon, N. (2017). *Harbors and Ports, Ancient*, pages 382–403. Springer Netherlands, Dordrecht.

Martins, K., Blenkinsopp, C. E., Deigaard, R., and Power, H. E. (2018). Energy dissipation in the inner surf zone: New insights from lidar-based roller geometry measurements. *Journal of Geophysical Research: Oceans*, 123:3386–3407.

Martins, K., Blenkinsopp, C. E., Power, H. E., Bruder, B., Puleo, J. A., and Bergsma, E. W. (2017). High-resolution monitoring of wave transformation in the surf zone using a lidar scanner array. *Coastal Engineering*, 128:37–43.

Martins, K., Blenkinsopp, C. E., and Zang, J. (2016). Monitoring individual wave characteristics in the inner surf with a 2-dimensional laser scanner (lidar). *Journal of Sensors*, 2016.

Masselink, G., Castelle, B., Scott, T., Dodet, G., Suanez, S., Jackson, D., and Floc'H, F. (2016). Extreme wave activity during 2013/2014 winter and morphological impacts along the atlantic coast of europe. *Geophysical Research Letters*, 43:2135–2143.

Masselink, G., Castelle, B., Scott, T., and Konstantinou, A. (2023). Role of atmospheric indices in describing shoreline variability along the atlantic coast of europe. *Geophysical Research Letters*, 50.

Masselink, G. and Puleo, J. A. (2006). Swash-zone morphodynamics. *Continental Shelf Research*, 26:661–680.

Masselink, G., Russell, P., Turner, I., and Blenkinsopp, C. (2009). Net sediment transport and morphological change in the swash zone of a high-energy sandy beach from swash event to tidal cycle time scales. *Marine Geology*, 267:18–35.

Mattern, J. P., Dowd, M., and Fennel, K. (2013). Particle filter-based data assimilation for a three-dimensional biological ocean model and satellite observations. *Journal of Geophysical Research: Oceans*, 118:2746–2760.

Mauff, B. L., Juigner, M., Ba, A., Robin, M., Launeau, P., and Fattal, P. (2018). Coastal monitoring solutions of the geomorphological response of beach-dune systems using multi-temporal lidar datasets (vendée coast, france). *Geomorphology*, 304:121–140.

McAllister, E., Payo, A., Novellino, A., Dolphin, T., and Medina-Lopez, E. (2022). Multispectral satellite imagery and machine learning for the extraction of shoreline indicators. *Coastal Engineering*, 174.

McCann, M. P., Anderson, D. L., Sherwood, C. R., Bruder, B., Bak, A. S., and Brodie, K. L. (2022). Coastalimagelib: An open- source python package for creating common coastal image products. *SoftwareX*, 20.

McCarroll, R., Valiente, N., Wiggins, M., Scott, T., and Masselink, G. (2023). Coastal survey data for perranporth beach and start bay in southwest england (2006–2021). *Scientific Data*, 10(1).

McFeeters, S. K. (1996). The use of the normalized difference water index (ndwi) in the delineation of open water features. *International Journal of Remote Sensing*, 17(7):1425–1432.

Mclaughlin, D., O'Neill, A., Derber, J., and Kamachi, M. (2006). Opportunities for enhanced collaboration within the data assimilation community. *Quarterly Journal of the Royal Meteorological Society*, 131:3683–3693.

McLean, R. and Shen, J.-S. (2006). From foreshore to foredune: Foredune development over the last 30 years at Moruya beach, New South Wales, Australia. *Journal of Coastal Research*, 22(1):28–36.

McLean, R., Thom, B., Shen, J., and Oliver, T. (2023). 50 years of beach–foredune change on the southeastern coast of Australia: Bengello beach, Moruya, NSW, 1972–2022. *Geomorphology*, 439.

Mentaschi, L., Vousdoukas, M., Garcia-Sanchez, G., Montblanc, T. F., Roland, A., Voukouvalas, E., Federico, I., Abdolali, A., Zhang, Y. J., and Feyen, L. (2023). A global unstructured, coupled, high-resolution hindcast of waves and storm surges. *EarthArXiv*.

Mentaschi, L., Vousdoukas, M. I., Pekel, J. F., Voukouvalas, E., and Feyen, L. (2018). Global long-term observations of coastal erosion and accretion. *Scientific Reports*, 8.

Michaud, H., Pasquet, A., Leckler, F., Baraille, R., Dalphinet, A., and Aouf, L. (2016). Improvements of the new french coastal wave forecasting system and application to a wave-current interaction study. *14th International Workshop on Wave Hindcasting and Forecasting & 5th Coastal Hazard Symposium SHOM & Meteo France.*

Miller, J. K. and Dean, R. G. (2004). A simple new shoreline change model. *Coastal Engineering*, 51:531–556.

Miller, R. N. and Ehret, L. L. (2014). Application of the implicit particle filter to a model of nearshore circulation. *Journal of Geophysical Research: Oceans*, 119:2363–2385.

Montaño, J., Coco, G., Antolínez, J. A., Beuzen, T., Bryan, K. R., Cagigal, L., Castelle, B., Davidson, M. A., Goldstein, E. B., Ibaceta, R., Idier, D., Ludka, B. C., Masoud-Ansari, S., Méndez, F. J., Murray, A. B., Plant, N. G., Ratliff, K. M., Robinet, A., Rueda, A., Sénéchal, N., Simmons, J. A., Splinter, K. D., Stephens, S., Townend, I., Vitousek, S., and Vos, K. (2020). Blind testing of shoreline evolution models. *Scientific Reports*, 10.

Montreuil, A. L. and Bullard, J. E. (2012). A 150-year record of coastline dynamics within a sediment cell: Eastern england. *Geomorphology*, 179:168–185.

Moore, L. J. (2000). Shoreline mapping techniques. *Journal of Coastal Research*, 16(1):111–124.

Moore, L. J., Ruggiero, P., and List, J. H. (2006). Comparing mean high water and high water line shorelines: Should prosy-datum offsets be incorporated into shoreline change analysis? *Journal of Coastal Research*, 22:894–905.

Morton, R. A. (1991). Accurate shoreline mapping: past present and future. In *Proceedings of the Coastal Sediments '91*, pages 997–1010.

Muir, F. M., Hurst, M. D., Richardson-Foulger, L., Rennie, A. F., and Naylor, L. A. (2024). Vedgesat: An automated, open-source toolkit for coastal change monitoring using satellite-derived vegetation edges. *Earth Surface Processes and Landforms*, 49:2405–2423.

Munk, W. H. (1950). Origin and generation of waves. *Coastal Engineering Proceedings*, 1(1):1.

Murray, A. B. (2007). Reducing model complexity for explanation and prediction. *Geomorphology*, 90:178–191.

Muslim, A. M., Foody, G. M., and Atkinson, P. M. (2006). Localized soft classification for super-resolution mapping of the shoreline. *International Journal of Remote Sensing*, 27(11):2271–2285.

Ojeda, E., Ruessink, B. G., and Guillen, J. (2008). Morphodynamic response of a two-barred beach to a shoreface nourishment. *Coastal Engineering*, 55:1185–1196.

Otsu, N. (1979). A threshold selection method from gray-level histograms. *IEEE Transactions on Systems, Man, and Cybernetics*, 9(1):62–66.

Palmsten, M. L. and Brodie, K. L. (2022). The coastal imaging research network (cirn). *Remote Sensing*, 14.

Palmsten, M. L. and Holman, R. A. (2012). Laboratory investigation of dune erosion using stereo video. *Coastal Engineering*, 60:123–135.

Pardo-Pascual, J. E., Almonacid-Caballer, J., Ruiz, L. A., and Palomar-Vázquez, J. (2012). Automatic extraction of shorelines from landsat tm and etm+ multi-temporal images with subpixel precision. *Remote Sensing of Environment*, 123:1–11.

Pelnard-Considére, R. (1957). Essai de théorie de l'évolution des formes de rivage en plages de sable et de galets. In *Journées de l'hydraulique, Question IV. Energie mécanique de la marée : Essais sur modèles*, pages 289–298.

Phillips, M. S., Blenkinsopp, C. E., Splinter, K. D., Harley, M. D., and Turner, I. L. (2019). Modes of berm and beachface recovery following storm reset: Observations using a continuously scanning lidar. *Journal of Geophysical Research: Earth Surface*, 124:720–736.

Pianca, C., Holman, R., and Siegle, E. (2015). Shoreline variability from days to decades: Results of long-term video imaging. *Journal of Geophysical Research: Oceans*, 120:2159–2178.

Pikelj, K., Ružić, I., Ilić, S., James, M. R., and Kordić, B. (2018). Implementing an efficient beach erosion monitoring system for coastal management in croatia. *Ocean and Coastal Management*, 156:223–238.

Pineau-Guillou, L. (2013). Projet pj0303 : Océanographie côtière opérationnelle action a030310p : Cper-previmer volet 2-etude et validation de configurations modèles physiques département océanographie et dynamique des ecosystèmes unité dynamiques de l'environnement côtier laboratoire physique hydrodynamique et sédimentaire-ode/dyneco/physed/2013-05 version 1.0 previmer validation des modèles hydrodynamiques 2d des côtes de la manche et de l'atlantique. Technical report, Ifremer.

Planet (2023). *Planet Imagery Product Specifications*. Planet Labs Inc.

Plant, N. G., Holland, K. T., and Haller, M. C. (2008). Ocean wavenumber estimation from wave-resolving time series imagery. *IEEE Transactions on Geoscience and Remote Sensing*, 46:2644–2658.

Plant, N. G. and Holman, R. A. (1997). Intertidal beach profile estimation using video images. *Marine Geology*, 140:24.

Plant, N. G., Holman, R. A., Freilich, M. H., and Birkemeier, W. A. (1999). A simple model for interannual sandbar behavior. *Journal of Geophysical Research: Oceans*, 104:15755–15776.

Pontee, N. (2013). Defining coastal squeeze: A discussion. *Ocean and Coastal Management*, 84:204–207.

Preoteasa, L., Vespremeanu-Stroe, A., Tătui, F., Zăinescu, F., Timar-Gabor, A., and Cîrdan, I. (2016). The evolution of an asymmetric deltaic lobe (sf. gheorghe, danube) in association with cyclic development of the river-mouth bar: Long-term pattern and present adaptations to human-induced sediment depletion. *Geomorphology*, 253:59–73.

Ranasinghe, R. (2020). On the need for a new generation of coastal change models for the 21st century. *Scientific Reports*, 10.

Ranasinghe, R. and Turner, I. L. (2006). Shoreline response to submerged structures: A review. *Coastal Engineering*, 53:65–79.

Ratliff, K. M. and Murray, A. B. (2014). Modes and emergent time scales of embayed beach dynamics. *Geophysical Research Letters*, 41:7270–7275.

Reimann, L., Vafeidis, A. T., and Honsel, L. E. (2023). Population development as a driver of coastal risk: Current trends and future pathways. *Cambridge Prisms: Coastal Futures*, 1.

Repina, O., Carvalho, R. C., Coco, G., Antolínez, J. A., de Santiago, I., Harley, M. D., Jaramillo, C., Splinter, K. D., Vitousek, S., and Woodroffe, C. D. (2025). Evaluating five shoreline change models against 40 years of field survey data at an embayed sandy beach. *Coastal Engineering*, 199.

Ribas, F., Simarro, G., Arriaga, J., and Luque, P. (2020). Automatic shoreline detection from video images by combining information from different methods. *Remote Sensing*, 12:1–23.

Ricker, M., Behrens, A., and Staneva, J. (2024). The operational cmems wind wave forecasting system of the black sea. *Journal of Operational Oceanography*, 17:165–186.

Ritchie, G. S. (1991). The history of hydrography an enlightened european era 1660-1800. *The International Hydrographic Review*, 68(1).

Robin, N., Billy, J., Castelle, B., Hesp, P., Lerma, A. N., Laporte-Fauret, Q., Marieu, V., Rosebery, D., Bujan, S., Destribats, B., and Michalet, R. (2021). 150 years of foredune initiation and evolution driven by human and natural processes. *Geomorphology*, 374.

Robinet, A., Castelle, B., Idier, D., Cozannet, G. L., Déqué, M., and Charles, E. (2016). Statistical modeling of interannual shoreline change driven by north atlantic climate variability spanning 2000–2014 in the bay of biscay. *Geo-Marine Letters*, 36:479–490.

Robinet, A., Castelle, B., Idier, D., Harley, M. D., and Splinter, K. D. (2020). Controls of local geology and cross-shore/longshore processes on embayed beach shoreline variability. *Marine Geology*, 422.

Robinet, A., Idier, D., Castelle, B., and Marieu, V. (2018). A reduced-complexity shoreline change model combining longshore and cross-shore processes: The lx-shore model. *Environmental Modelling and Software*, 109:1–16.

Roelvink, D., Huisman, B., Elghandour, A., Ghonim, M., and Reyns, J. (2020). Efficient modeling of complex sandy coastal evolution at monthly to century time scales. *Frontiers in Marine Science*, 7.

Roelvink, D., Reniers, A., van Dongeren, A., van Thiel de Vries, J., McCall, R., and Lescinski, J. (2009). Modelling storm impacts on beaches, dunes and barrier islands. *Coastal Engineering*, 56:1133–1152.

Roelvink, J. D., Walstra, D.-J. R., van der Wegen, M., and Ranasinghe, R. (2016). *Modeling of Coastal Morphological Processes*, pages 611–634. Springer International Publishing, Cham.

Ruessink, B. G. and Kroon, A. (1994). The behaviour of a multiple bar system in the nearshore zone of terschelling, the netherlands: 1965-1993. *Marine Geology*, 121:187–197.

Río, L. D. and Gracia, F. J. (2013). Error determination in the photogrammetric assessment of shoreline changes. *Natural Hazards*, 65:2385–2397.

Sallenger., J. A. H., Krabill, W. B., Swift, R. N., Brock, J., List, J., Hansen, M., Holman, R. A., Manizade, S., Sontag, J., Meredith, A., Morgan, K., Yunkel, J. K., Frederick, E. B., and Stockdon, H. (2003). Evaluation of airborne topographic lidar for quantifying beach changes. *Journal of Coastal Research*, 19(1):125–133.

Saye, S. E., van der Wal, D., Pye, K., and Blott, S. J. (2005). Beach-dune morphological relationships and erosion/accretion: An investigation at five sites in england and wales using lidar data. *Geomorphology*, 72:128–155.

Schepper, R., Almar, R., Bergsma, E., de Vries, S., Reniers, A., Davidson, M., and Splinter, K. (2021). Modelling cross-shore shoreline change on multiple timescales and their interactions. *Journal of Marine Science and Engineering*, 9.

Scott, T., Masselink, G., and Russell, P. (2011). Morphodynamic characteristics and classification of beaches in england and wales. *Marine Geology*, 286:1–20.

Senechal, N., Coco, G., Bryan, K. R., and Holman, R. A. (2011). Wave runup during extreme storm conditions. *Journal of Geophysical Research: Oceans*, 116.

Sestras, P., Badea, G., Badea, A. C., Salagean, T., Roșca, S., Kader, S., and Remondino, F. (2025). Land surveying with uav photogrammetry and lidar for optimal building planning. *Automation in Construction*, 173.

Shepard, F. P. (1936). Undertow, rip tide or "rip current". *Science*, 84(2173):181–182.

Shepard, F. P. (1950). Beach cycles in southern california: Beach erosion board, technical memorandum no. 20. *Beach Erosion Board, Office of the Chief of Engineers*.

Shepard, F. P., Emery, K. O., and Fond, E. C. L. (1941). Rip currents: A process of geological importance. *The Journal of Geology*, 49(4):337–369.

Shepard, F. P. and Inman, D. L. (1951). Sand movement on the shallow inter-canyon shelf at la jolla, california: Beach erosion board, technical memorandum no. 26. *Beach Erosion Board, Office of the Chief of Engineers*.

Sherwood, C. R., Dongeren, A. V., Doyle, J., Hegermiller, C. A., Hsu, T.-J., Kalra, T. S., Olabarrieta, M., Penko, A. M., Rafati, Y., Roelvink, D., Lugt, M. V. D., Veeramony, J., and Warner, J. C. (2022). Modeling the morphodynamics of coastal responses to extreme events: What shape are we in? *Annual Review of Marine Science*, 18:35.

Short, A. D. (1975). Offshore bars along the alaskan arctic coast. *The Journal of Geology*, 83(2):209–221.

Short, A. D. and Trembanis, C. A. (2004). Decadal scale patterns in beach oscillation and rotation narrabeen beach, australia—time series, pca and wavelet analysis. *Journal of Coastal Research*, 20:523–532.

Simmons, J. A. and Splinter, K. D. (2025). Data-driven shoreline modelling at timescales of days to years. *Coastal Engineering*, 197.

Small, C. and Nichols, J. R. (2003). A global analysis of human settlement in coastal zones. *Journal of Coastal Research*, 19:584–589.

Smith, G. L. and Zarillo, G. A. (1990). Calculating long-term shoreline recession rates using aerial photographic and beach profiling techniques. *Journal of Coastal Research*, 6(1):111–120.

Soille, P. (2004). *Erosion and Dilation*, pages 63–103. Springer Berlin Heidelberg, Berlin, Heidelberg.

Soloy, A., Turki, I., Lecoq, N., Ángel David Gutiérrez Barceló, Costa, S., Laignel, B., Bazin, B., Soufflet, Y., Louargant, L. L., and Maquaire, O. (2021). A fully automated method for monitoring the intertidal topography using video monitoring systems. *Coastal Engineering*, 167.

Splinter, K. D. and Coco, G. (2021). Challenges and opportunities in coastal shoreline prediction. *Frontiers in Marine Science*, 8.

Splinter, K. D., Gonzalez, M. V. G., Oltman-Shay, J., Rutten, J., and Holman, R. (2018a). Observations and modelling of shoreline and multiple sandbar behaviour on a high-energy meso-tidal beach. *Continental Shelf Research*, 159:33–45.

Splinter, K. D., Kearney, E. T., and Turner, I. L. (2018b). Drivers of alongshore variable dune erosion during a storm event: Observations and modelling. *Coastal Engineering*, 131:31–41.

Splinter, K. D., Turner, I. L., and Davidson, M. A. (2013). How much data is enough? the importance of morphological sampling interval and duration for calibration of empirical shoreline models. *Coastal Engineering*, 77:14–27.

Splinter, K. D., Turner, I. L., Davidson, M. A., Barnard, P., Castelle, B., and Oltman-Shay, J. (2014). A generalized equilibrium model for predicting daily to interannual shoreline response. *Journal of Geophysical Research: Earth Surface*, 119:1936–1958.

Splinter, K. D., Turner, I. L., Reinhardt, M., and Ruessink, G. (2017). Rapid adjustment of shoreline behavior to changing seasonality of storms: observations and modelling at an open-coast beach. *Earth Surface Processes and Landforms*, 42:1186–1194.

Staneva, J., Ricker, M., and Behrens, A. (2022). Black sea waves analysis and forecast (cmems bs-waves, eas5 system) (version 1), [$cmems_m od_b lk_w av_m y_2.5km_p t1h - i$]. Technical report, Copernicus Monitoring Environment Marine Service (CMEMS). Accessed on 06-August-2025.

Stockdon, H. F. and Holman, R. A. (2000). Estimation of wave phase speed and nearshore bathymetry from video imagery. *Journal of Geophysical Research: Oceans*, 105:22015–22033.

Stockdon, H. F., Jr., A. H. S., List, J. H., and Holman, R. A. (2002). Estimation of shoreline position and change using airborne topographic lidar data. *Journal of Coastal Research*, 18(3):502–513.

Stokes, C., Davidson, M., and Russell, P. (2015). Observation and prediction of three-dimensional morphology at a high-energy macrotidal beach. *Geomorphology*, 243:1–13.

Sánchez-García, E., Balaguer-Beser, A., and Pardo-Pascual, J. E. (2017). C-pro: A coastal projector monitoring system using terrestrial photogrammetry with a geometric horizon constraint. *ISPRS Journal of Photogrammetry and Remote Sensing*, 128:255–273.

Sánchez-García, E., Palomar-Vázquez, J. M., Pardo-Pascual, J. E., Almonacid-Caballer, J., Cabezas-Rabadán, C., and Gómez-Pujol, L. (2020). An efficient protocol for accurate and massive shoreline definition from mid-resolution satellite imagery. *Coastal Engineering*, 160.

Taylor, K. E. (2001). Summarizing multiple aspects of model performance in a single diagram. *Journal of Geophysical Research Atmospheres*, 106:7183–7192.

Thom, B. G. and Hall, W. (1991). Behaviour of beach profiles during accretion and erosion dominated periods. *Earth Surface Processes and Landforms*, 16:113–127.

Toimil, A., Camus, P., Losada, I. J., Cozannet, G. L., Nicholls, R. J., Idier, D., and Maspataud, A. (2020). Climate change-driven coastal erosion modelling in temperate sandy beaches: Methods and uncertainty treatment. *Earth-Science Reviews*, 202.

Toure, S., Diop, O., Kpalma, K., and Maiga, A. S. (2019). Shoreline detection using optical remote sensing: A review. *ISPRS International Journal of Geo-Information*, 8.

Traboulsi, M., Idier, D., Castelle, B., Robinet, A., Marieu, V., Durand, E., and McCarroll, R. J. (2025). A coupling approach for long-term 3d morphological evolution of sandy coasts under sea-level rise. *Environmental Modelling and Software*, 193.

Tran, Y. H. and Barthélemy, E. (2020). Combined longshore and cross-shore shoreline model for closed embayed beaches. *Coastal Engineering*, 158.

Turki, I., Medina, R., Coco, G., and Gonzalez, M. (2013). An equilibrium model to predict shoreline rotation of pocket beaches. *Marine Geology*, 346:220–232.

Turner, I. L., Harley, M. D., and Drummond, C. D. (2016a). Uavs for coastal surveying. *Coastal Engineering*, 114:19–24.

Turner, I. L., Harley, M. D., Short, A. D., Simmons, J. A., Bracs, M. A., Phillips, M. S., and Splinter, K. D. (2016b). A multi-decade dataset of monthly beach profile surveys and inshore wave forcing at narrabeen, australia. *Scientific Data*, 3.

Turner, I. L., Whyte, D., Ruessink, B., and Ranasinghe, R. (2007). Observations of rip spacing, persistence and mobility at a long, straight coastline. *Marine Geology*, 236:209–221.

Tătui, F. and Vespremeanu-Stroe, A. (2017). *Evolution and morphodynamics of danube delta shoreface*, pages 607–626. Springer.

USACE (1984). *Shore protection manual*, volume v.2. Vicksburg, Miss, Dept. of the Army, Waterways Experiment Station, United States Army Corps of Engineers, Coastal Engineering Research Center, 1984.

Uunk, L., Wijnberg, K. M., and Morelissen, R. (2010). Automated mapping of the intertidal beach bathymetry from video images. *Coastal Engineering*, 57:461–469.

Valverde, F., Taborda, R., East, A. E., and Lira, C. P. (2025). Historical coast snaps: Using centennial imagery to track shoreline change. *Remote Sensing*, 17.

Van Koningsveld, M., Davidson, M. A., and Huntley, D. A. (2005). Matching science with coastal management needs: The search for appropriate coastal state indicators. *Journal of Coastal Research*, 21:399–411.

van Rijn, L. C. and Huisman, B. J. (2025). Long term modelling of longshore sand transport and coastline changes along central coast of holland. *Coastal Engineering*, 202.

Vandenhove, M., Castelle, B., Lerma, A. N., Marieu, V., and Mazeiraud, V. (2025). Beach-dune dynamics and coastal management along the north-médoc coastline, southwest france: a decade of morphological change and erosion mitigation. *Geomorphology*, 482.

Vespremeanu-Stroe, A., Zăinescu, F., Preoteasa, L., Tătui, F., Rotaru, S., Morhange, C., Stoica, M., Hanganu, J., Timar-Gabor, A., Cârdan, I., and Piotrowska, N. (2017). Holocene evolution of the danube delta: An integral reconstruction and a revised chronology. *Marine Geology*, 388:38–61.

Vieira, M., Soares, C. G., Guimarães, P. V., Bergamasco, F., and Campos, R. M. (2025). Nearshore space-time ocean wave observation using low-cost video cameras. *Coastal Engineering*, 197.

Vitousek, S., Barnard, P. L., Limber, P., Erikson, L., and Cole, B. (2017). A model integrating longshore and cross-shore processes for predicting long-term shoreline response to climate change. *Journal of Geophysical Research: Earth Surface*, 122:782–806.

Vitousek, S., Buscombe, D., de la Peña, E. G., Calcraft, K., Lundine, M., Splinter, K. D., Coco, G., and Barnard, P. L. (2025). Are equilibrium shoreline models just convolutions? *Journal of Geophysical Research: Earth Surface*, 130.

Vitousek, S., Buscombe, D., Vos, K., Barnard, P. L., Ritchie, A. C., and Warrick, J. A. (2023a). The future of coastal monitoring through satellite remote sensing. *Cambridge Prisms: Coastal Futures*, 1.

Vitousek, S., Cagigal, L., Montaño, J., Rueda, A., Mendez, F., Coco, G., and Barnard, P. L. (2021). The application of ensemble wave forcing to quantify uncertainty of shoreline change predictions. *Journal of Geophysical Research: Earth Surface*, 126.

Vitousek, S., Vos, K., Splinter, K. D., Erikson, L., and Barnard, P. L. (2023b). A model integrating satellite-derived shoreline observations for predicting fine-scale shoreline response to waves and sea-level rise across large coastal regions. *Journal of Geophysical Research: Earth Surface*.

Vos, K., Harley, M. D., Splinter, K. D., Simmons, J. A., and Turner, I. L. (2019a). Sub-annual to multi-decadal shoreline variability from publicly available satellite imagery. *Coastal Engineering*, 150:160–174.

Vos, K., Harley, M. D., Turner, I. L., and Splinter, K. D. (2023a). Pacific shoreline erosion and accretion patterns controlled by el niño/southern oscillation. *Nature Geoscience*, 16(2):140 – 146. Cited by: 79; All Open Access, Green Open Access.

Vos, K., Splinter, K., Palomar-Vázquez, J., Pardo-Pascual, J., Almonacid-Caballer, J., Cabezas-Rabadán, C., Kras, E., Luijendijk, A., Calkoen, F., Almeida, L., Pais, D., Klein, A., Mao, Y., Harris, D., Castelle, B., Buscombe, D., and Vitousek, S. (2023b). Benchmarking satellite-derived shoreline mapping algorithms. *Communications Earth and Environment*, 4(1).

Vos, K., Splinter, K. D., Harley, M. D., Simmons, J. A., and Turner, I. L. (2019b). Coastsat: A google earth engine-enabled python toolkit to extract shorelines from publicly available satellite imagery. *Environmental Modelling and Software*, 122.

Vousdoukas, M. I., Kirupakaramoorthy, T., Oumeraci, H., de la Torre, M., Wübbold, F., Wagner, B., and Schimmels, S. (2014). The role of combined laser scanning and video techniques in monitoring wave-by-wave swash zone processes. *Coastal Engineering*, 83:150–165.

Vousdoukas, M. I., Ranasinghe, R., Mentaschi, L., Plomaritis, T. A., Athanasiou, P., Luijendijk, A., and Feyen, L. (2020). Sandy coastlines under threat of erosion. *Nature Climate Change*, 10:260–263.

Warrick, J. A., Buscombe, D., Vos, K., Bryan, K. R., Castelle, B., Cooper, J. A. G., Harley, M. D., Jackson, D. W., Ludka, B. C., Masselink, G., Palmsten, M. L., de Alegria-Arzaburu, A. R., Sénéchal, N., Sherwood, C. R., Short, A. D., Sogut, E., Splinter, K. D., Stephenson, W. J., Syvitski, J., and Young, A. P. (2024). Coastal shoreline change assessments at global scales. *Nature Communications*, 15.

Wijnberg, K. M. and Terwindt, J. H. J. (1995). Extracting decadal morphological behaviour from high-resolution, long-term bathymetric surveys along the holland coast using eigenfunction analysis. *Marine Geology*, 126:301–330.

Williams, W. W. (1947). The determination of gradients on enemy-held beaches. *The Geographical Journal*, 109(1/3):76–90.

Wilson, G. W., Özkan Haller, H. T., Holman, R. A., Haller, M. C., Honegger, D. A., and Chickadel, C. C. (2014). Surf zone bathymetry and circulation predictions via data assimilation of remote sensing observations. *Journal of Geophysical Research: Oceans*, 119:1993–2016.

Wright, L. D. and Short, A. D. (1984). Morphodynamic variability of surf zones and beaches: A synthesis. *Marine Geology*, 56:93–118.

Wright, L. D., Short, A. D., and Green', M. O. (1985). Short-term changes in the morphodynamic states of beaches and surf zones: An empirical predictive model*. *Marine Geology*, 62:339–364.

Wulder, M. A., Roy, D. P., Radeloff, V. C., Loveland, T. R., Anderson, M. C., Johnson, D. M., Healey, S., Zhu, Z., Scambos, T. A., Pahlevan, N., Hansen, M., Gorelick, N., Crawford, C. J., Masek, J. G., Hermosilla, T., White, J. C., Belward, A. S., Schaaf, C., Woodcock, C. E., Huntington, J. L., Lymburner, L., Hostert, P., Gao, F., Lyapustin, A., Pekel, J. F., Strobl, P., and Cook, B. D. (2022). Fifty years of landsat science and impacts. *Remote Sensing of Environment*, 280.

Xu, H. (2006). Modification of normalised difference water index (ndwi) to enhance open water features in remotely sensed imagery. *International Journal of Remote Sensing*, 27(14):3025–3033.

Xu, N. (2018). Detecting coastline change with all available landsat data over 1986-2015: A case study for the state of texas, usa. *Atmosphere*, 9.

Yamano, H., Shimazaki, H., Matsunaga, T., Ishoda, A., McClennen, C., Yokoki, H., Fujita, K., Osawa, Y., and Kayanne, H. (2006). Evaluation of various satellite sensors for waterline extraction in a coral reef environment: Majuro atoll, marshall islands. *Geomorphology*, 82:398–411.

Yates, M., Guza, R., O'Reilly, W., and Seymour, R. (2009a). Overview of seasonal sand level changes on southern california beaches. *Shore & Beach*, 77:39–46.

Yates, M. L., Guza, R. T., and O'Reilly, W. C. (2009b). Equilibrium shoreline response: Observations and modeling. *Journal of Geophysical Research: Oceans*, 114.

Yates, M. L., Guza, R. T., O'Reilly, W. C., Hansen, J. E., and Barnard, P. L. (2011). Equilibrium shoreline response of a high wave energy beach. *Journal of Geophysical Research: Oceans*, 116.

Zeigler, J. M. and Tuttle, S. D. (1961). Beach changes based on daily measurements of four cape cod beaches. *The Journal of Geology*, 69:583–599.

Zhang, J. and Larson, M. (2021). Decadal-scale subaerial beach and dune evolution at duck, north carolina. *Marine Geology*, 440.

Zăinescu, F. I., Vespremeanu-Stroe, A., and Tătui, F. (2019). The formation and closure of the big breach of sacalin spit associated with extreme shoreline retreat and shoreface erosion. *Earth Surface Processes and Landforms*, 44:2268–2284.

L'udovít Kovanič, Topitzer, B., Peťovský, P., Blišťan, P., Gergeľová, M. B., and Blišťanová, M. (2023). Review of photogrammetric and lidar applications of uav. *Applied Sciences (Switzerland)*, 13.